Politecnico di Bari

Department of Mechanics, Mathematics and Management
MECHANICAL AND MANAGEMENT ENGINEERING
Ph.D. Program
SSD: ING-IND/06–FLUID DYNAMICS
ING-IND/14–MECHANICAL DESIGN AND
MACHINE CONSTRUCTION

Final Dissertation

Prediction models for the dynamical behaviour of multi-phase annular seals

by
Gioacchino Grimaldi

Supervisors:

Prof. Ing. Giuseppe Pascazio

Prof. Ing. Luciano Afferrante

Coordinator of Ph.D Program:
Prof. Giuseppe Demelio

Course n°30, 01/11/2014-31/10/2017

Department of Mechanics, Mathematics and Management
MECHANICAL AND MANAGEMENT ENGINEERING
Ph.D. Program
SSD: ING-IND/06–FLUID DYNAMICS
ING-IND/14–MECHANICAL DESIGN AND
MACHINE CONSTRUCTION

Final Dissertation

Prediction models for the dynamical behaviour of multi-phase annular seals

---

by
Gioacchino Grimaldi

Referees:

Prof. Ing. Vittorio Michelassi

Prof. Ing. Paola Forte

Supervisors:

Prof. Ing. Giuseppe Pascazio

Prof. Ing. Luciano Afferrante

Coordinator of Ph.D Program:
Prof. Giuseppe Demelio

Course n°30, 01/11/2014-31/10/2017

Prediction models for the dynamical behaviour of multi-phase annular seals

Gioacchino Grimaldi

January 25, 2018

Abstract

An increasing interest has been devoted in the last two decades in the study and development of multiphase pumps. Multiphase pumps elaborate mixtures of immiscible fluids (both compressible and not) at high speed and power density per stage in order to reduce size and cost. These peculiarities make this kind of turbomachinery very attractive in different industrial sectors such as *Oil&Gas*, both for sub-sea and topside applications, chemical and pharmaceutical industry. Of primary importance, in the machine design phase, is the evaluation of the turbomachinery rotordynamic stability, to ensure high reliability and service continuity specially when maintenance works are difficult and expensive. In this respect, the evaluation of the seal rotordynamic coefficients is usually achieved through simplified bulk flow models, based on the Navier-Stokes equations averaged over the fluid meatus (i.e. the rotor-stator clearance); the problem closure is achieved with the aid of both numerical and experimental correlations. Bulk flow models are characterized by some important peculiarities such as ease of use and fastness. They show however some weakness. In the specific case of multiphase pumps, for example, the application of the single phase correlations to the multiphase field can lead to inaccuracy and misleading results. In this regard, the aim of this doctoral research is to propose a new bulk flow model for the characterization of the structural response of an annular pressure seal operating in the multiphase flow regime. The proposed model is based on the major hypothesis of a smooth stratification of the two fluids. It is hypothesized that the liquid is centrifuged toward the stator, leaving the rotor in contact only with the gas. This assumption allows to derive a two-layer bulk model for each of the two phases.

Chapter 1 introduces the usual notation of the structural stability analysis. The model of the seal structural response is outlined.

Chapter 2 reviews the literature in the field of the single phase annular pressure seal modeling and characterization. Both CFD and bulk flow models are scrutinized. Finally, both the methods are compared with experimental measurements.

Chapter 3 deals about the multi-phase annular seal modeling. The chapter especially analyzes the widest adopted two-phase bulk model in literature: the homogeneous two-phase model. A global review about the specific literature is introduced. A new general formulation of the boundary conditions is proposed. Model assessment in done through the comparison with experimental results.

Chapter 4 presents the new stratified bulk flow model. Bulk flow equations are introduced. Correlations of both momentum flux integrals and friction factors are modeled for each of the two phases depending on the specific flow regime (turbulent rather than laminar). Predicted mass flow rates shows good agreement with experimental results.

Contents

Chapter 1

Seal structural characterization

1.1 Introduction to the structural stability analysis

A fundamental part of the design of a turbomachine is the study of its structural stability. Stability entails capacity of the system to return to its initial configuration after the action of a disturbance. In the field of the turbomachines, concentrated parameter models are usually adopted to study rotordynamics (see [46] and [60]). The forces $\bar{f}$ acting on the system are related to the displacements $\bar{z}$ (which, in the case of a rotordynamic system, are the radial and axial displacements of the rotor at different axial positions) through

$$\bar{f} = \overline{\overline{M}}\ddot{\bar{z}} + \overline{\overline{C}}\dot{\bar{z}} + \overline{\overline{K}}\bar{z} \tag{1.1}$$

where $\overline{\overline{M}}$, $\overline{\overline{C}}$ and $\overline{\overline{K}}$ are respectively the inertia, damping and stiffness matrices, assumed independent of $\bar{z}$ and its time derivatives. The displacements of interest constituting the vector $\bar{z}$ usually refer to (i) a sudden change in the shaft section, or (ii) the point of application of an external force, or (iii) a support (*e.g.* bearings, seals) or (iv) a concentrated mass (*e.g.* impeller, toothed whells, ecc...).

The flexural and torsional degree of freedom (DOF) of the system can be considered uncoupled only if the suspended masses have negligible polar inertia moment, *i.e.* when they are fixed to the rotor with a negligible eccentricity. Flexural and torsional DOFs become also coupled in case of rotor unbalance.

By applying the Laplace transform (with $\bar{z}_0 = 0$ $\dot{\bar{z}}_0 = 0$), eq. (1.1) becomes:

$$\bar{F}(s) = \left[\overline{\overline{M}}s^2 + \overline{\overline{C}}s + \overline{\overline{K}}\right]\bar{Z}(s) = H(s)Z(s) \tag{1.2}$$

where $H(s)$ denotes the complex impedance of the system.

The stability condition of the system requires that the roots of $det[H(s)] = 0$ have negative real part, which corresponds to an exponential decaying of displacements after the action of an external disturbance.

1.2 Seal structural response

In order to characterize the seal structural response, the above matrix formulation is employed. Specifically, the components of the seal reaction force, acting on the rotor (F_y and F_x), are linearly correlated to the rotor radial displacements, velocity and acceleration through

$$\begin{bmatrix} F_x \\ F_y \end{bmatrix} = \begin{bmatrix} M_{xx} & M_{xy} \\ M_{yx} & M_{yy} \end{bmatrix} \begin{bmatrix} \ddot{x} \\ \ddot{y} \end{bmatrix} + \begin{bmatrix} D_{xx} & D_{xy} \\ D_{yx} & D_{yy} \end{bmatrix} \begin{bmatrix} \dot{x} \\ \dot{y} \end{bmatrix} + \begin{bmatrix} K_{xx} & K_{xy} \\ K_{yx} & K_{yy} \end{bmatrix} \begin{bmatrix} x \\ y \end{bmatrix} \tag{1.3}$$

This matrix relation is written under the assumption of the seal matrix coefficients not dependent on the displacement vector and its derivatives. Moreover, the force coefficients are considered independent of the rotor flexural DOF (this is not entirely correct in the case of long seal with $L/R > 1.5$). These simplifications hold for small to moderate eccentricity ($\varepsilon \leq 0.5$). When the rotor radial displacements reach the rotor-to-stator clearance, the rotor-seal interaction in no longer linear and (1.3) needs to be corrected.

In the frequency domain eq. (1.3) can be written as (overbars denote Fourier transforms of the variables)

$$\begin{bmatrix} \overline{F}_x \\ \overline{F}_y \end{bmatrix} = \begin{bmatrix} K_{xx} - \omega^2 M_{xx} + j\omega D_{xx} & K_{xy} - \omega^2 M_{xy} + j\omega D_{xy} \\ K_{yx} - \omega^2 M_{yx} + j\omega D_{yx} & K_{yy} - \omega^2 M_{yy} + j\omega D_{yy} \end{bmatrix} \begin{bmatrix} \overline{x} \\ \overline{y} \end{bmatrix} \tag{1.4}$$

The sum $H_{ij}(\omega) = K_{ij} - \omega^2 M_{ij} + j\omega D_{ij}$ is said complex impedance. For both rotor and stator perfectly circular the seal is isotropic, in the sense that its impedance is invariant under a rotation of the reference frame about the meridian axis. In such case, eq. (1.3) simplifies in:

$$\begin{bmatrix} F_x \\ F_y \end{bmatrix} = \begin{bmatrix} M & m \\ -m & M \end{bmatrix} \begin{bmatrix} \ddot{x} \\ \ddot{y} \end{bmatrix} + \begin{bmatrix} D & d \\ -d & D \end{bmatrix} \begin{bmatrix} \dot{x} \\ \dot{y} \end{bmatrix} + \begin{bmatrix} K & k \\ -k & K \end{bmatrix} \begin{bmatrix} x \\ y \end{bmatrix} \tag{1.5}$$

The reaction force can also be splitted into its direct (i.e. parallel to the rotor displacement) F_n and normal components F_t, respectively.

Under the assumption of a perfect circular orbit of the rotor around the stator center, the rotor vibration at the seal is described by the following time-dependent displacements

$$x(t) = \delta cos(\omega t); \quad y(t) = \delta sin(\omega t) \tag{1.6}$$

By substituting (1.6) into (1.5), for $t = 2k\pi$ ($k = 0, 1, 2..n$) will be $x = x_{max} = \delta$ and $y = 0$; then, direct and normal components of the reaction will be, respectively

$$F_n = F_x = (K - \omega^2 M + \omega d)\delta \tag{1.7a}$$
$$F_t = F_y = (-k + \omega^2 m + \omega D)\delta \tag{1.7b}$$

Eq. (1.7) allows to empirically derive stiffness, damping and mass coefficients of the seal by a parabolic fit on the measured (experimental) or computed (CFD or bulk-model) curves relating normal and tangential forces to the frequency of excitation. In figure 1.1 is sketched the rotor whirl motion and seal reaction forces. Here, the whirl is simplified as a circular orbital motion of the rotor center O' around the stator center O. The seal reaction force (not shown in figure), resulting by the pressure field inside the fluid film, can be decomposed into its direct (F_n) and quadrature (F_t) components that respectively oppose the rotor radial displacement and whirl orbital motion.

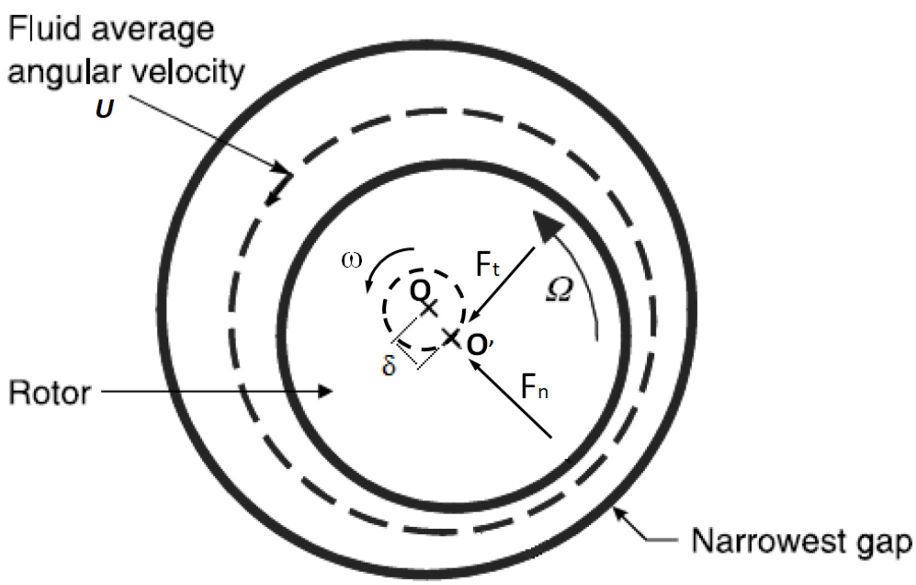

Figure 1.1: A simplified picture showing the rotor whirl motion.

When the quadrature component F_t becomes negative (*i.e.* it is opposed to that reported in the figure), the rotor whirl is no more damped but enhanced. In practice, the whirl instability threshold over which the tangential force enhances the rotor vibration can be easily calculated by enforcing $F_t < 0$ in (1.7b). For small values of m (as usually happens) this condition reduces to:

$$F_t = (-k + \omega D)\delta < 0 \tag{1.8}$$

When (1.8) is verified, the seal reaction force has a destabilizing effect on the rotor dynamic. The ratio between the frequency at which the tangential stiffness (F_t/δ) vanishes and the rotor speed $\omega_c/\Omega = k/(D\Omega)$ is known as "whirl ratio". Larger values of ω_c means larger range of frequency for which the tangential force is destabilizing, giving an increased risk of rotor instability.

1.3 Fluid induced instabilities

This section first introduces the past literature and the industrial progresses that had led to the today's knowledge about rotordynamics with a particular focus on the history of the progresses in the field of the fluid induced instability phenomena. The section concludes with an introduction on the modern industrial practice in the field on the fluid instability detection and reduction.

1.3.1 History

The first rotordynamic analysis was made by Rankine [53] in 1869. In his work, he stated (incorrectly) that the rotor can run in a stable equilibrium only at speeds lower that its first critical speed. This led to a design philosophy that promoted short bearing span and large shaft diameters. This wrong conviction was confuted by the experimental work of DeLaval that explained the "critical speed inversion" thanks to the analytical works on Foppl and DeLaval [21]. The influence of the bearings on the rotordynamic stability was partially recognized after the work of Reynolds [54]. Despite the advances promoted by the DeLaval's work, many vibration related failure were still observed. This led the Royal Society of London to commission H. H. Jeffcott for further analysis. His work [29] was the first to include the effect of damping in the rotordynamic analysis of an unbalanced shaft. In this way Jeffcott explained how whirling amplitude could be reduced by rotor balancing, higher damping and operating speeds far from the first critical speed.

In 1920, the failure of some furnace compressors under anomalous subsynchronous "whipping" led GE to further investigations made by Newkirk. He found [49] that the phenomenon was independent on the rotor unbalance, occurred on at speeds higher than the first critical speed, the frequency vibration was near the rotor first critical speed and occurred only on built-up rotors. Kimball, working with Newkirk, postulated [32] and later proved experimentally [33] that the internal friction or damping, much greater in built-up rotors, could produce internal moments that at supercritical speeds would lead the rotor whirling. In 1933, the concept of cross-coupled force appeared in the literature thanks to Smith [58]. J. S. Alford [1] in 1965 documented self-excited whirl in an axial compressor supported on ball and roller bearings. He hypothesized that the whirl could be induced by negative damping from labyrinth seals or an aerodynamic follower force due to the tip clearance variation around the circumference of the compressor blades thereafter known as Alford's force. J. W. Lund [38] in his doctoral thesis (1966) defined linearized force coefficients still today adopted in most computer simulations. Successively, Lund [37] (1974) published an algorithm for the computation of the damped eigenvalues of a rotor-bearing system where cross-coupled stiffness is taken into account. Many contributions on the theme came from the analytic and experimental analysis made for the design of the Space Shuttle fuel turbopump (Childs[10, 10]). Further developments in the field on the seal-induced rotordynamic instability follow in section 2.1.

1.3.2 Fluid instability detection

As stated before, interaction between rotor whirl motion and fluid flow produces a circumferential perturbation in the pressure field which causes self-excited radial forces (moments are usually neglected). Such forces can have a destabilizing effect when rotor angular speed exceeds his instability threshold.

The analytic computation of the unstable damped frequencies requires the solution of the characteristic polynomial of the system stiffness matrix, which can be analytically accomplished only in very simple cases (fourth order characteristic polynomial).

The fluid-rotor interaction can lead to two distinct kind of instability: fluid whirl and fluid whip.

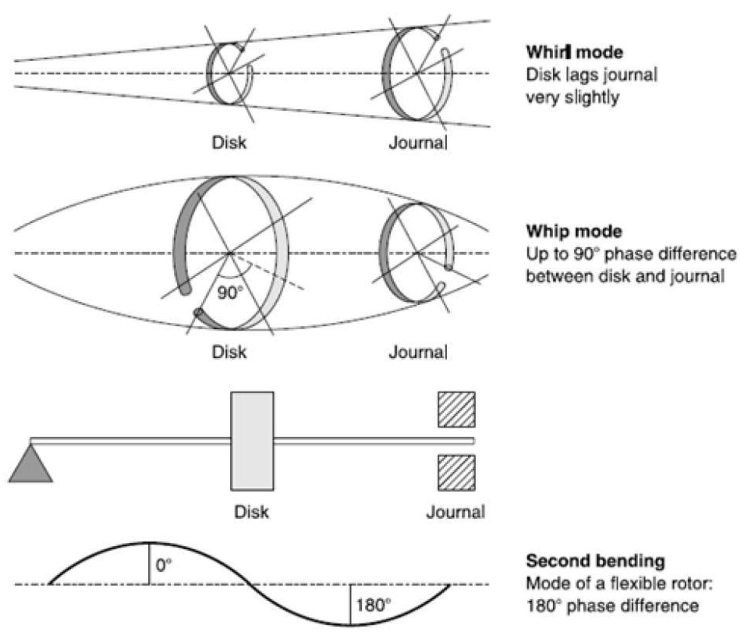

Figure 1.2: Sketch of the rotor whirl and whip motion.

The fluid whirl is characterized by large amplitude rotor vibrations with characteristic frequency of about $\omega \approx 0.5\Omega$. The fluid whirl usually appears at low rotational speeds, under this condition the rotor experiences rigid body vibrations, as shown in figure 1.2. Though the rigid body vibrations do not produces large deformations (and stresses) on the rotor, the large amplitude of the displacements can lead to support damages, noise and transmission of large amplitude vibrations to the surrounding environment.

The fluid whip, differently by the fluid whirl, is characterized by a constant frequency corresponding to the first natural frequency of the flexural mode. The fluid whip usually appears at higher velocity than the fluid whirl, though the transition between the two phenomena is gradual. The high deformations induced on the rotor can cause low cycle fatigue rotor failure.

Usually, whirl and whip motions are detected with the aid of proximity transducers mapping the rotor radial displacements. Figure 1.3 shows the full spectrum (both clockwise and counterclockwise orbits) cascade of the rotor lateral vibration measured at the fluid-lubricated bearing during start-up (with low constant angular acceleration).

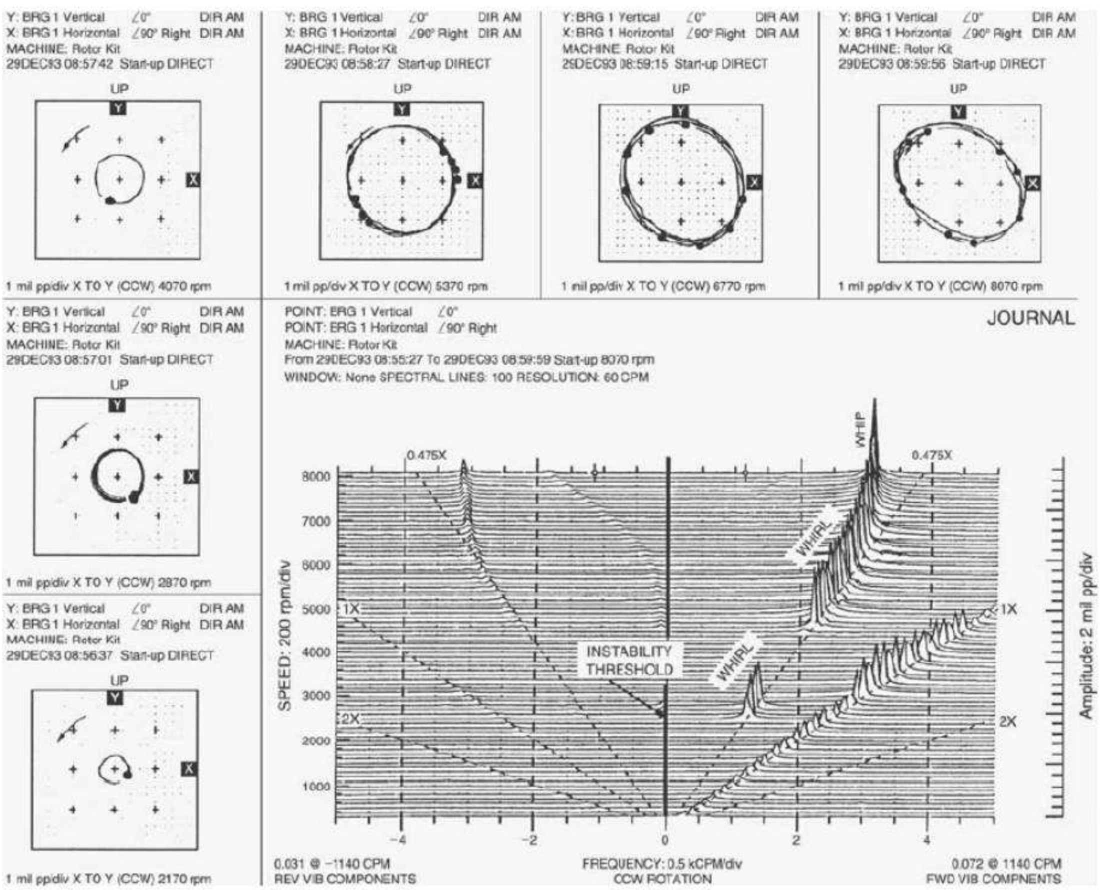

Figure 1.3: Example of full spectrum cascade of rotor lateral vibrations ([46] page 217).

The figure shows also the rotor orbits at several rotational speeds. When the rotor angular speed exceeds the instability threshold, the amplitude of the radial vibration starts to increase.

At higher eccentricities, the activation of fluid film nonlinear effects leads the rotor vibration to a new equilibrium condition. Large amplitude subsynchronous vibration ($\omega = 0.475\Omega$) overlaps to a synchronous vibration, due to rotor unbalance. The rotor vibrations reaches a new equilibrium characterized by high amplitude vibrations that activates nonlinear fluid film effects. When the rotor speed Ω increases, the fluid whirl gradually degenerates in fluid whip. No counterclockwise vibrations are present. The observed self-excited vibrations in fact shows almost circular orbits.

Both fluid whirl and whip can be observed even at higher rotational speeds (not shown in figure 1.3) associated with second and higher mode vibrations.

1.3.3 Fluid instability reduction

The fluid-induced destabilizing effect, given by the seal cross-coupled stiffness, may be attenuated by suppressing the fluid circumferential velocity inside the seal.

Different solutions are adopted in the industrial contest, with different performances and costs.

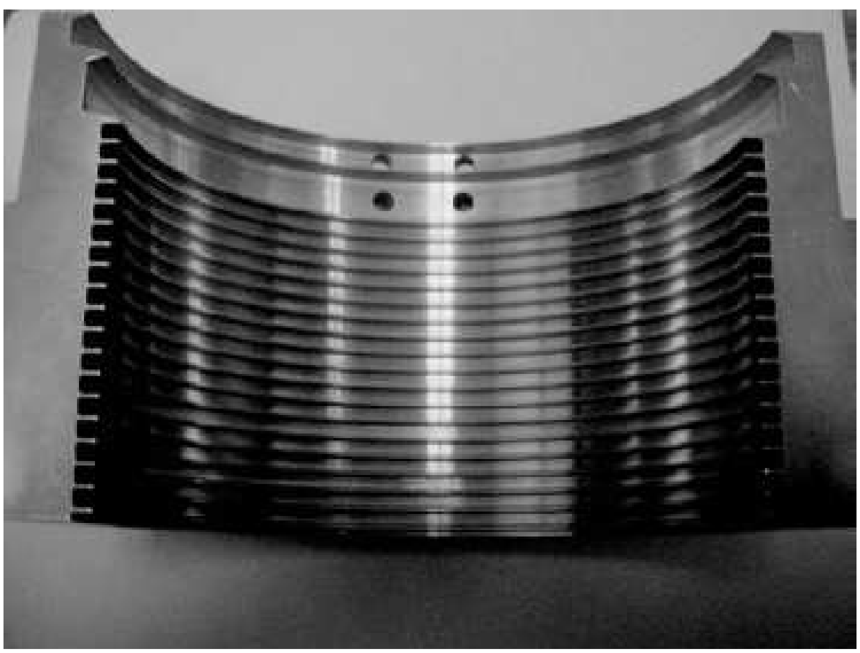

Figure 1.4: Gas labyrinth seal

Floating Ring Seals

The seal is confined by the rotor surface and a floating ring housed between the rotor and stator. The only force acting on the rotor is the sliding friction with the floating ring. At high pressure drops however, the ring is blocked by the static friction exchanged with the stator. In this condition the ring acts as a journal bearing and fluid instability could be induced. A way to prevent this drawback is to reduce the hydrodynamic axial length of the ring even if this reduces its damping capacity.

Gas labyrinth seal

The gas labyrinth seals are the most common shaft seals adopted for high-speed turbomachinery operating with gas fluid. They are usually adopted to improve the machine efficiency by the leakage reduction. Gas labyrinth seal are however characterized by negative whirl ratio especially in the tooth-on-rotor configuration, where faster circumferential flows are developed.

Pocket damper seal

A pocket damper seal is constituted by an axial series of circumferential cavities. With reference to figures 1.5-1.6, the cavities are axially confined by an inlet blade, identical to a labyrinth seal tooth and an outlet or downstream blade characterized by larger clearance or slots in the way that the leakage flow is not affected by the rotor vibration (δ is mush smaller than the outlet blades clearance or slots). The configuration with slots is characterized by a higher damping. The cavities are circumferentially confined by partition walls.

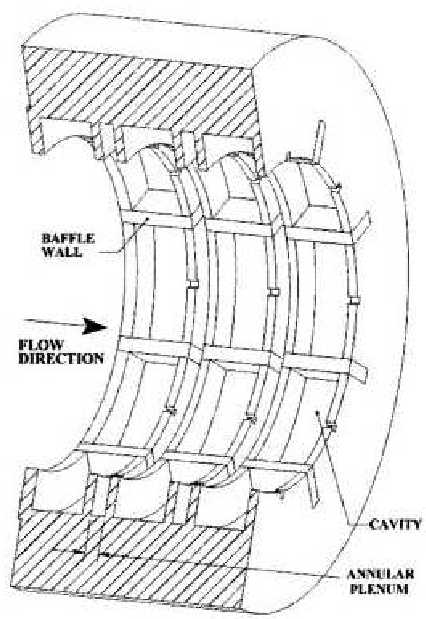

Figure 1.5: Pocket dumper seal

Between two consecutive cavities distribution there is an inactive annular volume (the annular plenum in the figures) with no partition walls where the pressure is constant around the circumference. Focusing on the fluid dynamics of every single cavity during the rotor vibration, there will be two principal effects acting on the cavity pressure: the inlet/outlet leakages variation and the volume variation during the rotor vibration. During the rotor vibration the leakage that flows into the cavity is modulated by the inlet blade while the outlet leakage variation is minimized because of the larger clearance or the presence of slot. This leads every single cavity to operate as a gas spring during the rotor vibration.

The damping action is mostly related to the compressibility of the working fluid. Hence, the pocket damper seal response is weakly influenced by the seal inlet swirl, turbulence and viscosity. When this consideration is applied to the rotor whirl motion, the resulting tangential force has always a stabilizing effect. Pocket damper seal can also present a ”fully partitioned” design. The only difference with the conventional geometry is that the partition walls extends also to the annular plenum. In this new design the ”partitioned” annular plenum gives to every cavity a different exit pressure in the way to enhance the damping action of the cavity. The pocket damper seal has been patented by the Texas $A\&M$ University. It is licensed and marketed under the trade name TAMSEAL by KMC, Inc. and Bearings Plus, Inc.

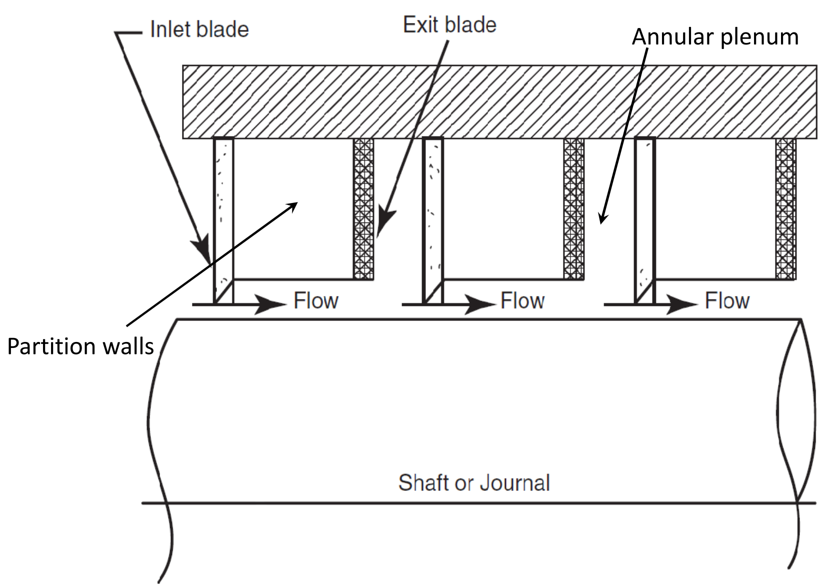

Figure 1.6: Axial distribution of the partition walls and blades in a pocket damper seal

Honeycomb and Hole-pattern seal

Figure 1.7 shows an example of an hole-pattern seal. Honeycomb and Hole-pattern seals were first adopted with the aim of reducing leakage. Successive analysis showed their positive effect in suppressing also fluid-induced instability. They explicate their stabilizing effect by reducing the fluid swirl (circumferential velocity) when the holes or the honeycombs are built on the stator. The main difference between the two types is in the manufacturing process. The manufacturing process of the honeycomb cell is more lengthy and expensive with respect to the simple drilling process required for the hole-pattern realization. Moreover, the materials adopted in the hole-pattern seal (bronze, aluminum or polymers) are more tolerant to the rub with the rotor with respect the materials used for the honeycombs cells (stainless steels or hastelloy).

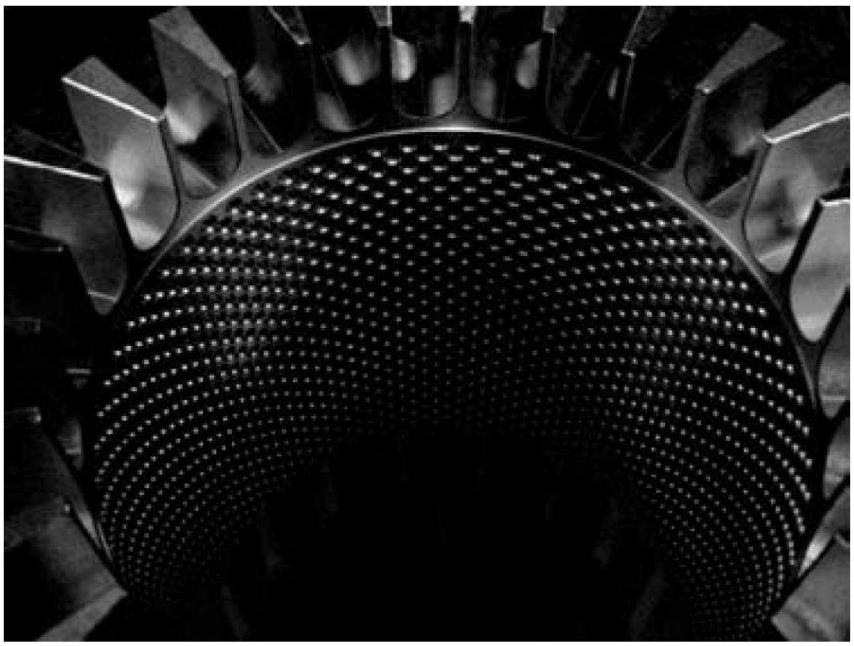

Figure 1.7: Example of hole-pattern seal

Brush seal

Brush seals consist of an array of bristle material (usually an high temperature materials) mounted on the stator. They were originally adopted with the only scope of reducing leakage. Successively it was discovered that bristles prevent also the fluid circumferential swirl, with great benefit for the rotor stability. Little inconvenient are the difficulties in the seal dynamic response prediction, both for CFD limits and absence of pressure drop correlations.

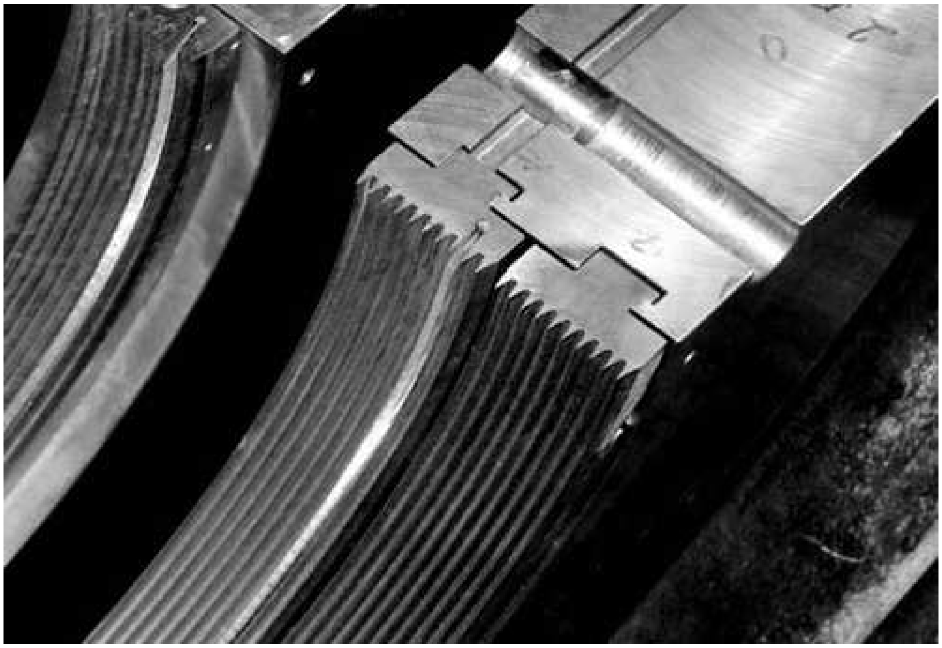

Figure 1.8: Brush seal

Chapter 2

Single phase flows in annular pressure seals

2.1 Introduction

Structural stability of turbomachinery such as turbopumps and compressors are greatly affected by the fluid structure interaction forces arising by the perturbed pressure field in elements as impeller, journal and thrust bearings and seals. The first to identify this kind of phenomena was Lomakin [36]. A first analytical description of the fluid induced forces was made by Black and Jensen [9, 26]. In their analysis they took into account the only frictional pressure drop (Yamada's friction model [62]) and time-dependent fluid inertia to obtain a close form solution. As pointed out by Childs [13], the weakness of the Black and Jensen analysis was in the derivation of "ad hoc" relations for different cases. In his work, Childs gave a closed form solution of the perturbed Hirs' equations [28] through the use of the "short bearing" assumption (negligible pressure induced circumferential flow). The comparison with the Black's model showed some discrepancies given by the different wall friction formulation. Successively Childs [14] integrated his work for the case of long seals concluding that the Hirs' formulation was not suitable in the case of short-seal. The bulk flow theory was then compared to experiments by Childs [11] concluding that direction dependent surface roughness could improve the stiffness damping. Childs and Nelson [12, 48]) compared the bulk model results to experiments in the case of compressible fluid finding that weak agreement in the predicted cross-coupled stiffness. Yang [63] and San Andres [55] analyzed the variation in the stiffness coefficients when temperature variation is taken into account in a liquid annular seal for cryogenic applications. Zirkelback and San Andres [66] proposed a transitional bulk friction factor for low-Re to low-Re applications. This chapter deals with the single phase (liquid or perfect gas) bulk model derivation and results. A new friction factor formulation, based on the Hirs' model is proposed. Experimental results are compared with both CFD and bulk-model predictions. Bulk-model predictions are compared with the single-phase experimental results of the tests done at the Turbomachinery Laboratory of the Texas $A\&M$ University "Experimental Study of the Static and Dynamic Characteristics of a Long (L/D=0.75) Smooth Seal with Mainly Air Mixtures" and "Experimental Study of the Static and Dynamic Characteristics of a Short (L/D=0.29)

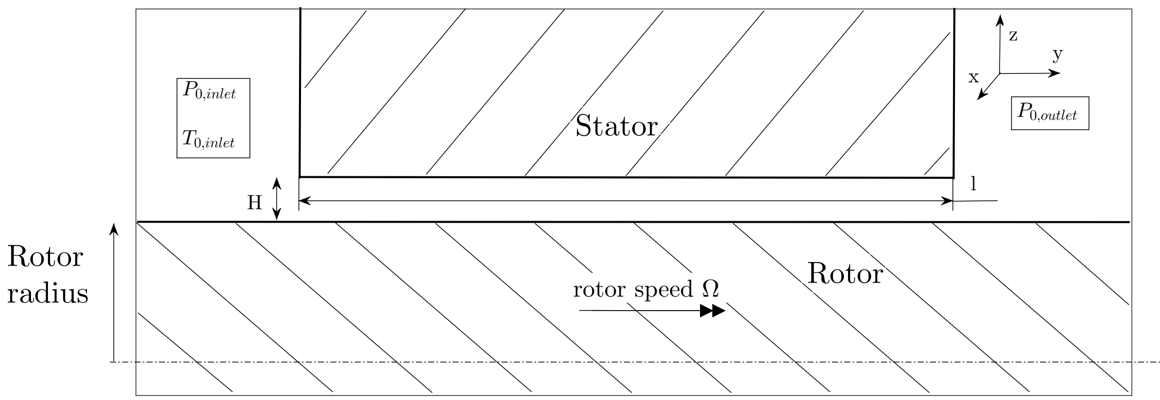

Figure 2.1: seal geometry

Smooth Seal with Mainly Air Mixtures".

2.2 Governing equations

The study of the fluid-structure interaction in an annular pressure seal requires the description of the relation elapsing between the velocity and the state variables (*i.e.* density and pressure) fields within the control volume delimited by the stator and rotor surfaces. These relations are expressed by the well known Navier-Stokes equations. For an general fluid (compressible or not), in an inertial Cartesian reference frame they take the form:

$$\frac{\partial \varrho}{\partial t} + \frac{\partial(\varrho u)}{\partial x} + \frac{\partial(\varrho v)}{\partial y} + \frac{\partial(\varrho w)}{\partial z} = 0 \tag{2.1a}$$

$$\frac{\partial(\varrho u)}{\partial t} + \frac{\partial(\varrho u^2)}{\partial x} + \frac{\partial(\varrho uv)}{\partial y} + \frac{\partial(\varrho uw)}{\partial z} = -\frac{\partial p}{\partial x} + \frac{\partial \tau_{xx}}{\partial x} + \frac{\partial \tau_{xy}}{\partial y} + \frac{\partial \tau_{xz}}{\partial z} \tag{2.1b}$$

$$\frac{\partial(\varrho v)}{\partial t} + \frac{\partial(\varrho uv)}{\partial x} + \frac{\partial(\varrho v^2)}{\partial y} + \frac{\partial(\varrho vw)}{\partial z} = -\frac{\partial p}{\partial y} + \frac{\partial \tau_{yx}}{\partial x} + \frac{\partial \tau_{yy}}{\partial y} + \frac{\partial \tau_{yz}}{\partial z} \tag{2.1c}$$

$$\frac{\partial(\varrho w)}{\partial t} + \frac{\partial(\varrho uw)}{\partial x} + \frac{\partial(\varrho vw)}{\partial y} + \frac{\partial(\varrho w^2)}{\partial z} = -\frac{\partial p}{\partial z} + \frac{\partial \tau_{zx}}{\partial x} + \frac{\partial \tau_{zy}}{\partial y} + \frac{\partial \tau_{zz}}{\partial z} \tag{2.1d}$$

In equation (2.1) p is the fluid pressure, u, v and w are the fluid velocities respectively in the x, y and z directions. At this stage no assumptions about the flow regime (laminar or turbulent) have been made. The geometry of the seal naturally suggests to adopt cylindrical coordinates for the analysis. The Navier-Stokes equations in cylindrical coordinates can be approximated as in equations (2.1), being $\partial/\partial r = O(1/H) \gg 1/R$. Hence, from now on will be $x = R\theta$ the circumferential coordinate, $z = r$ the radial coordinate and y the meridian coordinate.

For low values of the Reynold number, the convective terms in equations (2.1) are negligible and the pressure distribution over the journal surface is described by the well known Reynolds equation. When $Re_c \geq 2000$, the convective terms become a source of instability and turbulent transition is observed, the velocity field become chaotic and the Reynolds equation is no longer suitable. The complete numerical solution of the unsteady Navier-Stokes equations (Direct Numerical Simulations or DNS) in a give domain is still out of the possibility of today IT. It is well known that the computational cost of a DNS, growing approximately with Re^3, makes this kind of simulations accessible only for fundamental research, simple geometries and low to moderate Re, representing a benchmark for the turbulence modeling. The same reasons prevent the use of Large Eddy Simulations (LES) as a prediction tool of the dynamical behaviour of the seal. In case of incompressible seal, where the Re number is usually in the range $10^3 - 10^4$, LES can have however the fundamental role of a benchmark in the calibration process of the constants of a specific RANS model. In this regard, it is useful to notice that the turbulence statistics of a centered incompressible seal, where the asymptotic value of $U = \Omega R/2$ is reached, vary only in the radial direction (1D statistics) making the calibration process straightforward. For practical applications, the turbulent Navier-Stokes equations are usually solved through the RANS approach. The velocity and pressure can be decomposed into their averages and fluctuations:

$$[u\,v\,w](x,y,z,t) = [\overline{u}\,\overline{v}\,\overline{w}](x,y,z,t) + [u'\;v'\;w'](x,y,z,t) \tag{2.2}$$

This decomposition is referred as *Reynolds decomposition*. The equations above are therefore averaged over time to obtain the well known RANS (Reynolds Averaged Navier-Stokes) equations. For an incompressible fluid and body forces g_i negligible:

$$\frac{\partial \overline{u}}{\partial x} + \frac{\partial \overline{v}}{\partial y} + \frac{\partial \overline{w}}{\partial z} = 0 \tag{2.3a}$$

$$\frac{\overline{D}\overline{u}}{Dt} = -\frac{\partial \overline{p}}{\varrho \partial x} + \frac{\partial \tau_{xx}}{\partial x} + \frac{\partial \tau_{xy}}{\partial y} + \frac{\partial \tau_{xz}}{\partial z} - \frac{\partial \overline{u'^2}}{\partial x} - \frac{\partial \overline{u'v'}}{\partial y} - \frac{\partial \overline{u'w'}}{\partial z} \tag{2.3b}$$

$$\frac{\overline{D}\overline{v}}{Dt} = -\frac{\partial \overline{p}}{\varrho \partial y} + \frac{\partial \tau_{yx}}{\partial x} + \frac{\partial \tau_{yy}}{\partial y} + \frac{\partial \tau_{yz}}{\partial z} - \frac{\partial \overline{u'v'}}{\partial x} - \frac{\partial \overline{v'^2}}{\partial y} - \frac{\partial \overline{v'w'}}{\partial z} \tag{2.3c}$$

$$\frac{\overline{D}\overline{w}}{Dt} = -\frac{\partial \overline{p}}{\varrho \partial z} + \frac{\partial \tau_{zx}}{\partial x} + \frac{\partial \tau_{zy}}{\partial y} + \frac{\partial \tau_{zz}}{\partial z} - \frac{\partial \overline{u'w'}}{\partial x} - \frac{\partial \overline{w'v'}}{\partial y} - \frac{\partial \overline{w'^2}}{\partial z} \tag{2.3d}$$

where

$$\frac{\overline{D}}{Dt} = \frac{\partial}{\partial t} + \overline{u}\frac{\partial}{\partial x} + \overline{v}\frac{\partial}{\partial y} + \overline{w}\frac{\partial}{\partial z} \tag{2.4}$$

is the RANS material derivative.

The six new terms represent the variances ($\overline{u'^2}$, $\overline{v'2}$ and $\overline{w'^2}$) and covariances ($\overline{u'w'}$, $\overline{u'v'}$ and $\overline{v'w'}$) of the three velocity components and are known as *Reynolds stresses*. These six new variables make the problem undetermined. There are several RANS turbulence models to achieve the problem closure though the correct choice (or modeling) of the specific model is not trivial for the features of a turbulent annular seal: the turbulent flow is both pressure and shear driven in two normal directions (axial and circumferential). The most diffused RANS models in the industry are the "Linear eddy viscosity" models (LEVM), in particular in the $\kappa - \omega$ and $\kappa - \varepsilon$ version. The RANS models mentioned here gives their best results (in terms of accuracy) for simple shear or pressure driven flows, *i.e.* when can be defined a principal flow direction. In the case of a turbulent annular seal, the axial flow encounter the transverse rotor shear. The flow direction in this specific flow isn't parallel to the pressure gradient neither to the rotor velocity. Accurate dissertations about the turbulence modeling can be found in Pope [52], Wilcox [61] and Launder [34].

The solution of a single RANS simulation (3D domain), however, is more expensive in terms of time and costs with respect to a bulk model (1D-2D domain) where the Navier-Stokes equations are averaged over the clearance. In the first stage of the turbomachinery design, bulk-flow models represents the best compromise between accuracy, velocity and ease of use in the definition of the machine configuration. The bulk-flow model equations obtained by integrating the above equations over the clearance, lead to:

$$\frac{\partial(\rho H)}{\partial t} + \frac{\partial(\rho HU)}{\partial x} + \frac{\partial(\rho HV)}{\partial y} = 0 \tag{2.5a}$$

$$\frac{\partial(\rho HU)}{\partial t} + \frac{\partial I_{xx}}{\partial x} + \frac{\partial I_{xy}}{\partial y} = -H\frac{\partial P}{\partial x} + \tau_{xz}\big|_0^H \tag{2.5b}$$

$$\frac{\partial(\rho HV)}{\partial t} + \frac{\partial I_{xy}}{\partial x} + \frac{\partial I_{yy}}{\partial y} = -H\frac{\partial P}{\partial y} + \tau_{yz}\big|_0^H \tag{2.5c}$$

where:

$$U = \int_0^H \rho\overline{u}\; dz \tag{2.6a}$$

$$V = \int_0^H \rho\overline{v}\; dz \tag{2.6b}$$

$$I_{xx} = \int_0^H \rho\overline{u}^2\; dz \tag{2.6c}$$

$$I_{yy} = \int_0^H \rho\overline{v}^2\; dz \tag{2.6d}$$

$$I_{xy} = \int_0^H \rho\overline{uv}\; dz \tag{2.6e}$$

Although the above equations are obtained from the incompressible Navier-Stokes equations, they can be easily extended to the compressible case by subjoining to the previous equations, the energy and state equations (this is possible because the turbulent compressible flow is always subsonic and both velocity profiles and shear stresses correlations are almost the same as in the incompressible flows):

$$C_p\left[\rho H\frac{DT_b}{Dt}-T_b\frac{D(\rho H)}{Dt}\right]-T_b\beta_t H\frac{DP}{Dt}= \tag{2.7a}$$

$$Q_s+R\Omega\,\tau_{xz}|^H-U\,\tau_{xz}|_0^H-V\,\tau_{yz}|_0^H=L_w$$

$$T_b=f(P,\rho) \tag{2.7b}$$

Trivially is $T_b=\int_0^H T\,dz$, $P=\int_0^H p\,dz$, $\rho=\int_0^H \varrho\,dz$.

In equation (2.7a) $T_b\beta_t=-\frac{T}{\rho}\frac{\partial\rho}{\partial T}|_p$ is the volumetric expansion coefficient and its value spans from 1 in case of ideal gas to 0 for incompressible liquid. For turbulent flows, the velocity profile across the clearance is almost constant; the momentum-flux integrals I_{ij} can be approximated as:

$$I_{xx}=\rho U^2 H \tag{2.8a}$$

$$I_{yy}=\rho V^2 H \tag{2.8b}$$

$$I_{xy}=\rho UVH \tag{2.8c}$$

By substituting (2.8) into (2.5), the resulting system is (Yang et al. [63]):

$$\frac{\partial(\rho H)}{\partial t}+\frac{\partial(\rho HU)}{\partial x}+\frac{\partial(\rho HV)}{\partial y}=0 \tag{2.9a}$$

$$\frac{\partial(\rho HU)}{\partial t}+\frac{\partial(\rho U^2 H)}{\partial x}+\frac{\partial(\rho UVH)}{\partial y}=-H\frac{\partial P}{\partial x}+\tau_{xz}|_0^H \tag{2.9b}$$

$$\frac{\partial(\rho HV)}{\partial t}+\frac{\partial(\rho UVH)}{\partial x}+\frac{\partial(\rho V^2 H)}{\partial y}=-H\frac{\partial P}{\partial y}+\tau_{yz}|_0^H \tag{2.9c}$$

The second and third equation are simplified by differentiating and substituting eq.(2.9a):

$$\frac{\partial U}{\partial t}+U\frac{\partial U}{\partial x}+V\frac{\partial U}{\partial y}=-\frac{1}{\rho}\frac{\partial P}{\partial x}+\frac{\tau_{xz}|_0^H}{\rho H} \tag{2.10a}$$

$$\frac{\partial V}{\partial t}+U\frac{\partial V}{\partial x}+V\frac{\partial V}{\partial y}=-\frac{1}{\rho}\frac{\partial P}{\partial y}+\frac{\tau_{yz}|_0^H}{\rho H} \tag{2.10b}$$

In all the bulk equations above, H is the local height of the thin film (sinusoidal function of x), U the averaged circumferential velocity, V the averaged meridian velocity. Next, the averaged shear stresses on walls $\tau_{ij}|_0^H$ will be expressed as functions of the averaged velocity field.

2.3 Shear stresses on walls

As stated before, eqs.(2.9) derive from the integration of the classical Navier-Stokes equations over the clearance. Though this operation reduces the problem complexity, reducing the spatial dimensions and overcoming all the issues linked to the turbulence modeling, the wall shear stresses are now undefined. The solution of the PDEs problem requires the expression of $\tau_{ij}|_0^H$ as functions of the bulk velocity field. Different wall shear stress models have been proposed in the literature.

Here only the explicit friction factor formulations are reviewed, the Colebrook-White universal law of the wall is taken into account only as reference to evaluate the chosen models.

The first explicit wall shear stress law taken into account is the Moody's friction factor [42].

$$C_f = 0.001375 \left[1 + \left(2000 \frac{e}{D} + \frac{10^6}{Re} \right)^{\frac{1}{3}} \right] \tag{2.11}$$

Equation (2.11) were derived as an approximation of the general Colebrook-White equation [18, 17], e/D is the roughness to diameter ratio, $Re = VD/\nu$ is the pipe Reynolds number. This friction law is specifically derived for pipe flows, the application to the plane channel (an annular pressure seal can be seen as a turbulent channel flow with a streamwise moving wall) requires the formulation of (2.11) is terms of the equivalent hydraulic diameter $D_h = 2H$, operation that usually can introduces some inaccuracy.

The other wall shear stress law examined here is that proposed by Yamada et al. [62].

$$C_f = 0.065 \left(\frac{V_E H}{\nu} \right)^{-0.24} \tag{2.12a}$$

$$V_E = \sqrt{V_a^2 + \left(\frac{7\Omega R}{16} \right)^2} \tag{2.12b}$$

This friction law formulation shows however to the author some limits. In the two limits of pure Couette and Pouiseuille flow, with respectively $Re = \Omega RH/2\nu$ and $Re = VH/\nu$, (2.12) predicts, at given Re, a theoretical Couette wall shear stress higher than the Pouiseuille wall shear stress. This goes in contrast with the known literature that reports lower values of C_f for the Couette flow, as shown in figure 2.2.

In this regard, the figure below shows the universal friction laws fittings. Equation (2.13b) reports the universal friction law fitting by Pirozzoli et al.[51] from DNS of turbulent Couette flow (up to $Re_b = 21000$). Equation (2.13a) reports the universal friction law fitting by Nagib et al. [47] from DNS of turbulent Pouiseuille flow.

$$\sqrt{\frac{2}{C_f}} = \frac{1}{k}\log\left(\frac{Re_b}{2}\sqrt{\frac{C_f}{2}}\right) + C - \frac{1}{k} \quad k = 0.37 \quad C = 3.7 \quad Re_b = \Omega RH/2\nu \tag{2.13a}$$

$$\sqrt{\frac{2}{C_f}} = \frac{1}{k}\log\left(\frac{Re_b}{2}\sqrt{\frac{C_f}{2}}\right) + C + \overline{C} \quad k = 0.41 \quad C = 5 \quad \overline{C} = 0 \quad Re_b = VH/\nu \tag{2.13b}$$

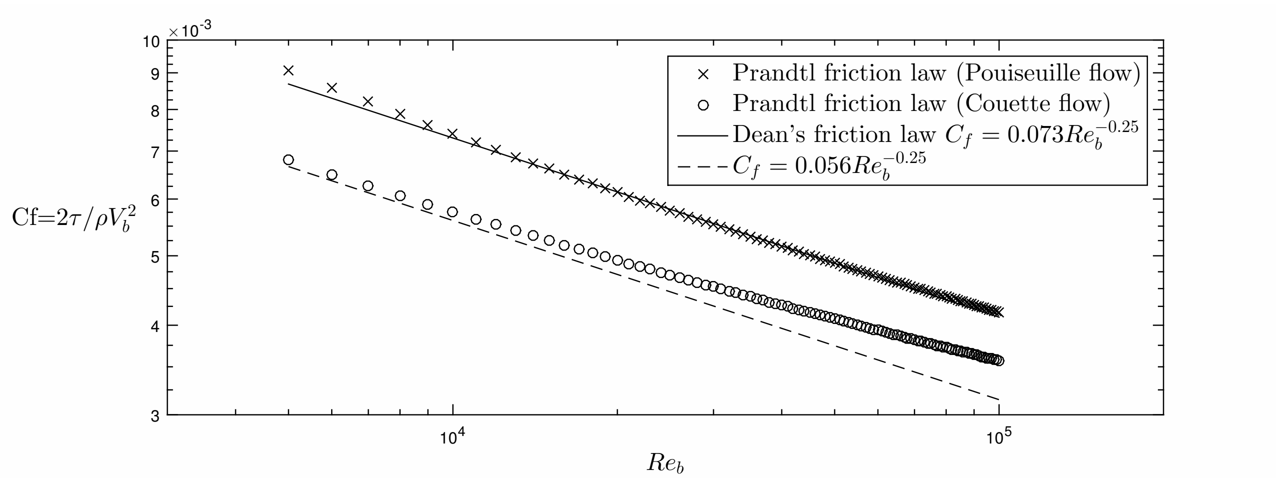

Figure 2.2: Friction laws comparisons. Dashed line - - : Couette fitting, solid line —— Dean's friction law, Symbols: × Pouiseuille universal friction law (2.13a), ∘ Couette universal friction law(2.13b)

Figure 2.2 shows the comparison of the explicit Dean's friction law [19] and the "Dean like" friction factor for the Couette flow with the two respective universal friction laws. While the Dean's predictions perfectly agree with the universal friction law in the rage scrutinized, some discrepancy con be observed between the Couette power law $C_f = 0.056Re_b^{-0.25}$ and the universal friction law for moderate Re.

In this doctoral dissertation a modified version of the model proposed by Hirs [28] will be adopted.

The Hirs model predicts the wall shear stress as:

$$\frac{\tau_w}{\frac{1}{2}\rho W_r^2} = C_{f,r} = n\,\mathrm{Re}_r^m = n\left(\frac{\rho W_r H}{\mu}\right)^m \tag{2.14}$$

where W_r is the bulk velocity magnitude relative to the wall. The coefficients m and n are empirical values obtained from curve fits of the experimental data. For the n coefficient an average value between the two different cases of Couette and Pouiseuille flow must be chosen.

In order to reduce the error and the uncertainty related to the choice of n, here a modified friction factor formulation is proposed. Taking for n the value proposed by Dean, the equivalent bulk velocity for the evaluation of C_f is defined as:

$$W_{r,eq} = \sqrt{9U_r^2 + V_r^2} \tag{2.15}$$

where U_r and V_r are respectively the circumferential and meridian velocity components with respect to wall. The equivalent friction factor becomes:

$$\frac{\tau_w}{\frac{1}{2}\rho W_r^2} = C_{f,r} = n\,\mathrm{Re}_{r,eq}^m = n\left(\frac{\rho W_{r,eq} H}{\mu}\right)^m \tag{2.16}$$

In this way, the two different values of n are recovered in the case of simple shear or pressure driven flow. For a pure Couette flow it is, in fact:

$$\frac{\tau_w}{\frac{1}{2}\rho W_r^2} = n\left(\frac{9\rho U_r H}{\mu}\right)^m = 3^m n\left(\frac{\rho U_r H}{\mu}\right)^m = n'\left(\frac{\rho U_r H}{\mu}\right)^m \tag{2.17}$$

For $n = 0.073$ and $m = -0.25$, $n' = 3^m n = 0.073/\sqrt[4]{3} = 0.056$, which is the value of n for the pure Couette flow.

2.3.1 Stator shear stresses

As stated before, the stresses that the bulk exchanges with the walls are related through eq.(2.16) to the relative velocity between wall and bulk. In the case of the stator, the relative velocity is simply the absolute velocity of the bulk, being the stator velocity null. Therefore in this case will be:

$$W_s = \sqrt{U^2 + V^2} \tag{2.18}$$

$$W_{s,eq} = \sqrt{9U^2 + V^2} \tag{2.19}$$

$$Re_{s,eq} = \frac{\rho W_{s,eq} H}{\mu} \tag{2.20}$$

$$|\tau_s| = \frac{\rho W_s^2}{2} n Re_{s,eq}^m \tag{2.21}$$

Eq.2.21 simply expresses the module of the shear stress. For the bulk flow equations (2.9a)-(2.7a) the axial and circumferential component must be computed. The shear stresses vector is parallel to the relative velocity vector; τ_s therefore is the vector sum of:

$$|\tau_{sm}| = \frac{|\tau_s|\, V}{W_s} \tag{2.22a}$$

$$|\tau_{sc}| = \frac{|\tau_s| U}{W_s} \tag{2.22b}$$

where τ_{sm} is the meridian component and τ_{sc} is the circumferential component.

2.3.2 Rotor shear stresses

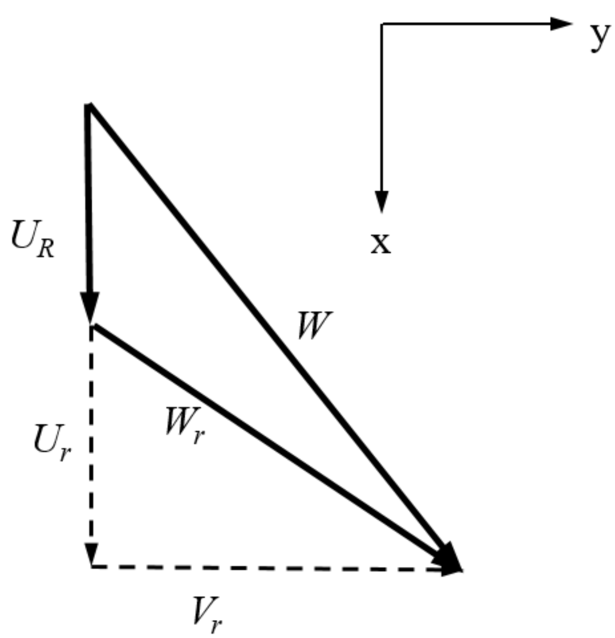

Figure 2.3: Relative motions between the average bulk velocity and the rotor velocity. W= bulk velocity, $U_R = \Omega R$= rotor circumferential velocity,W_r= relative velocity, U_r= circumferential relative velocity, V_r= axial relative velocity.

Figure 2.3 reports the relative motions between the rotor and the averaged bulk velocity. Following what said in section 2.3, the magnitude of the rotor bulk shear stress and the characteristic velocities that defines it are:

$$W_r = \sqrt{(U - \Omega R)^2 + V^2} \tag{2.23}$$

$$W_{r,eq} = \sqrt{9(U - \Omega R)^2 + V^2} \tag{2.24}$$

$$Re_{r,eq} = \frac{\rho W_{r,eq} H}{\mu} \tag{2.25}$$

$$|\tau_r| = \frac{\rho W_r^2}{2} n Re_{r,eq}^m \tag{2.26}$$

The meridian τ_{rm} and circumferential τ_{rc} components of the rotor stresses are defined following the assumption that the wall shear stress direction is parallel to the relative velocity vector U_r:

$$|\tau_{rm}| = -\frac{|\tau_r|\, V}{W_r} \tag{2.27a}$$

$$|\tau_{rc}| = \frac{|\tau_r|\,(\Omega R - U)}{W_r} \tag{2.27b}$$

In eq.(2.27b) , the expression of τ_{rc} doesn't need the minus sign because $(\Omega R - U)$ is always positive.

2.3.3 Meridian and Circumferential shear stresses

In the previous subsections the shear stresses were expressed through the Hirs formulation. The meridian stresses acting on the bulk $\tau_m = \tau_{rm} + \tau_{cm}$ results to be:

$$\begin{gathered} \tau_{yz}|_0^H = \tau_m = \tau_{rm} + \tau_{sm} = \\ -\frac{nV}{2}\rho\left(\frac{\rho H}{\mu}\right)^m \left(W_{s,eq}^m W_s + W_{r,eq}^m W_r\right) \end{gathered} \tag{2.28}$$

while the circumferential stresses are:

$$\begin{gathered} \tau_{yz}|_0^H = \tau_m = \tau_{rm} + \tau_{sm} = \\ \frac{n}{2}\rho\left(\frac{\rho H}{\mu}\right)^m \left[-W_{s,eq}^m W_s U + W_{r,eq}^m W_r (\Omega R - U)\right] \end{gathered} \tag{2.29}$$

By substituting eqs.(2.28)-(2.29) into eqs.(2.9a)-(2.9c) the problem results to be a 2-D non-linear PDEs system in the three variables U, V and P. The solution of this kind of PDEs can be only numeric.

2.4 Boundary conditions

The problem closure requires a right definition of the inlet and outlet boundary conditions. System in eqs.(2.9a)-(2.9c) needs three boundary conditions in case of incompressible flow. As usual these will concern the total inlet pressure, the outlet pressure and the inlet swirl. The boundary conditions can be written as:

$$P_{in} + \frac{1}{2}\rho V_{in}^2 = P_{0,in} - \zeta_i \frac{1}{2}\rho V_{in}^2 \tag{2.30a}$$

$$P_{out} + \frac{1}{2}\rho V_{out}^2 = P_{0,out} + \zeta_o \frac{1}{2}\rho V_{out}^2 \tag{2.30b}$$

$$U_{in} = U_0 \tag{2.30c}$$

where U_0 is the inlet swirl velocity, $\zeta_{i,o}$ are the inlet and outlet pressure loss coefficients. In

case of perfect gas flow, the boundary conditions concerning the inlet section will regard the total temperature, the isoentropic transformation at the inlet and the preswirl velocity.

$$C_p T_{in} + \frac{1}{2}V_{in}^2 = C_p T_{0,in} \tag{2.31a}$$

$$(T_{0,in}/T_{in})^{\frac{\gamma}{\gamma-1}} = (P_{0,in} - \zeta_i \frac{1}{2}\rho V_{in}^2)/P_{in} \tag{2.31b}$$

$$U_{in} = U_0. \tag{2.31c}$$

In the equations above $P_{0,in}$ and $P_{0,out}$ are the stagnation pressures respectively at the seal inlet and outlet.

A turbulent gas seal can be seen as a generalized *Fanno flow*. This means that the flow is subsonic if the inlet section is subsonic too. In a turbulent gas seal this condition is always verified. The outlet boundary condition is therefore defined in two steps: the problem is first solved by enforcing $Ma_{exit} = 1$. Then, it proceeds as follows:

$$\begin{aligned}
&if \quad P_{0,sonic} - \zeta_o 0.5 \rho_{sonic} V_{sonic}^2 > P_{0,out} \\
&BC: \quad Ma_{exit} = 1 \\
&else \\
&BC: \quad P_0 - \zeta_o 0.5 \rho V^2 = P_{0,out}
\end{aligned} \tag{2.32}$$

This means that, if the condition in (2.32) is verified, the solution found with $Ma_{exit} = 1$ is the problem solution, otherwise the outlet boundary condition will regard the total pressure relation.

2.5 Zero-order solution

For the solution of eqs.(2.9a-2.9c) a perturbation method will be used. For $H = const.$ the problem becomes axis-symmetric ($\frac{\partial}{\partial x} = 0$) and a simpler 1-D PDEs is obtained. The solution of the boundary value problem of the 1-D PDEs described above has been achieved with the aid of the software *Matlab*(function *bvp4c*).

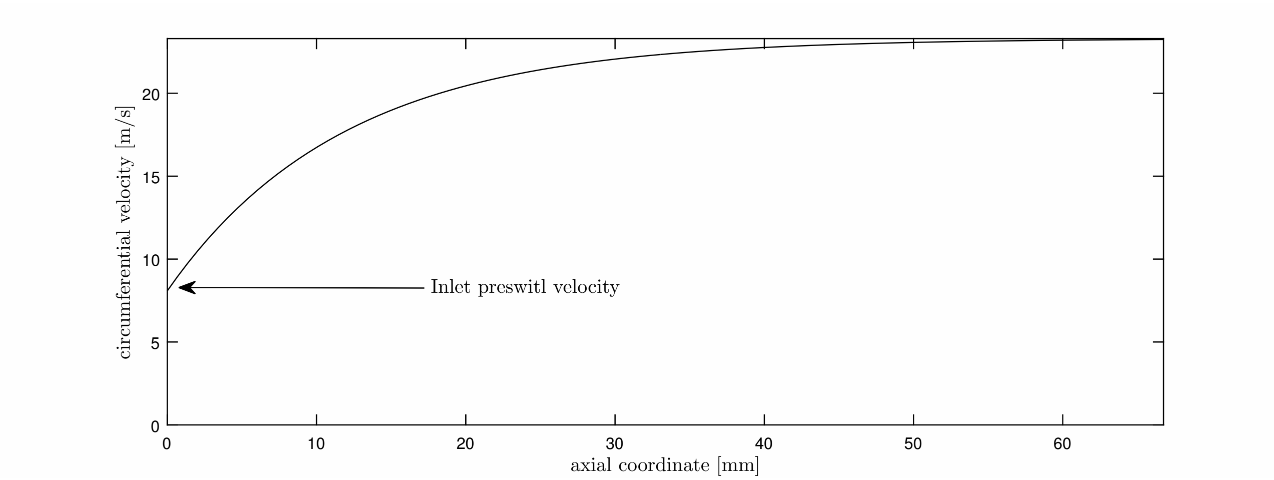

Figure 2.4: Axial variation of the bulk circumferential velocity. $\Delta P = 35.2bar$, $\Omega = 10000RPM$, D=89cm, L/R=1.5, $H = 0.18mm$, $\mu = 0.00364Pl$, $\rho = 900kg/m^3$

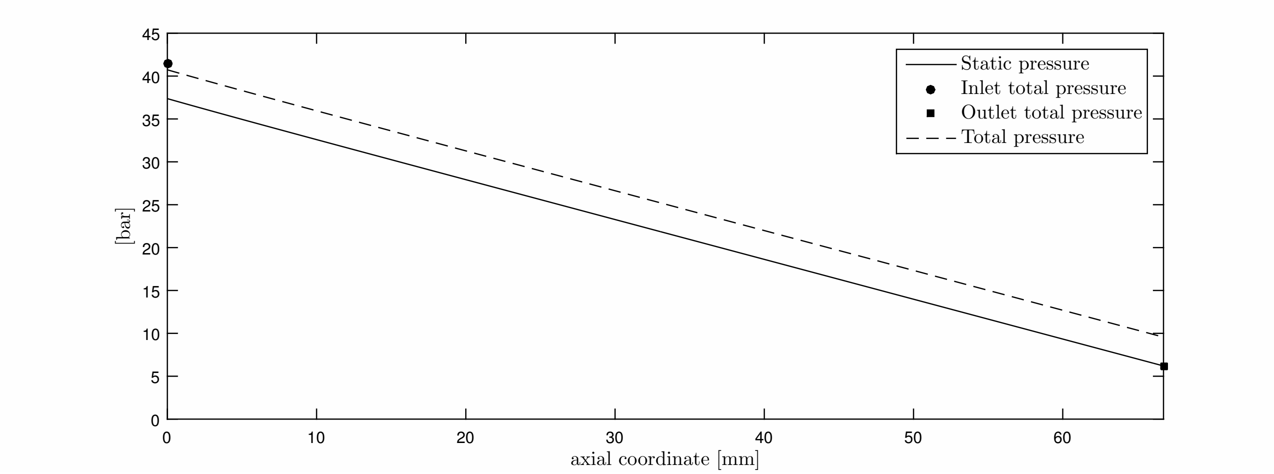

Figure 2.5: Axial variation of the bulk pressure. $\Delta P = 35.2bar$, $\Omega = 10000RPM$, D=89cm, L/D=0.75, $H = 0.18mm$, $\mu = 0.00364Pl$, $\rho = 900kg/m^3$, $\zeta_i = 0.2$, $\zeta_o = 1$

Figure 2.4 shows the variation of the circumferential velocity along the seal. The inlet circumferential velocity enters the seal with a discrete pre-swirl and rapidly reaches the asymptotic value of $\Omega R/2$. This value can also be justified by some physical considerations: being the bulk velocity at the seal inlet mainly meridian, τ_{sc} is negligible; the bulk, dragged by the rotor through τ_{rc}, is subject to a circumferential acceleration causing an increase of τ_{sc}. The circumferential acceleration continue until $\tau_{rc} = \tau_{sc}$ *i.e.* for $U = \frac{\Omega R}{2}$.

In Figure 2.5 the variation of the static pressure with the meridian coordinate is reported. Although the problem is highly non linear, the pressure gradient is constant along the whole seal length. In the inlet section a sudden loss of the total pressure can be observed as suggested by (2.30). In the outlet section there is no pressure recovery being $\zeta_o = 1$.

2.6 First-order solution

An experimental evidence in the study of pressure seals is that their structural response is almost constant with the rotor radial displacement for low eccentricity ε ($\varepsilon \leq 0.5$). This suggests the adoption of a perturbation method as solution strategy. The local height of the thin film H is expressed a as:

$$H = H_0 \left[1 - \varepsilon \cos(x/R - \omega t)\right] \tag{2.33}$$

where ε is the radial displacement to clearance ratio ($\varepsilon \ll 1$) and ω is the whirl angular velocity. The radial displacement causes a periodic perturbation of both the velocity and pressure fields. Given the non linear nature of the 2D equations of system (2.10), a single harmonic perturbation of the liquid height as in (2.33) causes a periodic perturbation of the variables that can be decomposed in an infinite Fourier series; in practice, as stated before, for small to moderate values of ε the only relevant harmonic component of the perturbed variables is the first. The flow variables are therefore expressed (as for the local height) through the superposition of the zero-order fields and a sinusoidal first-order field (the perturbations). The latter consist of a direct and quadrature components:

$$U_{1st}(x, y, t) = U + u_d(y) \cos(x/R - \omega t) + u_q(y) \sin(x/R - \omega t) \tag{2.34a}$$
$$V_{1st}(x, y, t) = V + v_d(y) \cos(x/R - \omega t) + v_q(y) \sin(x/R - \omega t) \tag{2.34b}$$
$$P_{1st}(x, y, t) = P + p_d(y) \cos(x/R - \omega t) + p_q(y) \sin(x/R - \omega t) \tag{2.34c}$$

The subscript $1st$ indicates the first-order field. Trivially, the components u_d, u_q are the perturbations (direct and quadrature components) of the bulk circumferential velocity. Same consideration holds for both $v_{d/q}$ and $p_{d/q}$ that constitute the perturbations respectively of the bulk axial velocity and pressure. The problem can be simplified by substituting the complex notation for both $\sin(x/R - \omega t)$ and $\cos(x/R - \omega t)$:

$$\cos\theta = \frac{(e^{j\theta} + e^{-j\theta})}{2} \tag{2.35a}$$
$$\sin\theta = \frac{(e^{j\theta} - e^{-j\theta})}{2j} \tag{2.35b}$$

After some algebraic passages, the generic variable $\Phi(x, y, t)$ can be expressed as:

$$\Phi(x, y, t) = \Phi(y) + \frac{\phi^*(y)}{2} e^{j\theta} + \frac{\phi(y)}{2} e^{-j\theta} \tag{2.36a}$$

$$\phi^*(y) = \phi_d(y) - j\phi_q(y) \tag{2.36b}$$

$$\phi(y) = \phi_d(y) + j\phi_q(y) \tag{2.36c}$$

In the above equations is $\theta = x/R - \omega t$.

The expression of the perturbed components in (2.36) make it possible to strongly simplify the matrix notation and the definition of the perturbed variables. In fact, the clockwise ϕ^* and the counterclockwise ϕ components of the perturbations are uncoupled and can be solved separately.

Taking into account the only clockwise components, the complex vector of the three variables perturbations is:

$$\overline{\chi} = \begin{bmatrix} u^* \\ v^* \\ p^* \end{bmatrix} \tag{2.37}$$

the perturbation of system (2.10) can be rearranged in the following linear ODEs system:

$$\overline{\overline{A}} \cdot \overline{\chi}'(y) + \overline{\overline{B}} \cdot \overline{\chi}(y) + \varepsilon \overline{C} = 0 \tag{2.38}$$

where is:

$$\overline{\overline{A}} = \begin{bmatrix} 0 & 1 & 0 \\ V & 0 & 0 \\ 0 & V & 1/\rho \end{bmatrix} \tag{2.39}$$

$$\overline{\overline{B}} = \begin{bmatrix} j/R & 0 & 0 \\ -\tau_{c,U}/\rho H + j(U/R - \omega) & -\frac{\tau_{c,V}}{\rho H} + U' & j/\rho R \\ -\tau_{a,U}/\rho H & -\tau_{a,V}/\rho H + j(U/R - \omega) & 0 \end{bmatrix} \tag{2.40}$$

$$\overline{C} = \begin{bmatrix} -j(U/R - \omega) \\ \tau_{c,H}/\rho - U'V \\ \tau_{a,H}/\rho - P'/\rho \end{bmatrix} \tag{2.41}$$

where generally $\tau_{a/c,s} = \frac{d\tau_{a/c}}{ds}$.

In the system above, $\overline{\overline{A}}$, $\overline{\overline{B}}$ and $\overline{C}$ depend only on the zero-order field. The fluid force acting on the rotor, mainly given by the pressure perturbation, can be divided into its direct (F_d)

component (*i.e.* the force component parallel to the rotor displacement) and quadrature (F_q) component (*i.e.* the force component normal to the rotor displacement).

In case of compressible perfect gas seal the vector of the complex variables is:

$$\overline{\chi}_{comp} = \begin{bmatrix} u^* \\ v^* \\ p^* \\ \rho^* \end{bmatrix} \tag{2.42}$$

the perturbation of the density field ρ^* has been joined to the three variables u^*, v^* and p^*. The perturbation of the temperature can be implicitly substituted in the system from the state equation for which is:

$$t^*/T = p^*/P - \rho^*/\rho \tag{2.43}$$

The perturbation of the continuity equation (2.9a), the system (2.10) and the energy equation (2.7a), gives to $\overline{\overline{A}}_{pg}$ the following form:

$$\overline{\overline{A}}_{pg} = \begin{bmatrix} 0 & \rho & 0 & V \\ V & 0 & 0 & 0 \\ 0 & V & 1/\rho & 0 \\ 0 & \frac{\gamma}{\gamma-1}P & \frac{1}{\gamma-1}V & 0 \end{bmatrix} \tag{2.44}$$

Matrix $\overline{\overline{B}}_{pg}$ will be:

$$\begin{bmatrix} j\rho/R & \rho' & 0 & V' + j(U/R-\omega) \\ \overline{\overline{B}}(2,1) & \overline{\overline{B}}(2,2) & \overline{\overline{B}}(2,3) & (-\tau_{c,\rho} + \tau_c/\rho)/\rho H \\ \overline{\overline{B}}(3,1) & \overline{\overline{B}}(3,2) + V' & 0 & \frac{-\tau_{a,\rho}+\tau_a/\rho}{/\rho H} - P'/\rho^2 \\ \frac{\gamma}{\gamma-1}jP/R & \frac{1}{\gamma-1}P' & \frac{1}{\gamma-1}[\gamma V' + j(U/R-\omega)] & 0 \end{bmatrix} \tag{2.45}$$

The $\overline{C}_{pg}$ vector is

$$\overline{C}_{pg} = \begin{bmatrix} -j\rho(U/R-\omega) \\ \tau_{c,H}/\rho - U'V \\ \tau_{a,H}/\rho - P'/\rho \\ -\frac{\gamma}{\gamma-1}P[j(U/R-\omega)+V'] - \frac{1}{\gamma-1}VP' + L_{w,H} \end{bmatrix} \tag{2.46}$$

The subscript pg indicates that the fluid considered is a perfect gas.

In the equations above, $L_{w,H}$ is the partial derivative of the entropy production term L_w defined in (2.7a) with respect H.

The incompressible boundary conditions are defined by the perturbation of (2.30):

$$p_{in}^* + (1+\zeta_i)\rho V_{x=0} v_{in}^* = 0 \tag{2.47a}$$
$$p_{out}^* + (1-\zeta_o)\rho V_{x=0} v_{out}^* = 0 \tag{2.47b}$$
$$u_{in}^* = 0 \tag{2.47c}$$

The perturbed "perfect gas" boundary conditions are demanded to chapter 3. In a reference frame rotating with an angular velocity of ω, the direct and cross-coupled pressure forces are expressed by:

$$F_n = \int_0^l dy \int_0^{2\pi} R d\theta P(\theta, y) \cos\theta \tag{2.48}$$
$$F_t = \int_0^l dy \int_0^{2\pi} R d\theta P(\theta, y) \sin\theta \tag{2.49}$$

By substituting (2.34c), they simplify to:

$$F_n = \int_0^{2\pi} R d\theta \cos^2\theta \int_0^l dy p_d(y) = \pi R L \overline{p}_d \tag{2.50}$$
$$F_t = \int_0^{2\pi} R d\theta \sin^2\theta \int_0^l dy p_q(y) = \pi R L \overline{p}_q \tag{2.51}$$

The final goal of the analysis is the evaluation of the seal structural impedance. The forces so computed are the same as in (1.7). The seal structural impedance is defined by three coefficient for each of the two directions. The normal and tangential stiffness at the given ω are:

$$H_n = F_n/(\varepsilon H) \tag{2.52a}$$
$$H_t = F_t/(\varepsilon H) \tag{2.52b}$$

As stated before, the first order equations derive from a linear perturbation of the complete 2D bulk flow model equations; this means that both F_n and F_t will show a linear trend with ε. The two stiffness values, computed as (2.52), are therefore independent on ε. A singular bulk model solution gives only one value for each of the two stiffnesses. This means that the extrapolation of the six coefficients requires at least three different solutions (different ω). In this case the seal structural coefficients will be extrapolated by a parabolic interpolation of the two forces as function of ω. If the sample points are more than three, a least square fitting is made. In this procedure, it is recommended to adopt for ω a wide enough range order to avoid local fluctuations of the coefficients. The results of the perturbed system and the comparisons with the experimental data are reported in 2.9.

2.7 CFD model

A more accurate evaluation of the seal structural response can be accomplished through a CFD simulation. The first attempt to compute the entire turbulent flow field inside the rotor-stator clearance of a smooth annular seal was made by Dietzen et al. [20] where a standard $k - \epsilon$ model was adopted to evaluate the seal stiffness coefficients through a perturbation approach. Tam et al. [59] modeled the turbulent Reynolds stresses following the Prandtl mixing-length approach. The prediction obtained in both investigations showed reasonable agreement with the experimental results. Athavale et al.[4] also applied a perturbation strategy to the 2D centered rotor solution to evaluate the stiffness coefficient for small ε. Ha et al.[27] solved a complete 3D RANS simulation of an eccentric annular seal. They formulated the problem in a moving reference frame, rotating at a given whirl angular velocity to solve the problem with a single steady-state simulation. This last approach is followed here. In the last decades, most of the research effort, on the CFD ground, has been devoted to the study of the structured pressure seals. As introduced in 1.3.3, the fluid whirl inside the seal is usually reduced by adopting a structured (usually hole-pattern) stator. Moore and Palazzolo [43] investigated the accuracy of the $\kappa - \epsilon$ RANS model in the prediction of the turbulence statistics inside a groove of an annular liquid grooved seal finding an underestimation of both turbulent intensity and inlet pre-swirl. Chochua and Soulas [15] used a transient CFD analysis coupled with a deforming mesh to obtain the rotordynamic seal coefficients enforcing a rotor one-direction shaking. Yang and Feng [62] realized the same CFD simulations of Chochua and Soulas but enforcing a rotor circular whirl orbit. These last approach produced better more accurate predictions of the seal dynamic behaviour. Migliorini et al. [41] proposed an hybrid CFD-bulk approach: the zero-order field is computed by a steady state CFD simulation on a reduce angular sector of the seal. The first-order bulk flow model is then implemented adopting the CFD solution for the zero-order field. The perturbation of the friction coefficients is neglected. This last approach has shows an excellent compromise between fastness and accuracy.

2.7.1 Mesh generation

The mesh has been generated through the aid of the software *Pointwise*. The geometry consists of a cylindrical extrusion of circular crown with a slightly eccentric inner cylindrical surface. The simplicity of the geometry allows to adopt a structured mesh for the domain discretization. In this specific case, the axial and radial cell distribution have been defined taking into account two opposite needs: the solution accuracy and the time usage. For each case analyzed in this thesis, the axial and radial cell numbers obtained by the following has been also checked by a mesh refinement study assessing the independence of the results from the adopted grid.

Radial mesh distribution

The first step to ensure a good radial discretization of the domain is the right evaluation of the first cell height. It is well known, in fact, that a turbulent flow, differently from a laminar one, is characterized by two different scales: the inertial scale and the near-wall scale. The inertial scale, characterized by greater length and time scales, requires a coarser mesh distribution (and greater time steps in case of unsteady simulations).

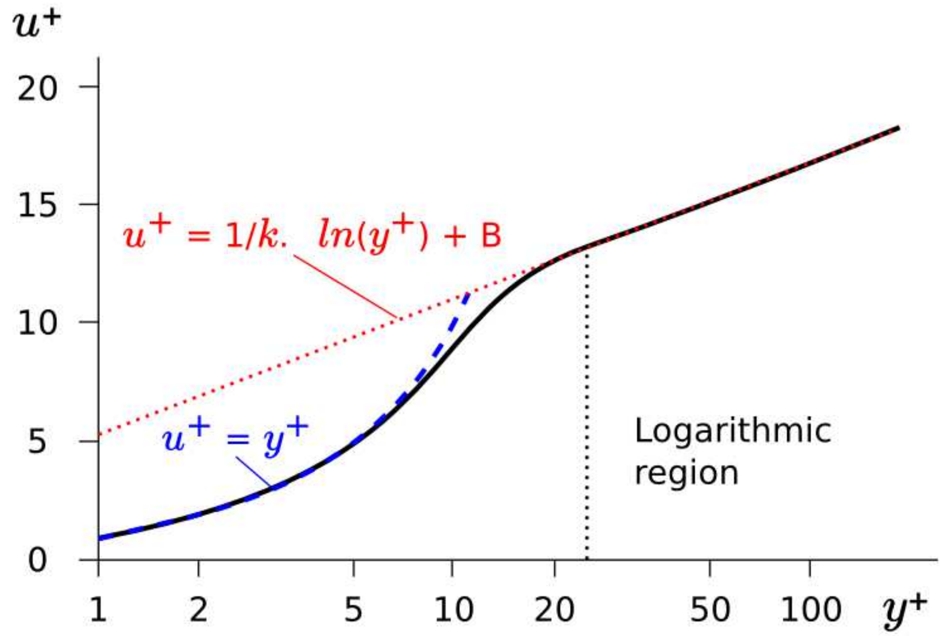

Figure 2.6: Universal law of wall

The near-wall scale is characterized by small length and time scales. The universal velocity profile, shown in figure 2.6, is defined in terms of the dimensionless wall distance $y^+ = xv_*/\nu$ where $u_* = \sqrt{\tau_w/\rho}$ is the friction velocity, ν is the usual kinematic viscosity and x is the distance from the wall. Joining all the definitions gives:

$$y^+ = \frac{xv_*}{\nu} = \frac{x}{\nu}\sqrt{\frac{\tau_w}{\rho}} \tag{2.53}$$

Equation (2.53) says that the greater is τ_w, the greater will be y^+ at given x.

In a RANS simulation, the first cell height is usually in the range $1 \div 5$ for a wall-resolved simulation and $30 \div 50$ for a wall-modeled. For a better accuracy, it has been preferred to adopt a wall-resolved solution strategy, with an estimated first cell height of about $y_1^+ = 1$. This choice, and (2.53) leads to:

$$x_1 = y_1^+\nu\sqrt{\frac{\rho}{\tau_w}} \simeq \nu\sqrt{\frac{\rho}{\Delta PH/2L}} = \mu\sqrt{\frac{2L}{\rho\Delta PH}} \tag{2.54}$$

The approximation of (2.54) holds when the flow is mainly pressure driven.

The radial distribution is then defined by a geometric growth of the cell heights, with a growth ratio $\alpha = 1.1 \div 1.2$, The growth ratio is limited in this interval to avoid convergence instability or inaccuracy. Said N, the number of cells between the symmetry plane at $x = H/2$ and the wall, it will be:

$$H/2 = x_1 \sum_{k=0}^{N} \alpha^k = x_1 \frac{\alpha^{N+1} - 1}{\alpha - 1} \tag{2.55}$$

Given a first value for the growth rate $r = \alpha - 1 = 0.1 \div 0.2$, the geometric growth of cells , for the total fluid gap H, will count a number of cells N_r given by the following expression:

$$N_r = 2N = 2 \cdot round \left[\log \left(1 + \frac{Hr}{2x_1} \right) / \log(1 + r) \right] - 2 \tag{2.56}$$

Once the value of N is determined through eq.(2.56), the exact value of α will be obtained by (2.55).

Axial mesh distribution

The most important factor that determines the axial mesh distribution is the cell aspect ratio, in this specific case the ratio between the axial and the radial dimension of the cell. Given a constant axial spacing, the highest aspect ratio will be found at the wall. The choice of the limit aspect ratio doesn't follow specific rules except that of convergence stability and accuracy. In this case, the magnitude order of the cell aspect ratio has been determined by comparing the axial and radial gradient on the plane of the dimensional analysis:

$$\frac{\partial/\partial x}{\partial/\partial y} = O\left(\frac{1/\Delta x_c}{1/\Delta y_c}\right) = O\left(\frac{1/H}{1/L}\right) \tag{2.57}$$

In equation (2.57) Δx_c and Δy_c are respectively the radial and axial cell length. Taking $\Delta x_c = x_1$ (*i.e.* the radial cell dimension at the wall), from (2.57) results:

$$\Delta y_c = O\left(\frac{x_1 L}{H}\right) \tag{2.58}$$

For Δy_c has been chosen a first attempt value of $x_1 L/H$.

The axial cells distribution needs also a local inlet refinement in the way to accurately reproduce the local flow field in the inlet development length. Called y_1 the axial length of the first cell at the inlet, by adopting a geometric growth until the axial cell dimension is about Δy_c, the inlet cell number is:

$$N_i = round\left[log(\Delta y_c/y_1)/log(\alpha)\right] \tag{2.59}$$

The length of the inlet geometric growth L_i, remembering (2.55), is:

$$L_i = y_1 \sum_{k=0}^{N_i} \alpha_i^k = x_1 \frac{\alpha_i^{N_i+1} - 1}{\alpha_i - 1} \tag{2.60}$$

As for α, even for α_i a value in the range $1.1 \div 1.2$ is recommended.

The number of cells in the constant spacing region $N_{a,1D}$ will be:

$$N_{a,1D} = round\left(\frac{L - L_i}{y_1 \alpha^{N_i}}\right) \tag{2.61}$$

At this stage, it only must be verified that the asymptotic spacing $(L - L_i)/N_{a,1D}$ and the last cell of the inlet geometric growth, respect the length ratio limit:

$$1/\alpha < \frac{(L - L_i)/N_{a,1D}}{y_1 \alpha^{N_i}} < \alpha \tag{2.62}$$

Usually y_1 has the same magnitude order of x_1. The above condition is usually verified without the need of any correction on α_i or N_i.

The total axial cells number N_a is:

$$N_a = N_i + N_{a,1D} \tag{2.63}$$

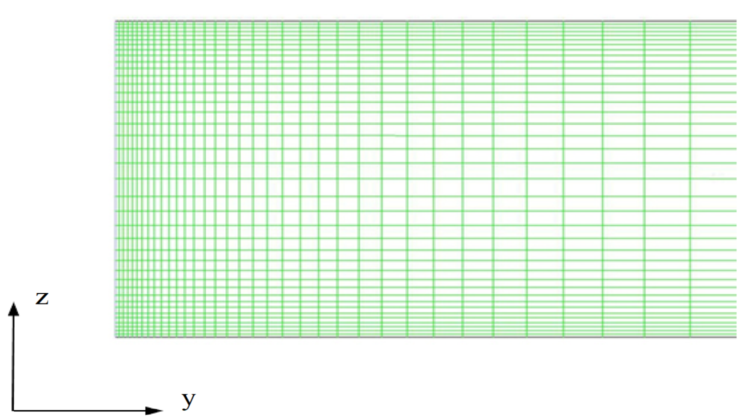

Figure 2.7: Inlet mesh distribution. Axis defined as in figure 2.1

Figure 2.8: Outlet mesh distribution. Axis defined as in figure 2.1

Figure 2.7 depicts the inlet mesh. The mesh size grows both in radial and axial directions. As stated before, the axial spacing become constant after the first N_i elements. The constant-spacing axial mesh is depicted in figure 2.8

2.7.2 Solution settings and boundary conditions

As stated before, the choice of the correct turbulence model depends on the degree of accuracy needed and the physical quantities we are interested in. The prediction of the seal structural response requires nothing but to estimate the radial and tangential fluid dynamic forces exchanged between the rotor and the fluid film. This kind of integral quantities can be estimated with reasonable accuracy also with a simple LEVM models. The CFD results obtained here have been computed with the $\kappa - \omega$ turbulence model in the SST version. Differently from the $\kappa - \varepsilon$ model, $\kappa - \omega$ shows better wall flows reconstruction, improved stability and convergence. The inlet and outlet boundary conditions about pressure and temperature are trivially the same as defined for the bulk- flow model. The usage of a turbulence model however requires the definitions of further boundary conditions about the inlet/outlet turbulent intensity I_t and length scale l_t. Following the Fluent guide, the RANS boundary conditions are defined as follows:

$$I_t = 0.16 Re_h^{-1/8} \tag{2.64a}$$
$$l_t = 0.07 D_h = 0.14 H \tag{2.64b}$$

The turbulent intensity was about 5% on the range scrutinized. The numerical solution has been obtained through a Pressure-based solver with a segregated scheme.

2.8 Experimental setup and data reduction

The experimental studies mentioned in this thesis have been realized by the Turbomachinery Laboratory of the Mechanical Engineering Department of Texas $A\&M$ University. The test rig photograph and its section view are reported respectively in figures 2.9-2.10.

The stator assembly is radially supported by two hydraulic shakers and axially by two opposed sets of three pitch stabilizers installed in an equilateral triangle pattern on each end of the stator assembly to control the stators axial positon and enable the alignment between the stator and rotor. The rotor is supported by two hydrostatic bearings fed by silicone oil at 69 bars. The hydrostatic bearings provide very high stiffness compared with that developed by test seals.

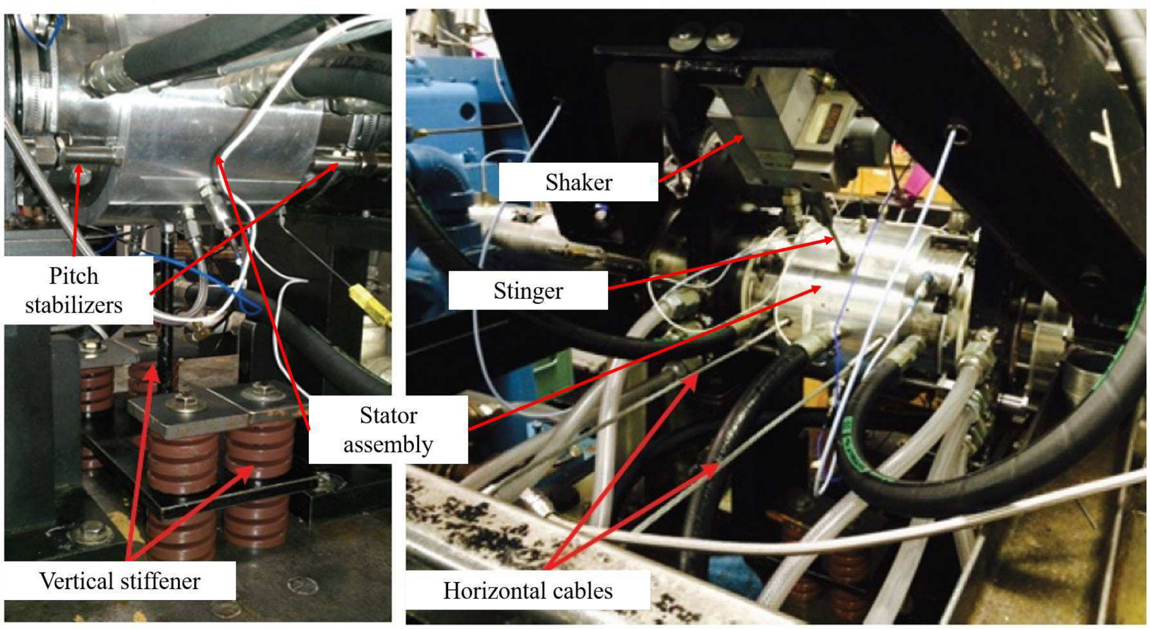

Figure 2.9: Test rig photograph

The hydraulic shakers are connected to the stator assembly via two orthogonal-oriented stingers. They control the static position of the stator and also excite the stator with a pseudo-random excitation force in the frequency range $10 - 350$Hz. The magnitude of the excitation force is adjusted so that the peak-to-peak relative displacement is less than 20% of the radial clearance H. The horizontal cable and the vertical stiffener are installed to stabilize the rotor as documented by Picardo et al. [50] and Mehta et al. [40]. Figure 2.11 depicts a section view of the stator assembly. Two seals are installed in the stator back to back to minimize the net axial thrust induced by the pressure drop through each seal. The test fluid (single/two phase flow) is injected into the stator through two inlet axis-symmetric ports at the center annulus of the stator, as shown in section B-B of figure 2.11. Then, the test fluid flows through a multi-port inlet preswirl guide ring, which directs the flow into the seal. In this specific case, the zero preswirl guids has been adopted.

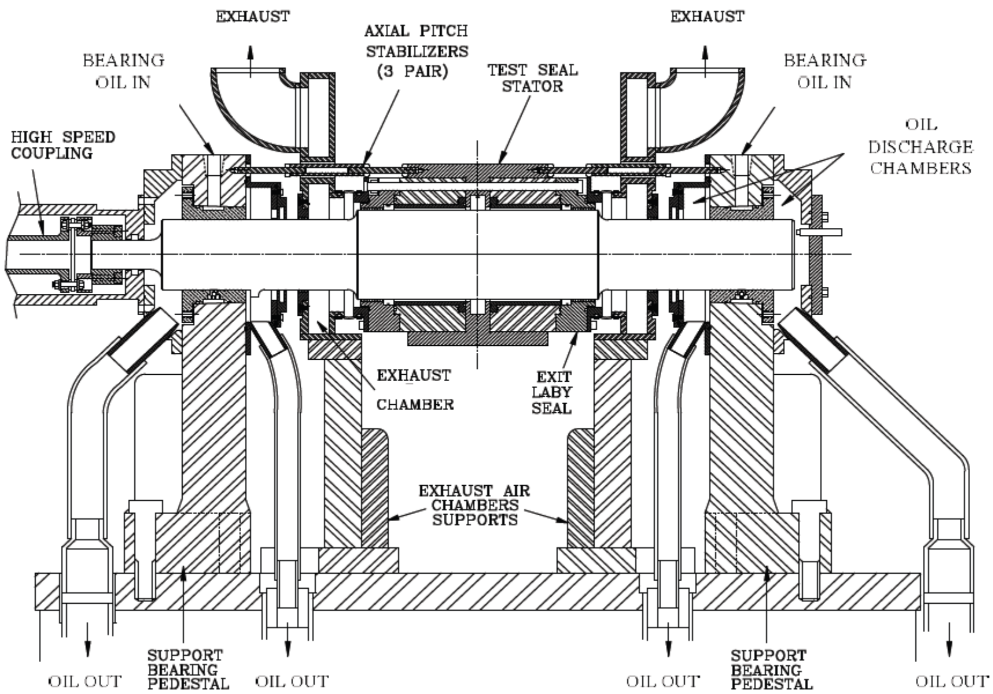

Figure 2.10: Test rig axial section view

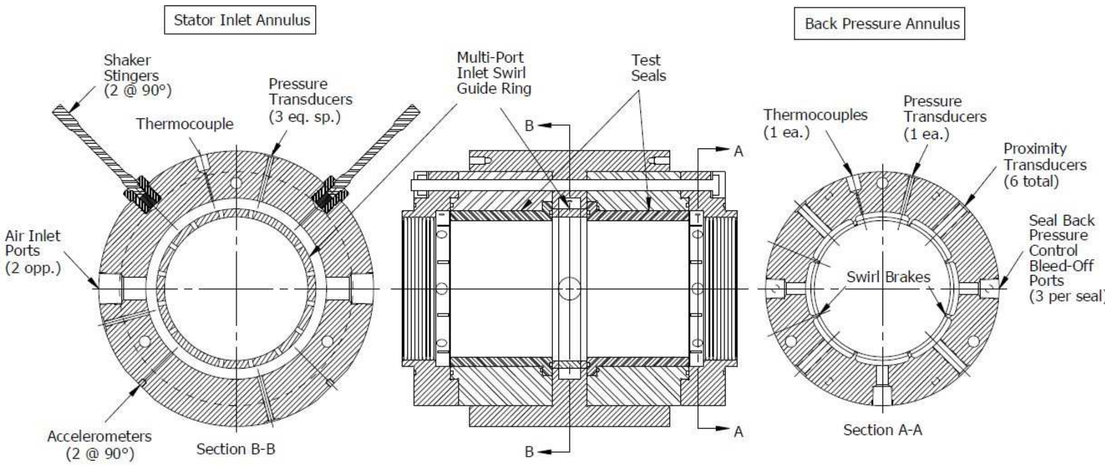

Figure 2.11: Test rig radial section view

After flowing through test seals, he fluid either exits through radial exit ports or axially through the back-pressure labyrinth seals.A bleed valve is placed in the downstream of the exit ports to controls the exit pressure of the test seals. Swirl brakes are used upstream of the exit labyrinths to minimize their cross-coupled stiffness coefficients. The stator is excited in only one direction at time by 640 excitations lasting 0.1024 seconds. All the 640 measurements are divided into 10 group of 64 records. For each group, the stator-to-rotor relative displacements, the stator accelerations and the shakers forces are recorded. The time records are successively transformed to the frequency domain by a FFTs. The 10 groups of forces and displacements are then combined to form 100 complex force matrices and displacement matrices. 100 complex impedance matrices are obtained by inverting the following matricial equation:

$$\begin{bmatrix} F_{XX} & F_{XY} \\ F_{YX} & F_{YY} \end{bmatrix} - \begin{bmatrix} M_{sXX} & M_{sXY} \\ M_{sYX} & M_{sYY} \end{bmatrix} \begin{bmatrix} A_{sXX} & A_{sXY} \\ A_{sYX} & A_{sYY} \end{bmatrix} = \begin{bmatrix} H_{XX} & H_{XY} \\ H_{YX} & H_{YY} \end{bmatrix} \begin{bmatrix} D_{XX} & D_{XY} \\ D_{YX} & D_{YY} \end{bmatrix} \tag{2.65}$$

The seal coefficients, as defined in section 1.2 are compared with the experimental data as follows:

$Re(H_{XX})$ and $Re(H_{YY})$ are compared with $K - M\omega^2$;
$Re(H_{XY})$ and $-Re(H_{YX})$ are compared with $k - m\omega^2$;
$Im(H_{XX})$ and $Im(H_{YY})$ are compared with $D\omega$;
$Im(H_{XY})$ and $-Im(H_{YX})$ are compared with $d\omega$.

In the following impedance plots, the crosses and the circles correspond to the impedance data obtained by the two independent stator shaking in the two orthogonal shakers directions represented in the section B-B of figure 2.11.

2.9 Results

In figure 2.12 a comparison is shown between the experimental results and both the CFD and bulk model predictions for the specific operating condition outlined in the caption. There is a satisfactory agreement between measurements and both CFD and bulk model results. Experimental measurements show some seal stiffness anisotropy between the two orthogonal shakers directions represented in figure by crosses and circles. To the author, the stiffness anisotropy could be explained by a non perfect axial symmetry of the inlet velocity given by the two axis-symmetric ports. Some discrepancy between CFD and bulk predictions of both the direct and quadrature static stiffness K and k can be explained by different values of the inlet preswirl velocity U_0 and the inlet pressure losses. As usual, in order to simplify the CFD computations, the fluid flow in the inlet chamber is not reconstructed; this leads to some degree of inaccuracy being both the local pressure loss and the preswirl velocity only hypothesized. Here, the CFD simulations have been made by enforcing zero preswirl and no inlet pressure loss at the inlet section. To better understand the accuracy of both CFD and bulk model results, figures 2.22-2.24 report the variations of every single seal coefficient with Ω for the three pressure variations ΔP_0. Figures 2.28-2.30 report the comparison for the "short seal" case of every single seal coefficient with Ω for the three pressure variations ΔP_0. Figures 2.40-2.36 report the comparison between the bulk-model predictions and the experimental measurements for the cases of both long ($L/R = 1.5$) and short ($L/R = 0.58$) perfect gas seal.

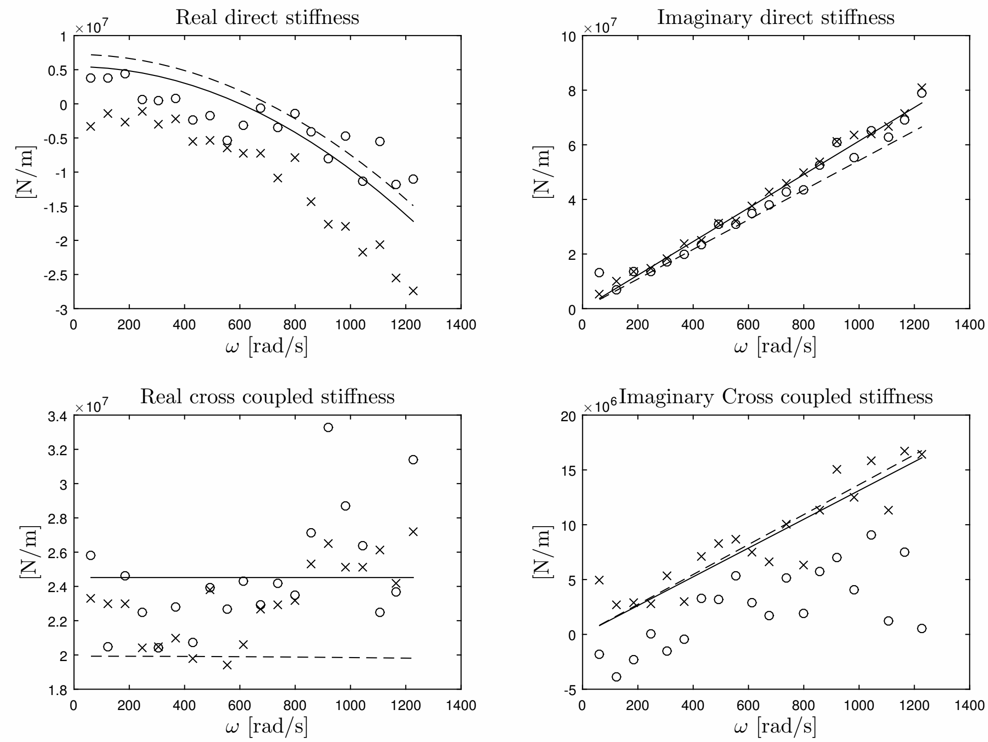

Figure 2.12: Stiffness comparison. $\Delta P_0 = 35.2bar$, $\Omega = 10000RPM$, D=89cm, L/D=0.75, $H = 0.18mm$, $\mu = 0.00364Pl$, $\rho = 900kg/m^3$, $\zeta_i = 0.2$, $\zeta_o = 1$.—— solid line: CFD, - - dashed line: bulk flow model, Symbols ○ and ×: measurements

2.9.1 Incompressible flow

Long seal L/R=1.5

Leakage Comparison

Figures 2.13-2.15 show the comparison between the predicted and the measured leakage. CFD predictions underestimate the seal leakage while bulk flow is in reasonable agreement though underestimates the leakage reduction with the rotor speed Ω. The CFD error can be explained, as outlined in section 2.2, by the RANS turbulence model adopted, (linear eddy viscosity $\kappa - \omega$) unable to mimic the effect of the transverse shear such as the formation of the Taylor vortexes (Lauder and Sandham [34] pages 77-78). Moreover, the low experimental Re number values encountered suggest that the flow regime could be transitional, circumstance that would introduce further modeling problems. On the other hand, the bulk modeling allows to avoid all the turbulence modeling issues once a reasonable friction law is formulated.

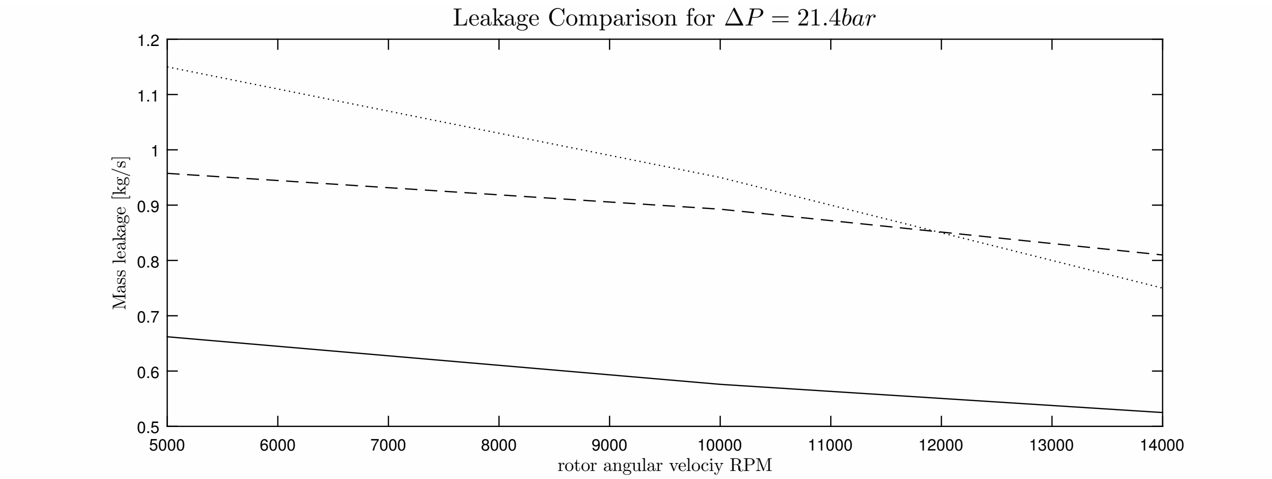

Figure 2.13: Leakage comparison. $\Delta P_0 = 21.4bar$, D=89cm, L/R=1.5, $H = 0.18mm$, $\mu = 0.00364Pl$, $\rho = 900kg/m^3$, $\zeta_i = 0.2$, $\zeta_o = 1$.—— solid line: CFD, - - dashed line: bulk flow model, ········ dotted line: measurements

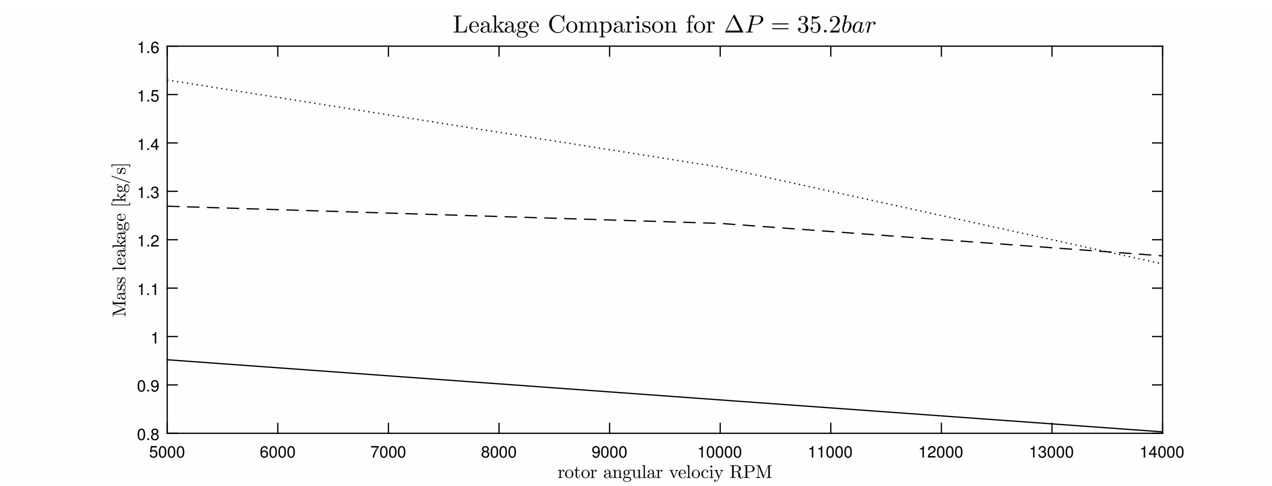

Figure 2.14: Leakage comparison. $\Delta P_0 = 35.2bar$, D=89cm, L/R=1.5, $H = 0.18mm$, $\mu = 0.00364Pl$, $\rho = 900kg/m^3$, $\zeta_i = 0.2$, $\zeta_o = 1$.—— solid line: CFD, - - dashed line: bulk flow model, ········ dotted line: measurements

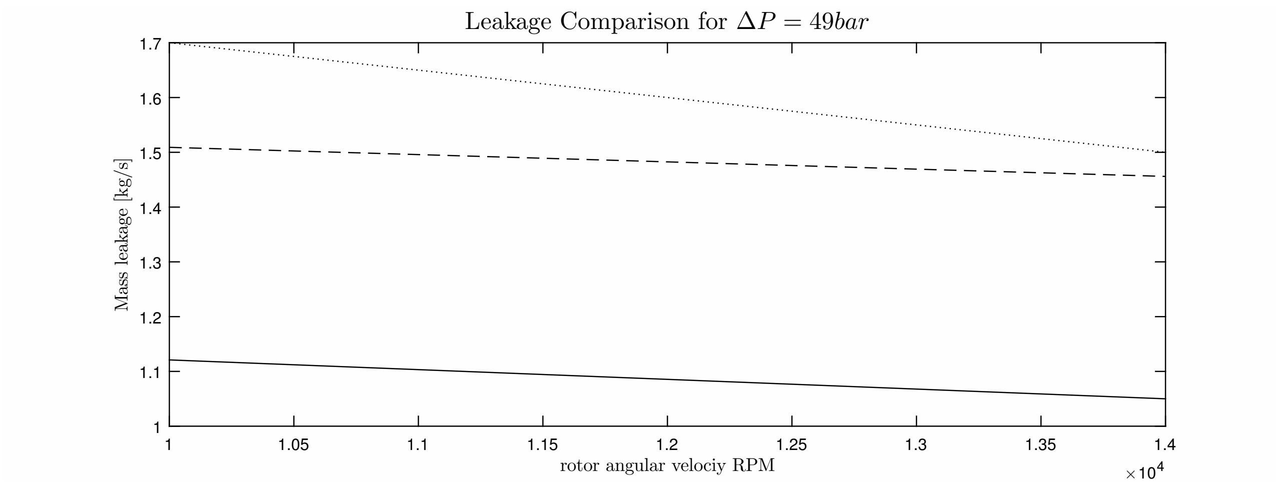

Figure 2.15: Leakage comparison. $\Delta P_0 = 49bar$, D=89cm, L/R=1.5, $H = 0.18mm$, $\mu = 0.00364Pl$, $\rho = 900kg/m^3$, $\zeta_i = 0.2$, $\zeta_o = 1$.—— solid line: CFD, - - dashed line: bulk flow model ········· dotted line: measurements

Static Direct Stiffness K

There is not a complete agreement between the measured and the predicted values. The experimental dispersion in some case makes it impossible to determine the sole constant sign (for example the case reported in figure 2.12). While this is a source of uncertainty in the process of code validation, it is not a big deal in the application (*i.e.* in the rotordynamic stability analysis) where the K contribution to the direct stiffness is negligible from moderate to high whirl pulse ω.

Both CFD and bulk model shows a similar decreasing trend with the increase of the pressure gradient and the rotor velocity Ω while the experimental results shows an opposite trend with Ω. At this regard, it must be pointed that the bulk model direct stiffness predictions are strongly affected by the inlet loss coefficient ζ_i as shown in the figures 2.16-2.17.

Further investigations are therefore needed in order to correctly model both the inlet and outlet loss coefficients $\zeta_{i,o}$ variations with the Reynolds number and the inlet swirl velocity.

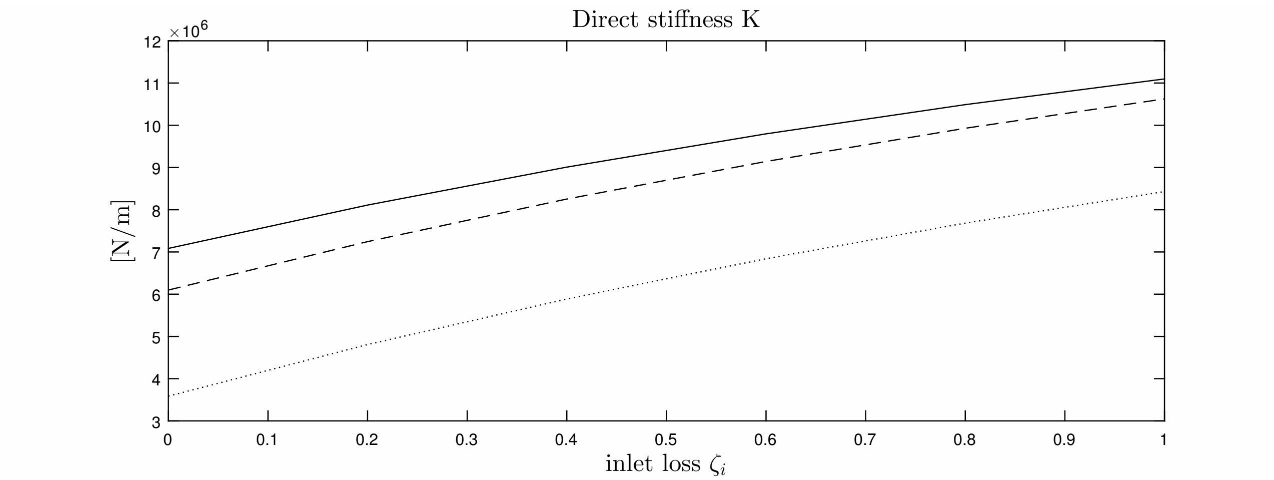

Figure 2.16: Variation of K with the inlet loss coefficient ζ_i. ΔP_0=35.2 bar L/R=1.5. —— solid line: $\Omega = 5000 RPM$, - - dashed line: $\Omega = 10000 RPM$, ········ dotted line: $\Omega = 14000 RPM$.

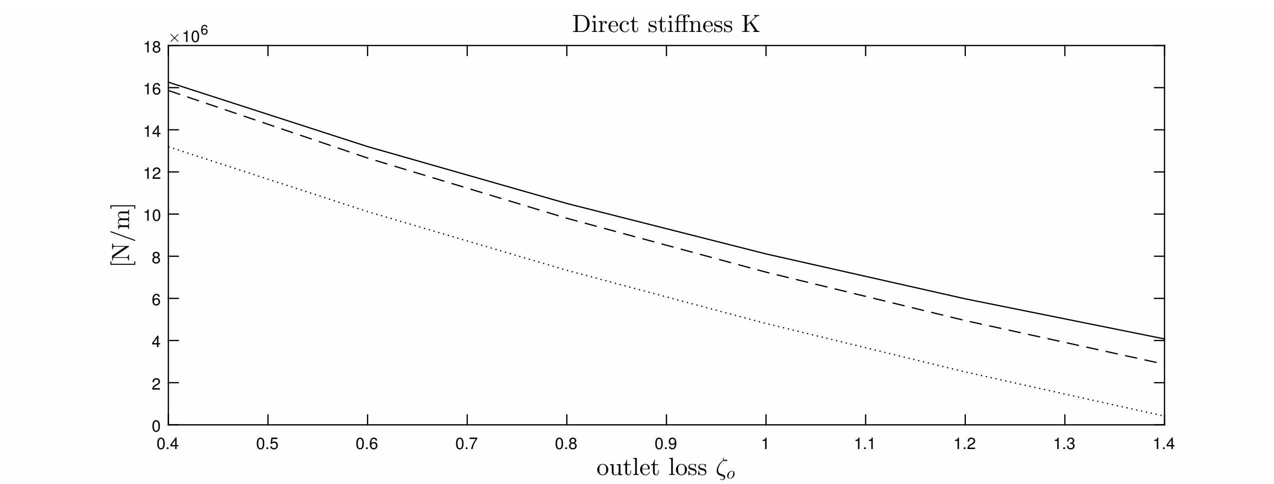

Figure 2.17: Variation of K with the outlet loss coefficient ζ_o. ΔP_0=35.2 bar L/R=1.5. —— solid line: $\Omega = 5000 RPM$, - - - dashed line: $\Omega = 10000 RPM$, ········ dotted line: $\Omega = 14000 RPM$.

Static Quadrature Stiffness k

Figures 2.22-2.24 show overall good agreement between the predicted (both CFD and bulk model) and the measured values of k. Both predictions and measurements show a linear increase in k with the rotor speed Ω while it is almost independent of the pressure gradient. Figures

2.18-2.19 show the variation of k with the inlet and outlet pressure loss coefficients. Differently from K, k is almost independent of ζ_i while slightly increase with ζ_o.

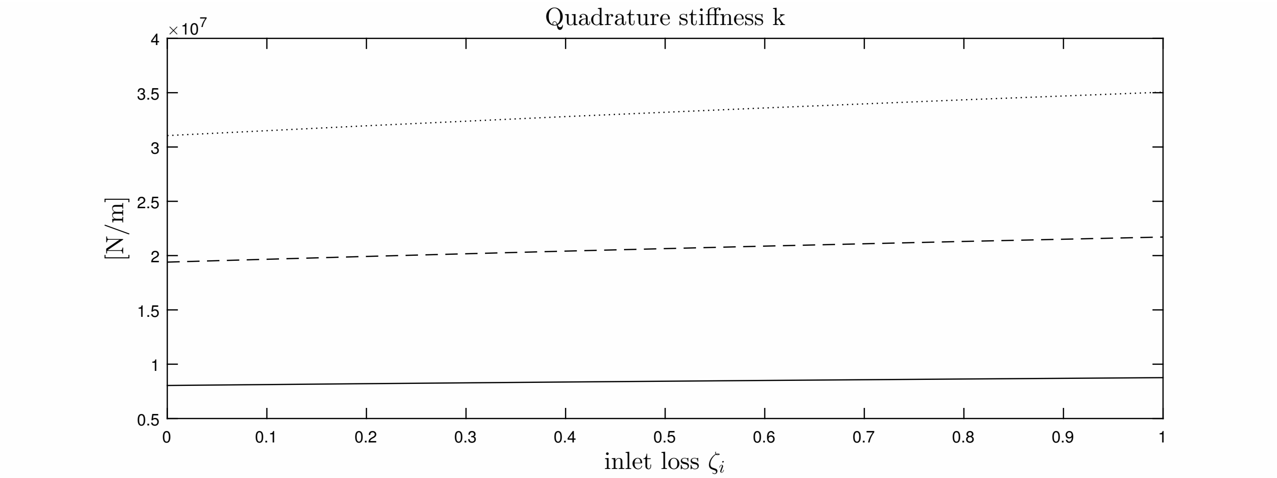

Figure 2.18: Variation of k with the inlet loss coefficient ζ_i. ΔP_0=35.2 bar L/R=1.5. —— solid line: $\Omega = 5000RPM$, - - dashed line: $\Omega = 10000RPM$, ········ dotted line: $\Omega = 14000RPM$.

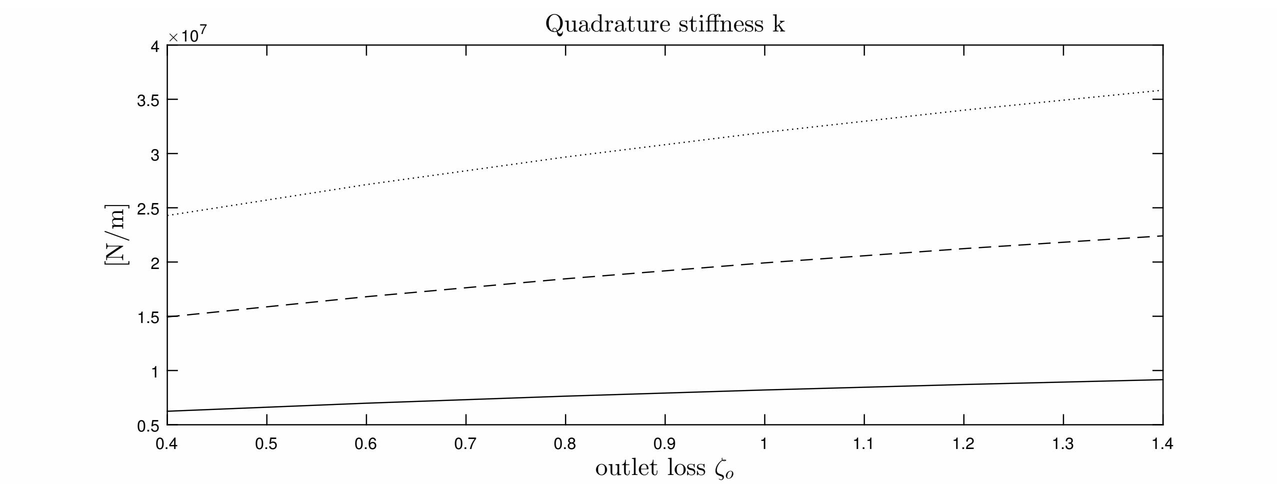

Figure 2.19: Variation of k with the outlet loss coefficient ζ_o. ΔP_0=35.2 bar L/R=1.5. —— solid line: $\Omega = 5000RPM$, - - dashed line: $\Omega = 10000RPM$, ········ dotted line: $\Omega = 14000RPM$.

Direct Damping D

Direct Damping measurements are in good agreement with both CFD and bulk model predicted values. While the predicted CFD values of D is slightly higher than the measured values, the bulk mode predictions are slightly lower. The deviation however is around 10%. The variation of D with the loss coefficients is negligible as shown figures 2.20-2.21.

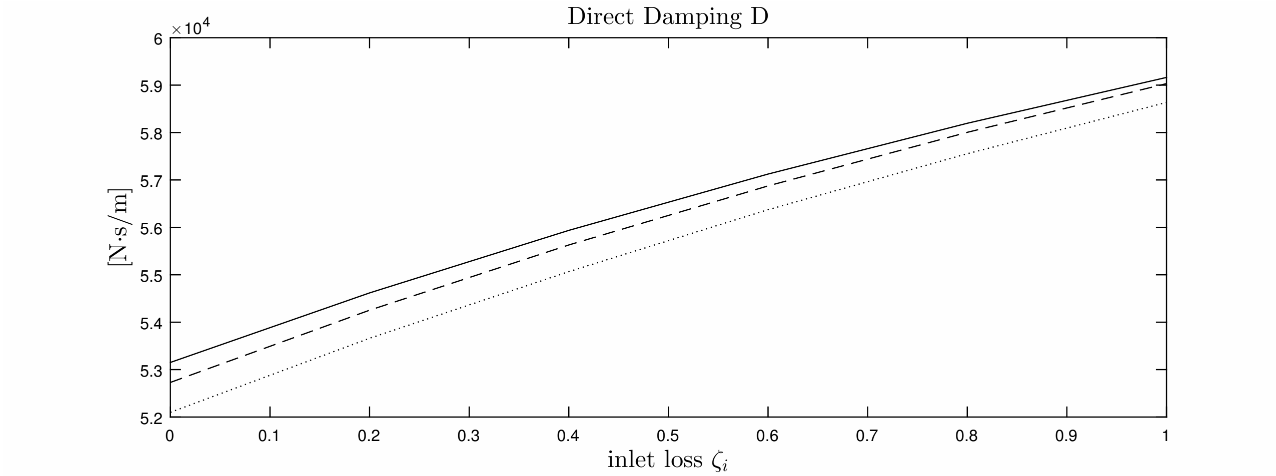

Figure 2.20: Variation of D with the inlet loss coefficient ζ_i. ΔP_0=35.2 bar L/R=1.5. —— solid line: $\Omega = 5000 RPM$, – – dashed line: $\Omega = 10000 RPM$, ········· dotted line: $\Omega = 14000 RPM$.

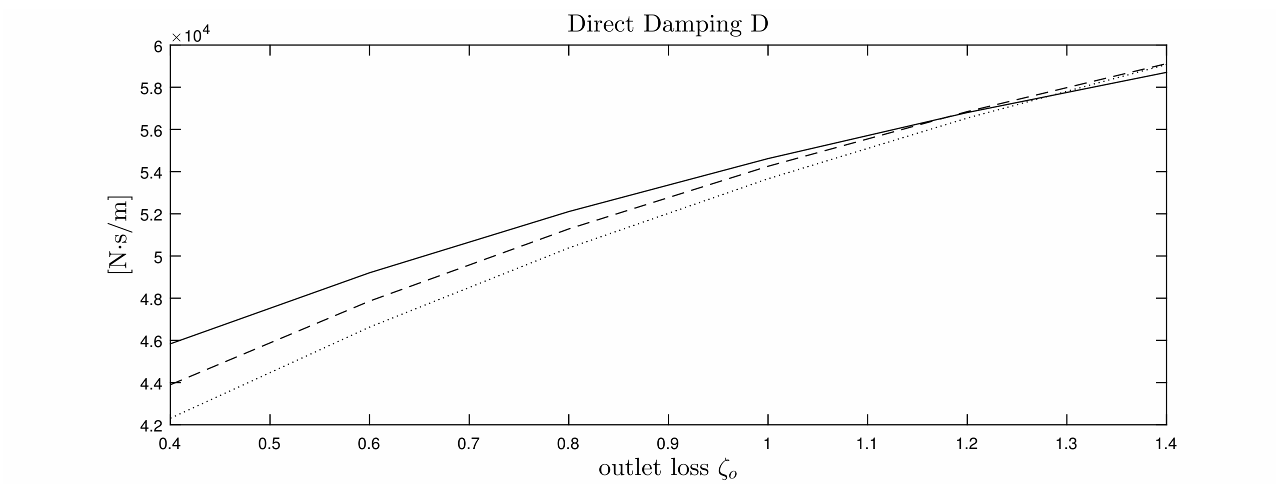

Figure 2.21: Variation of D with the outlet loss coefficient ζ_o. ΔP_0=35.2 bar L/R=1.5. —— solid line: $\Omega = 5000 RPM$, – – dashed line: $\Omega = 10000 RPM$, ········· dotted line: $\Omega = 14000 RPM$.

Quadrature Damping d

Quadrature damping predictions are in good agreement with the measured values. Quadrature damping coefficient d seems to be almost independent on ΔP, while grows almost linearly with Ω. The bulk-model predicted value is almost constant with both the inlet and outlet loss coefficients $\zeta_{i,o}$ (not reported here).

Direct Mass M

Predicted Direct mass coefficients M show a reasonable agreement with the measured values. While both CFD and bulk model, predict an almost constant added mass M, the measured values show a decrease with ΔP. The rotor speed Ω has only little effect on M. The bulk predictions of M are weakly affected by the loss coefficients $\zeta_{i,o}$.

Quadrature Mass m

The predicted quadrature mass m is almost null in every operating condition. This is in agreement with the known literature. The measurements, however, show a negative value of m that linearly increase with the rotor speed Ω. The prediction doesn't change in substance if a variation of the loss coefficients $\zeta_{i,o}$ is considered.

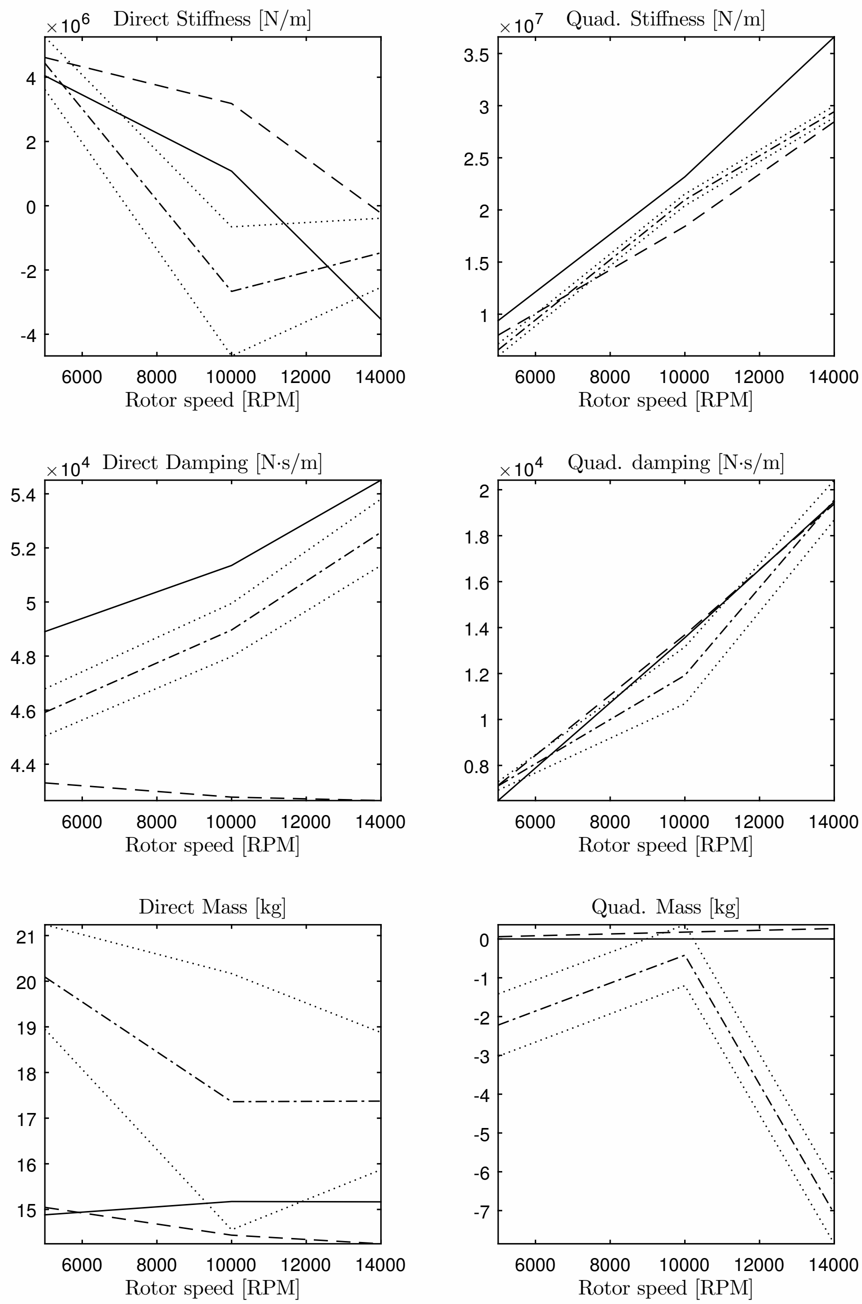

Figure 2.22: Stiffness variation with the rotor speed Ω. $\Delta P_0 = 21.4bar$, D=89cm, L/R=1.5, $H = 0.18mm$, $\mu = 0.00364Pl$, $\rho = 900kg/m^3$, $\zeta_i = 0.2$, $\zeta_o = 1$.—— solid line: CFD, - - dashed line: bulk flow model, dotted lines ··········: measurements bounds, $-\cdot-\cdot$ dot dashed line: measurement average.

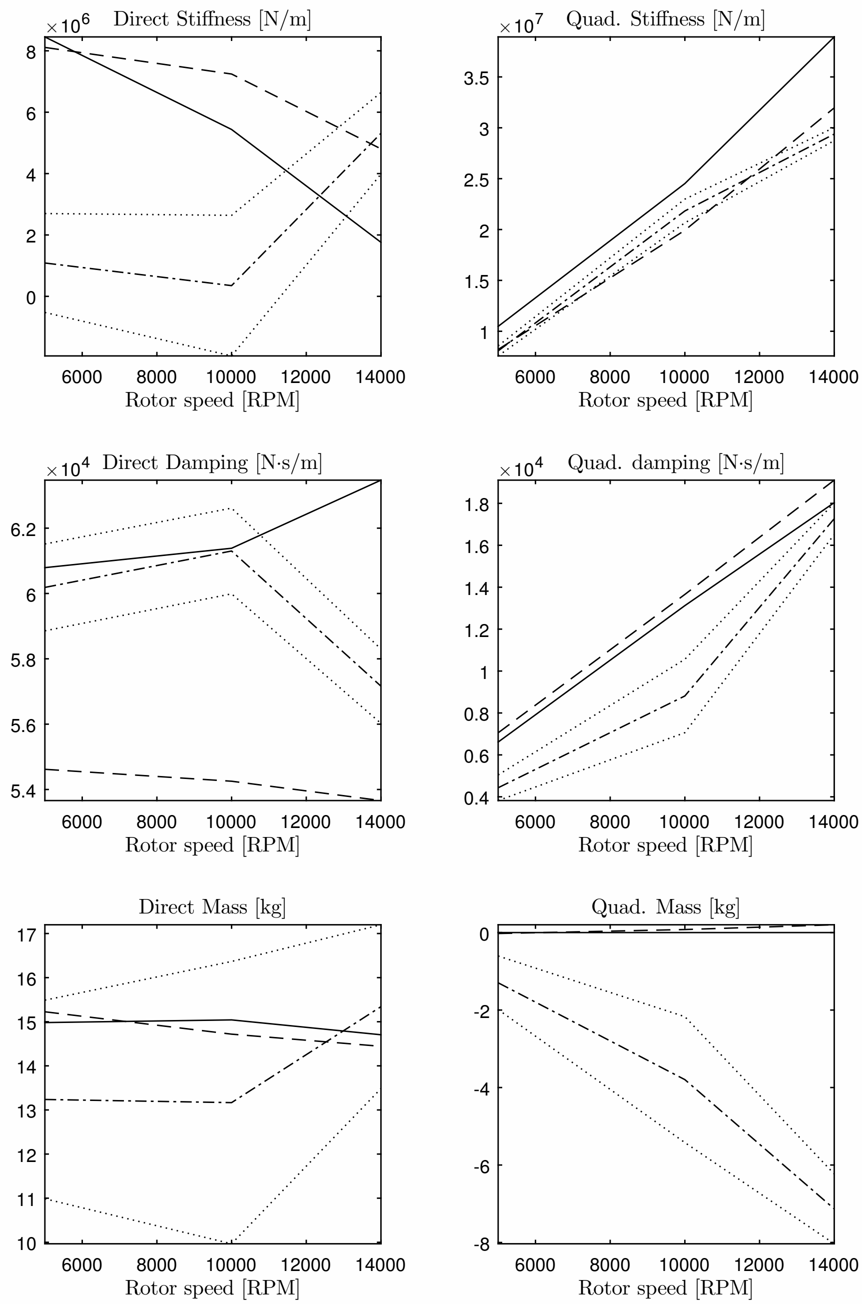

Figure 2.23: Stiffness variation with the rotor speed Ω. $\Delta P_0 = 35.2bar$, D=89cm, L/R=1.5, $H = 0.18mm$, $\mu = 0.00364Pl$, $\rho = 900kg/m^3$, $\zeta_i = 0.2$, $\zeta_o = 1$.—— solid line: CFD, - - dashed line: bulk flow model, dotted lines ··········: measurements bounds, $-\cdot-$ dot dashed line: measurement average.

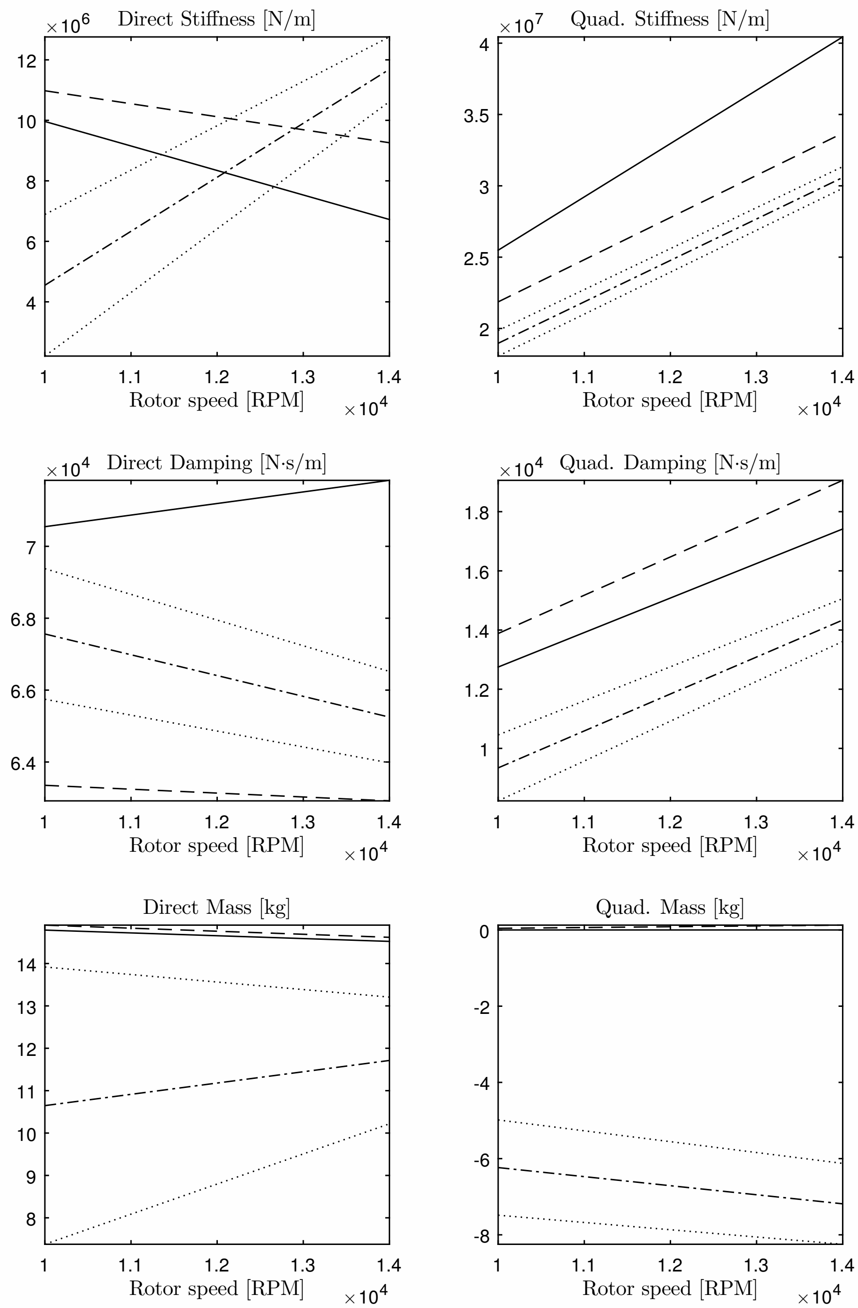

Figure 2.24: Stiffness variation with the rotor speed Ω. $\Delta P_0 = 49bar$, D=89cm, L/R=1.5, $H = 0.18mm$, $\mu = 0.00364Pl$, $\rho = 900kg/m^3$, $\zeta_i = 0.2$, $\zeta_o = 1$.—— solid line: CFD, - - dashed line: bulk flow model, dotted lines ⋯⋯: measurements bounds, $-\cdot-$ dot dashed line: measurement average.

Short seal L/R=0.58

Leakage Comparison

Figures2.25-2.27 show the comparisons between the bulk predictions and measured leakage value for the short seal case. There is a good agreement for lower values of the rotor speed Ω. The error becomes important for the higher values of the the rotor speed. The two different trends of the measured and predicted leakage could be explained by an increasing in both the inlet and outlet loss coefficients for the higher values of the rotor speed. Unfortunately, the literature scrutinized so far, presents only few contributions on the specific theme of the inlet and outlet loss coefficients. Mullins and Barret [45] adopted a local friction factor model, in their model assumed the wall shear stresses to increase from zero at the seal inlet to the fully developed value at the end. Shapiro et al. [57] documented higher values of the wall friction at the entrance of a round tube, decreasing to the fully developed value at about forty diameters. Elrod et al. [25] adopted a flat-plate-like model to describe the local behavior of the wall shear stresses in the inlet proximity. Still Elrod et al.[24] modeled the inlet and outlet friction coefficient with an empirical inlet and outlet friction polynomial multipliers obtained by local fitting of the experimental pressure gradient.

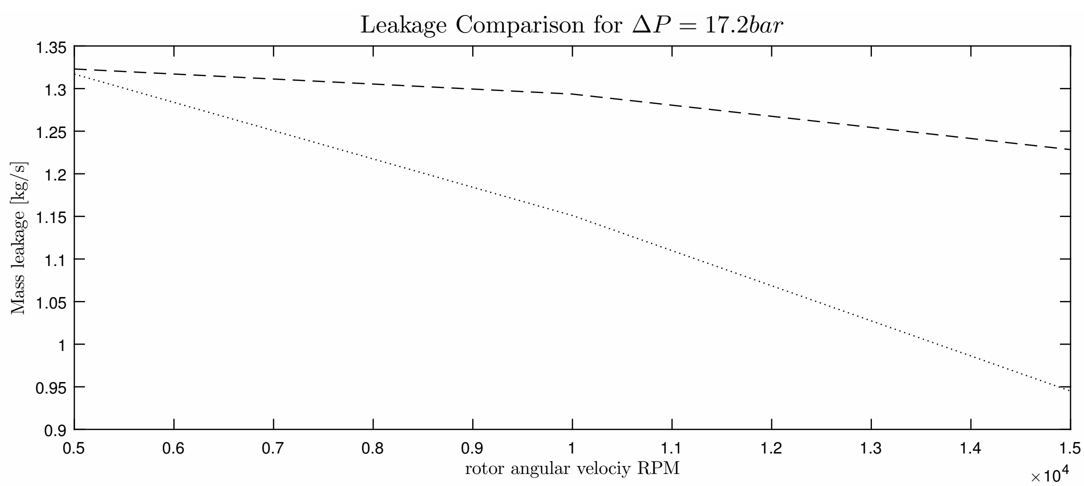

Figure 2.25: Leakage comparison. $\Delta P_0 = 17.2bar$, D=89cm, L/R=0.58, $H = 0.18mm$, $\mu = 0.00364Pl$, $\rho = 900kg/m^3$, $\zeta_i = 0.2$, $\zeta_o = 1$. – – dashed line: bulk flow model ··········· dotted line: measurements

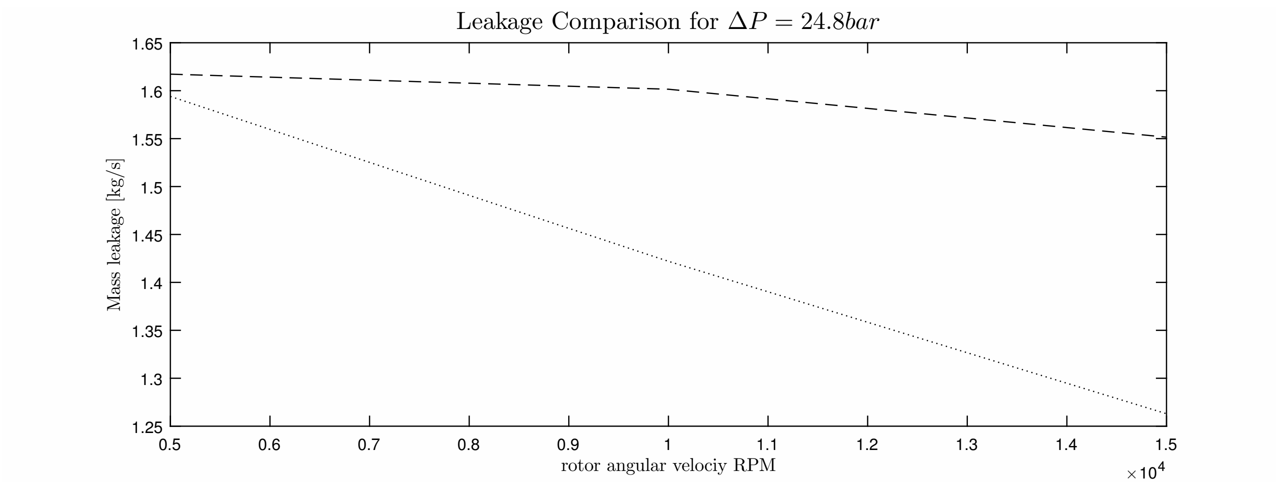

Figure 2.26: Leakage comparison. $\Delta P_0 = 24.8bar$, D=89cm, L/R=0.58, $H = 0.18mm$, $\mu = 0.00364Pl$, $\rho = 900kg/m^3$, $\zeta_i = 0.2$, $\zeta_o = 1$. – – dashed line: bulk flow model ··········· dotted line: measurements

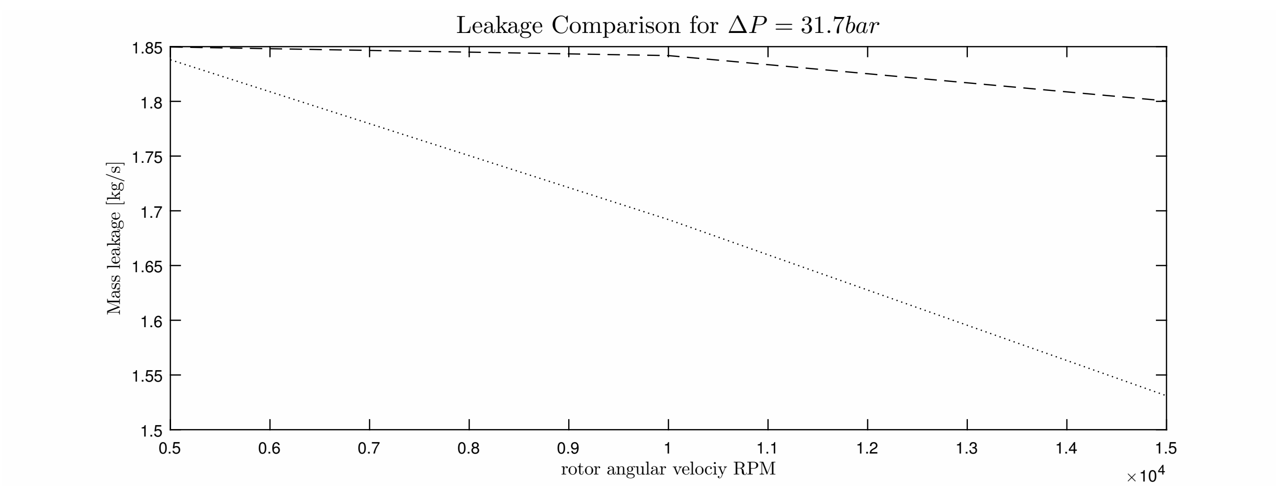

Figure 2.27: Leakage comparison. $\Delta P_0 = 31.7bar$, D=89cm, L/R=0.58, $H = 0.18mm$, $\mu = 0.00364Pl$, $\rho = 900kg/m^3$, $\zeta_i = 0.2$, $\zeta_o = 1$. – – dashed line: bulk flow model ··········· dotted line: measurements

Static Direct Stiffness K

Figures 2.28-2.30 shows the comparison between the predicted and measured values of K. The direct stiffness measurements show an increasing trend (almost linear) with the rotor speed Ω while the pressure gradient has little effect on it. The case characterized by ΔP=17.2 bar shows however a variation of k with the rotor speed, different with respect to the other two cases. This strange behavior is still unexplained.

The bulk model predictions of K, differently from the measured values, are constant with the variation of Ω while increase with δP.

Static Quadrature Stiffness k

Figures 2.28-2.30 show the comparison between the predicted and measured values of k. As for the long seal case, the measured quadrature stiffness grows with Ω while ΔP has only little effect on it. The bulk model predicted values are in good agreement when ΔP=17.2 bar, for higher values of the pressure drop, measured and predicted k agrees only for higher values of Ω.

Direct Damping D

Figures 2.28-2.30 shows the comparison between the predicted and measured values of D. Comparison shows the same trends of measured and predicted D values. However, the predicted values are constantly lower than the measured ones of about 30%.

Quadrature Damping d

Figures 2.28-2.30 shows the comparison between the predicted and measured values of d. The quadrature damping (both measured and predicted) grows almost linearly with the rotor speed Ω. The predicted values are constantly lower than the measured ones.

Direct Mass M

Figures 2.28-2.30 shows the comparison between the predicted and measured values of M. The predicted direct mass M is about constant in every operating condition (about $1kg$). The measured direct mass shows a constant value too but far greater than the predicted one (about $7kg$).

Quadrature Mass m

Figures 2.28-2.30 shows the comparison between the predicted and measured values of m. The measured values show a slightly increasing trend with ΔP, while decrease with Ω. The measured values however are negligible with respect the cross coupled damping. The predicted quadrature mass m is almost null as for the long seal case, its value is in the dispersion range of the measured values for all the operating conditions scrutinized.

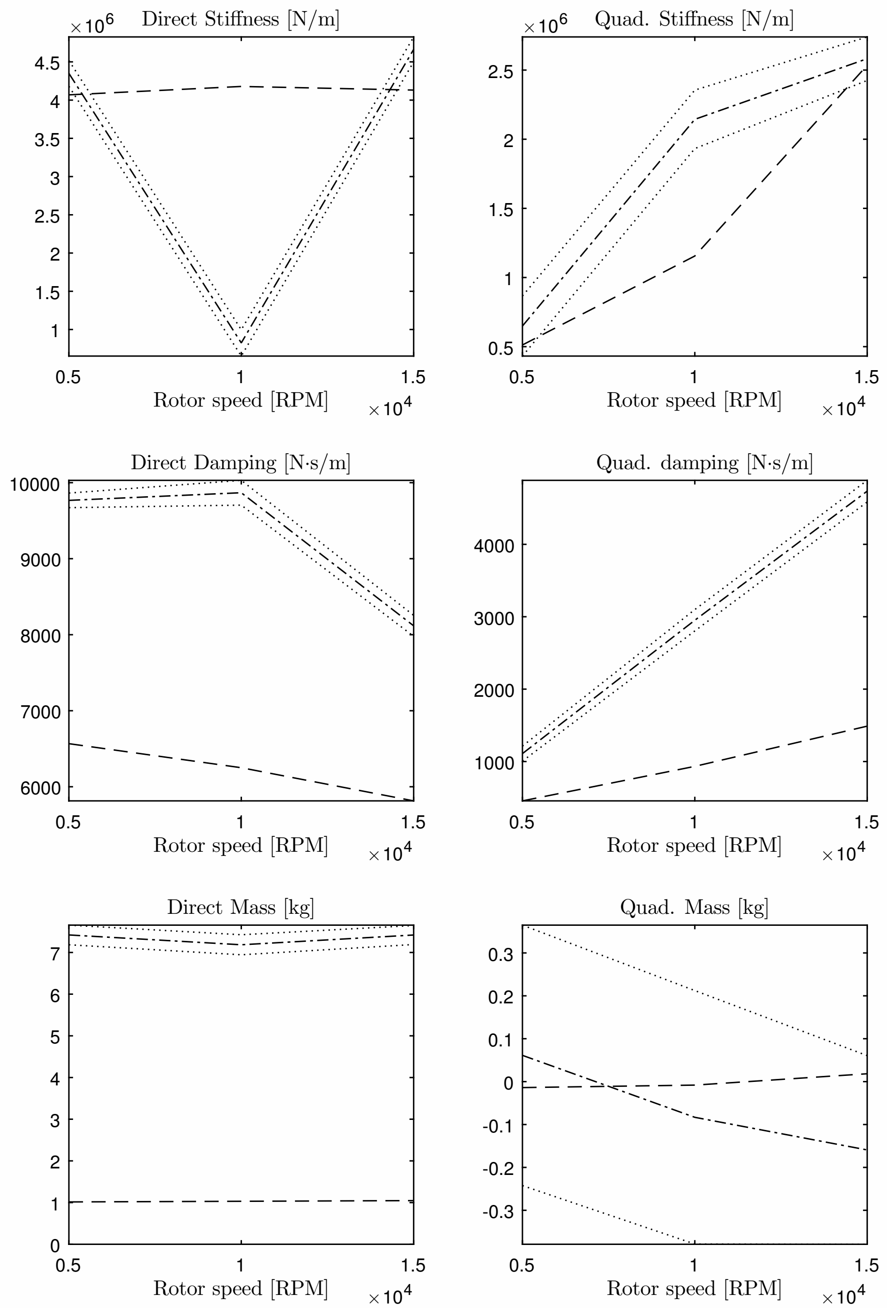

Figure 2.28: Stiffness variation with the rotor speed Ω. $\Delta P_0 = 17.2bar$, D=89cm, L/R=0.58, $H = 0.18mm$, $\mu = 0.00364Pl$, $\rho = 900kg/m^3$, $\zeta_i = 0.2$, $\zeta_o = 1$. $---$ dashed line: bulk flow model, dotted lines ⋯⋯⋯: measurements bounds, $-\cdot-\cdot$ dot dashed line: measurement average.

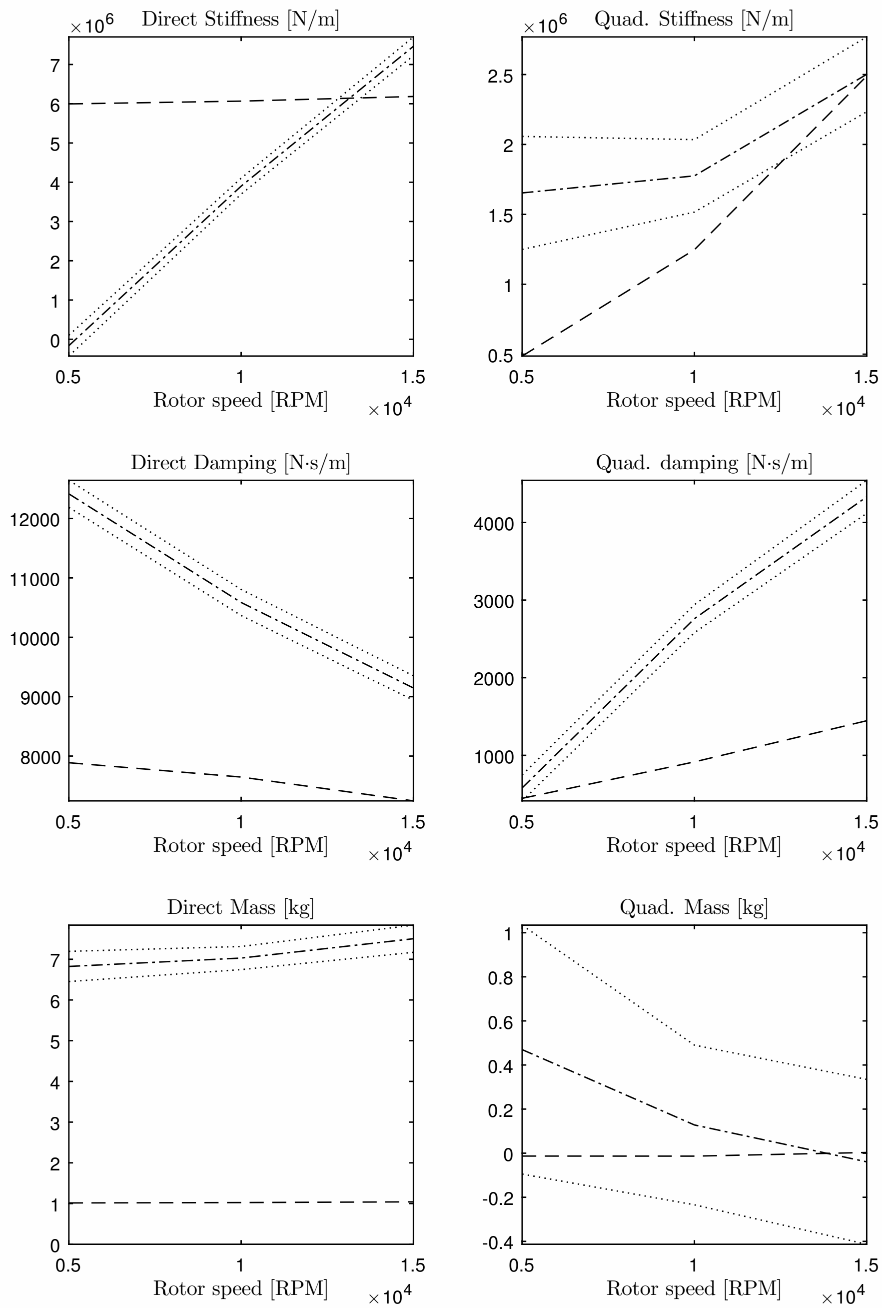

Figure 2.29: Stiffness variation with the rotor speed Ω. $\Delta P_0 = 24.8bar$, D=89cm, L/R=0.58, $H = 0.18mm$, $\mu = 0.00364Pl$, $\rho = 900kg/m^3$, $\zeta_i = 0.2$, $\zeta_o = 1$. $---$ dashed line: bulk flow model, dotted lines ··········: measurements bounds, $-\cdot-$ dot dashed line: measurement average.

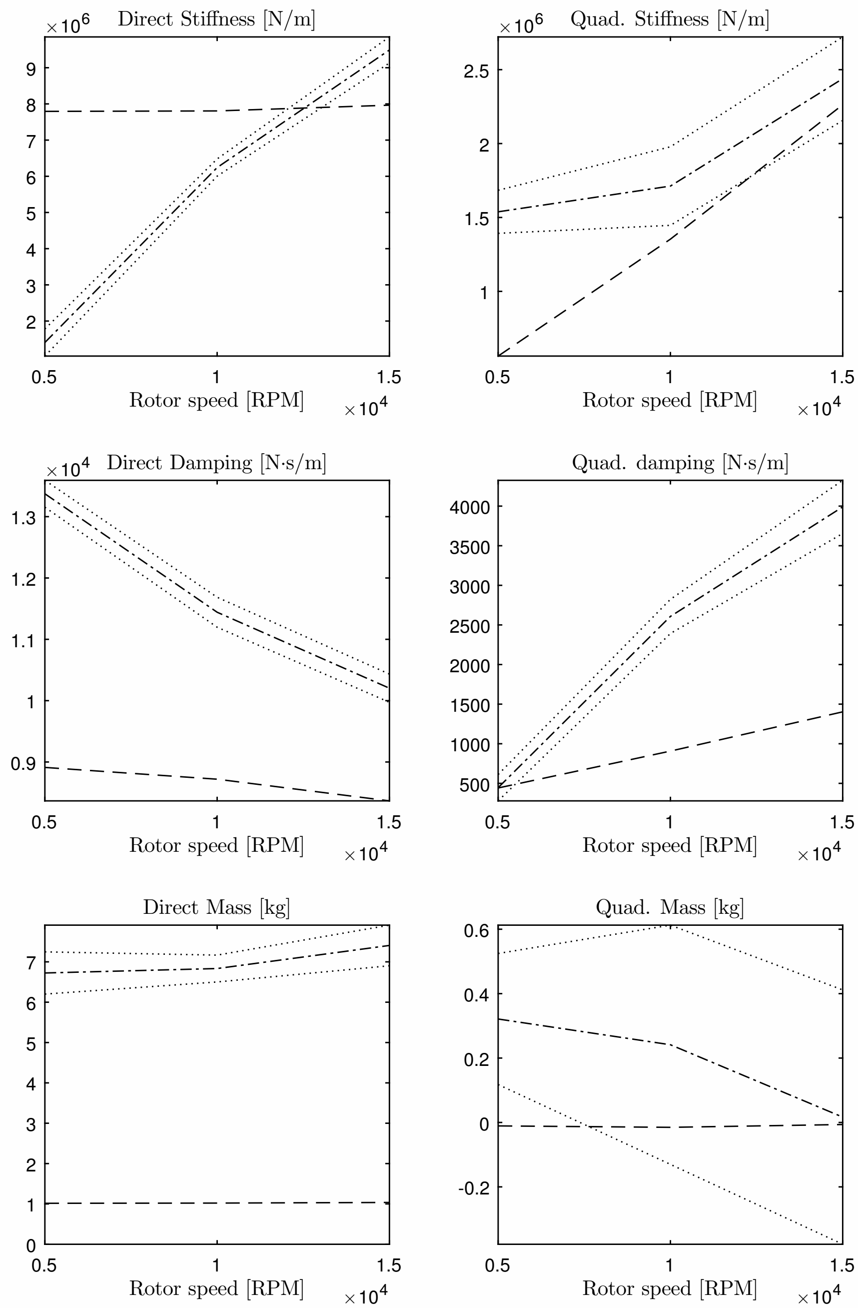

Figure 2.30: Stiffness variation with the rotor speed Ω. $\Delta P_0 = 31.7 bar$, D=89cm, L/R=0.58, $H = 0.18mm$, $\mu = 0.00364Pl$, $\rho = 900kg/m^3$, $\zeta_i = 0.2$, $\zeta_o = 1$. $---$ dashed line: bulk flow model, dotted lines ··········: measurements bounds, $-\cdot-$ dot dashed line: measurement average.

2.9.2 Perfect gas flow

Long seal L/R=1.5

Leakage Comparison

Figures 2.31-2.33 show the comparison between predicted and measured leakages for a perfect gas flow. As can be seen, there is close agreement between predictions and measurements.

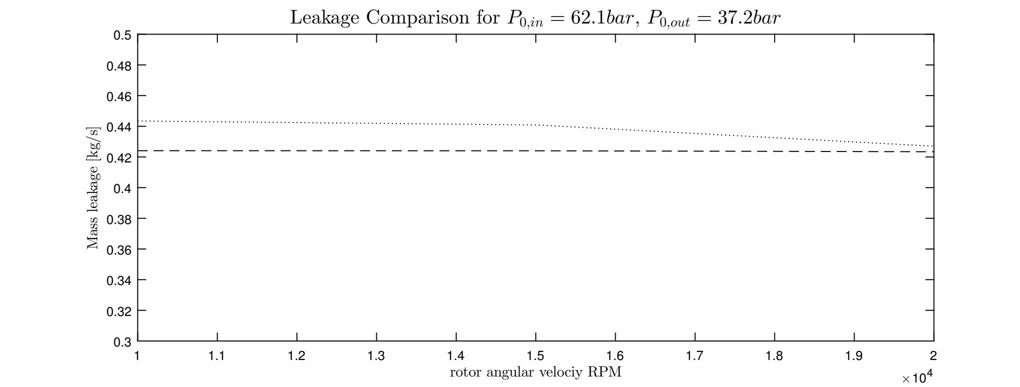

Figure 2.31: Leakage comparison. $P_{0,in} = 62.1bar$, $P_{0,out} = 37.2bar$, D=89cm, L/R=1.5, $H = 0.18mm$, $\mu_g = 1.82 \times 10^{-5} Pl$, $R_g = 287J/kg/K$, $\zeta_i = 0.2$, $\zeta_o = 1$. - - dashed line: bulk flow model ·········· dotted line: measurements

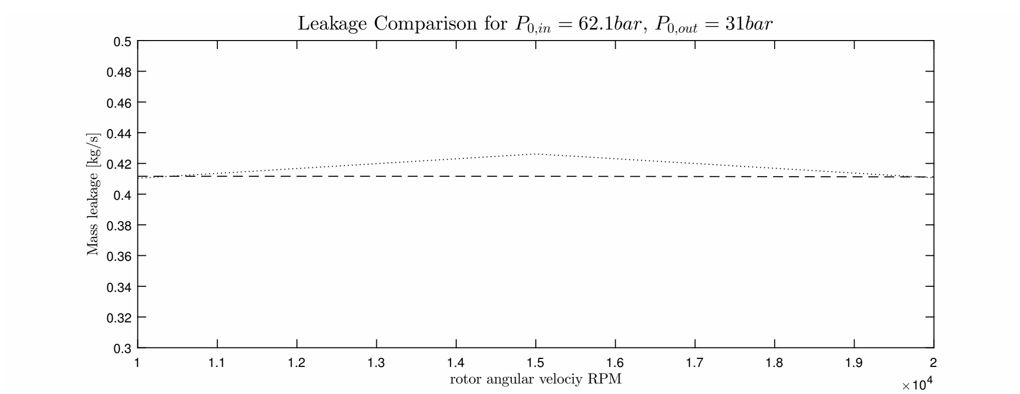

Figure 2.32: Leakage comparison. $P_{0,in} = 62.1bar$, $P_{0,out} = 31bar$, D=89cm, L/R=1.5, $H = 0.18mm$, $\mu_g = 1.82 \times 10^{-5} Pl$, $R_g = 287J/kg/K$, $\zeta_i = 0.2$, $\zeta_o = 1$. - - dashed line: bulk flow model ·········· dotted line: measurements

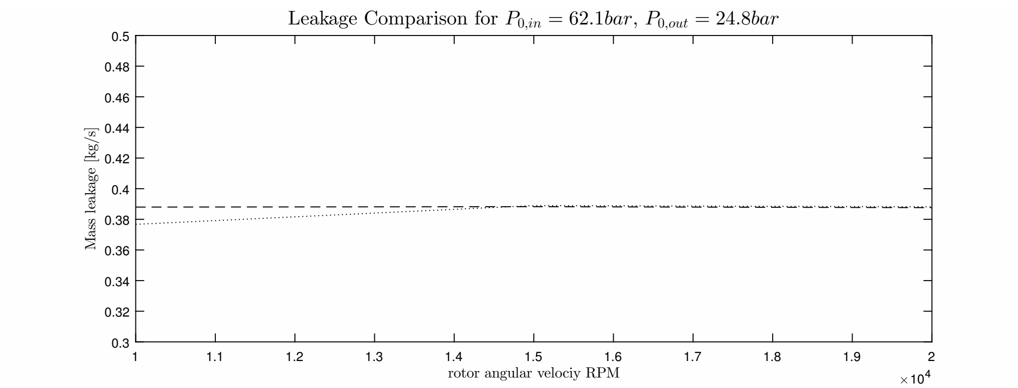

Figure 2.33: Leakage comparison. $P_{0,in} = 62.1bar$, $P_{0,out} = 24.8bar$, D=89cm, L/R=1.5, $H = 0.18mm$, $\mu_g = 1.82 \times 10^{-5}Pl$, $R_g = 287J/kg/K$, $\zeta_i = 0.2$, $\zeta_o = 1$. -- dashed line: bulk flow model ··········· dotted line: measurements

Static Direct Stiffness K

Figures 2.34-2.36 show the comparison between the predicted and measured values of K. Both predicted and measured values show a little decrease with the pressure gap. Predictions overestimates the measured values of about $3-4$ times.

Static Quadrature Stiffness k

Figures 2.34-2.36 show the comparison between the predicted and measured values of k. Both measured and predicted values of the quadrature static stiffness increase with the rotor speed Ω. The outlet total pressure has little effect on both predicted and measured values. Predictions underestimate the measured values with a variable bias of about $1000 - 2000N/mm$.

Direct Damping D

Figures 2.34-2.36 show the comparison between the predicted and measured values of D. Both measurements and predictions are almost constant with the rotor speed and the outlet total pressure. The predicted values however are almost 20% lower than the measured one in the whole operating range.

Quadrature Damping d

Figures 2.34-2.36 show the comparison between the predicted and measured values of d. The measured quadrature damping is almost constant with the rotor speed. There is reasonable agreement between predictions and measurements.

Direct Mass M

Figures 2.34-2.36 show the comparison between the predicted and measured values of M. The measured direct added mass is almost constant with the rotor speed, predictions show the same trend. The bulk-model predicts an increasing trend of the added direct mass with the pressure gap from $0.2kg$ for the low pressure gap case to $0.6kg$ for the high pressure gap case. Measured values are almost null.

Quadrature Mass m

Figures 2.34-2.36 show the comparison between the predicted and measured values of m. Both measured and predicted quadrature masses show a weak variation with Ω. The predicted values $(0.2-0.4kg)$ are almost constant with the outlet total pressure. Measurements show a negligible quadrature added mass.

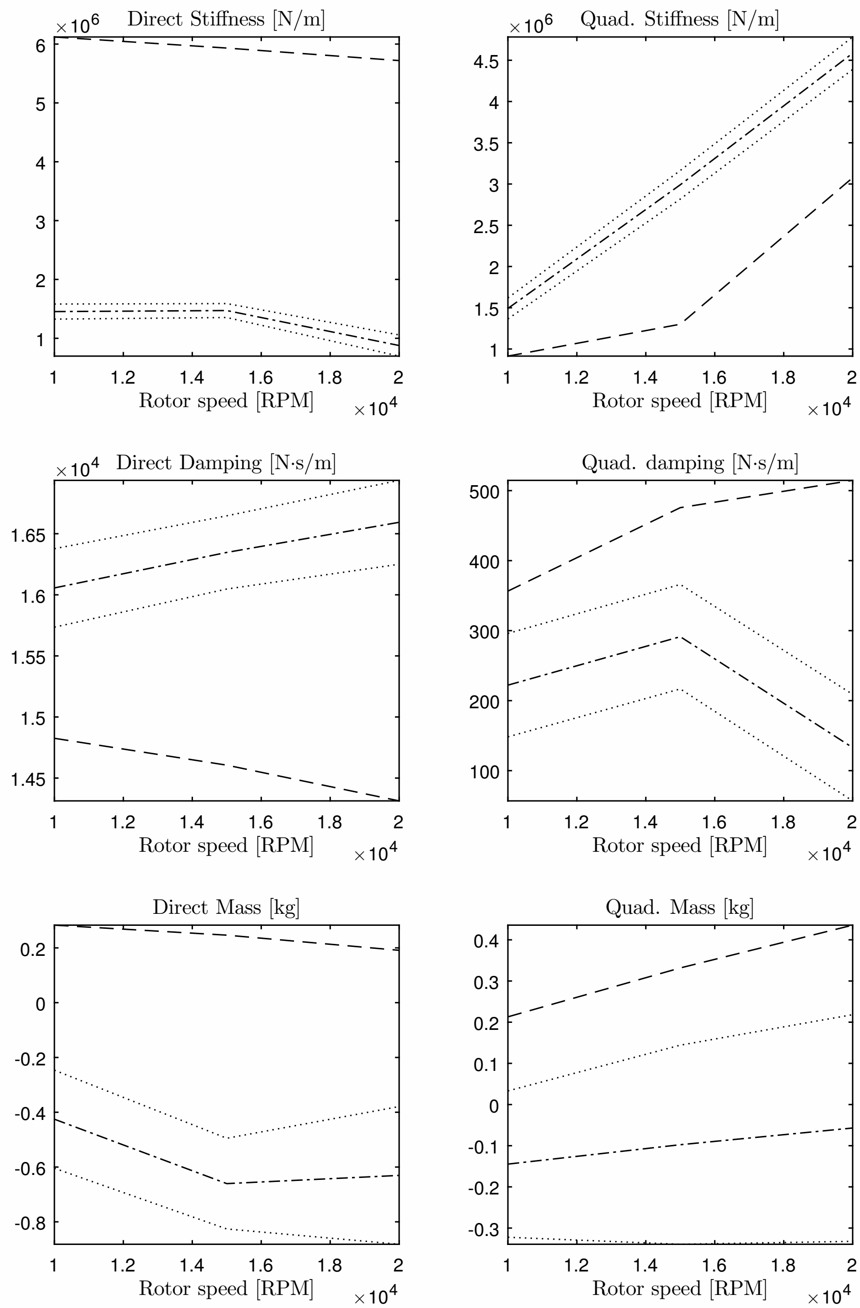

Figure 2.34: Stiffness variation with the rotor speed Ω. $P_{0,in} = 62.1bar$, $P_{0,out} = 24.8bar$, D=89cm, L/R=1.5, $H = 0.18mm$, $\mu_g = 1.82 \times 10^{-5} Pl$, $R_g = 287 J/kg/K$, $\zeta_i = 0.2$, $\zeta_o = 1$. dashed line: bulk flow model, dotted lines ············: measurements bounds, $- \cdot - \cdot$ dot dashed line: measurement average.

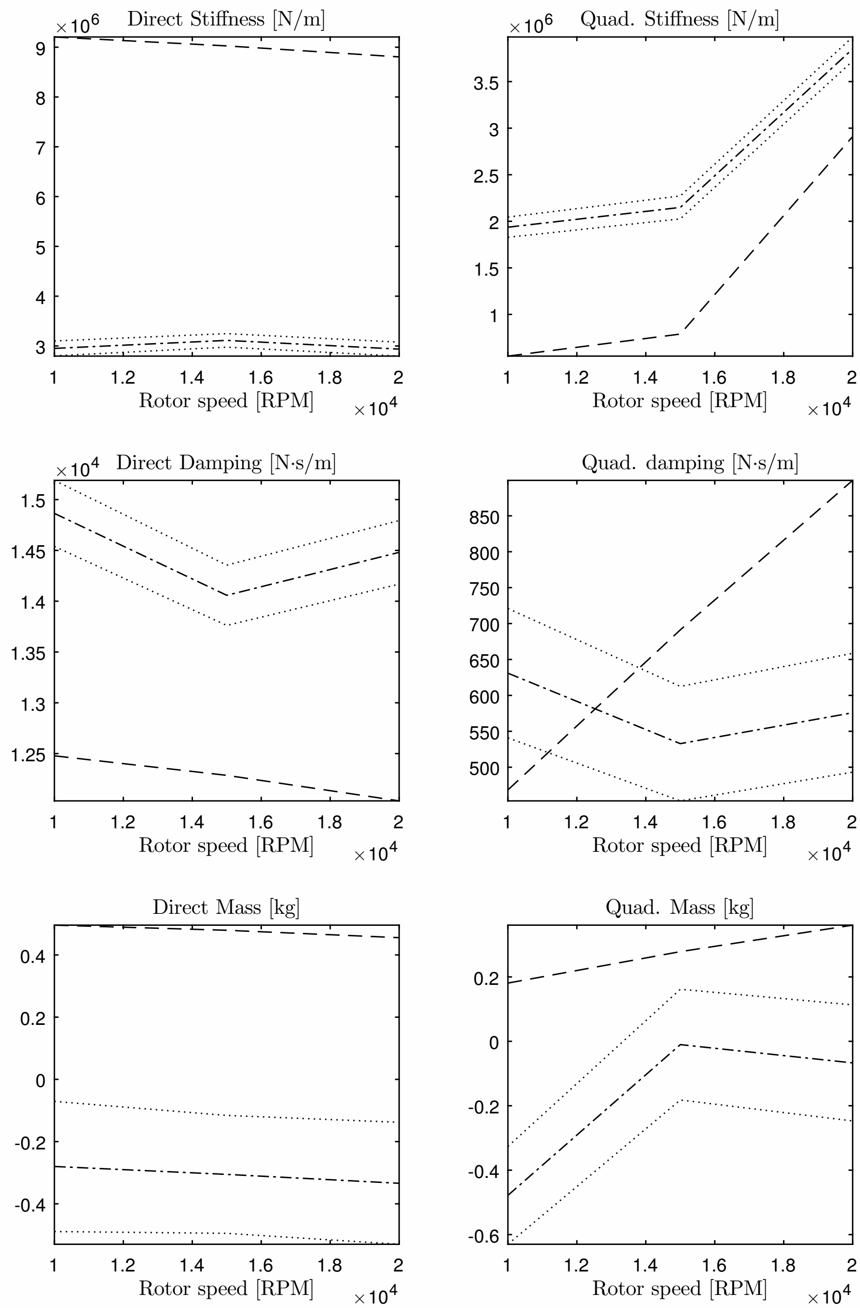

Figure 2.35: Stiffness variation with the rotor speed Ω. $P_{0,in} = 62.1 bar$, $P_{0,out} = 31 bar$, D=89cm, L/R=1.5, $H = 0.18mm$, $\mu_g = 1.82 \times 10^{-5} Pl$, $R_g = 287 J/kg/K$, $\zeta_i = 0.2$, $\zeta_o = 1$. dashed line: bulk flow model, dotted lines ⋯⋯: measurements bounds, $-\cdot-$ dot dashed line: measurement average.

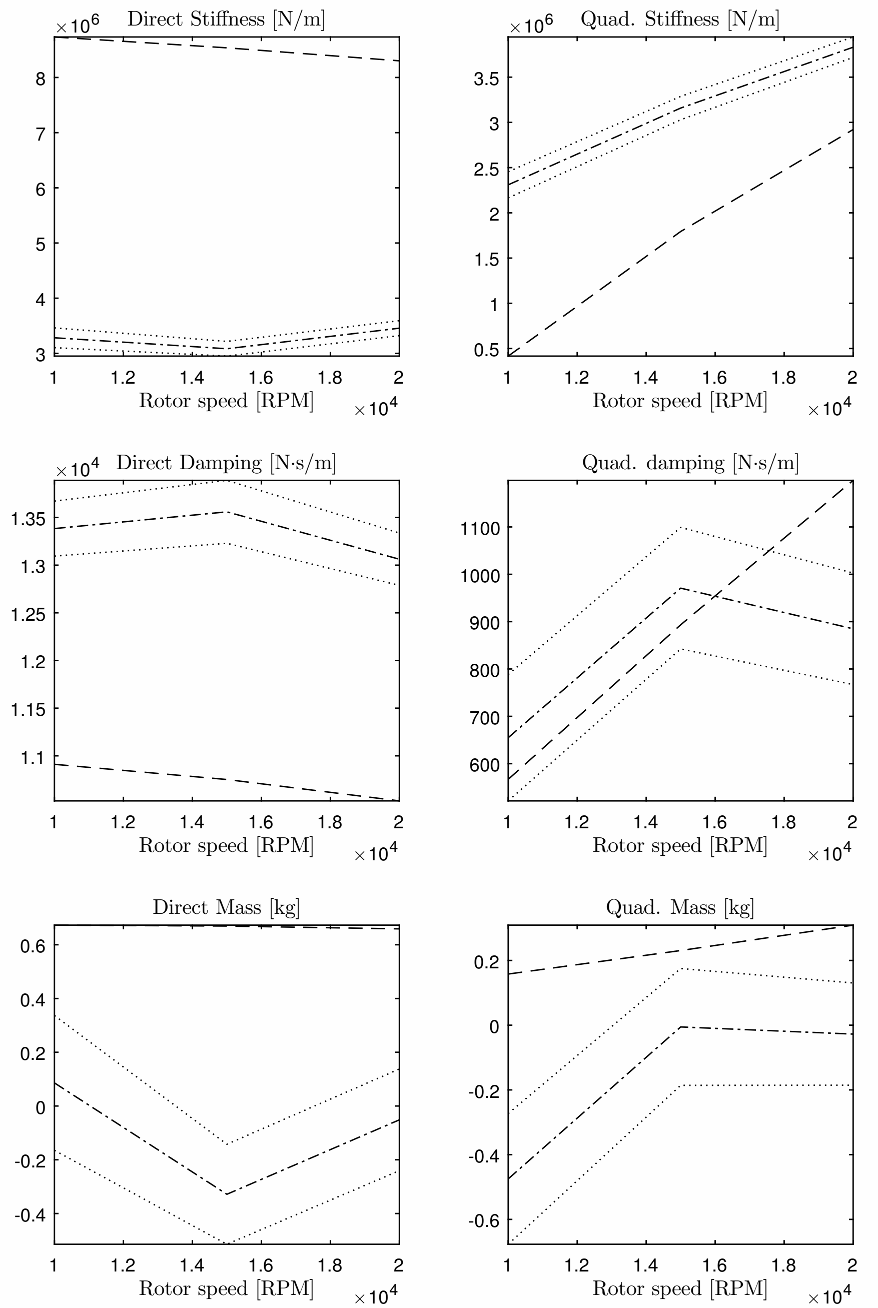

Figure 2.36: Stiffness variation with the rotor speed Ω. $P_{0,in} = 62.1bar$, $P_{0,out} = 37.2bar$, D=89cm, L/R=1.5, $H = 0.18mm$, $\mu_g = 1.82 \times 10^{-5}Pl$, $R_g = 287J/kg/K$, $\zeta_i = 0.2$, $\zeta_o = 1$. dashed line: bulk flow model, dotted lines ⋯⋯: measurements bounds, $-\cdot-$ dot dashed line: measurement average.

Short seal L/R=0.58

Leakage Comparison

Figures 2.37-2.39 show the comparison between predicted and measure mass flow rates in case of perfect gas flow in a short seal. Differently from the long seal case, there is a constant error of about 10%. An adjustment of the inlet or outlet loss coefficients could get better agreement. The need of different loss coefficients between long and short seal remains unexplained.

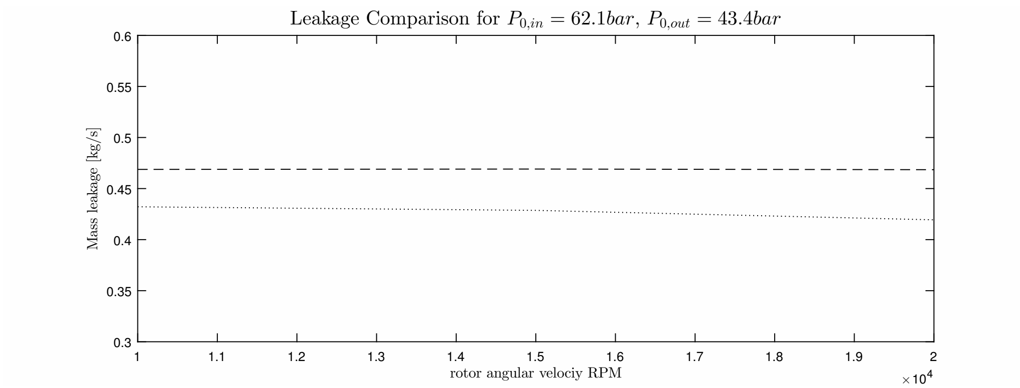

Figure 2.37: Leakage comparison. $P_{0,in} = 62.1bar$, $P_{0,out} = 43.4bar$, D=89cm, L/R=0.58, $H = 0.18mm$, $\mu_g = 1.82 \times 10^{-5} Pl$, $R_g = 287 J/kg/K$, $\zeta_i = 0.2$, $\zeta_o = 1$. – – dashed line: bulk flow model ········· dotted line: measurements

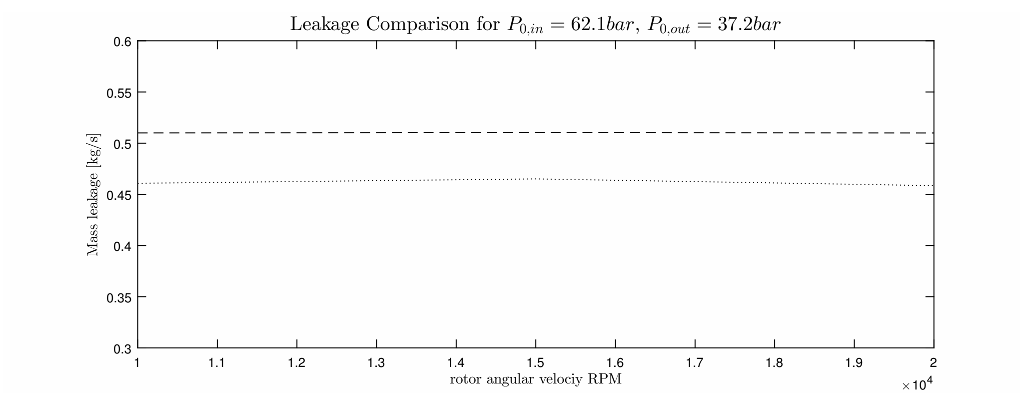

Figure 2.38: Leakage comparison. $P_{0,in} = 62.1bar$, $P_{0,out} = 37.2bar$, D=89cm, L/R=0.58, $H = 0.18mm$, $\mu_g = 1.82 \times 10^{-5} Pl$, $R_g = 287 J/kg/K$, $\zeta_i = 0.2$, $\zeta_o = 1$. – – dashed line: bulk flow model ········· dotted line: measurements

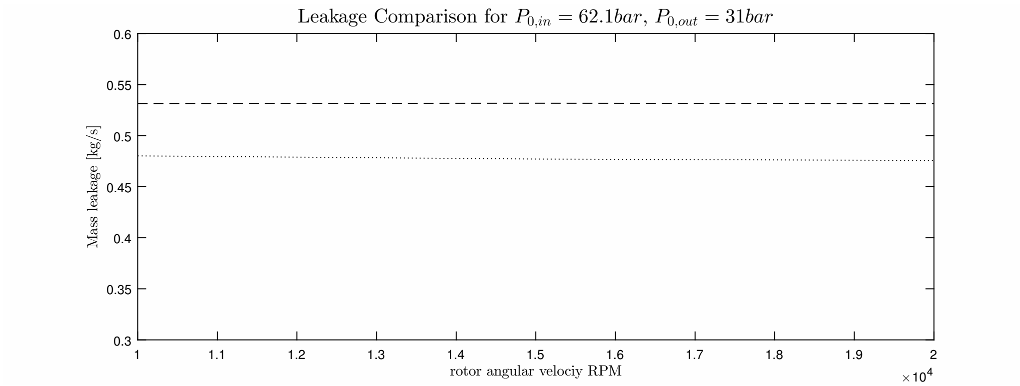

Figure 2.39: Leakage comparison. $P_{0,in} = 62.1bar$, $P_{0,out} = 31bar$, D=89cm, L/R=0.58, $H = 0.18mm$, $\mu_g = 1.82 \times 10^{-5} Pl$, $R_g = 287J/kg/K$, $\zeta_i = 0.2$, $\zeta_o = 1$. - - dashed line: bulk flow model ··········· dotted line: measurements

Static Direct Stiffness K

Figures 2.40-2.42 show the comparison between the predicted and measured values of K. The measured static direct stiffness is almost constant with both the pressure gap and the rotor speed. The bulk predictions show the same trend with the rotor speed though overestimate the measurements of about $20 \div 30\%$.

Static Quadrature Stiffness k

Figures 2.40-2.42 show the comparison between the predicted and measured values of k. The predicted bulk-model values of k vary in the range $200 < k < 400N/mm$, showing and increasing trend with Ω as the measured ones. Predictions are in reasonable agreement with the measured values that show a wide dispersion around the average. The measured averaged values increase with the rotor speed from 0 to about $200N/mm$ with a confidence range of about $300N/mm$.

Direct Damping D

Figures 2.40-2.42 show the comparison between the predicted and measured values of D. Both measured and predicted direct damping show almost constant values with the rotor speed Ω. The bulk-model predicted values of D show a decrease with the outlet total pressure as the measured ones. In all the cases, bulk model predictions underestimate the measured value of about $20 - 40\%$.

Quadrature Damping d

Figures 2.40-2.42 show the comparison between the predicted and measured values of d. The measured values are almost constant with the different operating conditions, with an average value spanning in the range $50 < d < 150 N \cdot /s$ though a wide dispersion affects the accuracy. The bulk-predicted values falls on the lower border of the dispersion range.

Direct Mass M

Figures 2.40-2.42 show the comparison between the predicted and measured values of M. The measured added direct masses show values of about $0.6 \div 1 Kg$ while the bulk model predicts almost null added direct masses.

Quadrature Mass m

Figures 2.40-2.42 show the comparison between the predicted and measured values of m. The measured quadrature added masses is almost null in every operating condition. The predicted values are in excellent agreement with the measured ones.

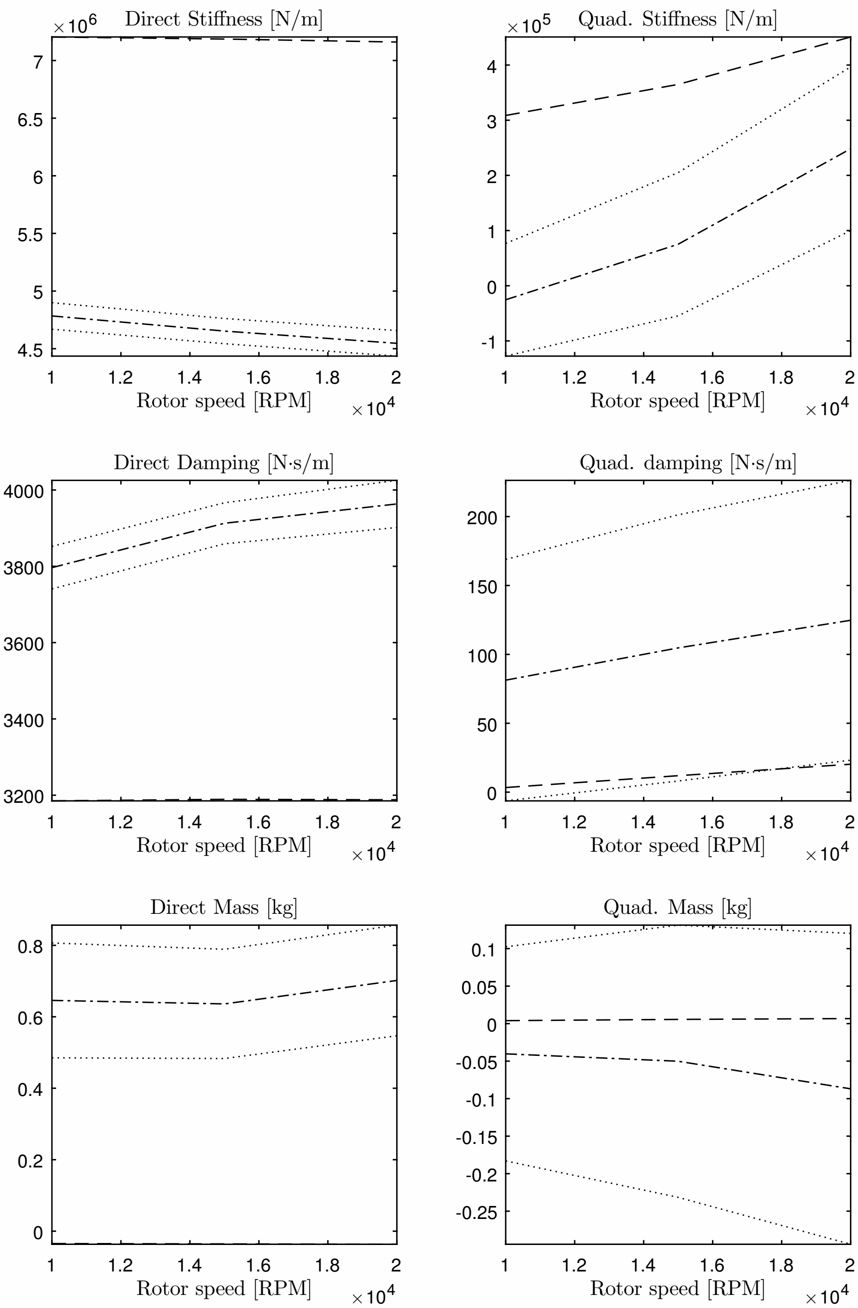

Figure 2.40: Stiffness variation with the rotor speed Ω. $P_{0,in} = 62.1bar$, $P_{0,out} = 31bar$, D=89cm, L/R=0.58, $H = 0.18mm$, $\mu_g = 1.82 \times 10^{-5} Pl$, $R_g = 287 J/kg/K$, $\zeta_i = 0.2$, $\zeta_o = 1$. dashed line: bulk flow model, dotted lines ············: measurements bounds, $-\cdot-\cdot$ dot dashed line: measurement average.

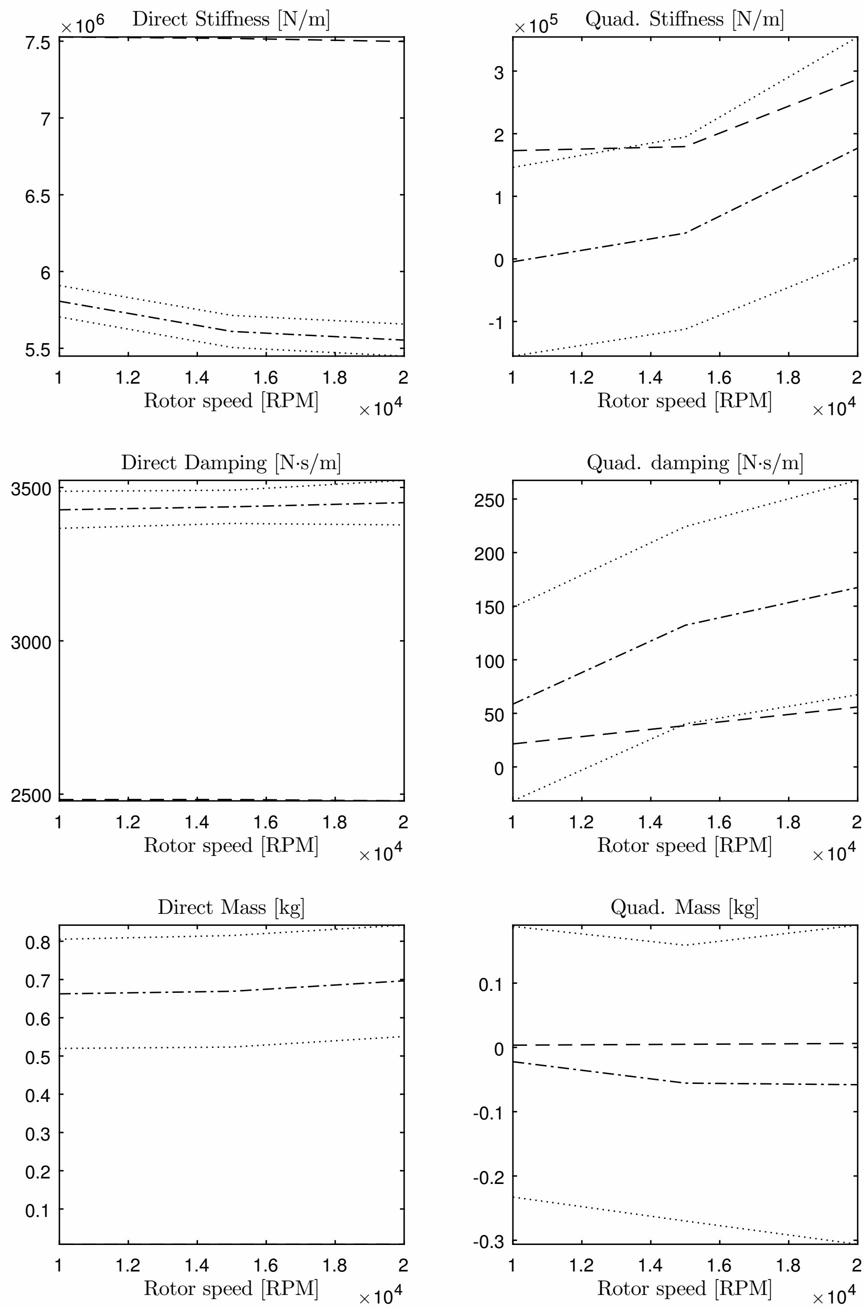

Figure 2.41: Stiffness variation with the rotor speed Ω. $P_{0,in} = 62.1bar$, $P_{0,out} = 37.2bar$, D=89cm, L/R=0.58, $H = 0.18mm$, $\mu_g = 1.82 \times 10^{-5} Pl$, $R_g = 287J/kg/K$, $\zeta_i = 0.2$, $\zeta_o = 1$. dashed line: bulk flow model, dotted lines ⋯⋯: measurements bounds, $-\cdot-$ dot dashed line: measurement average.

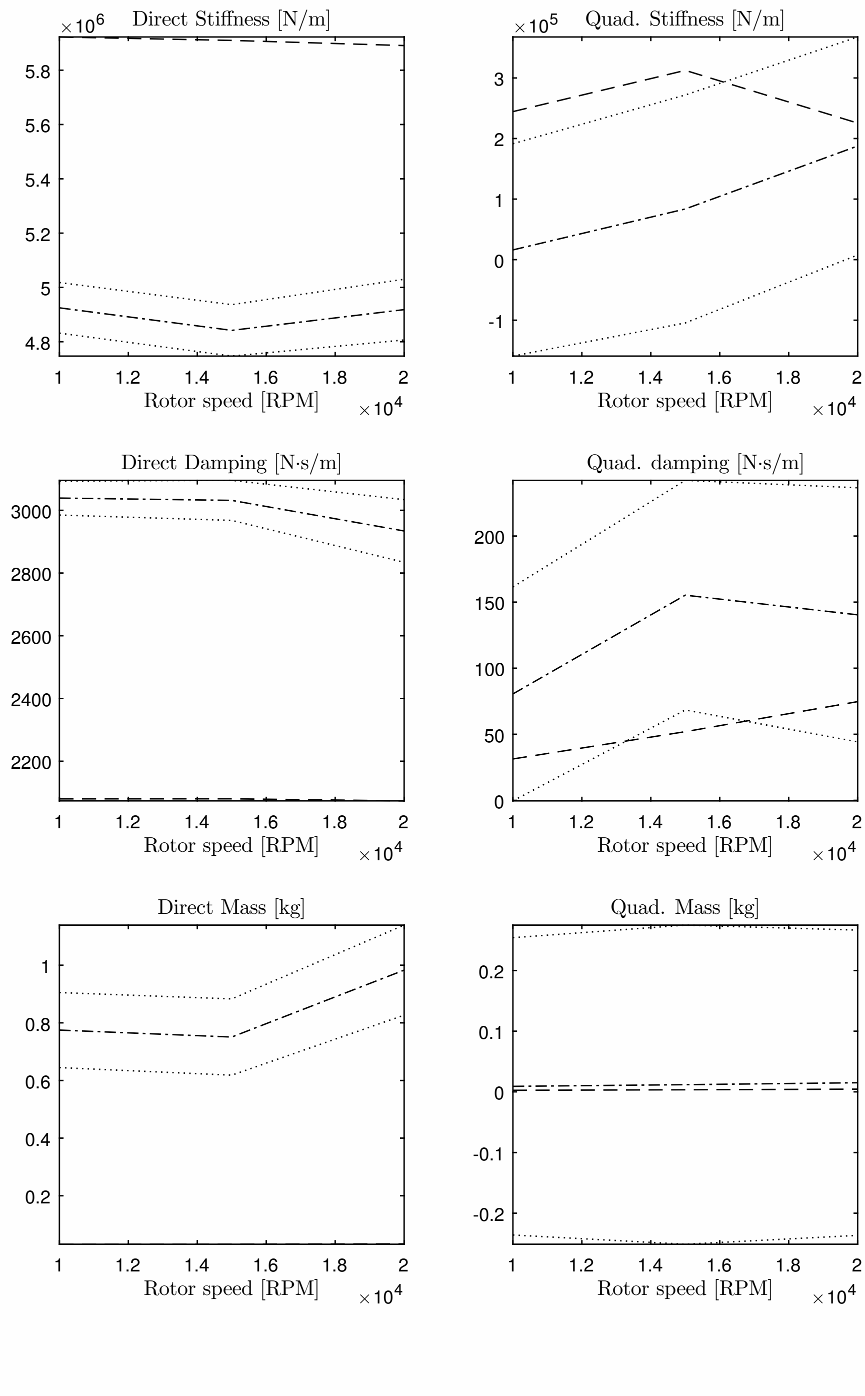

Figure 2.42: Stiffness variation with the rotor speed Ω. $P_{0,in} = 62.1bar$, $P_{0,out} = 43.4bar$, D=89cm, L/R=0.58, $H = 0.18mm$, $\mu_g = 1.82 \times 10^{-5} Pl$, $R_g = 287J/kg/K$, $\zeta_i = 0.2$, $\zeta_o = 1$. dashed line: bulk flow model, dotted lines ············: measurements bounds, $-\cdot-\cdot$ dot dashed line: measurement average.

2.10 Conclusions

In this chapter a global review on the main themes related to the modeling of a single-phase bulk-flow inside an annular pressure seal operating with either perfect gas and liquid fluid has been presented. A modified wall shear stress formulation has been introduced based on the Hirs formulation [28]. Leakage comparisons show better agreement between bulk model predictions and experimental measurements in the perfect-gas flow cases where a maximum error of about 10% has been observed. In the liquid case, despite the correction of the wall shear stress model, the bulk predictions underestimate the leakage reduction with the rotor speed. To the author, possible causes of these discrepancies can be found in an unsuitable wall-friction law in the low-Re range. Discrete agreement between measured and predicted rotordynamic response has emerged. As shown in the next chapter, better agreement with the experimental data can be reached with an adequate choice of the inlet and outlet pressure loss coefficients. The CFD simulations have been also conducted in the case of incompressible long seal. The CFD has shown poor agreement in the leakage prediction. To the author the discrepancies can be mainly related to the limits of turbulence model adopted (RANS $\kappa-\varepsilon$ SST) unable to adequate predicts the turbulent field in case of transitional swirled flow.

Chapter 3

Homogeneous two-phase flows in annular pressure seals

3.1 Introduction

This chapter deals with the homogeneous two-phase (gas-liquid) bulk-flow modeling. The homogeneous model is developed under the assumption of no mass transfer between the two phases. In facts, in the experimental cases considered, no liquid boiling is observed and the mass transfer between the two phases, mainly related to the liquid diffusion in the gas phase, can be neglected Many contributions can be found in literature dealing with the problem of two phase flows in mini/micro channels. The first two-phase model was introduced by Lockhart and Martinelli [35]. Starting from the experimental analysis of two-phase flows of different mixtures (air with different liquids: water, benzene, kerosene and oils), and considering different pipe diameters (0.0586 to 1.017 inches), they proposed an analytic model to predict pressure drop and liquid hold-up. The Lockhart-Martinelli model is the first model based on a "separated flow" approach, in which the two friction multipliers ϕ_l^2 and ϕ_g^2 (respectively the ratio between the two phase pressure gradient and the pressure gradient which would exist if the liquid/gas phase is assumed to flow alone) are correlated to the Lockhart-Martinelli parameter $\chi = \phi_g \phi_l$. A further contribution on the two-phase flows has been given by Dukler [22, 23]. He developed an homogeneous model based on a "dynamic similarity analysis" to better fit experimental data by adopting new definitions of the mixture equivalent density and viscosity. Many studies have integrated the work of Dukler, by adding transition criteria between the different flow patterns. In particular, a global review on the transition criteria and the related literature can be found in Barnea [5]. In his work, Barnea proposed a unification between the different transition criteria (bubble/disperse bubbly flow, stratified/non stratified flow, stratified/annular flow, annular/intermittent flow) based on a logical path.

A new formulation of the equivalent two-phase viscosity (in the context of the homogeneous models) has been proposed in Beattie and Whallie [6]. They proposed a hybrid definition of the equivalent mixture viscosity that, at given void fraction, interpolates between the Einstein formula for the bubbly equivalent mixture viscosity and the mixture viscosity of an annular flow. Müeller, Steinhagen and Heck [44] developed a separated-flow model based on a empirical two-phase extrapolation between all liquid flow and all vapor flow. Kim [30, 31] presented an accurate evaluation of the whole literature about the two-phase bulk modeling based on the comparison with a wide experimental database. Moreover, he proposed a new approach based on the Lockhart-Martinelli method "by incorporating appropriate dimensionless relations in a separated flow model to account for both small channel size and different combinations of liquid and vapor states".

Although a wide literature exists on the theme of multiphase flows in both circular and rectangular (with different aspect ratios) channels, the application of the two-phase models presented so far to the case of the annular pressure seals isn't straightforward. The presence of a circumferential flow with the consecutive centrifugal force acting on the two fluids does not make it possible to extend the transition criteria and the pressure drop models to this specific case. Moreover, no flow pattern maps are available in the literature for this kind of two-phase flows. The most used approach (see for example, Arauz and San Andres [2, 3, 64] and Beatty and Hughes [7]), is based on the "homogeneous mixture" assumption (*i.e.* finely mixed bubbly flow). The two-phase flow is simplified in an equivalent single phase flow characterized by an equivalent state equation and mixture viscosity. The homogeneous model produces quite accurate predictions of mass leakage of multiphase seals, but usually underestimates the leakage decrease with the inlet gas volume fraction (GVF) in the region characterized by high GVF. The homogeneous bulk-model predictions are finally compared to the experimental results of the tests done at the Turbomachinery Laboratory of the Texas *A&M* University "Experimental Study of the Static and Dynamic Characteristics of a Long (L/D=0.75) Smooth Seal with Mainly Air Mixtures", "Experimental Study of the Static and Dynamic Characteristics of a Short (L/D=0.29) Smooth Seal with Mainly Air Mixtures", "Experimental Study of the Static and Dynamic Characteristics of a Long (L/D=0.75) Smooth Seal with Mainly Oil Mixtures" and "Experimental Study of the Static and Dynamic Characteristics of a Short (L/D=0.29) Smooth Seal with Mainly Oil Mixtures".

3.2 Homogeneous constitutive model

In the first chapter bulk-flow equations have been introduced for single phase flows. The simplest way for taking account of the phase interaction is to adopt an homogeneous multiphase model.

The homogeneous multiphase model is indicated in all cases where the phases are finely mixed (like in a bubbly mixture). The main assumption is that the two phases share the same temperature, pressure and velocity. The state equation for an homogeneous mixture of an incompressible liquid and a perfect gas is:

$$\frac{p}{\rho} = \lambda R_g T + (1-\lambda)\frac{p}{\rho_l} \tag{3.1}$$

where R_g is the perfect gas constant, p is the static pressure, T is the temperature, ρ is the mixture density, and ρ_l is the liquid density. The quantity λ represents the *gas mass fraction*

(GMF) usually denoted as *quality*. In the limit of $\lambda = 0$ and $\lambda = 1$, the cases of incompressible liquid of density ρ_l and perfect gas with specific gas constant R_g are respectively recovered.

The *gas volume fraction* Ψ (GVF), usually denoted as *void fraction*, is related to the GMF through the following relation:

$$\Psi = \frac{\lambda}{\lambda + (1-\lambda)\frac{\rho_g}{\rho_l}} \tag{3.2}$$

ρ_g being the gas density.

3.3 Mixture equivalent viscosity

In the previous section the equivalent state equation for an homogeneous mixture has been introduced. However, a two-phase homogeneous model needs also to introduce an equivalent viscosity to correctly model the mixture wall friction. In this case however the task is not so straightforward as for the mixture density or every other intensive property. Various models are proposed in the literature (Cicchitti et al. [16], Dukler [23], Beattie and Whalley [6], Mc Adams [39]) with the aim to define an equivalent mixture viscosity able to mimic the real pressure drop of the two-phase flow. However, no one proved to give better results with respect to the others. For this reason, the first and simplest model, introduced by McAdams et al. (1942) [39], has been adopted:

$$\frac{1}{\mu_{tp}} = \frac{\lambda}{\mu_g} + \frac{1-\lambda}{\mu_l} \tag{3.3}$$

where μ_{tp}, μ_g and μ_l are respectively the equivalent viscosity of the mixture, the gas viscosity, and the liquid viscosity.

3.4 zeroth-order solution

The zeroth-order solution refers to the case of centered seal, i.e. zero eccentricity ($\delta = 0$, with reference to figure 1.1) In this case, dependence on the time t and circumferential coordinate x vanishes. Further, the clearance H is constant ($H = H_0 = const$). As a result, the continuity equation reduces to:

$$\rho V = Q = const. \tag{3.4}$$

where Q is the leakage per unit length *i.e.* $Q = q/(2\pi HR)$, being q the total leakage. By substituting ((3.4)) into ((3.1)) the temperature can be expressed as:

$$T = \frac{P}{\lambda R_g}\left[\frac{V}{Q} - \frac{1-\lambda}{\rho_l}\right] \tag{3.5}$$

Therefore by substituting (3.4)-(3.5) into (2.10a)-(2.10b) and (2.7a), the zeroth-order system equation simplifies in

$$Q\frac{\partial U}{\partial y} = \frac{\tau_c}{H} \tag{3.6a}$$

$$Q\frac{\partial V}{\partial y} + \frac{\partial P}{\partial y} = \frac{\tau_m}{H} \tag{3.6b}$$

$$\alpha P\frac{\partial V}{\partial y} + (\alpha - 1)\left(V - Q\frac{1-\lambda}{\rho_l}\right)\frac{\partial P}{\partial y} = \frac{\Omega R\, \tau_{xz}|_0 - U\tau_c - V\tau_m}{H} \tag{3.6c}$$

where $\alpha = C_p/(\lambda R_g)$, U and V are the circumferential and meridian velocity, P is the pressure and τ_c and τ_m are the circumferential and meridian shear stress, respectively. In equation (3.6c) the thermal exchange with the rotor and stator surfaces has been neglected (adiabatic flow) being unknown the working temperature of the structure. The assumption of an adiabatic flow inside the seal does not alter however the overall structural response of the seal (Zhou et al.[65]).

To solve the system (3.6c) we need to find the three field variables U, V, P and the parameter Q. Hence, to be the problem well posed, four boundary conditions are required.

3.4.1 Zeroth-order boundary conditions

In this subsection the homogeneous two-phase flow boundary conditions are outlined. Despite [63], the boundary conditions are generalized for an homogeneous mixture when the equivalent mixture state equation (3.5) holds true.

Inlet energy conservation

The inlet energy conservation equation is obtained by integrating the energy conservation equation between the inlet reservoir and the inlet section of the seal. The equation is then corrected to take into account the total pressure loss due to the local wall friction. Therefore, the energy balance equation and the correlation between the stagnation pressures before and after the inlet section can be written as

$$C_pT + \frac{1-\lambda}{\rho_l}P + \frac{1}{2}V^2 = C_pT_{0,in} + \frac{1-\lambda}{\rho_l}P_{0,in} = C_pT_{0,post} + \frac{1-\lambda}{\rho_l}P_{0,post} \tag{3.7a}$$

$$P_{0,post} = P_{0,pre} - \zeta_i\frac{\rho V_{in}^2}{2} \tag{3.7b}$$

where

$$C_p = \lambda C_{p,G} + (1-\lambda)C_l \tag{3.8}$$

and $C_{p,g}$ and C_l respectively are the specific heat at constant pressure of the gas and liquid phase. The subscripts *pre* and *post* denote the values that the quantities take before and after the inlet section. Notice $P_{0,pre}$ depends on the specific operating conditions, while $P_{0,post}$ is function of the inlet density and axial velocity through eq. (3.7b).

Inlet polytropic conditions

The isoentropic inlet condition for a centered seal is obtained from (3.6c) by considering a frictionless ($\tau = 0$), adiabatic ($Q_s = 0$) transformation between the stagnation condition and the inlet section. The power law obtained is:

$$T^\alpha / P = T_0^\alpha / P_0 \tag{3.9}$$

By substituting (3.5) into (3.9), the isoentropic condition becomes:

$$P^{\alpha-1}\left[\frac{V}{Q} - \frac{1-\lambda}{\rho_l}\right]^\alpha = (\lambda R_g T_0)^\alpha / P_0 \tag{3.10}$$

The isoentropic condition however is not exactly verified at the seal inlet being the local wall friction higher that the asymptotic value reached as the flow develops.

Taking into account the local loss of the total pressure observed at the seal inlet, the polytropic boundary condition is defined as follows:

$$P^{\alpha-1}\left[\frac{V}{Q} - \frac{1-\lambda}{\rho_l}\right]^\alpha = (\lambda R_g T_{0,post})^\alpha / P_{0,post}. \tag{3.11}$$

$P_{0,post}$ and $T_{0,post}$ are evaluated by taking into account the local pressure loss and the energy conservation equation.

$$P_{0,post} = P_{0,in} - \zeta_i \frac{\rho V_{in}^2}{2} \tag{3.12a}$$

$$C_p T_{0,post} + \frac{1-\lambda}{\rho_l} P_{0,post} = C_p T_{0,in} + \frac{1-\lambda}{\rho_l} P_{0,in} \tag{3.12b}$$

The value of $T_{0,post}$ resulting from the above equations is

$$T_{0,post} = T_{0,pre} + \frac{1-\lambda}{2 C_p \rho_l} \zeta_i \rho V^2 \tag{3.13}$$

Inlet pre-swirl

A perfect axial flow at the seal inlet requires $U_{y=0} = 0$; in practice, in annular seals, this is never verified unless swirl brakes are integrated in the inlet reservoir. Consequently, an inlet preswirl condition needs to be considered to have a non zero inlet circumferential velocity $U_0 = U_{pre}$. Being $U_\infty = \Omega R/2$, U_{pre} usually spans in the range $0.2 < U_{pre}/U_\infty < 0.5$ (see Zhang et al. [64]).

Outlet condition

To obtain the outlet boundary condition equation, some insight on the global behavior of the compressible annular seal is needed.

The first consideration is about the variation of the Mach number along the meridian coordinate. A homogeneous multiphase flow can be seen as a generalized subsonic *Fanno Flow* (see Chapter 2). As a result, the lowest exit stagnation pressure is obtained at the sonic condition $Ma = 1$.

The outlet sonic condition can be quickly derived by simply putting the determinant of the matrix system equal to zero. The system in eqs.(3.6) can be written in the following equivalent matrix form

$$A(\overline{v}) \cdot \overline{v} = F(\overline{v}) \tag{3.14}$$

where

$$\overline{v} = \begin{bmatrix} U \\ V \\ P \end{bmatrix} \tag{3.15a}$$

$$A = \begin{bmatrix} Q & 0 & 0 \\ 0 & Q & 1 \\ 0 & \alpha P & (\alpha-1)[V - Q(1-\lambda)/\rho_l] \end{bmatrix} \tag{3.15b}$$

$$F = \frac{1}{H} \begin{bmatrix} \tau_c \\ \tau_m \\ \Omega R \tau_{xz}|^H - U\tau_c - V\tau_m \end{bmatrix} \tag{3.15c}$$

The above non linear ODEs have a solution only if $det(A) \neq 0$. For the particular case of a subsonic *Fanno flow* (which is the case of every compressible flow in an annular pressure seal) it must be $det(A) < 0$.

The sonic speed relation is:

$$\frac{1}{V^2_{sonic}} = \frac{\alpha}{\alpha - 1}\frac{\Psi}{P}\left[\rho_l(1-\Psi) + \rho_g \Psi\right] \tag{3.16}$$

The expression reported in (3.16) is the same as in Minnaert [56] replacing $\alpha/(\alpha-1) = k$, where k is the polytropic exponent of the gas transformation $\rho_g^k/p = const$ during the sonic wave propagation.

After some algebraic manipulations the following equation is obtained

$$V_{exit} - \left(Q \frac{1-\lambda}{\rho_l} + Ma^2 \frac{P_{exit}}{Q} \frac{C_p}{C_p - \lambda R_g} \right) = 0 \tag{3.17}$$

In the equation above, the theoretical Mach number is $Ma_{exit} = 1$; however, in numerical calculations this condition cannot be enforced because this would reproduce infinite spatial gradients of V and P approaching the exit (the axial gradient of U is always discrete, being the first row of matrix A linearly independent of the other two). Hence, in the next calculations, we assume $Ma_{exit} = 0.99$. This boundary condition must be applied at every first run of the zeroth order calculation. If the outlet sonic total pressure (*i.e.* the total pressure corresponding to $Ma_{exit} = 1$) is higher than the outlet stagnation pressure $P_{0,exit}$, the solution found by enforcing $Ma_{exit} = 1$ is the solution sought. Otherwise, the boundary condition changes into the classical subsonic outlet boundary condition:

$$C_p T \left[1 - \left(\frac{P_{0,out}}{P} \right)^{\frac{1}{\alpha}} \right] + \frac{V_{exit}^2}{2} + \frac{1-\lambda}{\rho_l} (P - P_{0,out}) = 0 \tag{3.18}$$

What said so far can be summarized as follows

$$\begin{aligned}
&if \quad P_{0,sonic} - 0.5\zeta_o \rho_{sonic} V_{sonic}^2 = P_{0,out} > P_{0,exit} \\
&BC: \quad Ma_{exit} = 1 \\
&else \\
&BC: \quad C_p T \left[1 - \left(\frac{P_{0,out}}{P} \right)^{\frac{1}{\alpha}} \right] + \frac{V_{exit}^2}{2} + \frac{1-\lambda}{\rho_l} (P - P_{0,out}) = 0 \\
&\qquad P_{0,out} - \zeta_o 0.5 \rho_{sonic} V_{sonic}^2 = P_{0,exit}
\end{aligned} \tag{3.19}$$

In the logical path above, the local pressure loss is taken into account as usual through the outlet loss coefficient ζ_o. The sonic outlet total pressure $P_{0,sonic}$ is evaluated by solving the following non linear algebraic equation once the sonic solution is obtained:

$$C_p T_{sonic} \left[1 - \left(\frac{P_{0,sonic}}{P_{sonic}} \right)^{\frac{1}{\alpha}} \right] + \frac{V_{sonic}^2}{2} + \frac{1-\lambda}{\rho_l} (P_{sonic} - P_{0,sonic}) = 0 \tag{3.20}$$

3.5 Leakage predictions vs. experiments

Here the comparison between the experimental data and the leakage predictions is reported when the homogeneous two-phase model is adopted. Geometric data and fluid properties of the experimental tests are: $R = 44.5mm$, $H = 0.18mm$, $\rho_l = 900kg/m^3$, $\mu_l = 3.64 \cdot 10^{-3} Pl$, $R_g = 287J/kg/K$, $\mu_g = 1.82 \cdot 10^{-5} Pl$, $T_{0,inlet} = 295K$. The "mainly oil" cases present $P_{0,outlet} = 6.2bar$, while in the "mainly air" cases is $P_{0,inlet} = 62.1bar$.

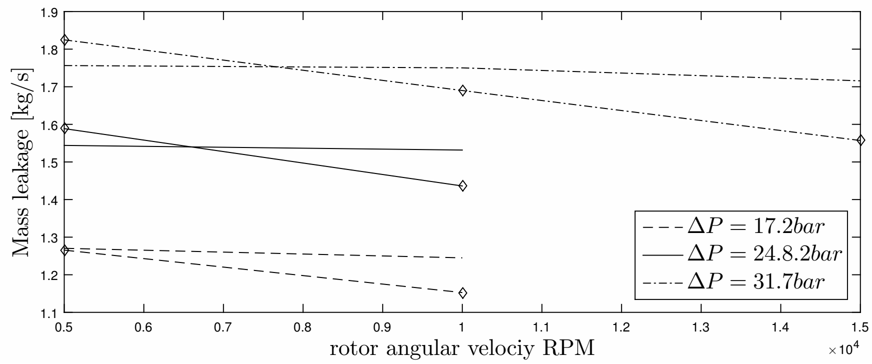

(a) GVF_{inlet}=3%.

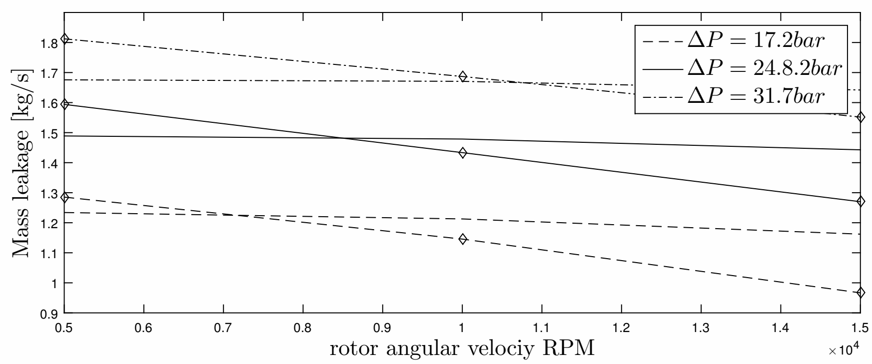

(b) GVF_{inlet}=6%.

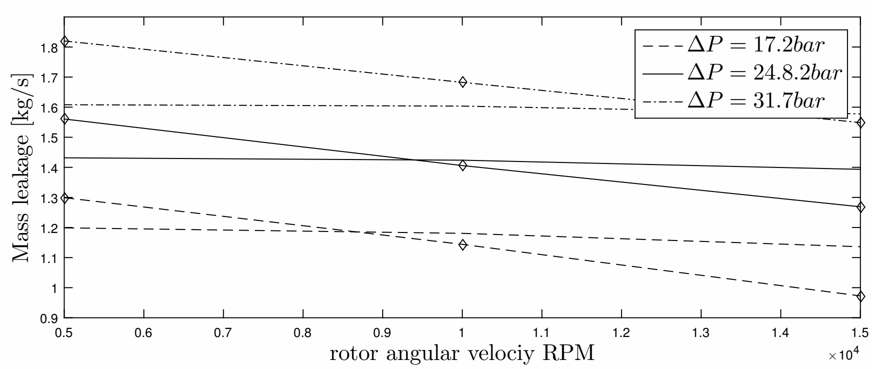

(c) GVF_{inlet}=8.9%

Figure 3.1: Leakage comparison between experimental data and homogeneous bulk model predictions. $L/R = 0.58$, $\diamond$ experimental results.

In figures 3.1,3.2 the leakage comparison for the short seal case is reported. As observed in the case of a single-phase incompressible seal, the bulk model underestimates the effects of the rotor angular speed on the leakage reduction. While the measured leakage decrease with Ω, the model predictions remain almost unchanged. Same results are obtained in the long seal case.

Figures 3.3-3.4 report the same kind of comparison in case of high GVFs. The predicted mass leakage is almost invariant under a change of the rotor speed, same behaviour show the experimental measurements. In fact, at high GVFs, the axial Reynolds number is far greater than the circumferential one and the wall friction factor is only slightly modified by a change in the rotor angular speed.

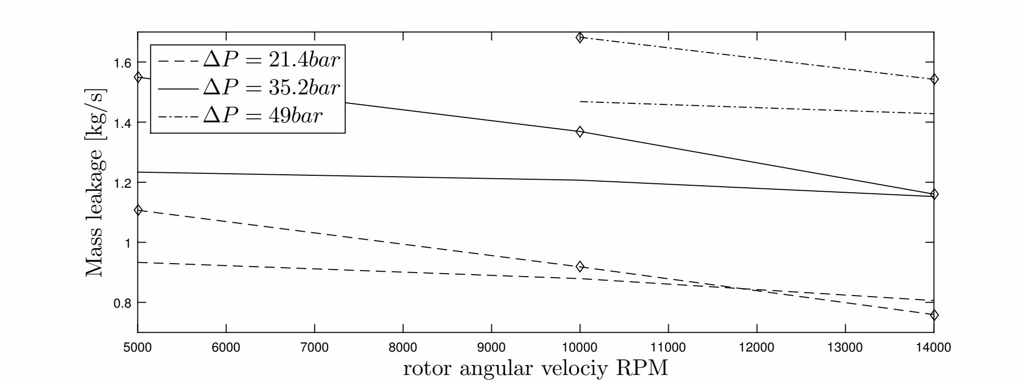

(a) GVF_{inlet}=4.2%.

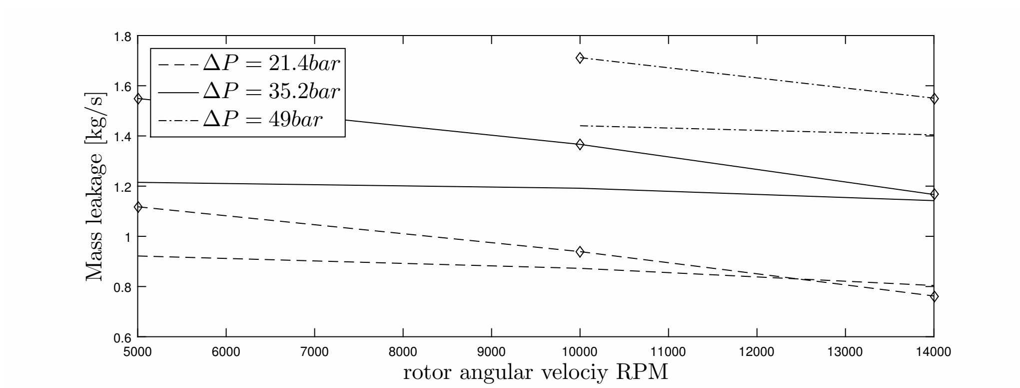

(b) GVF_{inlet}=6.2%.

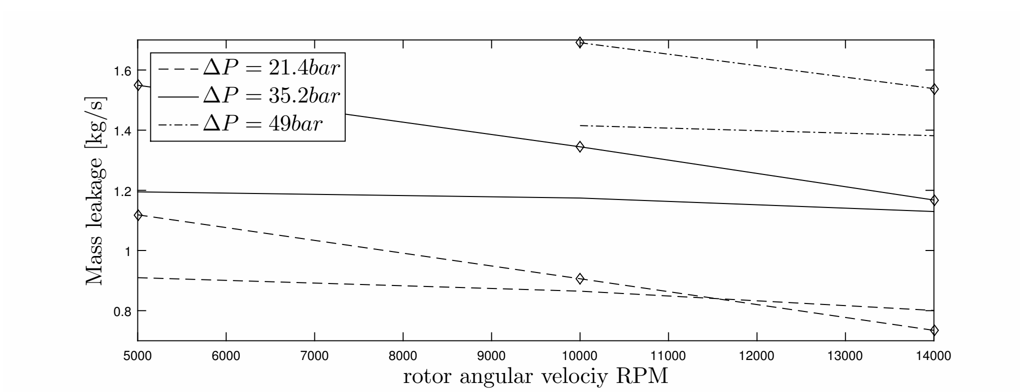

(c) GVF_{inlet}=8.2%

Figure 3.2: Leakage comparison between experimental data and homogeneous bulk model predictions. $L/R = 1.5$, $\diamond$ experimental results.

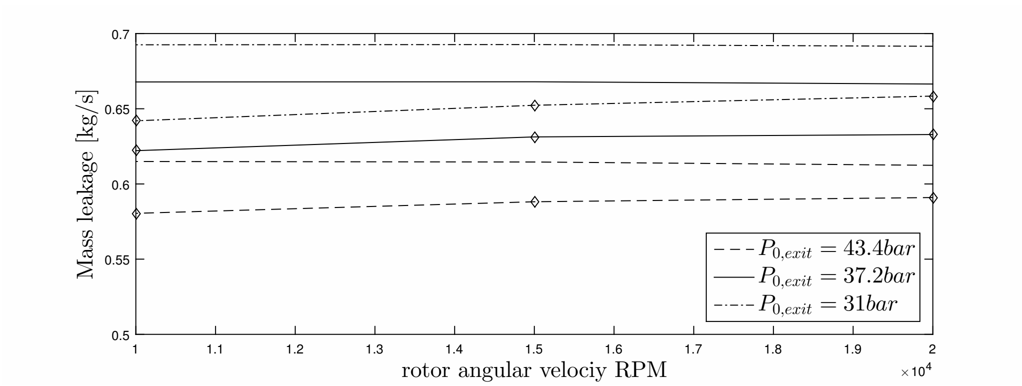

(a) GVF_{inlet}=92.1%.

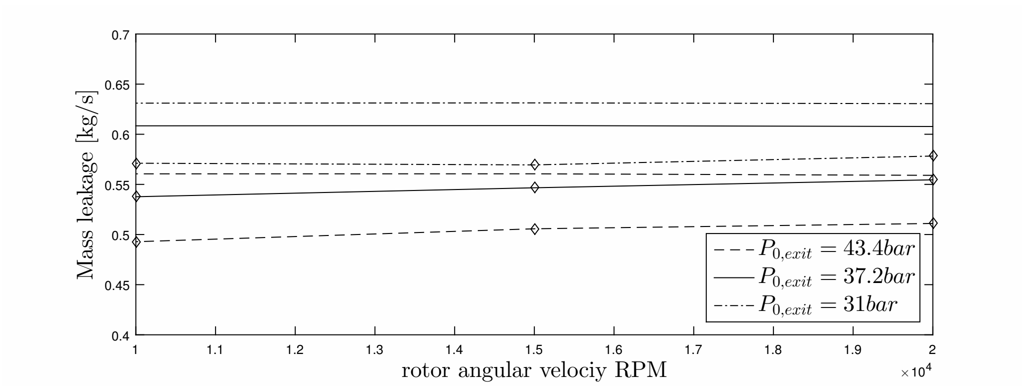

(b) GVF_{inlet}=95.1%.

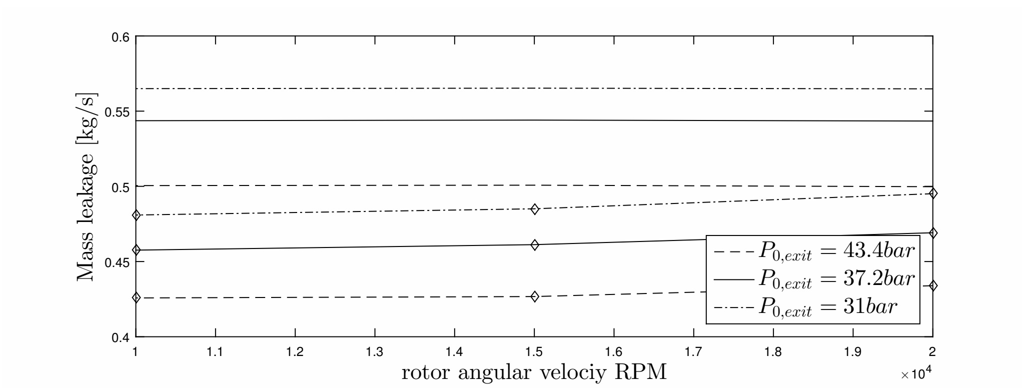

(c) GVF_{inlet}=98.1%

Figure 3.3: Leakage comparison between experimental data and homogeneous bulk model predictions. $L/R = 0.58$, $\diamond$ experimental results.

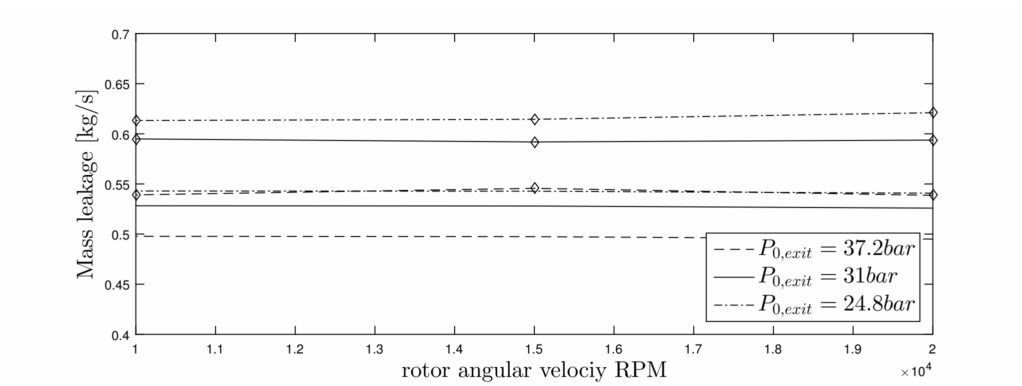

(a) GVF_{inlet}=92.6%.

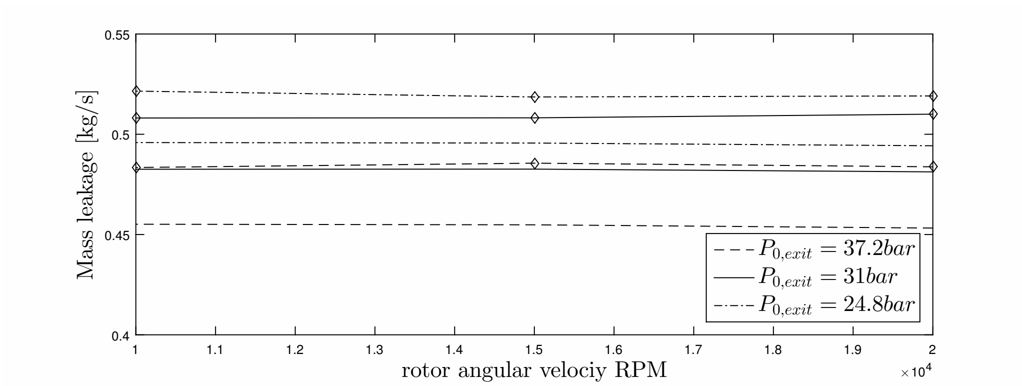

(b) GVF_{inlet}=95.5%.

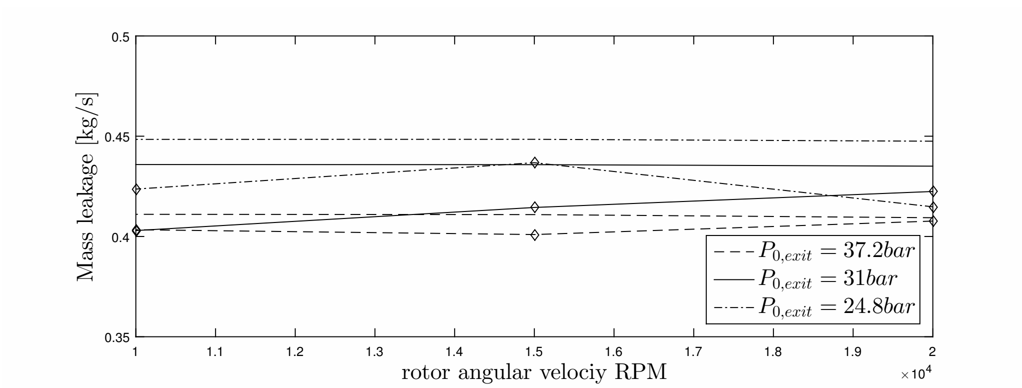

(c) GVF_{inlet}=98.2%

Figure 3.4: Leakage comparison between experimental data and homogeneous bulk model predictions. $L/R = 1.5$, $\diamond$ experimental results.

The figures that follow, report the solution in case of sonic condition at the seal exit. The circumferential velocity asymptotically goes to $\Omega R/2$ approaching the seal exit. As stated before, the pressure and axial velocity gradients grows unlimited approaching the seal exit while the circumferential gradient doesn't.

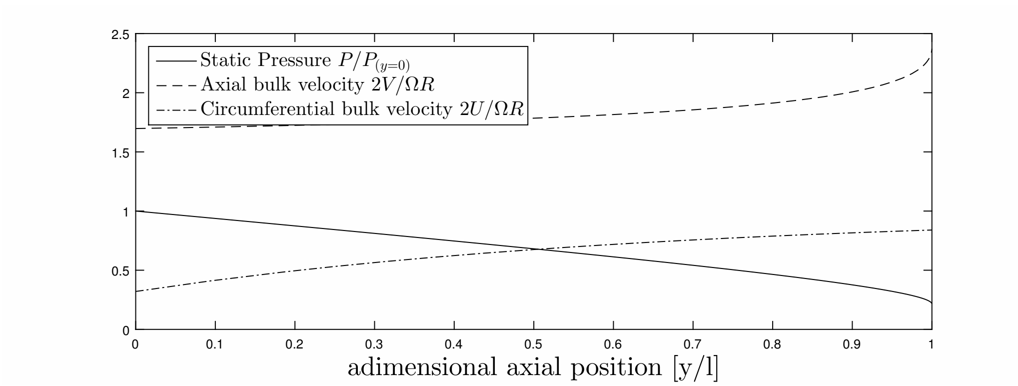

(a) Variation along the seal of the bulk velocities and pressure.

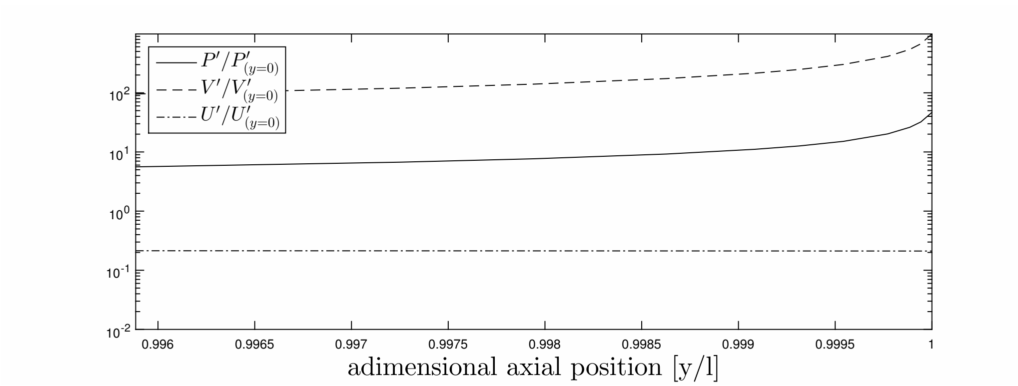

(b) Variation along the seal of the gradients.

Figure 3.5: Variation along the seal of the bulk velocities and pressure in the case of sonic flow at the seal exit. $GVF_{inlet} = 8.9\%$, ΔP_0=31.7 bar, $\Omega = 10000RPM$, $L/R = 0.58$

In the figure that follows is shown the mixture temperature variation across the clearance. It is important to observe that even a small amount of liquid phase (inlet$GVF = 95.5\%$) gives to the mixture an almost isothermal behaviour along the whole seal.

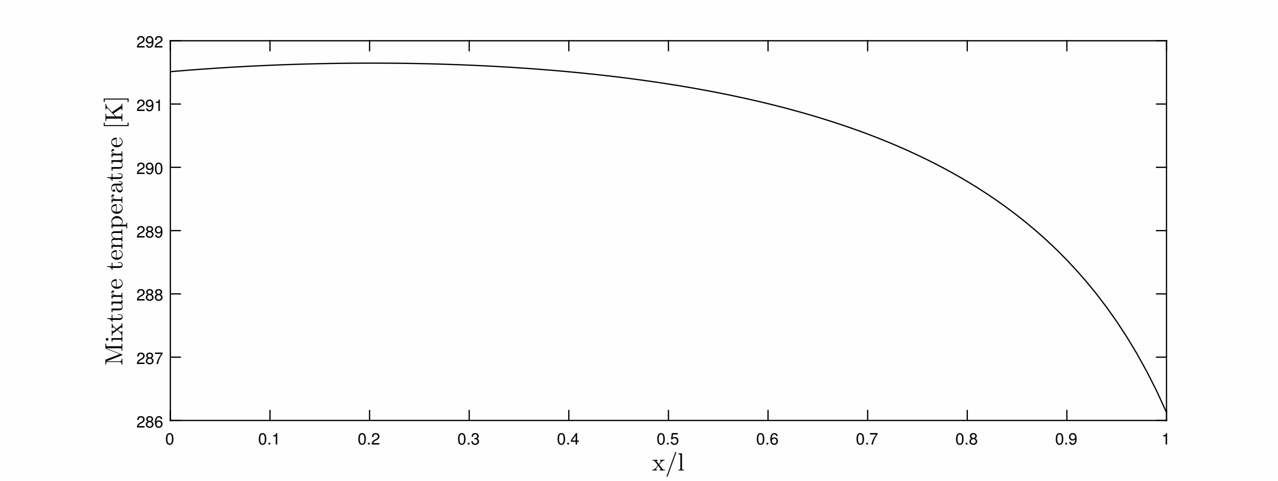

Figure 3.6: Temperature variation along the seal. $GVF_{inlet} = 95.5\%$, P_r=0.5 bar, $\Omega = 15000RPM$, $L/R = 1.5$

3.6 First-order solution

As explained in Chapter 2, the most important application of the bulk flow models in the cases of journal bearings or annular pressure seals is the rapid evaluation of the structural response of the element to the rotor vibrations. Bulk flow models are preferred with respect to the CFD solution for their fastness and ease of use. For small rotor eccentricity ($\varepsilon = \delta/H << 1$), the "eccentric rotor" solution can be evaluated through a "small perturbation approach" that linearizes the bulk Navier-Stokes equations, leading to a further gain in terms of fastness.

Under the above assumption and according to same procedure introduced in Chapter 2, a solution to the problem given by the system of equations (2.9),(2.7a),(3.1) is obtained by superposing to the zeroth-order field, the perturbation related to the orbital motion of the rotor (whirl) of infinitesimal amplitude εH. To this end, the following perturbations in the pressure, velocity and density fields need to be considered

$$P(x, y, t) = P + p_d(y)\cos(x/R - \omega t) + p_q(y)\sin(x/R - \omega t) \tag{3.21a}$$

$$U(x, y, t) = U + u_d(y)\cos(x/R - \omega t) + u_q(y)\sin(x/R - \omega t) \tag{3.21b}$$

$$V(x, y, t) = V + v_d(y)\cos(x/R - \omega t) + v_q(y)\sin(x/R - \omega t) \tag{3.21c}$$

$$\rho(x, y, t) = \rho + \rho_d(y)\cos(x/R - \omega t) + \rho_q(y)\sin(x/R - \omega t) \tag{3.21d}$$

where P, U, V, ρ are the zero-order solutions. The perturbed temperature that must be introduced in the energy equation is instead directly obtained through the equation of state in the following form

$$T(x, y, t) = T + \Delta P\frac{T}{P} - \Delta\rho\frac{P}{\lambda R_g \rho^2} \tag{3.22}$$

where

$$\Delta P(x,y,t) = P_d(y)\cos(x/R-\omega t) + P_q(y)\sin(x/R-\omega t) \tag{3.23a}$$
$$\Delta \rho(x,y,t) = \rho_d(y)\cos(x/R-\omega t) + \rho_q(y)\sin(x/R-\omega t) \tag{3.23b}$$

As previously made in the chapter 2, the perturbations are expressed in complex notation.

The complex variables vector is:

$$\overline{\chi}_{comp} = \begin{bmatrix} u^* \\ v^* \\ p^* \\ \rho^* \end{bmatrix} \tag{3.24}$$

And the perturbed linear ODEs is:

$$\overline{\overline{A}}_h \cdot \overline{\chi}'(y) + \overline{\overline{B}}_h \cdot \overline{\chi}(y) + \varepsilon \overline{C}_h = 0 \tag{3.25}$$

The subscript h indicates homogeneous two-phase flow.

By perturbing eqs. (2.10a)-(2.10b) and (3.6c), the first-order equation system is obtained

The perturbation of the continuity equation (2.9a), the system (2.10) and the energy equation 2.7a, gives to $\overline{\overline{A}}_h$ the following form:

$$\overline{\overline{A}}_h = \begin{bmatrix} 0 & \rho & 0 & V \\ V & 0 & 0 & 0 \\ 0 & V & 1/\rho & 0 \\ 0 & \alpha P_c & (\alpha-1)VP_c/P & -\alpha\frac{(1-\lambda)}{\rho_l}PV \end{bmatrix} \tag{3.26}$$

Where $P_c = \lambda \rho R_g T$, here called "correct pressure", is an equivalent pressure of a perfect gas of density ρ and specific gas constant λR_g.

Matrix $\overline{\overline{B}}_h$ will be:

$$\begin{bmatrix} \overline{\overline{B}}_{pg}(1,1) & \overline{\overline{B}}_{pg}(1,2) & \overline{\overline{B}}_{pg}(1,3) & \overline{\overline{B}}_{pg}(1,4) \\ \overline{\overline{B}}_{pg}(2,1) & \overline{\overline{B}}_{pg}(2,2) & \overline{\overline{B}}_{pg}(2,3) & \overline{\overline{B}}_{pg}(2,4) \\ \overline{\overline{B}}_{pg}(3,1) & \overline{\overline{B}}_{pg}(3,2) & \overline{\overline{B}}_{pg}(3,3) & \overline{\overline{B}}_{pg}(3,4) \\ \overline{\overline{B}}_{h}(4,1) & \overline{\overline{B}}_{h}(4,2) & \overline{\overline{B}}_{h}(4,3) & \overline{\overline{B}}_{h}(4,4) \end{bmatrix} \tag{3.27}$$

where is:

$$\overline{\overline{B}}_h(4,1) = j\alpha\frac{P_c}{R} - \frac{L_{w,U}}{H} \tag{3.28a}$$
$$\overline{\overline{B}}_h(4,2) = \alpha\left(P_c' - P_c\frac{P'}{P}\right) - \frac{L_{w,V}}{H} \tag{3.28b}$$
$$\overline{\overline{B}}_h(4,3) = \frac{P_c}{P}\left[\alpha V' + j(\alpha-1)(U/R-\omega)\right] - \alpha V\frac{1-\lambda}{\rho_l}\rho' \tag{3.28c}$$
$$\overline{\overline{B}}_h(4,4) = \frac{1-\lambda}{\rho_l}P\left[V\frac{P'}{P} - \alpha V' - j\alpha(U/R-\omega)\right] - \alpha V\frac{1-\lambda}{\rho_l}P' - \frac{L_{w,\rho}}{H} \tag{3.28d}$$

The $\overline{C}_h$ vector is

$$\begin{bmatrix} \overline{C}_{pg}(1) \\ \overline{C}_{pg}(2) \\ \overline{C}_{pg}(3) \\ \overline{C}_h(4) \end{bmatrix} \tag{3.29}$$

$$\overline{C}_h(4) = P_c \left[\frac{VP'}{P} - \alpha j(U/R - \omega) \right] - \alpha(P_c V)' + L_{w,H} \tag{3.30}$$

In the equations above $\overline{\overline{B}}_{pg}(i,j)$ and $\overline{\overline{C}}_{pg}(i,j)$, have been used when the terms in the homogeneous two-phase model were formally identical to the perfect gas model.

3.6.1 First-order boundary conditions

The first-order boundary conditions are obtained by perturbing the zeroth-order boundary conditions with the only caution of taking into account the perturbation of Q as $\Delta Q = \Delta\rho V + \Delta V \rho$.

The perturbed boundary conditions becomes:

Perturbed inlet energy conservation equation

$$v^*_{in} V + C_p t^*_{in} + \frac{1-\lambda}{\rho_l} p^*_{in} = 0 \tag{3.31}$$

where t^*_{in} is the temperature perturbation at the seal inlet.

Perturbed polytropic inlet equation

$$\alpha \left(\frac{t^*_{in}}{T_{in}} - \frac{\Delta T_{0,post}}{T_{0,post}} \right) = \frac{p^*_{in}}{P_{in}} - \frac{\Delta P_{0,post}}{P_{0,post}} \tag{3.32}$$

where is

$$\Delta P_{0,post} = -\frac{\zeta_i}{2} \left(\rho^*_{in} V^2_{in} + 2Qv{*}_{in} \right) \tag{3.33a}$$

$$C_p \Delta T_{0,post} + \frac{1-\lambda}{\rho_l} \Delta P_{0,post} = 0 \tag{3.33b}$$

Perturbed inlet pre-swirl

$$u^*_{in} = 0 \tag{3.34}$$

Perturbed outlet equation

If the zeroth-order solution achieves the sonic condition at the outlet section, the perturbed outlet boundary condition derives from the perturbation of equation (3.17). After some manipulations the equation takes the form:

$$v_{in}^*/V_{in} + 0.5t_{in}^*/T_{in} + \rho_{in}^*/\rho_{in} - p_{in}^*/P_{in} = 0 \tag{3.35}$$

In case of subsonic outlet flow, the perturbed subsonic outlet condition is

$$v_{out}^* V + C_p t_{out}^* + \frac{1-\lambda}{\rho_l} p_{out}^* = C_p \Delta T_{0,pre} + \frac{1-\lambda}{\rho_l} \Delta P_{0,pre} \tag{3.36}$$

where is

$$\alpha \left(\frac{t_{out}^*}{T_{out}} - \frac{\Delta T_{0,pre}}{T_{0,pre}} \right) = \frac{p_{out}^*}{P_{out}} - \frac{\Delta P_{0,pre}}{P_{0,pre}} \tag{3.37a}$$

$$\Delta P_{0,pre} = \frac{\zeta_o}{2} \left(\rho_{out}^* V_{out}^2 + 2Q v_{out}^* \right) \tag{3.37b}$$

3.7 Results and comparisons

3.7.1 First-order solution

With reference to figure 2.1, results are presented for the following values of the geometric parameters and operating conditions:

Geometry:
$R = 44\ mm$, $L = 66.7\ mm$ (long seal)-25.8 mm (short seal), $H = 0.18\ mm$.

Fluid properties:
$\rho_l = 900\ kg/s$, $\mu_l = 3.64 \times 10^{-3}\ Pa \cdot s$, $\mu_g = 1.82 \times 10^{-5}\ Pa \cdot s$, and $R = 287\ J/kg/K$.

Operating conditions:

Mainly oil mixtures long seal:

$GVF_{inlet} = 4.2\%, 6.2\%, 8.2\%$,
$P_{0,exit} = 6.2 bar$,
$T_{0,inlet} = 295\ K$,
$\Delta P_0 =$ 21.4-35.2-49 bar.

Mainly oil mixtures short seal:

$GVF_{inlet} = 3\%,\ 6\%,\ 8.9\%,$
$P_{0,exit} = 6.2 bar,$
$T_{0,inlet} = 295\ K,$
$\Delta P_0 =$ 17.2-24.8-31.7 bar.

Mainly air mixtures long seal:

$GVF_{inlet} = 92.6\%,\ 95.5\%,\ 98.2\%,$
$P_{0,in} = 62.1\ bar,$
$T_{0,inlet} = 295\ K,$
$Pr = P_{0,out}/P_{0,in} =$ 0.4-0.5-0.6.

Mainly air mixtures short seal:

$GVF_{inlet} = 92.1\%,\ 95.1\%,\ 98.1\%,$
$P_{0,in} = 62.1\ bar,$
$T_{0,inlet} = 295\ K,$
$Pr = P_{0,out}/P_{0,in} =$ 0.5-0.6-0.7.

The figures related to the comparisons between experimental and predicted seal coefficients are presented in Appendix B.

Here a global assessment of the accuracy of the homogeneous bulk model predictions for every impedance coefficient is presented.

Static Direct Stiffness K

The following analysis refers to the figures B.1-B.36. Homogeneous bulk model predictions of K for the "long seal mainly oil" cases show good agreement in low pressure gap case. Under these operating conditions, both experimental values and predictions show a decreasing trend with Ω. Negligible effects has GVF. In case of moderate pressure gap, experimental results show a minimum at $\Omega = 10000 RPM$ while predictions, with the only exception of $GVF =$ 8.2%, show higher values. In the case characterized by high pressure gradient, predictions underestimate measurements. The rotor angular speed has little effects on K.

Constant behaviour with the rotor speed is observed in the predictions of the "short seal mainly oil" case, negligible effect has the pressure gap. Experimental results show an increasing trend with Ω at moderate and high pressure gap, GVF has negligible effects. Generally, the agreement between measurements and predictions in not satisfactory.

In the high GVF region, bulk flow model constantly overestimates of a factor $2 \div 4$ the experimental results. In the "long seal" case no particular trends are observed with both the pressure gap and the rotor speed with the only exception of $Pr = 0.4$ where both predictions and measurements show lower values with respect other Pr values. In the "short seal" case, both measured and predicted values slightly increase with the inlet GVF. Both the rotor speed and the pressure gap show no effects on K.

Static Quadrature Stiffness k

The following analysis refers to the figures B.1-B.36. Predictions show almost perfect agreement with the measurement in the cases "long seal mainly oil". Little overestimation of the measured values is observed in the high pressure gap case. Quadrature static stiffness (both predicted and measured) linearly grows with the rotor speed. Reasonable agreement is observed in the "short seal mainly oil" cases. Predictions follow the measurement trends with both the rotor speed and the pressure gap but there are higher margins between them.

In the "long seal mainly gas" case both experimental results and bulk model predictions linearly grow with the rotor speed while the pressure gap is almost irrelevant in the range analyzed. The predicted values however underestimate the measured ones of a factor $2 \div 3$. Better agreement is observed in the "short seal mainly air" case. Here, the predicted values of k fall in the dispersion range of the measured experimental data (95% of confidence). Experimental results are weakly influenced by both the rotor speed and the pressure gap.

Direct Damping D

The following analysis refers to the figures B.1-B.36. Very good agreement is observed in the "long seal mainly oil" case for $\Delta P_0 = 49bar$. In the other cases, predictions underestimate the measured values of about $1.5 \div 2$ times. These discrepancies are exalted by the opposite trend with the rotor speed observed in the predictions and measurements: while the first decrease, the seconds increase. Both measured and predicted values grow with the pressure gap. Good agreement is also observed in the "short seal mainly oil" case where both measurements and predictions grow with the pressure gap. Predictions underestimate measurements of about $15 \div 20\%$

In the "long seal mainly gas" case, bulk model predictions are in good agreement with the experimental data. No dependence on Ω is observed. The bulk model error is under the 30%. Good agreement is also observed in the "short seal mainly gas" case. Both experimental results and bulk model predictions decrease with the inlet GVF and grow with ΔP_0. The greatest error is observed in the case characterized by $Pr = 0.7$ where the predictions are about 30% smaller than the measured one.

Quadrature Damping d

The following analysis refers to the figures B.1-B.36. The cases "long seal mainly oil" show good agreement between the predictions and experimental values. The greatest discrepancies are observed when the rotor speed reaches its maximum value of $14000RPM$. In the "short seal mainly oil" case the measured values show a linear increase with the rotor speed in the case of low and moderate pressure gap. In the case of high pressure gap, the values become almost constant in the range $\Omega = 10000 \div 15000RPM$. Measured values show a decrease with the inlet GVF. Predictions underestimate the increase with the rotor speed, leading to an error of about 100% when $\Omega = 15000RPM$. When the homogeneous bulk model predicts a sonic velocity at the seal exit ($GVF = 6.2 - 8.9\%$ and $\Delta P = 24.8 - 31.7bar$), higher errors are observed.

Experimental values show a decrease in the case "long seal mainly air" with both the inlet GVF and the pressure gap. The behaviour with Ω varies depending on the pressure gap and GVF, increasing for lower pressure gap and inlet GVF while decreasing for high inlet GVF (98.2%) and pressure gap. Predicted values generally follow the measured ones showing an overestimation usually smaller than 50%. Higher discrepancies are observed when $GVF = 98.2\%$. The case "short seal mainly air" is characterized by an increasing trend of the measured values with the rotor speed while opposite behaviour is observed with the pressure gap. Inlet GVF has only weak effects on the measured values. Predicted values are $3-4$ times lower than the measured ones.

Direct Mass M

The following analysis refers to the figures B.1-B.36. In the case "long seal mainly oil", both measured and predicted values are weakly affected by the rotor speed, while they show a little decrease with both the GVF and the pressure gap. In case of low pressure gap, the predictions are about an half of the measured values. This error disappears when the pressure gap increases.

The case "short seal mainly oil" shows almost constant values at low GVF (3%) with the rotor speed; at higher $GVFs$ a decreasing trend with the rotor speed is observed. No particular trends are observed with the variation of the pressure gap. Measured values are usually in the range $7-3kg$. Model predicts in most cases a negligible direct mass.

In the "long seal mainly air" case, the bulk model predicts an added direct mass of about $0 \div 1Kg$ while measurements are in the range $-1 \div 0$. Though the comparison is not satisfactory, both measured and predicted values are negligible with respect to the direct static stiffness K in the rotordynamic seal characterization. The cases characterized by $Pr = 0.6$ show a predicted value of about $-1kg$ while the measured ones span in the range $-0.5 \div 0.5$. Even better agreement is observed in the case of $Pr = 0.4, 0.5$ with an added direct mass of about $-0.5 \div -1.5kg$. Same considerations apply in the "short seal mainly air" case.

Quadrature Mass m

The following analysis refers to the figures B.1-B.36. The case "long seal mainly oil", for $\Delta P_0 = 21.4-35.2bar$ is characterized by a decreasing trend with the rotor speed of the measured values. The case with $\Delta P_0 = 49bar$ is characterized by measured values in the range $-5 \div -8kg$. In all cases, predictions show the same trend on the measured values showing however opposite sign. The case "short seal mainly oil" case is characterized by a good agreement between predictions and measurements. Both of them show almost null values in the whole range.

Good agreement is observed in the "long seal mainly gas" case with predicted values only slightly larger than the measured ones (usually they overlap the upper confidence limit). Perfect agreement is observed in the "short seal mainly gas" case with both measured and predicted values almost null.

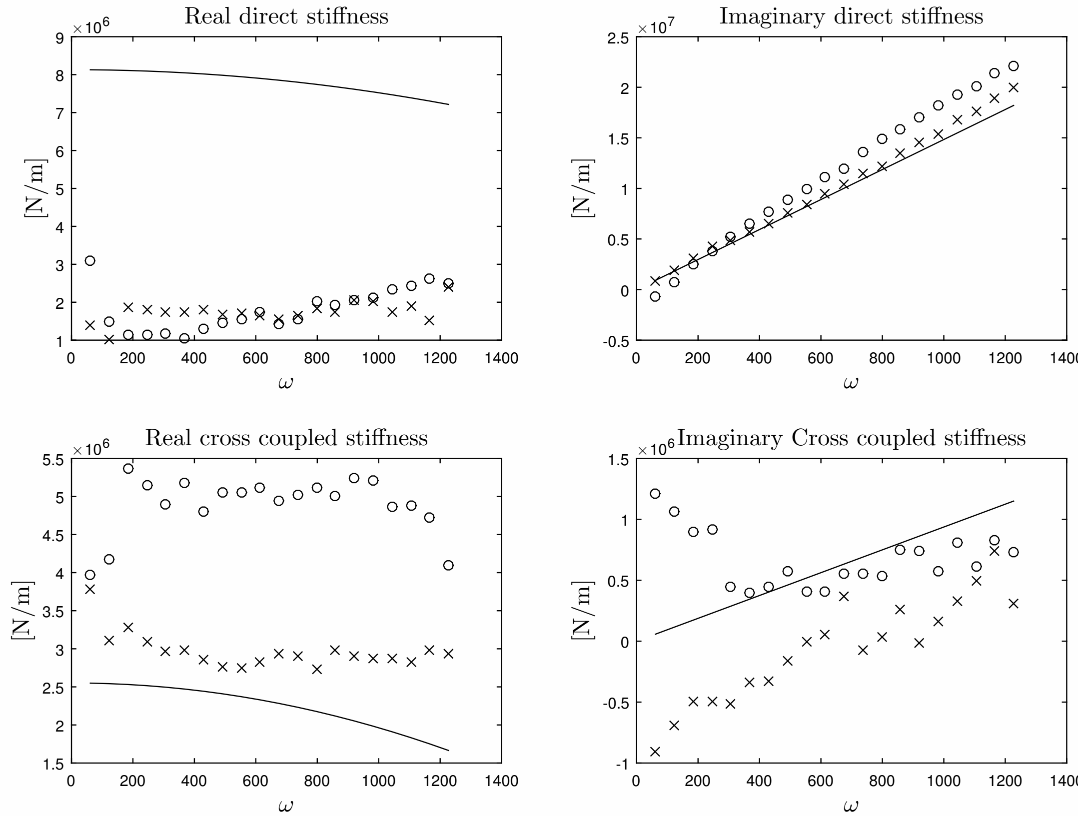

Figure 3.7: Comparison between measured and predicted impedance. $L/R = 1.5$, inlet $GVF = 95.5\%$, $\Omega = 15000RPM$, $P_{0,out} = 31bar$, $\zeta_i = 0.2$, $\zeta_o = 1$.

3.8 Sensitivity analysis

In this section the sensitivity of the bulk model predictions to the model parameters is shortly discussed. The most immediate calibration can be made on the two pressure loss coefficients ζ_i and ζ_o. In figure 3.8 are reported the bulk model results in the same operating conditions of figure 3.7 when a different outlet loss coefficient $\zeta_o = 1.8$ is taken into account.

The deviation between the predicted and measured values of the static direct and quadrature stiffness (the static direct stiffness is the intercept with the vertical axis *i.e.* of the real, direct or quadrature, stiffness curve) is completely recovered while the damping and mass coefficients are almost unchanged. In particular, the correction of the static quadrature stiffness coefficient k makes it possible to accurately predict the whirl frequency instability threshold $\omega_c = k/C$ over which the seal has a stabilizing effect on the rotor dynamics (the seal reacts with a quadrature force F_t opposite to the whirl motion of the rotor). Higher values of the loss coefficient ζ_o and the respective increased pressure loss at the seal outlet could be explained by the presence of a circumferential velocity or the local interaction between the two phases.

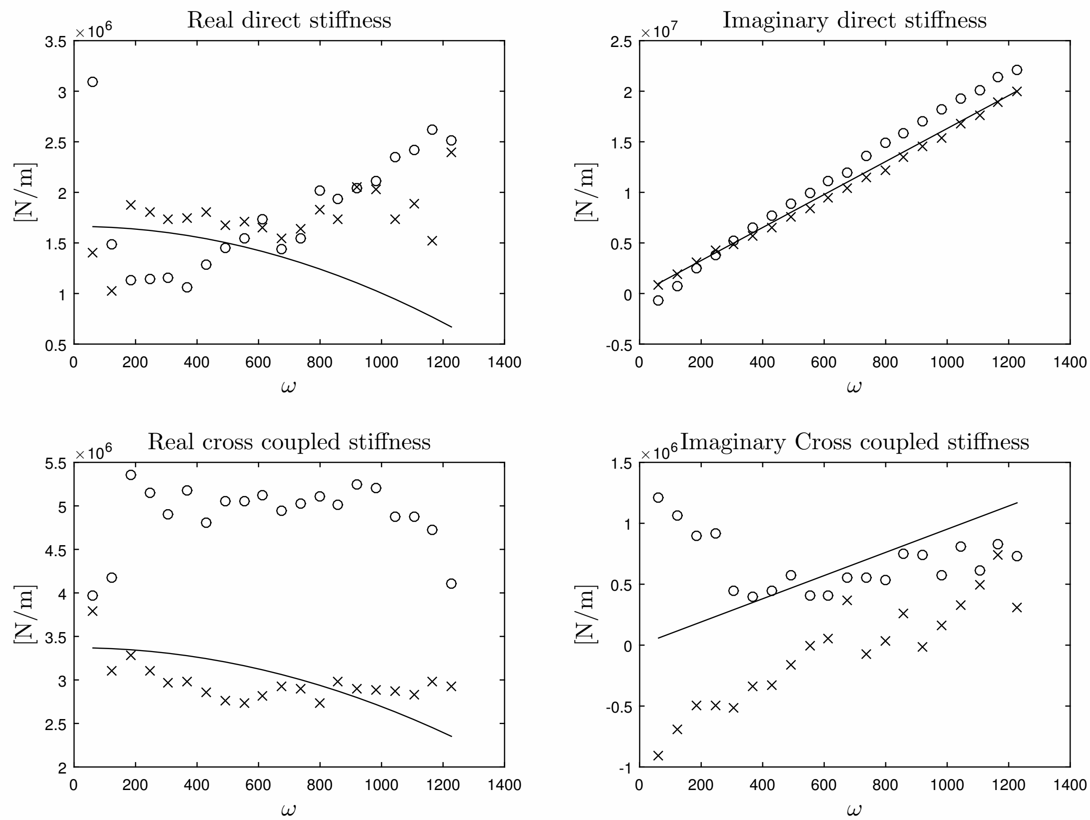

Figure 3.8: Comparison between measured and predicted impedance. $L/R = 1.5$, inlet $GVF =$ 95.5%, $\Omega = 15000RPM$, $P_{0,out} = 31bar$,$\zeta_i = 0.2$, $\zeta_o = 1.8$.

In figure 3.10 are reported the bulk model results in the same operating conditions of figure 3.9 when a different outlet loss coefficient $\zeta_o = 1.5$ is taken into account. As for the previous example, a higher value of ζ_o makes it possible to correct the predicted value of K. How to correct the bulk model to predict correct mass coefficients is still an open question. Predicted mass coefficients take the same sign both in the high and low GVF region while experimental results are characterized by low negative added masses for high $GVFs$ values.

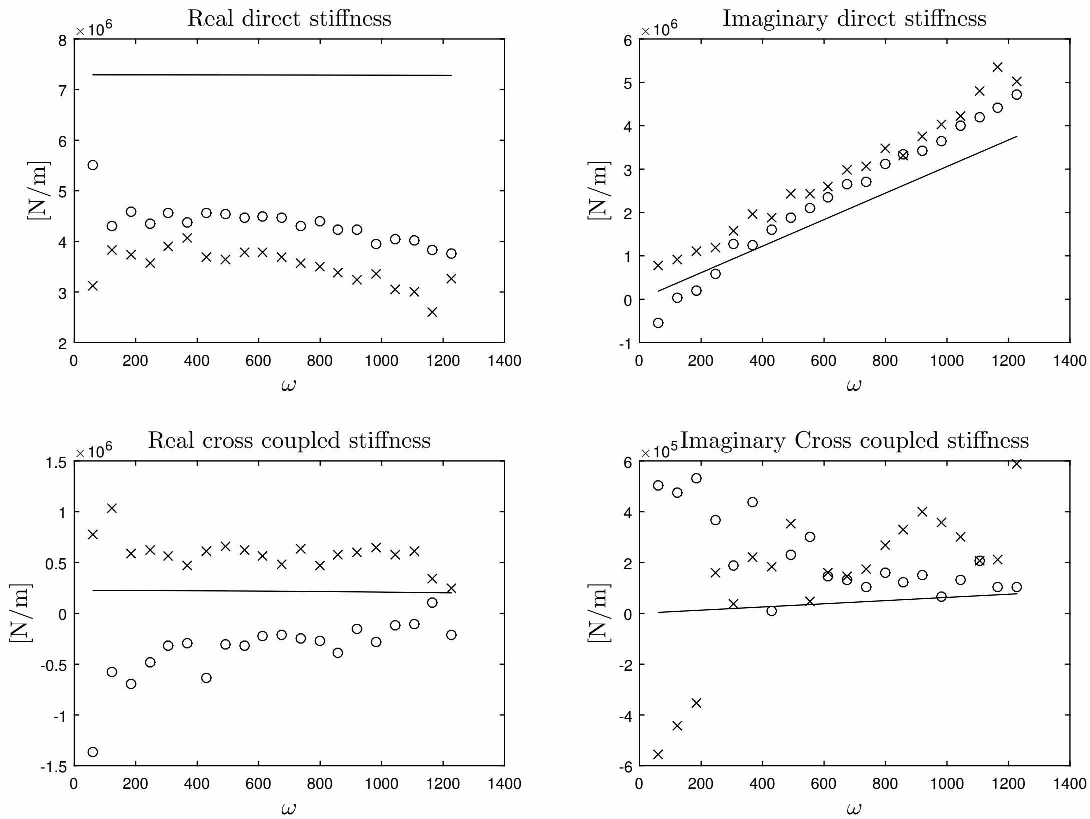

Figure 3.9: Comparison between measured and predicted impedance. $L/R = 0.58$, inlet $GVF = 95.1\%$, $\Omega = 15000RPM$, $P_{0,out} = 37.2bar$, $\zeta_i = 0.2$, $\zeta_o = 1$.

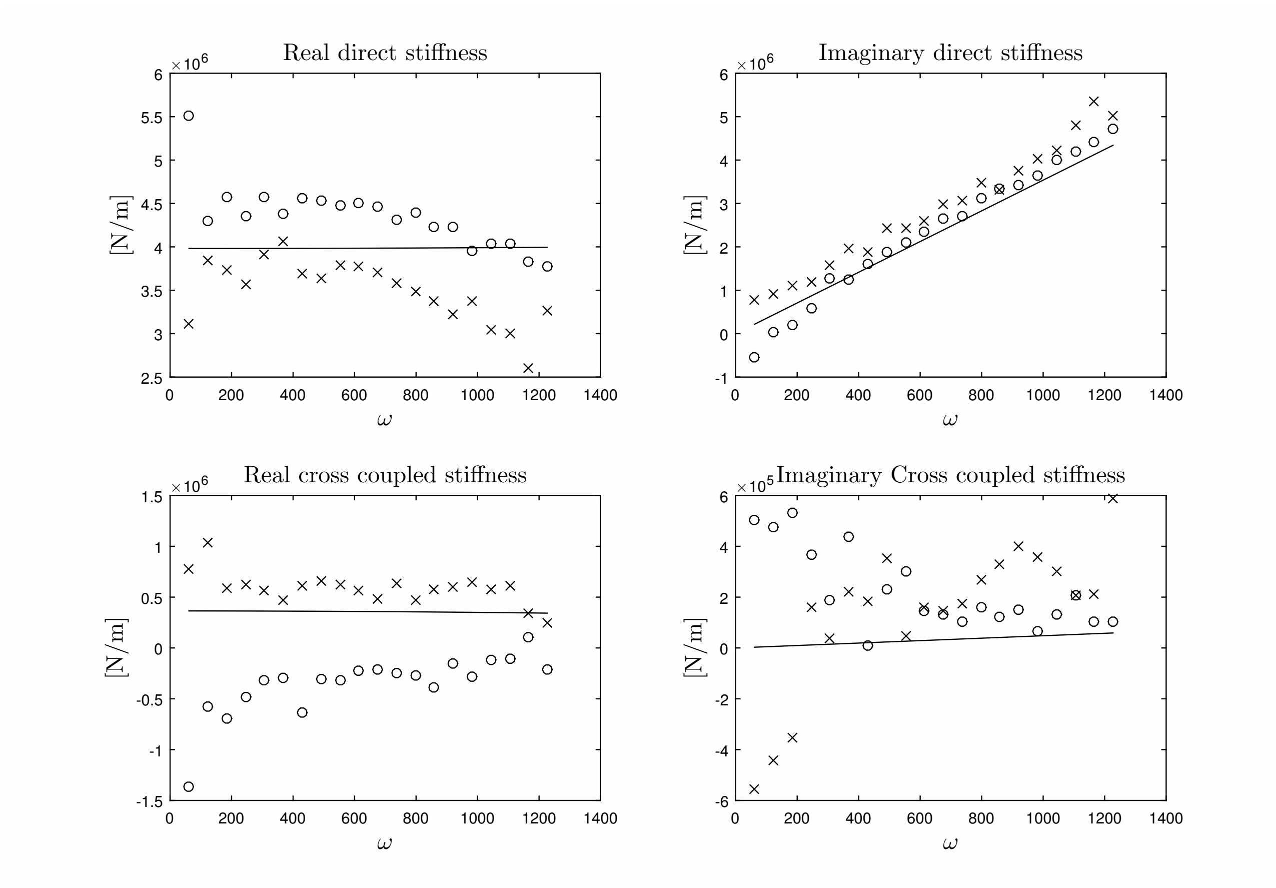

Figure 3.10: Comparison between measured and predicted impedance. $L/R = 0.58$, inlet $GVF = 95.1\%$, $\Omega = 15000RPM$, $P_{0,out} = 37.2bar$, $\zeta_i = 0.2$, $\zeta_o = 1.5$.

3.9 Conclusions

In this chapter the accuracy of the homogeneous two-phase bulk model predictions through experimental results has been introduced and widely evaluated. Differently from [63], with the only exception of the inlet pre-swirl equation, boundary conditions are obtained by analytic integration of (3.6) between the inlet/outlet reservoir and the inlet/outlet seal section. Boundary conditions so formalized, constitute a generalization of the "single phase" (both incompressible and perfect gas) ones. Comparisons between predicted and measured leakages, reported in 3.5, are not completely satisfactory. To the author, this suggests the necessity of a correction of the bulk shear stresses in the way to better estimate the leakage variation with the rotor speed Ω. Reasonable agreement is observed between predicted and measured seal coefficients especially in the evaluation of the damping coefficients. As shown in section 3.8 the predicted values of the two static stiffnesses are sensitive to the pressure loss coefficients and accurate calibration of them is needed for a correct estimation of the seal instability threshold ω_c.

Chapter 4

Stratified two-phase flows in annular pressure seals

4.1 Introduction

In annular smooth pressure seals, when liquid particles come in contact with the rotor surface, experience centrifugal forces that are typically of three (or four) order of magnitude larger than the standard gravity force. Consequently, they are 'centrifuged' toward the stator with the resulting formation of a stratified two phase flow. This specific flow configuration is difficult to investigate experimentally, being the rotor-stator clearance of the order of 100 μm. For this reason, in this chapter a bulk model is proposed to investigate the system behavior when a stratification of the liquid and gas phases occurs. A first attempt in this direction has been done by Beatty and Hughes [8], who modeled both phases as layers in turbulent regime; moreover, they calculated the axial wall shear stresses according to the model proposed in Yamada [62] for the rotor surface, and with the Blasius equation

$$f = \frac{\tau}{\frac{1}{8}\rho u^2} = 0.26 Re^{-0.25} \tag{4.1}$$

Re being the axial Reynolds number, for the stator surface. Interface shear was neglected for the liquid flow and approximated to the axial rotor shear for the gas flow. The circumferential flow was considered homogeneous. The stratified bulk flow model so formulated predicted slightly higher leakage rates than the homogeneous one. The sensitivity of the predicted leakages to the rotor speed was "markedly lower" for the stratified model with respect to the homogeneous model.

In the present analysis, the liquid flow is considered in laminar regime (this assumption is later verified to be consistent being the values assumed by the Reynolds number Re far less than 1000). Laminar correlations (momentum flux integral and interface shear) are obtained by integrating the Navier-Stokes equations over the liquid height. Turbulent flow correlations are modeled as in Hirs [28], by considering the interface as a smooth moving wall. The Hirs wall shear stress model is however slightly modified with the correction introduced in chapter 2. The wall friction factor is computed through a modified Reynolds number that takes into account

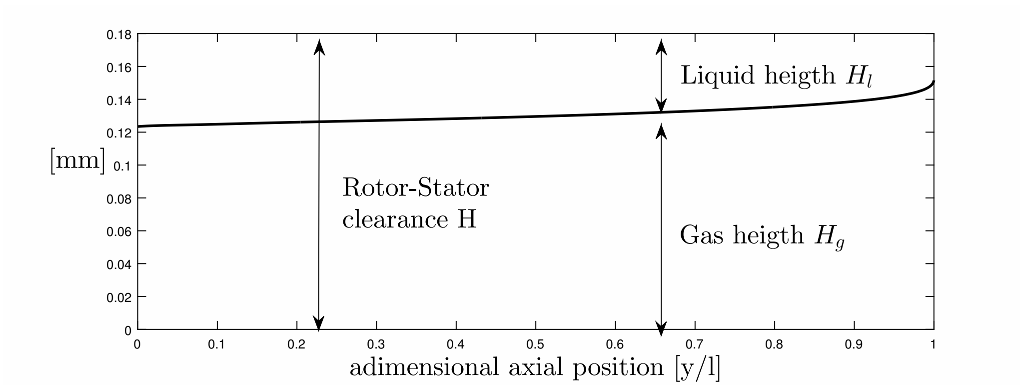

Figure 4.1: Sketch of the stratified bulk flow model geometry.

the difference between the calibration constants of the friction law in the two different cases of the Couette and Poisseuille flow. Finally, the interface velocity is calculated by ensuring the shear stress continuity at the interface. The stratified bulk-model leakage predictions are finally compared to the experimental results of the tests done at the Turbomachinery Laboratory of the Texas $A\&M$ University "Experimental Study of the Static and Dynamic Characteristics of a Long (L/D=0.75) Smooth Seal with Mainly Air Mixtures" and "Experimental Study of the Static and Dynamic Characteristics of a Short (L/D=0.29) Smooth Seal with Mainly Air Mixtures".

4.2 Mathematical formulation

4.2.1 Governing equations

The geometry of the system under investigation is sketched in Fig.4.1.

In the region between rotor and stator the liquid particles experience a radial acceleration of the order of $\Omega^2 R$, being Ω the angular velocity of the rotor and R its radius. As a result, they are centrifuged toward the stator, leaving the rotor surface in contact with the only gas phase of lower density. In this case, the bulk-flow equations can be separately written for each of the two phases by integrating the Navier-Sotkes equations over the corresponding height (the subscript g and l refer respectively to the gas and liquid component, x is the circumferential coordinate, and y is the axial one). The equations that follows are obtained under the assumption of no mass transfer between the two phases for the same reasons outlined in the Introduction of chapter 3. Therefore, for the liquid phase we can write:

$$\frac{\partial H_l}{\partial t} + \frac{\partial (H_l U_l)}{\partial x} + \frac{\partial (H_l V_l)}{\partial y} = 0 \tag{4.2a}$$

$$\rho_l \frac{\partial (H_l U_l)}{\partial t} + \frac{\partial I_{xx,l}}{\partial x} + \frac{\partial I_{xy,l}}{\partial y} = -H_l \frac{\partial P}{\partial x} + \tau_{xz}|_{H_i}^{H_s} \tag{4.2b}$$

$$\rho_l \frac{\partial (H_l V_l)}{\partial t} + \frac{\partial I_{xy,l}}{\partial x} + \frac{\partial I_{yy,l}}{\partial y} = -H_l \frac{\partial P}{\partial y} + \tau_{yz}|_{H_i}^{H_s} \tag{4.2c}$$

ρ_l being the liquid density, H_l the height of the liquid film, P the internal pressure, U_l and V_l the mean circumferential and meridian velocities, respectively, $\tau_{ij}|_{H_i}^{H_s}$ the bulk mean shear stresses in the liquid phase, and $I_{xx,l}$, $I_{xy,l}$ and $I_{yy,l}$ the momentum flux integrals.

For the gas phase, with the same symbolism used for the liquid flow, we have

$$\frac{\partial (H_g \rho_g)}{\partial t} + \frac{\partial (\rho_g H_g U_g)}{\partial x} + \frac{\partial (\rho_g H_g V_g)}{\partial y} = 0 \tag{4.3a}$$

$$\frac{\partial (\rho_g H_g U_g)}{\partial t} + \frac{\partial I_{xx,g}}{\partial x} + \frac{\partial I_{xy,g}}{\partial y} = -H_g \frac{\partial P}{\partial x} + \tau_{xz}|_{H_r}^{H_i} \tag{4.3b}$$

$$\frac{\partial (\rho_g H_g V_g)}{\partial t} + \frac{\partial I_{xy,g}}{\partial x} + \frac{\partial I_{yy,g}}{\partial y} = -H_g \frac{\partial P}{\partial y} + \tau_{yz}|_{H_r}^{H_i} \tag{4.3c}$$

$$\begin{aligned} & C_p \left[\rho_g H_g \frac{DT}{Dt} - T \frac{D(\rho_g H_g)}{Dt} \right] - H_g \frac{DP}{Dt} = \\ & = R\Omega\, \tau_{xz}|_{H_r} - U_g\, \tau_{xz}|_{H_r}^{H_i} - V_g\, \tau_{yz}|_{H_r}^{H_i} - U_i\, \tau_{xz}|^{H_i} - V_i\, \tau_{yz}|^{H_i} \end{aligned} \tag{4.3d}$$

where C_p is the constant pressure specific heat and T is the temperature. Subscripts i, s, and r refer to the interface of separation of the fluid phases, and the stator and rotor surfaces, respectively. Superscripts and subscripts of the vertical bars refer respectively to the upper and lower integral extremes.

For a rotor perfectly coaxial with the stator (zero eccentricity), the bulk flow can be considered perfectly axis-symmetric. Under this assumption the flow is stationary and variations of the quantities in the circumferential x direction can be neglected. In this case, the above equations (4.2a-4.3d) simplify as follows:

$$\frac{\partial (H_l V_l)}{\partial y} = 0; \qquad \frac{\partial I_{xy,l}}{\partial y} = \tau_{xz}|_{H_r}^{H_i}; \qquad \frac{\partial I_{yy,l}}{\partial y} = -H_l \frac{\partial P}{\partial y} + \tau_{yz}|_{H_i}^{H_s} \tag{4.4a}$$

for the liquid laminar flow, and

$$\frac{\partial (\rho_g H_g V_g)}{\partial y} = 0; \qquad \frac{\partial I_{xy,g}}{\partial y} = \tau_{xz}|_{H_r}^{H_i}; \qquad \frac{\partial I_{yy,g}}{\partial y} = -H_g \frac{\partial P}{\partial y} + \tau_{yz}|_{H_r}^{H_i} \tag{4.5a}$$

$$\begin{aligned} & C_p \frac{\partial (\rho_g H_g T_g V_g)}{\partial y} - H_g V_g \frac{\partial P}{\partial y} = \\ & R\Omega\, \tau_{xz}|_{H_r} - U_g\, \tau_{xz}|_{H_r}^{H_i} - V_g\, \tau_{yz}|_{H_r}^{H_i} - U_i\, \tau_{xz}|^{H_i} - V_i\, \tau_{yz}|^{H_i} \end{aligned} \tag{4.5b}$$

for the gas flow.

Notice, in the framework of stratified flows, each phase can be separately studied with the assumptions of non-constant film thickness and non-zero interface velocity.

Two mass equations must also be considered to close the system of the governing equations,

$$\rho_l V_l H_l = Q_l; \qquad \rho_g V_g H_g = Q_g \tag{4.6a}$$

where Q_l and Q_g are the mass flow rates of the two liquid and gas phase, respectively.

The above five differential equations and two algebraic mass equations are however not sufficient to determine all the unknown quantities (V_g, V_l, U_g, U_l, ρ_g, T_g, P, H_l, H_g, V_i, U_i). Four additional equations are therefore required to completely define the problem. One equation can be obtained by observing that the stratified liquid and gas flows completely fill the gap H between stator and rotor, with the obvious consequence that $H_l + H_g = H$. Another equation is given by the state equation of the compressible domain $T_g = f(\rho_g, P_g)$. Finally, the last two equations are gained by ensuring continuity of shear stresses at the interface, *i.e.*

$$\tau_{xz,l} = \tau_{xz,g}; \qquad \tau_{yz,l} = \tau_{yz,g} \tag{4.7}$$

To solve the above equations, we need to calculate the momentum flux integrals and the wall shear stresses. To this end the flow regime and the nature of the interface between liquid and gas phases need to be defined. Specifically, we will assume smooth liquid-gas interface.

Moreover, the liquid phase is assumed in laminar regime, and the corresponding momentum flux integrals $I_{yy,l}$, $I_{xy,l}$ and shear stresses are analytically calculated under the following assumptions:

- $H/L \ll 1$ and negligible variation of the fluid height in the seal axial direction ($H = const$);
- negligible variation of the interface velocity in the seal axial direction ($V_i = const$, $U_i = const$);
- negligible viscous diffusion in x and y direction.

The assumption of a laminar liquid phase will be later verified in section 4.3 by calculating the axial liquid *Re* number. In general the liquid flow regime, depending on its *Re*, can be turbulent too. In this case the momentum fluxes and the wall/interface shear stresses correlations must be expressed as shown below for the turbulent gas phase.

Momentum flux integrals

Laminar liquid phase The laminar axial momentum flux integral is defined as

$$I_{yy,l} = \int_{H_l} \rho_l v^2(z) dz = \frac{\rho_l H_l}{2} \int_{-1}^{1} v^2(\eta) d\eta \tag{4.8}$$

where $\eta = 2z/H_l$ is the normalized radial coordinate and $v(\eta)$ is the meridian velocity field in the laminar region, given by (see appendix A)

$$v(\eta) = \frac{3V_p}{2}(1 - \eta^2) + \frac{V_i}{2}(1 - \eta) \tag{4.9}$$

In the above eq. (4.9) V_i is the interface meridian velocity and $V_p \simeq -\left(H_l^2/12\mu\right)\frac{\partial p}{\partial y}$ is the pressure driven averaged meridian velocity. The mean liquid velocity in the meridian direction is obtained by integrating (4.9) over the clearance H, obtaining $V_l = V_p + V_i/2$.

Therefore, substituting (4.9) into (4.8) and performing the integral, the laminar momentum flux integral takes the following expression in terms of the interface velocity

$$I_{yy,l} = \rho_l H_l \left[\frac{6}{5}V_l^2 + \frac{23}{60}V_i^2 - \frac{7}{10}V_i V_l\right] \tag{4.10}$$

The cross-coupled momentum flux integral is instead defined as

$$I_{xy,l} = \int_{H_l} \rho_l u(z,y)v(z)dz = \frac{\rho_l H_l}{2}\int_{-1}^{1} u\left(\eta,\zeta\right)v(\eta)d\eta \tag{4.11}$$

where $v\left(\eta\right)$ and $u(\eta,\zeta)$ are, respectively, the meridian and circumferential velocity fields, being $\zeta = 2y/H_l$ the normalized meridian coordinate. The circumferential velocity can be divided in an asymptotic term and a decaying one (it is referred as "decaying" because of its exponential decay along the seal meridian axis).

$$u = u_\infty(\eta) - u_{tr}(\eta,\zeta) \tag{4.12}$$

The asymptotic term $u_\infty(\eta)$ linearly depends on η, while $u_{tr}(\eta,\zeta)$ can be written as (see appendix A)

$$u_{tr}(\eta,\zeta) = Ae^{-\lambda\zeta}\phi(\eta) \tag{4.13}$$

with $\phi\left(\eta\right)$ solution of the following ODE equation

$$\phi'' + \phi\left[\frac{225}{16}\left(\frac{1}{5+2\chi}\right)(1-\eta^2) + \frac{75}{16}\chi\left(\frac{1}{5+2\chi}\right)(1-\eta)\right] = 0 \tag{4.14}$$

where $\chi = Re_i/Re_p$, being $Re_p = V_p H_l/\nu_l$ and $Re_i = V_i H_l/\nu_l$.

Therefore, by substituting (4.9) (4.12), the cross-coupled moment flux becomes

$$I_{xy,l} = \rho_l H_l\left[\frac{U_i V_i}{3} + \frac{U_i V_p}{2} - \frac{3V_p Ae^{-\lambda\zeta}}{4}(2-M_2) - \frac{V_i Ae^{-\lambda\zeta}}{4}(2-M_1)\right] \tag{4.15}$$

where $M_n = \int_{-1}^{1}\eta^n\phi(\eta)d\eta$ (with $n = 1, 2$).

The mean circumferential velocity is obtained by integrating (4.12) over the liquid height

$$U_l = 1/2\int_{-1}^{1} u(\eta,\zeta)d\eta = U_i/2 - U_{tr} \tag{4.16}$$

where U_i is the swirl (circumferential) interface velocity and $U_{tr} = Ae^{-\lambda\zeta}$. Finally, taking into account that $V_p = V_l - V_i/2$ and $Ae^{-\lambda\zeta} = U_{tr} = U_i/2 - U_l$, and observing that $\chi > 6$ (as explained in appendix A), the expression of $I_{xy,l}$ simplifies

$$I_{xy,l} = \rho_l H_l\left[\frac{U_i V_i}{8} - \frac{U_i V_l}{9} + \frac{6U_l V_l}{5} - \frac{V_i U_l}{12}\right] \tag{4.17}$$

Turbulent gas phase For the gas phase, under the assumption of fully developed turbulent flow, the momentum flux integrals are merely given by

$$I_{yy,g} = \rho_g H_g V_g^2 \tag{4.18a}$$
$$I_{xy,g} = \rho_g H_g V_g U_g \tag{4.18b}$$

Bulk shear stresses

Laminar liquid phase The axial laminar bulk shear stress in (A.1b) is simply obtained as:

$$\tau_{yz}|_{H_i}^{H_s} = \mu \int_{-H_l/2}^{H_l/2} \frac{d^2 v}{dz^2} dz = \mu \left(\left.\frac{dv}{dz}\right|_s - \left.\frac{dv}{dz}\right|_i \right) \tag{4.19}$$

By substituting (4.9) is (4.19), the solution of the integral integral leads to:

$$\tau_{yz}|_{H_i}^{H_s} = 6\mu_l \frac{V_i - 2V_l}{H_l} \tag{4.20}$$

The circumferential bulk shear stress is instead given by

$$\tau_{xz}|_{H_i}^{H_s} = \mu \int_{-H_l/2}^{H_l/2} \frac{d^2 u}{dz^2} dz = \mu \left(\left.\frac{du}{dz}\right|_s - \left.\frac{du}{dz}\right|_i \right) \tag{4.21}$$

As shown in appendix A the circumferential velocity at given axial position is expressed as:

$$u = u_\infty - u_{tr}(\eta, \zeta) = U_i(1-\eta)/2 - U_{tr,0} e^{-\lambda\zeta} \phi(\eta) \tag{4.22}$$

By substituting (4.22) into (4.21) is easy to observe that the asymptotic component u_∞ gives no contribution to the integral and that the resulting bulk laminar circumferential stress can be obtained by integrating (4.14) over the domain $-1 < \eta < 1$ and multiplying for $2\mu A e^{-\lambda\zeta}/H_l$. The final result is

$$\tau_{xz}|_{H_i}^{H_s} = -\frac{75\mu_l U_{tr}}{8H_l} \left(\frac{6 + 2\chi - 3M_2 - \chi M_1}{5 + 2\chi} \right) \approx -\frac{5\mu_l (U_i - 2U_l)}{H_l} \tag{4.23}$$

The above approximation gives an error smaller than 5% in the range $6 < \chi < 60$.

Turbulent gas phase The turbulent bulk shear stress is expressed through the Hirs formulation. The Hirs formulation is slightly modified as better explained in chapter 2.

For hybrid flows (both pressure and shear driven), as in the case of turbulent flow in pressure seals, an equivalent friction factor is introduced

$$\frac{\tau_w}{\frac{1}{2}\rho W_r^2} = f_r = n Re_{r,eq}^m = n \left(\frac{\rho W_{r,eq} H}{\mu} \right)^m \tag{4.24}$$

where $W_{r,eq}$ is an equivalent turbulent velocity, defined as

$$W_{r,eq} = \sqrt{9U_r^2 + V_r^2} \tag{4.25}$$

In the above expression U_r and V_r are, respectively, the circumferential and meridian velocity with respect to the wall, which corresponds to the smooth interface in this specific case. Notice, in the limit of vanishing U_r or V_r, the values 0.073 or 0.055 are recovered for the coefficient n, respectively.

Therefore, the turbulent shear stresses on stator and smooth interface can be respectively written as

$$f_s = n\left(\frac{\rho W_{s,eq} H}{\mu}\right)^m; \qquad f_i = n\left(\frac{\rho W_{i,eq} H}{\mu}\right)^m \tag{4.26a}$$

$$W_{i,eq} = \sqrt{9(U_g - U_i)^2 + (V_g - V_i)^2}; \qquad W_{s,eq} = \sqrt{9(\Omega R - U_g)^2 + V_g^2} \tag{4.26b}$$

Continuity of shear stresses at the interface According to the above expressions of shear stresses, the continuity condition ((4.7)) at the liquid-gas interface can be written as

$$-\frac{f_i}{2}\rho_g W_i (U_g - U_i) \simeq \frac{-2\mu_l}{H_l}\left[U_i/2 + 3U_{tr}\right] = \mu_l \frac{6U_l - 4U_i}{H_l} \tag{4.27}$$

for the circumferential shear stresses, and

$$-\frac{f_i}{2}\rho_g W_i (V_g - V_i) = \mu_l \frac{6V_l - 4V_i}{H_l} \tag{4.28}$$

for the axial ones.

4.2.2 Boundary conditions

To correctly formulate the boundary conditions, the knowledge of the local flow pattern in both the inlet and outlet sections is required. However, a fluid flow needs some length (the so-called entrance length) to fully develop its velocity profile. Therefore, in this region the stratification could be not completely developed. Similar considerations can be done also at the outlet section with the further complication that a transonic ($Ma \simeq 1$) regime can be observed.

Although both leakage and structural response predictions are considerably affected by the inlet and outlet flow field (also in the case of single phase flows), an accurate description of the local behavior (local skin friction factors and momentum fluxes) still misses in literature. What is usually made therefore, is to correct the model with empirical pressure loss coefficients, whose uncertainty affect the model accuracy (mainly for the structural response predictions).

Here the flow is considered completely stratified along the whole seal length; inlet and outlet total pressures are corrected with empirical pressure loss coefficients, ζ_i and ζ_o, respectively, in order to accurately match experimental data.

Inlet gas total pressure and temperature

The inlet pressure loss is taken into account by loss coefficient ζ_i; therefore, the effective inlet total pressure is

$$P_{0,inlet} = P_0 - \zeta_i \rho_g V_g^2/2 \tag{4.29}$$

The inlet total temperature of the gas flow is instead equal to the total temperature of the inlet ambient

$$T_{0,inlet} = T_{inlet} + \frac{V_g^2}{2C_p} = T_0 \tag{4.30}$$

Outlet gas total pressure

Equations (4.4-4.5) can be generally rewritten in the more compact matrix form as:

$$A(\overline{v})\overline{v}' = B(\overline{v}) \tag{4.31}$$

being $\overline{v} = [V_l \quad U_l \quad V_g \quad U_g \quad P]^T$ the vector of the unknown quantities, $\overline{v}'$ indicates the axial derivatives of the unknown vector. A and B are square matrices whose elements are functions of problem unknown. The solution of the above system (4.31) in a generic point $0 < y < l$ exists and is unique if and only if $det(A) \neq 0$.

Therefore, at the outlet section we can write $det(A_{y=l}) \leq 0$, and neglecting the variation of the ratio V_i/V_l in the axial direction, this condition becomes

$$Ma^{-2} \leq 1 - \frac{\gamma P H_l}{H_g \rho_l V_l^2 \alpha} \tag{4.32}$$

whereMa is the Mach number, $\alpha = \frac{6}{5} + \frac{23}{60}\beta^2 - \frac{7}{10}\beta$, and $\beta = V_{i,out}/V_{l,out}$. Notice (4.32) reduces to $Ma \leq 1$ in the case of a single-phase perfect gas flow (i.e. Fanno flow).

Figure 4.2 shows the variation along the axial direction of Ma^{-2} and its upper bound $Ma_{\lim}^{-2} = 1 - \frac{\gamma P H_l}{H_g \rho_l V_l^2 \alpha}$ given in (4.32) at different ratio $Pr = P_{0,exit}/P_0$. The Mach number being less than 1, acceleration occurs and for low Pr (less than 0.4) the flow can become choked at the exit section ($Ma_{exit}^{-2} = Ma_{\lim,exit}^{-2}$).

The boundary condition (4.32) is satisfied only if the outlet total pressure at the outlet section is larger than the external total pressure *i.e.*

$$P_{0,out} - \frac{\zeta_o}{2}\rho_g V_g^2 > P_{0,exit} \tag{4.33}$$

Vice versa, when (4.33) is not satisfied, the boundary condition becomes the usual *low Mach* boundary condition as for the classical *Fanno flow*.

$$P_{0,out} - \frac{\zeta_o}{2}\rho_g V_g^2 = P_{0,exit} \tag{4.34}$$

GVF equation

At the inlet section, fixed the gas volume fraction (GVF), an additional boundary condition is obtained by observing that GVF is given by the ratio between the gas volume rate and the total flow rate

$$GVF = \frac{\rho_g V_g}{\rho_g V_g + \rho_l V_l} \tag{4.35}$$

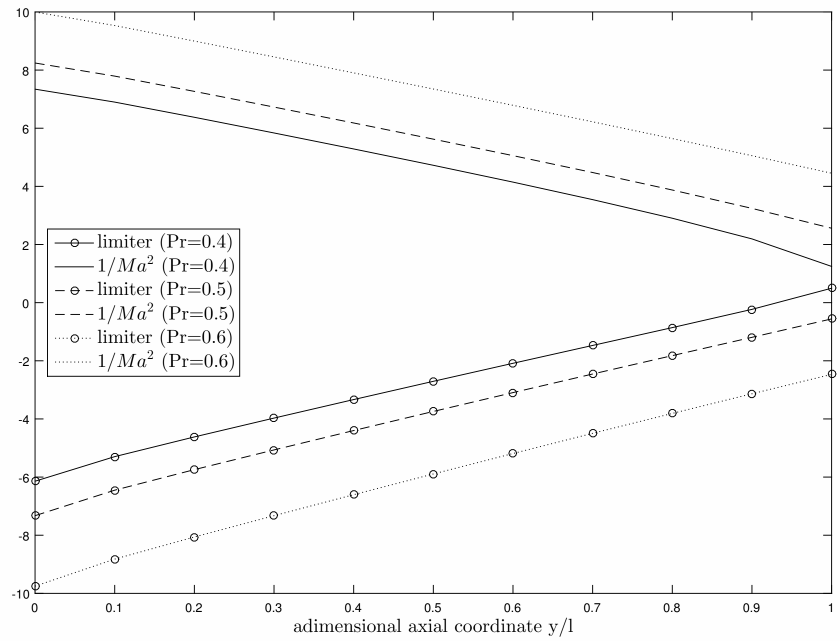

Figure 4.2: Variation of Ma^{-2} and Ma_{lim}^{-2} in the axial direction for three different pressure ratio $Pr = P_{0,exit}/P_0$ ($L/D = 0.75$, $GVF_{inlet} = 0.885$, $P_0 = 62.1bar$, $\Omega = 1.5 \times 10^4 RPM$).

Inlet interface velocity

Since $V_l - V_i/2 = V_p$, where $V_p \simeq -\left(H_l^2/12\mu\right)\frac{\partial p}{\partial y}$ is the average meridian velocity related to the pressure gradient existing in the laminar region, the inlet interface velocity can be easily correlated to the average liquid velocity and local pressure gradient

$$V_i/2 - V_l = \frac{H_l^2}{12\mu}\frac{\partial p}{\partial y} \tag{4.36}$$

Inlet liquid and gas circumferential velocity

The local flow pattern in the proximity of the inlet section is not known *a priori*. In particular, the circumferential component of the flow is usually damped because of the presence in the inlet chamber of swirl-brakes, which are typically used to enhance the seal stiffness. Moreover, even for zero inlet circumferential velocity, the liquid particles can be rapidly centrifuged toward the stator making the real inlet circumferential liquid velocity significantly different with respect to the one usually expected in the single phase case. Stating the above considerations, the liquid and gas circumferential velocities at the inlet section can be therefore related to the rotor angular velocity Ω by

$$U_{l,inlet} = \alpha_l \Omega R, \qquad U_{g,inlet} = \alpha_g \Omega R \tag{4.37}$$

where α_l and α_g are the ratio between the velocities of the liquid and gas flows and the rotor circumferential one, respectively.

4.3 Results

In this section a comparison in terms of oil leakage is proposed between the stratified model and the homogeneous one introduced in of chapter 3, where the two phases are considered finely mixed, and hence sharing the same temperature and velocity. Moreover, experimental data mentioned in the introduction are also shown as a reference. In all plots, we have assumed $\Omega = 1.5 \times 10^4$RPM, $\mu_l = 3.64 \cdot 10^{-3} Pl$, $\mu_g = 1.82 \cdot 10^{-5} Pl$, $\rho_l = 900 kg/m^3$, $K_{gas} = 287 J/kg \cdot K$, $P_{0,inlet} = 62.1 bar$, $T_0 = 295K$, $D = 90mm$, $H = 0.18mm$.

Figure 4.3 shows the effect of the inlet GVF on the oil leakage for different pressure ratios $Pr = P_{0,exit}/P_0$, and seal length ($L/D = 0.75$, figure 4.3a $L/D = 0.29$, figure 4.3b). As expected, increasing GVF the oil leakage reduces, and both experimental data and stratified bulk model predictions show that such reduction is almost linear. Moreover, an increase in the pressure ratio Pr entails a reduction in oil leakage; however, such effect is not significantly pronounced. This behavior is likewise observed in long and short seals. Finally, notice theoretical predictions are in good agreement with measured data.

A direct comparison between stratified and homogeneous bulk model is proposed in figures 4.4-4.5, for the case of long (figure 4.4) and short seal (figure 4.5). Experimental data are also shown as a reference. In both cases, the stratified model seems to match experimental data more closely, and it is the only one able to get the change in local slope observed experimentally at high GVF ($GVF \simeq 0.98 - 0.99$). The homogeneous model predictions show instead a continuous linear decrease of the oil leakage for all values of GVF. Notice in the short seal case ($L/D = 0.29$), where the inlet development length is a consistent portion of the whole seal length, significantly larger values of the inlet and outlet loss coefficients ζ need to be considered to adequately take into account the pressure losses occurring in the inlet and outlet sections.

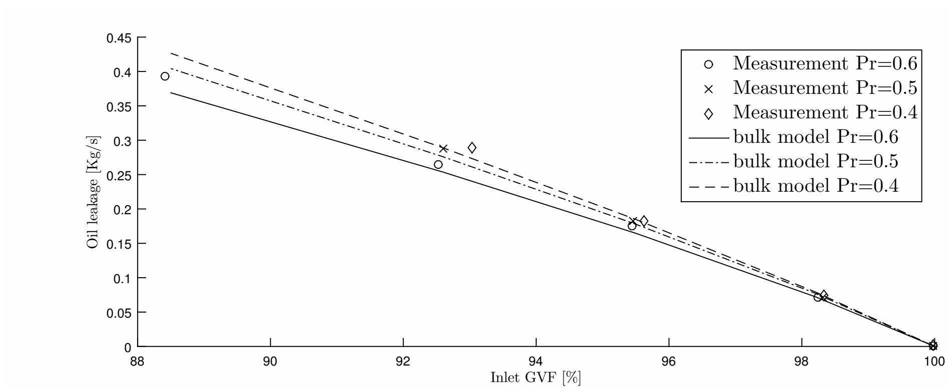

(a) Oil leakage comparison for $L/D = 0.75$

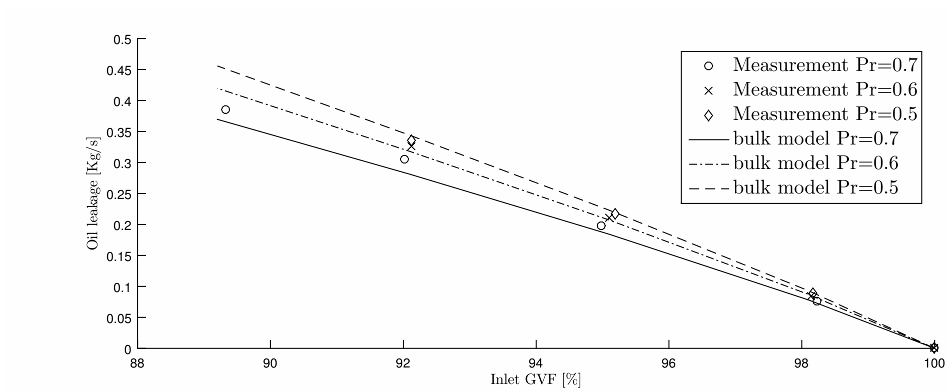

(b) Oil leakage comparison for $L/D = 0.29$

Figure 4.3: Comparison between stratified bulk model predictions and measured oil leakage. Results are obtained for $D = 90mm$, $H = 0.18mm$, $T_0 = 295K$, $P_0 = 62.1bar$, $\rho_l = 900kg/m^3$, $\mu_l = 3.64 \cdot 10^{-3}Pl$, $\mu_g = 1.82 \cdot 10^{-5}Pl$, $\zeta_i = 0.2$, $\zeta_o = 0.5$, $\Omega = 15000RPM$.

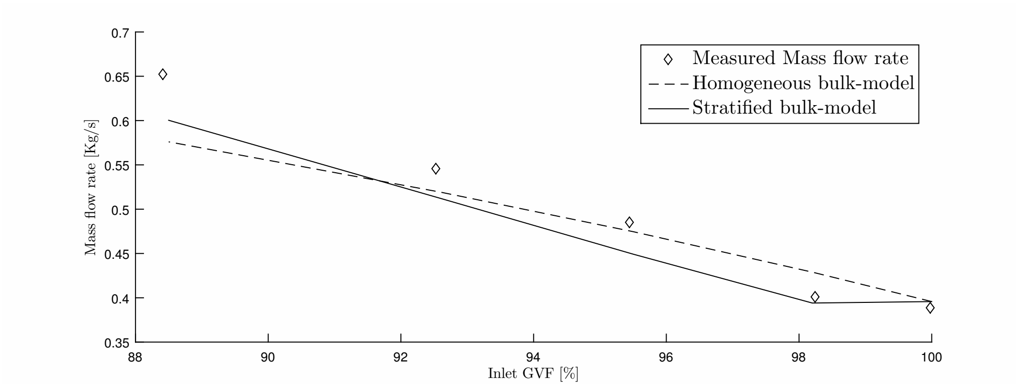

(a) Leakage comparison, $P_{0,exit} = 0.6P_0$

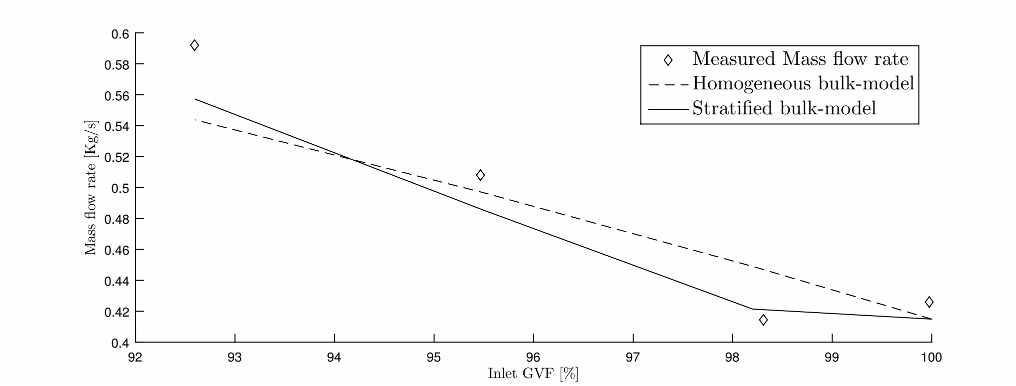

(b) Leakage comparison, $P_{0,exit} = 0.5P_0$

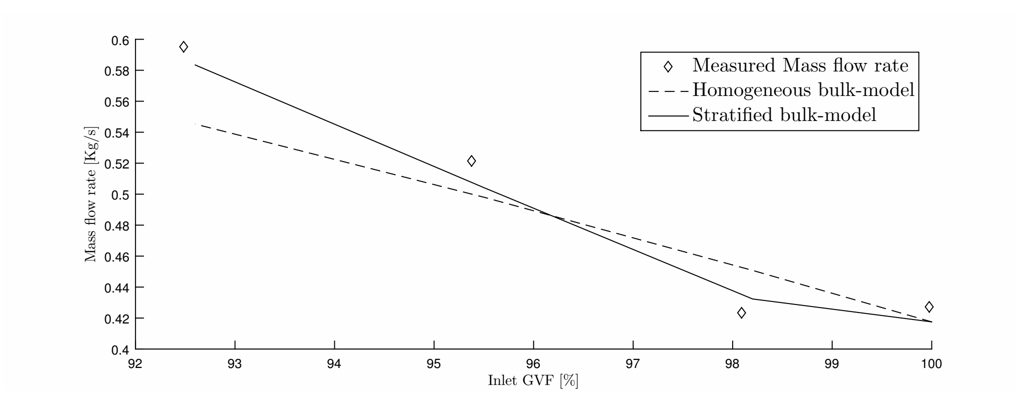

(c) Leakage comparison, $P_{0,exit} = 0.4P_0$

Figure 4.4: Comparison between stratified and homogeneous bulk model predictions in the case of long seal ($D = 90mm$, $L/D = 0.75$) and different value of the pressure ratio $\mathrm{Pr} = P_{0,exit}/P_0$. Results are obtained for $H = 0.18mm$, $T_0 = 295K$, $P_0 = 62.1bar$, $\rho_l = 900kg/m^3$, $\mu_l = 3.64 \cdot 10^{-3}Pl$, $\mu_g = 1.82 \cdot 10^{-5}Pl$, $\zeta_i = 0.2$, $\zeta_o = 0.5$, $\Omega = 15000RPM$.

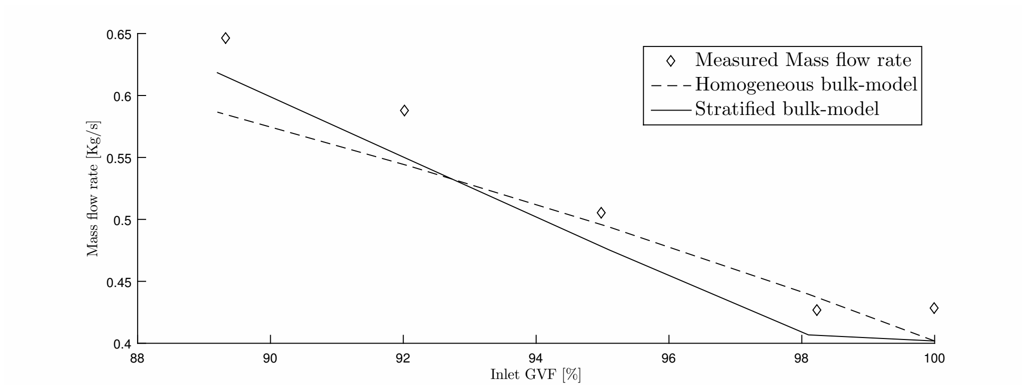

(a) Leakage comparison, $P_{0,exit} = 0.7P_0$

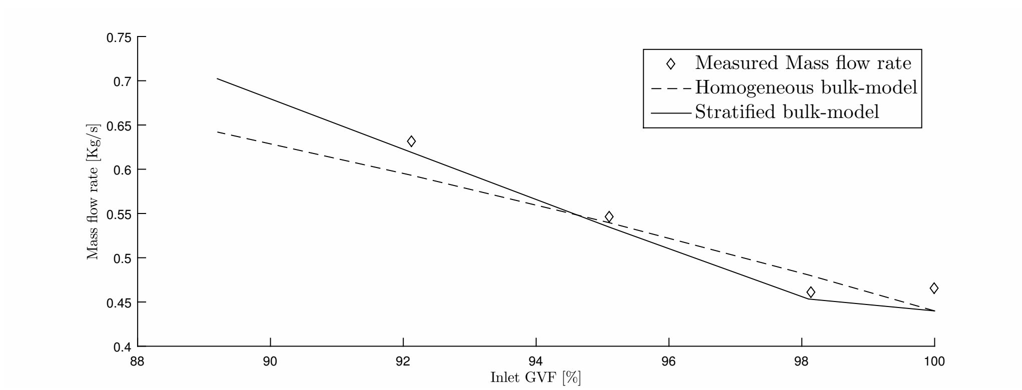

(b) Leakage comparison, $P_{0,exit} = 0.6P_0$

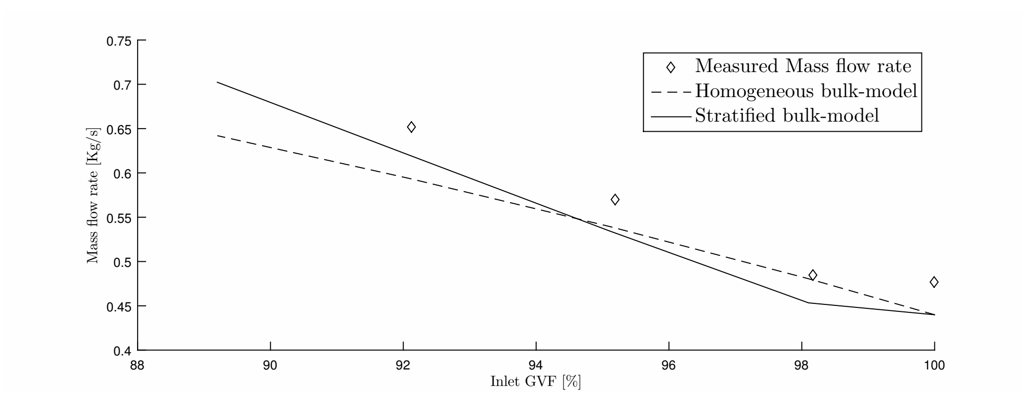

(c) Leakage comparison, $P_{0,exit} = 0.5P_0$

Figure 4.5: Comparison between stratified and homogeneous bulk model predictions in the case of long seal ($D = 90mm$, $L/D = 0.29$) and different value of the pressure ratio $\Pr = P_{0,exit}/P_0$. Results are obtained for $H = 0.18mm$, $T_0 = 295K$, $P_0 = 62.1bar$, $\rho_l = 900kg/m^3$, $\mu_l = 3.64 \cdot 10^{-3}Pl$, $\mu_g = 1.82 \cdot 10^{-5}Pl$, $\zeta_i = 1$, $\zeta_o = 1$, $\Omega = 15000RPM$.

Results given in figure 4.6 show the variation of the Reynolds number Re of the liquid phase (calculated on the basis of the liquid average velocity) with the gas volume fraction for long (figure 4.6a) and short (figure 4.6b) seal. The Reynolds number is a decreasing function of GVF, and larger values are obtained for smaller pressure ratios Pr and for the short seal. However, Re typically takes very small values, in the range $20 - 100$. As a result, our assumption to consider the liquid phase in laminar regime is fully justified.

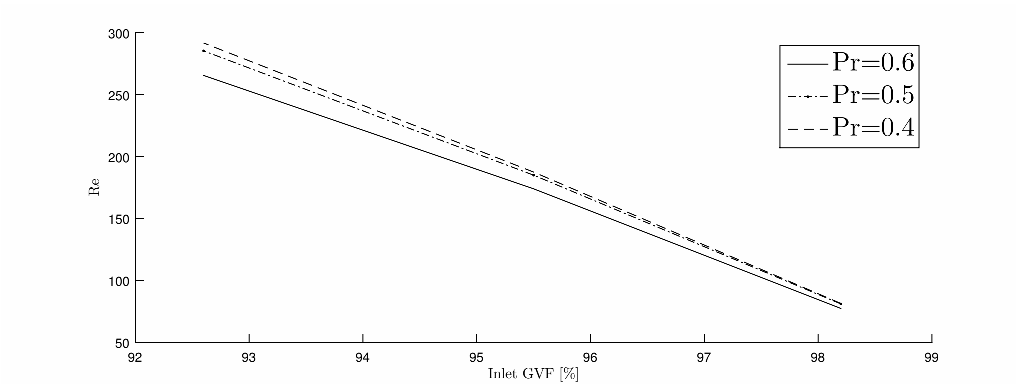

(a) Liquid Reynold number for $L/D = 0.75$

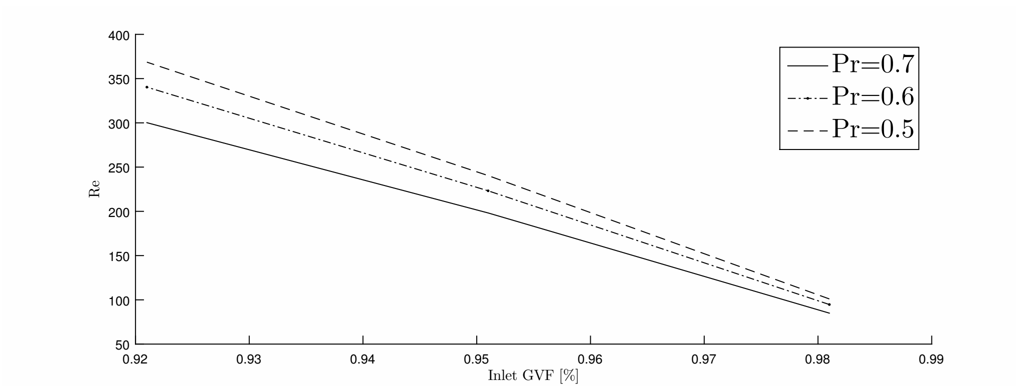

(b) Liquid Reynold number for $L/D = 0.29$

Figure 4.6: The variation of the liquid Reynold number VH/ν with the inlet gas volume fraction GVF.

Figure 4.7 shows the variation in the axial direction of the three meridian velocities V_l, V_g and V_i in a specific operating condition ($P_0 = 62.1$ bar, $P_{0,out} = 31$ bar, $\Omega = 1.5 \times 10^4$ RPM, and $GVF_{inlet} = 0.982$). The gas velocity, as expected, is about an order of magnitude greater than the liquid and interface ones, and significantly increases as we approach to the outlet section. Notice also the values of the ratio V_i/V_l are in the range $1.5 < V_i/V_l < 2$, as can be easily demonstrated with simple considerations (see appendix A).

Finally, the variation in the axial direction of the three circumferential velocities U_l, U_g, U_i (obtained with the stratified model) and the bulk circumferential one calculated with the homogeneous multiphase model is shown in figure 4.8. The circumferential homogeneous velocity takes slightly smaller values with respect to the gas circumferential velocity predicted by the stratified model; further, in both cases, curves show an asymptotic trend toward about $\Omega R/2$. About the liquid bulk circumferential velocity U_l we have assumed that at the inlet section its value is ΩR in view of the fact that the liquid is centrifuged toward the stator with a cir-

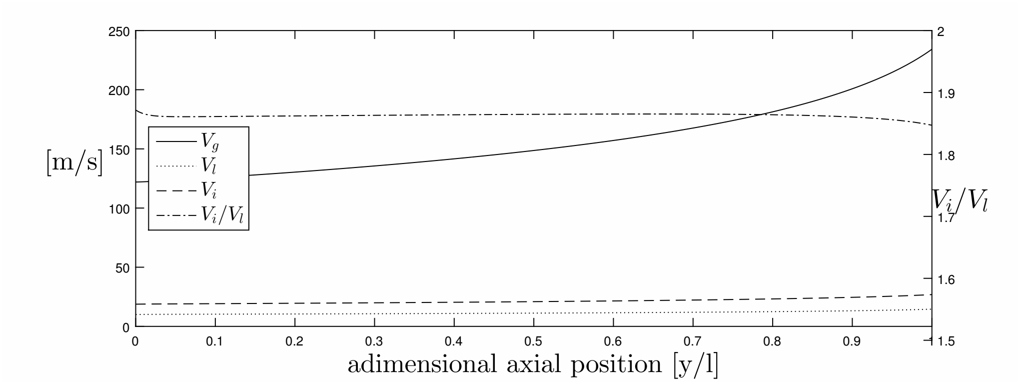

Figure 4.7: The variation of the bulk meridian velocities in the axial direction for the long seal case ($D = 90mm$, $L/D = 0.75$, $P_0 = 62.1bar$, $P_{0,out} = 31bar$, $\Omega = 15000RPM$, $GVF_{inlet} = 98.2\%$).

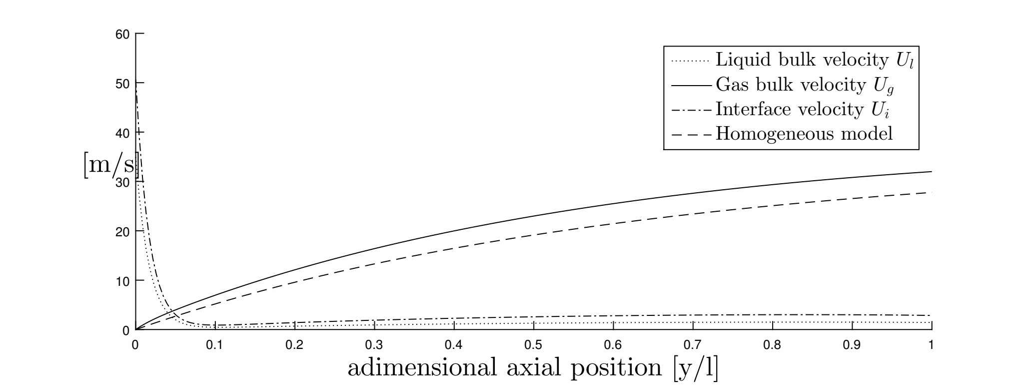

Figure 4.8: The variation of the bulk circumferential velocities in the axial direction for the long seal case ($D = 90mm$, $L/D = 0.75$, $P_0 = 62.1bar$, $P_{0,out} = 31bar$, $\Omega = 15000RPM$, $GVF_{inlet} = 98.2\%$). Prediction of the homogeneous model is also shown for comparison.

cumferential velocity of about ΩR, when it gets in the seal. The inlet interface circumferential velocity U_i is instead obtained by the interface shear stress continuity (4.7). Both U_l and U_i shows a strong initial decrease in a small spatial range (about $0.1L$); then an asymptotic value is approached with $U_{i,\lim} \simeq 2U_{l,\lim}$. As a result, according to (4.23) the circumferential bulk shear stress will vanish. Once the liquid circumferential velocity approaches to its asymptotic value $U_{l,\lim} = 1.42m/s$, the centrifugal acceleration becomes $U_{l,\lim}^2/R = 45.37m/s^2$, and hence about 4.6 times larger tan the gravity acceleration). Notice, this value is very smaller than the hypothesized one ($\Omega^2 R \simeq 10^4 g$).

4.4 Conclusions

A new bulk flow model, based on a two phase smooth-stratified flow, for prediction of leakage in annular pressure seals has been proposed. The model is based on the assumption that the liquid flow is in laminar regime, while the gas component is in turbulent regime. Analytic expressions have been derived for the momentum fluxes, interface and wall shear stresses in the laminar domain, under the assumption of negligible variation of both the liquid height and interface velocity in the axial direction. Correlations between the rotor and interface shear stresses in the turbulent domain have been formulated following the Hirs approach. The interface velocity has been implicitly derived by enforcing the shear stress continuity at the interface.

Results in terms of oil leakage show a good agreement between experimental data and theoretical predictions of the proposed stratified model, provided to assume convenient values of the inlet and outlet pressure loss coefficients. The stratified model correctly predicts the dependence of the oil leakage on the gas volume fraction, and in particular the change in slope observed at high values of GVF. Such behavior is not captured by the homogeneous model with finely mixed phases.

The predicted circumferential velocities show an asymptotic trend with the axial coordinate. In particular, the model predicts a liquid circumferential velocity much smaller than the gas one. As a result, centrifugal accelerations are much lower than expected, but anyway much higher than the gravity one.

The stratified-flow bulk model here formalized can also be adopted to predict the rotordynamic coefficients of the seal. As outlined in section 3.8, also in this case could be observed strong sensitivity of the model predictions to the loss coefficients $\zeta_{i,o}$. Trivially, this new model has the potential to predict the seal rotordynamic coefficients better than other multiphase bulk models once the fundamental hypothesis of smooth stratification of the two fluids is verified.

In this regard, further investigations are required to better describe the interface interactions between the two phases, as local droplets, bubbles or surface waves dynamics may occur. Moreover, a better understanding of the flow phenomena in the inlet and outlet regions is also necessary in view of more accurate predictions of both leakage and rotordynamics performance.

Chapter 5

Conclusions

This doctoral thesis has dealt with the bulk modeling of the fluid flow inside an annular pressure seal operating in both single and multi-phase (gas and liquid) conditions.

Chapter 1 has introduced the theme of the rotordynamic stability analysis. In this regard the concepts of the seal complex impedance H_{ij} and instability threshold ω_c have been defined through the seal rotordynamic coefficients. Is also reported a short historical review on the progresses made in this field in the past century. The chapter ends with an overview of the sealing systems usually adopted in the industrial practice.

Chapter 2 has dealt with the bulk modeling of an annular pressure seal operating under single-phase (liquid or perfect gas) flow regime. A new friction law, based on the Hirs formulation [28], has been introduces to take into account the different calibration constants in the two different cases of Couette and Pouiseuille flow. Discrete agreement between bulk-predicted and measured leakages and rotordynamic coefficients has emerged.

Chapter 3 has concerned with the multi-phase bulk flow modeling when is adopted the hypothesis of homogeneous two-phase (gas-liquid) flow. Under this hypothesis is derived a new formulation of the bulk boundary conditions that holds for every GVF. Bulk-predicted leakage and rotordynamic coefficients are in reasonable agreement with the experimental data though is emerged the need of an accurate calibration of the outlet loss coefficient ζ_o to correctly predict the instability threshold ω_c.

Chapter 4 has outlined a new two-phase bulk flow model based on the hypothesis of smooth stratification of the two fluids. Under the action of the centrifugal forces generated by the rotor angular speed the liquid is centrifuged toward the stator leaving the rotor in contact with the only gas phase. Predicted leakages has shown very good agreements with the experimental results marking an improvement over the homogeneous model predictions.

Bibliography

[1] J. Alford. Protecting turbomachinery from self-excited rotor whirl. *Journal of Engineering for Power*, 87(4):333–343, 1965.

[2] G. L. Arauz and L. San Andres. Analysis of two-phase flow in cryogenic damper seals part i: theoretical model. *Journal of tribology*, 120(2):221–227, 1998.

[3] G. L. Arauz and L. San Andres. Analysis of two-phase flow in cryogenic damper seals part ii: model validation and predictions. *Journal of tribology*, 120(2):228–233, 1998.

[4] M. Athavale and R. Hendricks. A small perturbation cfd method for calculation of seal rotordynamic coefficients. *International Journal of Rotating Machinery*, 2(3):167–177, 1996.

[5] D. Barnea. A unified model for predicting flow-pattern transitions for the whole range of pipe inclinations. *International Journal of Multiphase Flow*, 13(1):1–12, 1987.

[6] D. Beattie and P. Whalley. A simple two-phase frictional pressure drop calculation method. *International Journal of Multiphase Flow*, 8(1):83–87, 1982.

[7] P. Beatty and W. Hughes. Turbulent two-phase flow in annular seals. *ASLE transactions*, 30(1):11–18, 1987.

[8] P. Beatty and W. Hughes. Stratified two-phase flow in annular seals. *ASME J. Tribol*, 112(2):372–381, 1990.

[9] H. Black. Effects of hydraulic forces in annular pressure seals on the vibrations of centrifugal pump rotors. *Journal of Mechanical Engineering Science*, 11(2):206–213, 1969.

[10] D. Childs. Ssme turbopump technology improvements via transient rotordynamic analysis. Technical report, The University of Louisville/Speed Scientific School, 1975.

[11] D. Childs and C.-H. Kim. Analysis and testing for rotordynamic coefficients of turbulent annular seals with different, directionally-homogeneous surface-roughness treatment for rotor and stator elements. *Journal of Tribology*, 107(3):296–305, 1985.

[12] D. Childs, C. Nelson, C. Nicks, J. Scharrer, D. Elrod, and K. Hale. Theory versus experiment for the rotordynamic coefficients of annular gas seals: Part 1test facility and apparatus. *Journal of Tribology*, 108(3):426–431, 1986.

[13] D. W. Childs. Dynamic analysis of turbulent annular seals based on hirs' lubrication equation. *Journal of lubrication technology*, 105(3):429–436, 1983.

[14] D. W. Childs. Finite length solutions for rotordynamic coefficients of turbulent annular seals. *ASME Journal of Lubrication Technology*, 105(3):437–445, 1983.

[15] G. Chochua and T. A. Soulas. Numerical modeling of rotordynamic coefficients for deliberately roughened stator gas annular seals. *Journal of tribology*, 129(2):424–429, 2007.

[16] A. Cicchitti, C. Lombardi, M. Silvestri, G. Soldaini, and R. Zavattarelli. Two-phase cooling experiments: pressure drop, heat transfer and burnout measurements. Technical report, Centro Informazioni Studi Esperienze, Milan, 1959.

[17] C. F. Colebrook. Turbulent flow in pipes, with particular reference to the transition region between the smooth and rough pipe laws. *Journal of the Institution of Civil Engineers*, 11(4):133–156, 1939.

[18] C. F. Colebrook and C. M. White. Experiments with fluid friction in roughened pipes. *Proceedings of the Royal Society of London A: Mathematical, Physical and Engineering Sciences*, 161(906):367–381, 1937.

[19] R. Dean. Reynolds number dependence of skin friction and other bulk flow variables in two-dimensional rectangular duct flow. *Journal of Fluids Engineering*, 100(2):215–223, 1978.

[20] F. Dietzen and R. Nordmann. Calculating rotordynamic coefficients of seals by finite-difference techniques. *Journal of Tribology*, 109(3):388–394, 1987.

[21] A. Dimarogonas. *Vibration for Engineers*. Prentice-Hall, 2 edition, 1995.

[22] A. Dukler, M. Wicks, and R. Cleveland. Frictional pressure drop in two-phase flow: A. a comparison of existing correlations for pressure loss and holdup. *AIChE Journal*, 10(1):38–43, 1964.

[23] A. Dukler, M. Wicks, and R. Cleveland. Frictional pressure drop in two-phase flow: B. an approach through similarity analysis. *AIChE Journal*, 10(1):44–51, 1964.

[24] D. Elrod, D. Childs, and C. Nelson. An annular gas seal analysis using empirical entrance and exit region friction factors. *Journal of Tribology*, 112(2):196–204, 1990.

[25] D. Elrod, C. Nelson, and D. Childs. An entrance region friction factor model applied to annular seal analysis- theory versus experiment for smooth and honeycomb seals. *ASME, Transactions, Journal of Tribology*, 111:337–343, 1989.

[26] H. F Black and D. N Jenssen. Dynamic hybrid bearing characteristics of annular controlled leakage seals. *Proceedings of the Institution of Mechanical Engineers, Conference Proceedings*, 184:92–100, 09 1969.

[27] T. W. Ha and B. S. Choe. Numerical simulation of rotordynamic coefficients for eccentric annular-type-plain-pump seal using cfd analysis. *Journal of mechanical science and technology*, 26(4):1043–1048, 2012.

[28] G. Hirs. A bulk-flow theory for turbulence in lubricant films. *Journal of Lubrication Technology*, 95(2):137–145, 1973.

[29] H. H. Jeffcott. Xxvii. the lateral vibration of loaded shafts in the neighbourhood of a whirling speed.the effect of want of balance. *The London, Edinburgh, and Dublin Philosophical Magazine and Journal of Science*, 37(219):304–314, 1919.

[30] S.-M. Kim and I. Mudawar. Universal approach to predicting two-phase frictional pressure drop for adiabatic and condensing mini/micro-channel flows. *International Journal of Heat and Mass Transfer*, 55(11):3246–3261, 2012.

[31] S.-M. Kim and I. Mudawar. Universal approach to predicting two-phase frictional pressure drop for mini/micro-channel saturated flow boiling. *International Journal of Heat and Mass Transfer*, 58(1):718–734, 2013.

[32] A. Kimball. Internal friction theory of shaft whirling. *General Electric Review*, 27(4):244–251, 1924.

[33] A. Kimball. Measurement of internal friction in a revolving deflected shaft. *General Electric Review*, 28:554, 1925.

[34] B. E. Launder. *Closure Strategies for Turbulent and Transitional Flows.* Cambridge University Press, 2002.

[35] R. Lockhart and R. Martinelli. Proposed correlation of data for isothermal two-phase, two-component flow in pipes. *Chem. Eng. Prog*, 45(1):39–48, 1949.

[36] A. A. Lomakin. Calculation of the critical speed and the conditions to ensure dynamic stability of the rotors in high pressure hydraulic machines, taking account of the forces in the seals. *Energomashinostroenie*, 14(4):1–5, 1958.

[37] J. Lund. Stability and damped critical speeds of a flexible rotor in fluid-film bearings. *Journal of Engineering for Industry*, 96(2):509–517, 1974.

[38] J. W. Lund. *SELF-EXCITED, STATIONARY WHIRL ORBITS OF A JOURNAL IN A SLEEVE BEARING.* PhD thesis, Rensselaer Polytechnic Institute, 1967.

[39] W. McAdams, W. Wood, and R. Bryan. Vaporization inside horizontal tubes-ii-benzeneoil mixtures. *ASME, Transactions*, 66:671–684, 1942.

[40] N. J. Mehta and D. W. Childs. Measured comparison of leakage and rotordynamic characteristics for a slanted-tooth and a straight-tooth labyrinth seal. *Journal of Engineering for Gas Turbines and Power*, 136(1):012501, 2014.

[41] P. J. Migliorini, A. Untaroiu, H. G. Wood, and P. E. Allaire. A computational fluid dynamics/bulk-flow hybrid method for determining rotordynamic coefficients of annular gas seals. *Journal of Tribology*, 134(2):022202, 2012.

[42] L. Moody. Friction factors for pipe flow. *Transaction of the ASME*, 66(8):671–684, 1944.

[43] J. J. Moore and A. B. Palazzolo. Cfd comparison to 3d laser anemometer and rotordynamic force measurements for grooved liquid annular seals. *TRANSACTIONS-AMERICAN SOCIETY OF MECHANICAL ENGINEERS JOURNAL OF TRIBOLOGY*, 121:306–314, 1999.

[44] H. Müller-Steinhagen and K. Heck. A simple friction pressure drop correlation for two-phase flow in pipes. *Chemical Engineering and Processing: Process Intensification*, 20(6):297–308, 1986.

[45] Z. Mullins and L. Barrett. Mobile Systems IV. Technical Report UVA/643092/MAE83/203, University of Virginia, 1983.

[46] A. Muszynska. *Rotordynamics (Mechanical Engineering) by Muszynska, Agnieszka(May 20, 2005) Hardcover*. CRC Press, 1602.

[47] H. M. Nagib and K. A. Chauhan. Variations of von kármán coefficient in canonical flows. *Physics of Fluids*, 20(10):101518, 2008.

[48] C. Nelson, D. Childs, C. Nicks, and D. Elrod. Theory versus experiment for the rotordynamic coefficients of annular gas seals: Part 2constant-clearance and convergent-tapered geometry. *Journal of Tribology*, 108(3):433–437, 1986.

[49] B. Newkirk. Shaft whipping. *General Electric Review*, 27(3):169–178, 1924.

[50] A. Picardo and D. W. Childs. Rotordynamic coefficients for a tooth-on-stator labyrinth seal at 70 bar supply pressures: measurements versus theory and comparisons to a hole-pattern stator seal. *Journal of engineering for gas turbines and power*, 127(4):843–855, 2005.

[51] S. Pirozzoli, M. Bernardini, and P. Orlandi. Turbulence statistics in couette flow at high reynolds number. *Journal of Fluid Mechanics*, 758:327–343, 2014.

[52] S. B. Pope. *Turbulent Flows*. Cambridge University Press, 1 edition, 10 2000.

[53] M. W. J. Rankine. On the centrifugal force of rotating shafts. *The Engineer*, 27:249, 1869.

[54] O. Reynolds. On the theory of lubrication and its application to mr. beauchamp tower's experiments, including an experimental determination of the viscosity of olive oil. *Proceedings of the Royal Society of London*, 40(242-245):191–203, 1886.

[55] L. San Andres, Z. Yang, and D. W. Childs. Thermal effects in cryogenic liquid annular sealspart ii: Numerical solution and results. *Journal of tribology*, 115(2):277–284, 1993.

[56] M. M. Sc.D. Xvi. on musical air-bubbles and the sounds of running water. *The London, Edinburgh, and Dublin Philosophical Magazine and Journal of Science*, 16(104):235–248, 1933.

[57] A. Shapiro, R. Smith, and U. S. N. A. C. for Aeronautics. *Friction Coefficients in the Inlet Length of Smooth Round Tubes*. Number v. 1785 in Friction Coefficients in the Inlet Length of Smooth Round Tubes. National Advisory Committee for Aeronautics, 1948.

[58] D. Smith. The motion of a rotor carried by a flexible shaft in flexible bearings. *Proceedings of the Royal Society of London. Series A, Containing Papers of a Mathematical and Physical Character*, 142(846):92–118, 1933.

[59] L. Tam, A. Przekwas, A. Muszynska, R. Hendricks, M. Braun, and R. Mullen. Numerical and analytical study of fluid dynamic forces in seals and bearings. *Journal of vibration, acoustics, stress, and reliability in design*, 110(3):315–325, 1988.

[60] J. M. Vance, F. Y. Zeidan, and B. Murphy. *Machinery Vibration and Rotordynamics*. Wiley, 1 edition, 5 2010.

[61] D. C. Wilcox. *Turbulence Modeling for CFD (Third Edition)*. D C W Industries, 3rd edition, 11 2006.

[62] Y. Yamada. Resistance of a flow through an annulus with an inner rotating cylinder. *Bulletin of JSME*, 5(18):302–310, 1962.

[63] Z. Yang, L. San Andres, and D. W. Childs. Thermal effects in cryogenic liquid annular sealspart i: Theory and approximate solution. *Journal of tribology*, 115(2):267–276, 1993.

[64] M. Zhang, J. McLean, and D. Childs. Experimental study of the static and dynamic characteristics of a long smooth seal with two-phase, mainly-air mixtures. *Journal of Engineering for Gas Turbines and Power*, 08 2017.

[65] Y. Zhou, L. San Andres, and D. W. Childs. Importance of heat transfer from fluid film to stator in turbulent flow annular seals. *Wear*, 160(2):269–277, 1993.

[66] N. Zirkelback and L. San Andres. Bulk-flow model for the transition to turbulence regime in annular pressure seals. *Tribology transactions*, 39(4):835–842, 1996.

Appendix A

Velocity field in the liquid phase

Axial velocity

Under the assumptions of (i) negligible variation of the fluid height in the seal axial direction ($H = const$), (ii) negligible variation of the interface velocity in the seal axial direction ($V_i = const$, $U_i = const$), and (iii) negligible viscous diffusion in x and y direction, the governing equations for the laminar flow can be written as

$$\frac{\partial v}{\partial y} = 0 \tag{A.1a}$$

$$\frac{\partial^2 v}{\partial z^2} = \frac{1}{\mu}\frac{\partial p}{\partial y} \tag{A.1b}$$

$$v\frac{\partial u}{\partial y} = \nu\frac{\partial^2 u}{\partial z^2} \tag{A.1c}$$

By integrating equations (A.1a-A.1c) with respect to the normalized radial coordinate $\eta = 2z/H_l$ ($-1 < \eta < 1$), the axial velocity filed is obtained

$$v(\eta) = \frac{3V_p}{2}(1-\eta^2) + \frac{V_i}{2}(1-\eta) \tag{A.2}$$

where V_i is the interface meridian velocity and $V_p = -\frac{H_l^2}{12\mu}\frac{\partial p}{\partial y}$ is the pressure driven averaged meridian velocity. The mean liquid velocity in the meridian direction V_l is obtained by integrating (4.9) over the clearance H, then obtaining

$$V_l = V_p + V_i/2 \tag{A.3}$$

In the case of non-constant liquid height (and remembering however that $\frac{\partial H_l}{\partial y} = O(H/L) \ll 1$), (4.9) can be generalized in the form

$$v(\eta) = \frac{3V_p(y)}{2}(1-\eta^2) + \frac{V_i(y)}{2}(1-\eta) \tag{A.4}$$

where $V_p(y)$ is the velocity component that takes into account the pressure gradient effect on the laminar velocity field, while $V_i(y)$ takes into account the drag due to the gas, which flows at higher velocity.

Eqs. (4.9)-(A.2) suggest that, being $V_p > 0$, V_i must be less than $2V_l$. Moreover, at high GVFs, for the gas to exert a drag force on the liquid flow the derivative $\partial v/\partial\eta|_{\eta=-1}$ must be negative. This leads to $V_i > 3/2V_l$. Therefore, the interface axial velocity takes values only in the range

$$1.5 < V_i/V_l < 2 \tag{A.5}$$

Circumferential velocity

Solution of equation (A.1c) is a more challenging task. The circumferential velocity can be divided in an asymptotic term and a transitional one

$$u = u_\infty(\eta) - u_{tr}(\eta, \zeta) \tag{A.6}$$

where $\zeta = 2y/H_l$ is the normalized axial coordinate. The asymptotic profile of the circumferential velocity is derived from (A.1c) by enforcing $\partial/\partial y = 0$ and integrating between the stator and the smooth fluid interface with non-zero circumferential velocity U_i. The linear velocity profile obtained is that corresponding to the classical laminar Couette flow $u_\infty = (1-\zeta)U_i/2$.

About $u_{tr}(\eta,\zeta)$, by introducing the *ansatz*

$$u_{tr}(\eta,\zeta) = Ae^{-\lambda\zeta}\phi(\eta) \tag{A.7}$$

into equation (A.1c), after some algebraic manipulations the following ODE is obtained

$$\phi'' + \lambda\phi\left[\frac{3Re_p}{4}(1-\eta^2) + \frac{Re_i}{4}(1-\eta)\right] = 0 \tag{A.8}$$

where $Re_p = V_pH_l/\nu_l$ and $Re_i = V_iH_l/\nu_l$. (A.8) is a second order ordinary differential equation with variable coefficients. Before investigating the solution of such ODE, the relation between λ, Re_p and Re_i must be evaluated. Such relation has been found empirically by a non linear regression performed on CFD results. By neglecting the circumferential curvature effects, the laminar axis-symmetric flow of the liquid can be compared to a Steady-state laminar channel-like flow with non zero axial and circumferential velocity at the lower wall. CFD laminar steady-state 2D channel flow simulations with non-zero velocity at the "inner wall" have been performed. Constant channel height and "inner wall" velocities have been enforced on the basis of the considerations made in A. The dimensional analysis suggests that the general solution depends on the three groups $Re_a = V_aH/\nu$, $Re_{i,c} = U_iH/\nu$ and $Re_{i,a} = V_iH/\nu$ where V_a, U_w and V_w are respectively, the axial average velocity, the circumferential "inner wall" velocity and the axial "inner wall" velocity.

Through equations (A.1c) and (A.7), the numerical value of λ for every CFD run is obtained by linear regression of $\ln(U_w/2 - U_{H/2}) = \ln U_{tr,0} - \lambda\zeta$, where $U_{H/2}$ is the circumferential velocity at the channel centerline.

At give values of Re_a and $Re_{i,a}$ the computed rate of decay λ was independent on $Re_{i,c}$.

The empirical correlation found between λ, Re_a and $Re_{i,a}$ is

$$\lambda Re_p = \frac{75}{4}\left(2\frac{Re_{i,a}}{Re_p} + 5\right)^{-1} \tag{A.9}$$

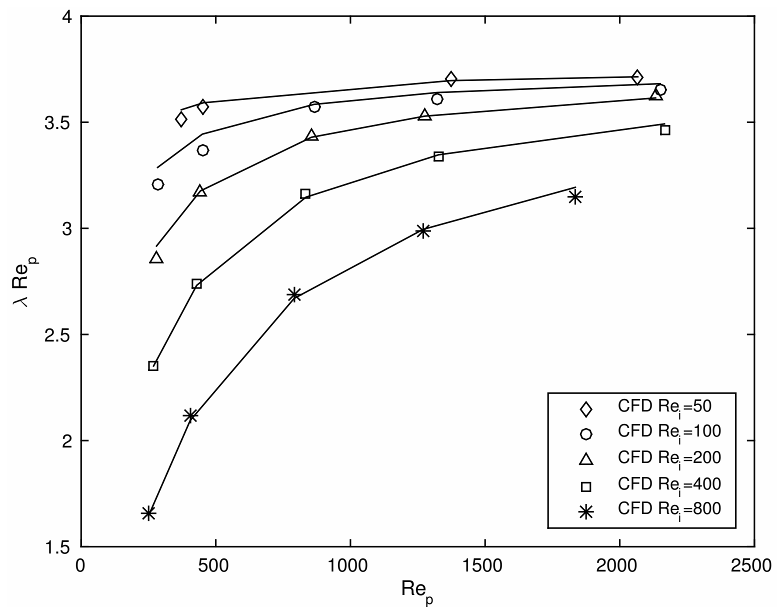

Figure A.1: Comparisons between CFD results and equation (A.9)

Figure A.1 shows that such equation correctly matches CFD results. where $Re_p = Re_a - Re_{i,a}/2$. In the following, Re_i will indicate the axial interface velocity Reynolds number $Re_{i,a}$.

Therefore, by introducing (A.9)) into (A.8), the ODE simplifies in

$$\phi'' + \phi\left[\frac{225}{16}\left(\frac{1}{5+2\chi}\right)(1-\eta^2) + \frac{75}{16}\chi\left(\frac{1}{5+2\chi}\right)(1-\eta)\right] = 0 \qquad \text{(A.10)}$$

being $\chi = Re_i/Re_p$. Equation (A.10) is a sort of "quantum oscillator"-like equation, which reduces to the quantum oscillator one for $\chi = 0$.

From equation (A.5) it is easy to demonstrate that

$$\chi = V_i/V_p > 6 \qquad \text{(A.11)}$$

Eq. (A.10) shows that the only parameter affecting the radial profile of the transitional circumferential velocity is the ratio χ. The module A of u_{tr} can be obtained by the inlet swirl boundary condition

$$1/2\int_{-1}^{1} d\eta\left[u_\infty(\eta) - u_{tr}(\eta,0)\right] = U_i/2 - \frac{A}{2}\int_{-1}^{1}\phi(\eta)d\eta = U_{inlet} \qquad \text{(A.12)}$$

If $\phi(\eta)$ is defined so as to have $\int_{-1}^{1}\phi(\eta)d\eta = 2$ the inlet swirl condition becomes

$$U_i/2 - A = U_{inlet} \qquad \text{(A.13)}$$

In practice, the above boundary condition requires the inlet values of the swirl (circumferential) interface velocity U_i and the average inlet pre-swirl U_{inlet} that are usually unavailable (they depends on the geometry of the inlet chamber); the two values therefore should be treated as calibration constants.

In the stratified bulk model, the bulk circumferential velocity is obtained by integrating (4.12) over the liquid height:

$$U_l = 1/2 \int_{-1}^{1} u(\eta, \zeta) d\eta = U_i/2 - U_{tr} \tag{A.14}$$

where is $U_{tr} = Ae^{-\lambda\zeta}$.

Appendix B

Homogeneous bulk flow model predictions vs. experiments

Appendix B

Homogeneous bulk flow model predictions vs. experiments

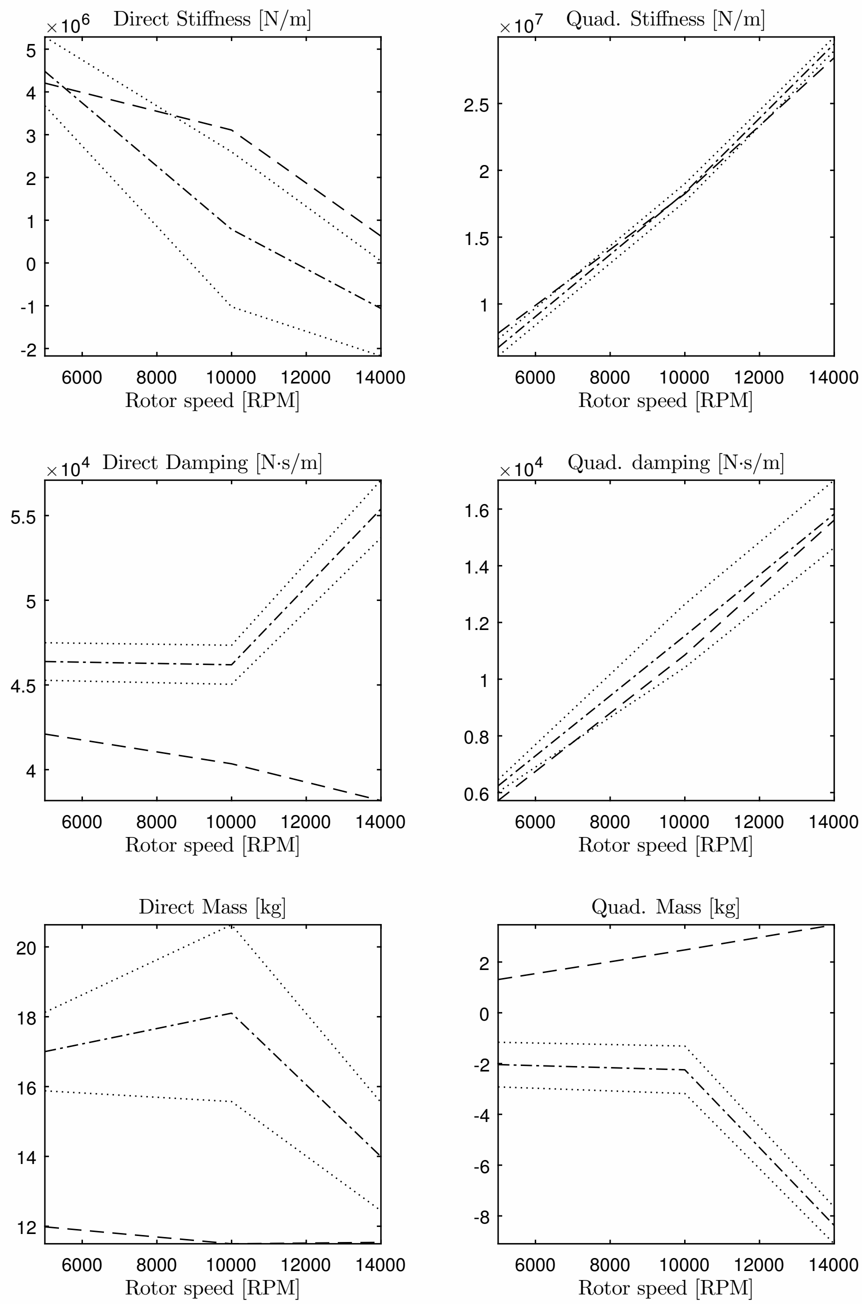

Figure B.1: Stiffness variation with the rotor speed Ω. inlet $GVF = 4.2\%$ $\Delta P_0 = 21.4bar$, D=89cm, L/R=1.5, $H = 0.18mm$, $\mu = 0.00364Pl$, $\rho = 900kg/m^3$, $\zeta_i = 0.2$, $\zeta_o = 1$. -- dashed line: bulk flow model, dotted lines ⋯⋯: measurements bounds (95% of confidence), dot dashed line: measurement average.

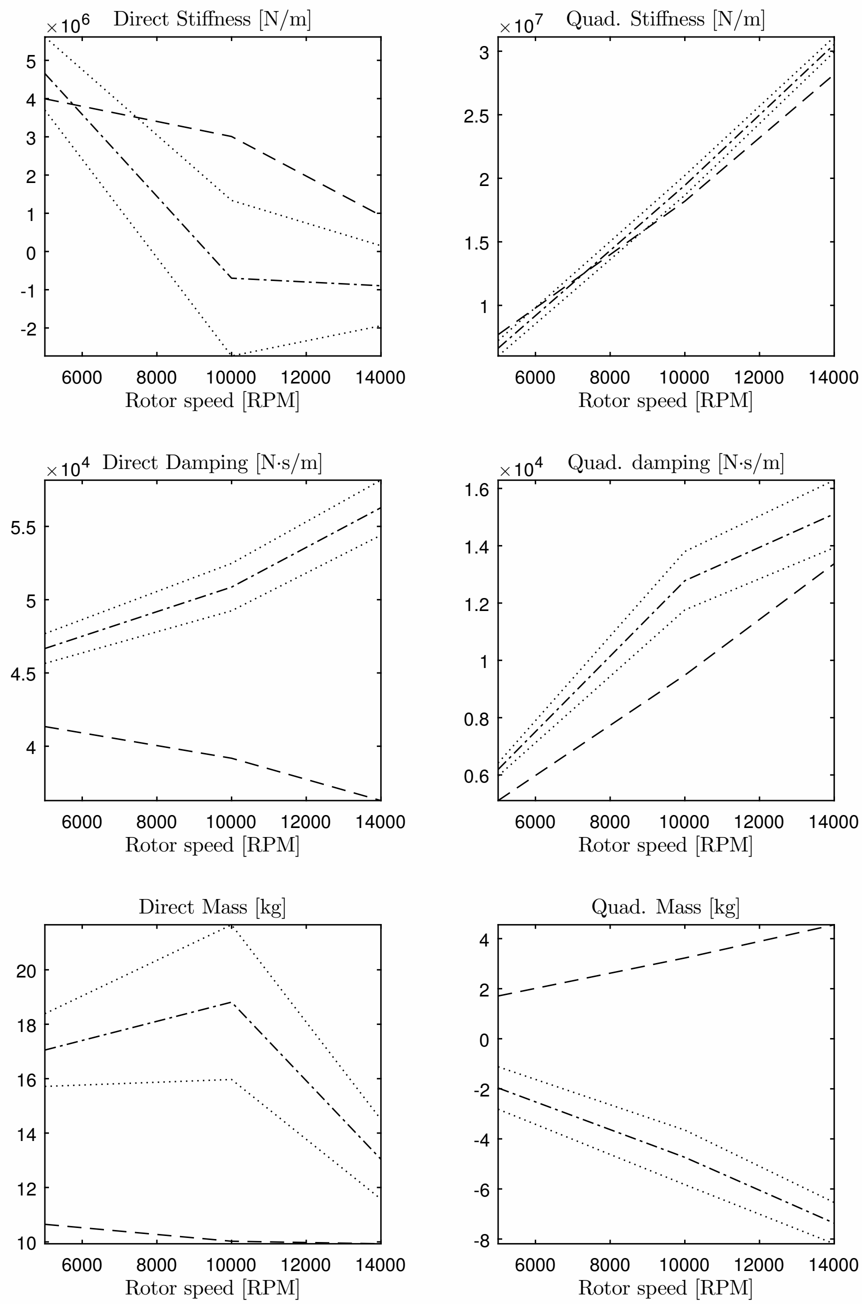

Figure B.2: Stiffness variation with the rotor speed Ω. inlet $GVF = 6.2\%$ $\Delta P_0 = 21.4bar$, D=89cm, L/R=1.5, $H = 0.18mm$, $\mu = 0.00364Pl$, $\rho = 900kg/m^3$, $\zeta_i = 0.2$, $\zeta_o = 1$. – – dashed line: bulk flow model, dotted lines ⋯⋯: measurements bounds (95% of confidence), dot dashed line: measurement average.

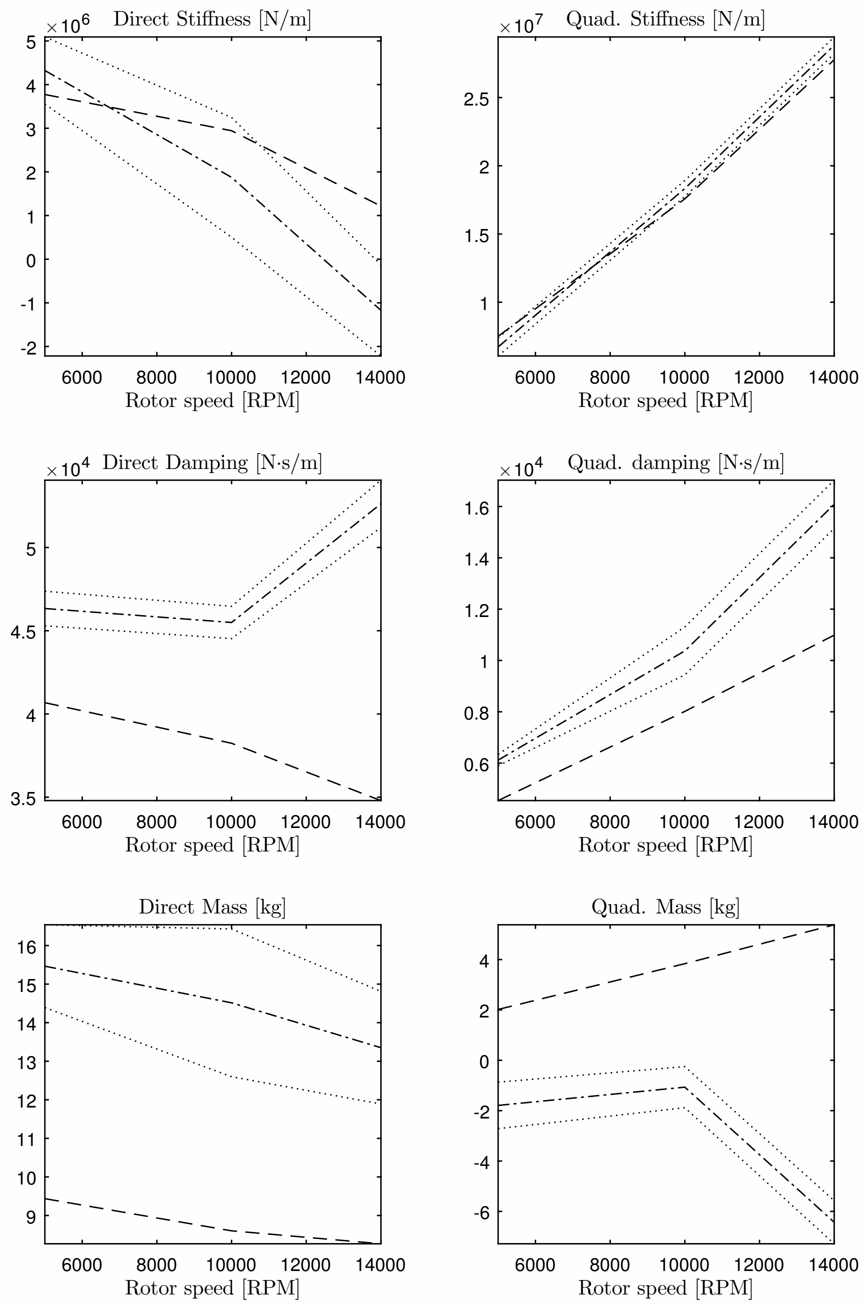

Figure B.3: Stiffness variation with the rotor speed Ω. inlet $GVF = 8.2\%$ $\Delta P_0 = 21.4bar$, D=89cm, L/R=1.5, $H = 0.18mm$, $\mu = 0.00364Pl$, $\rho = 900kg/m^3$, $\zeta_i = 0.2$, $\zeta_o = 1$. - - dashed line: bulk flow model, dotted lines ⋯⋯: measurements bounds (95% of confidence), dot dashed line: measurement average.

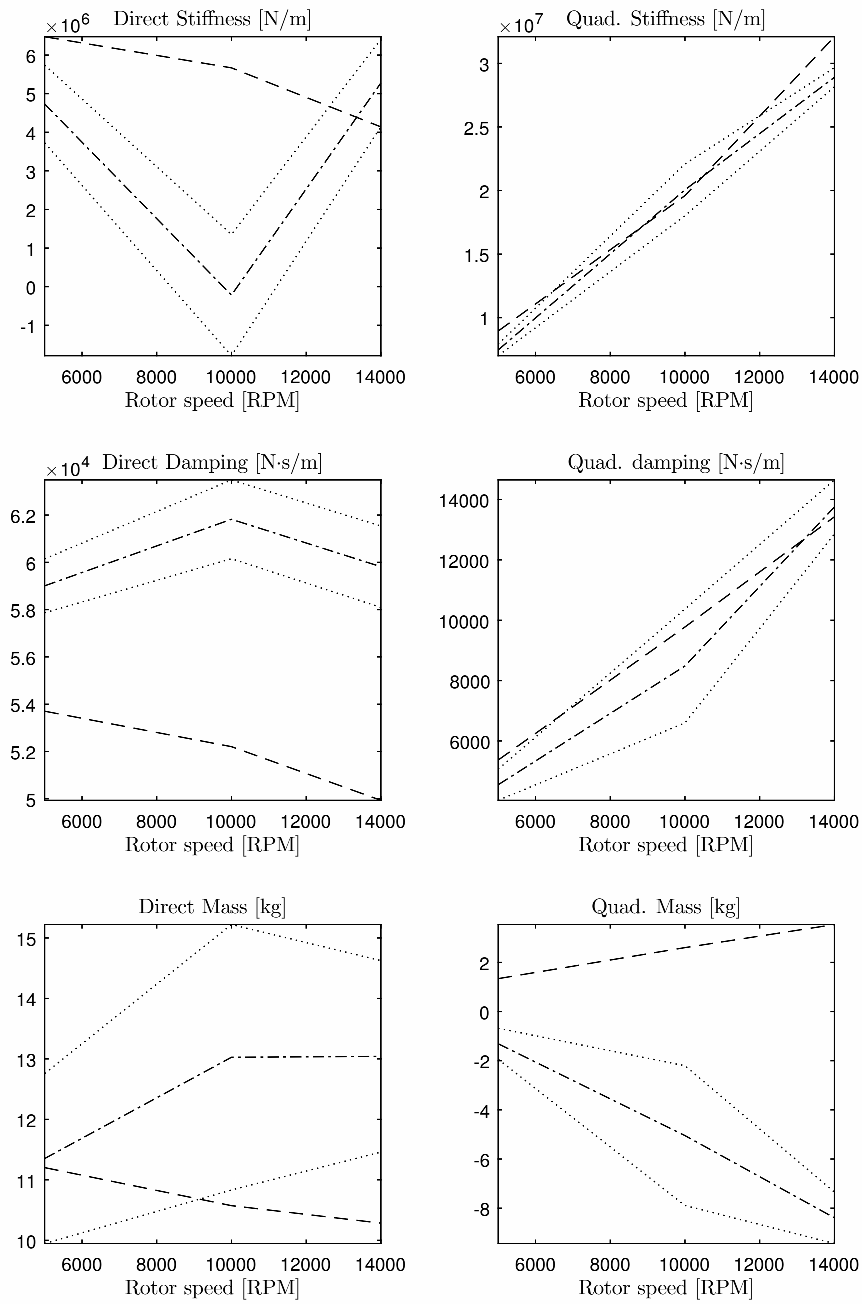

Figure B.4: Stiffness variation with the rotor speed Ω. inlet $GVF = 4.2\%$ $\Delta P_0 = 35.2bar$, D=89cm, L/R=1.5, $H = 0.18mm$, $\mu = 0.00364Pl$, $\rho = 900kg/m^3$, $\zeta_i = 0.2$, $\zeta_o = 1$. - - dashed line: bulk flow model, dotted lines ⋯⋯: measurements bounds (95% of confidence), dot dashed line: measurement average.

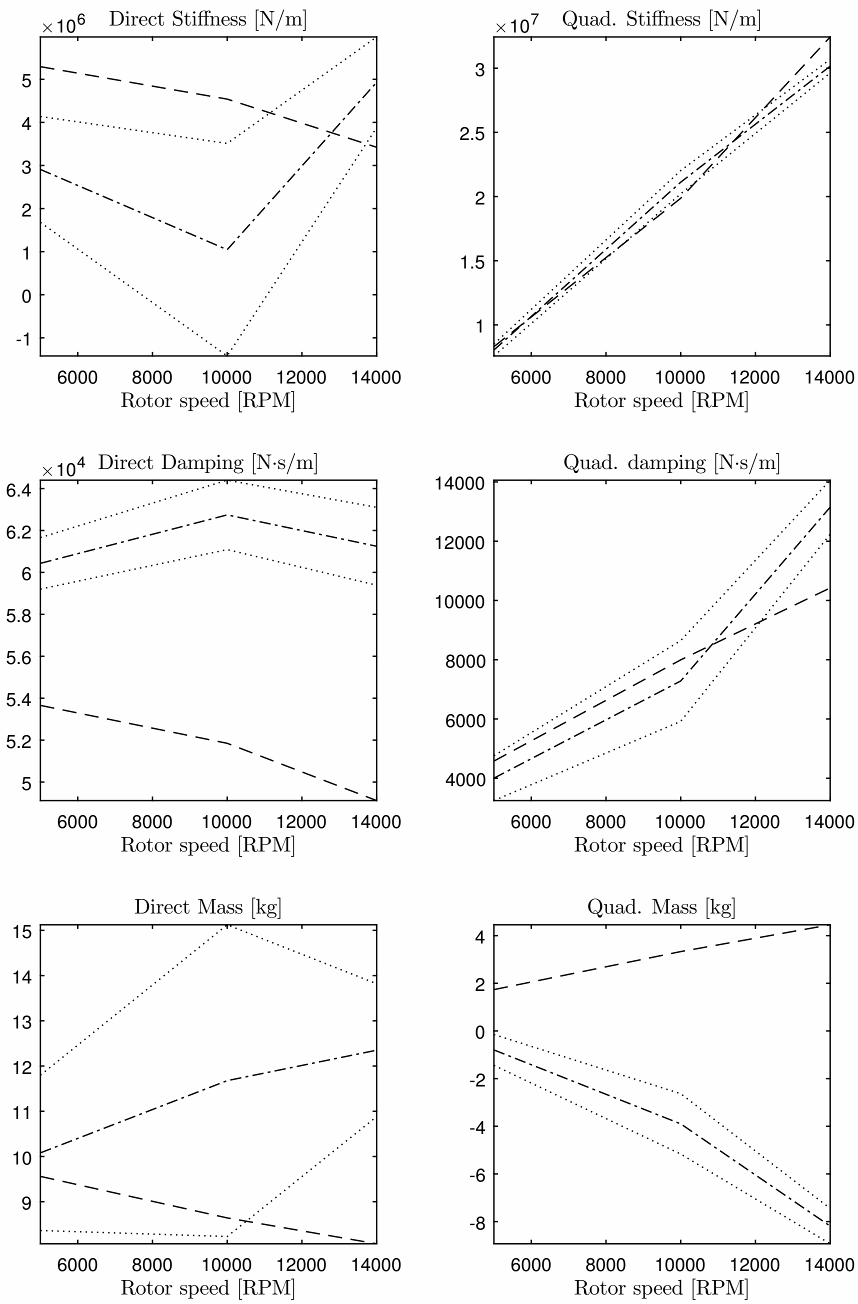

Figure B.5: Stiffness variation with the rotor speed Ω. inlet $GVF = 6.2\%$ $\Delta P_0 = 35.2bar$, D=89cm, L/R=1.5, $H = 0.18mm$, $\mu = 0.00364Pl$, $\rho = 900kg/m^3$, $\zeta_i = 0.2$, $\zeta_o = 1$. - - dashed line: bulk flow model, dotted lines ⋯⋯: measurements bounds (95% of confidence), dot dashed line: measurement average.

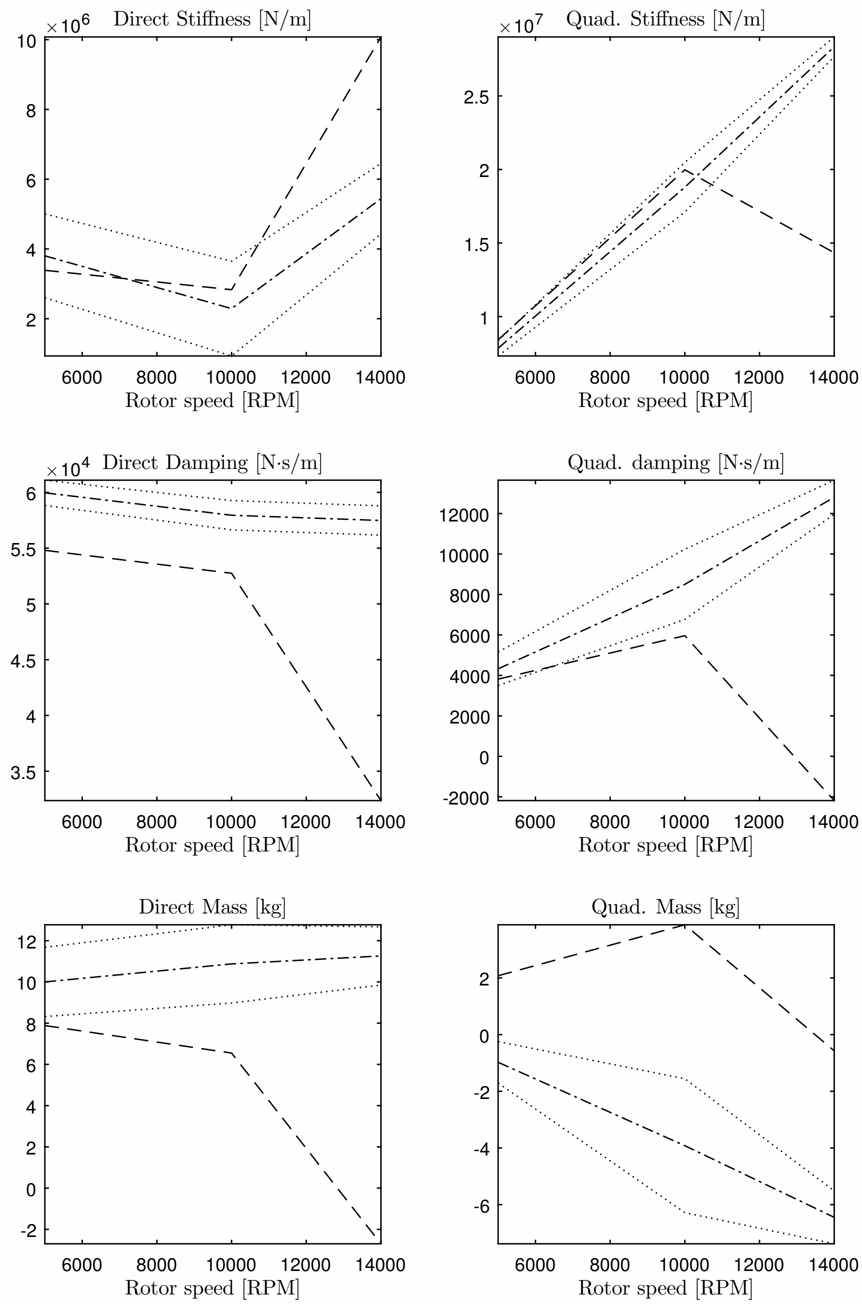

Figure B.6: Stiffness variation with the rotor speed Ω. inlet $GVF = 8.2\%$ $\Delta P_0 = 35.2bar$, D=89cm, L/R=1.5, $H = 0.18mm$, $\mu = 0.00364Pl$, $\rho = 900kg/m^3$, $\zeta_i = 0.2$, $\zeta_o = 1$. $--$ dashed line: bulk flow model, dotted lines ⋯⋯: measurements bounds (95% of confidence), dot dashed line: measurement average.

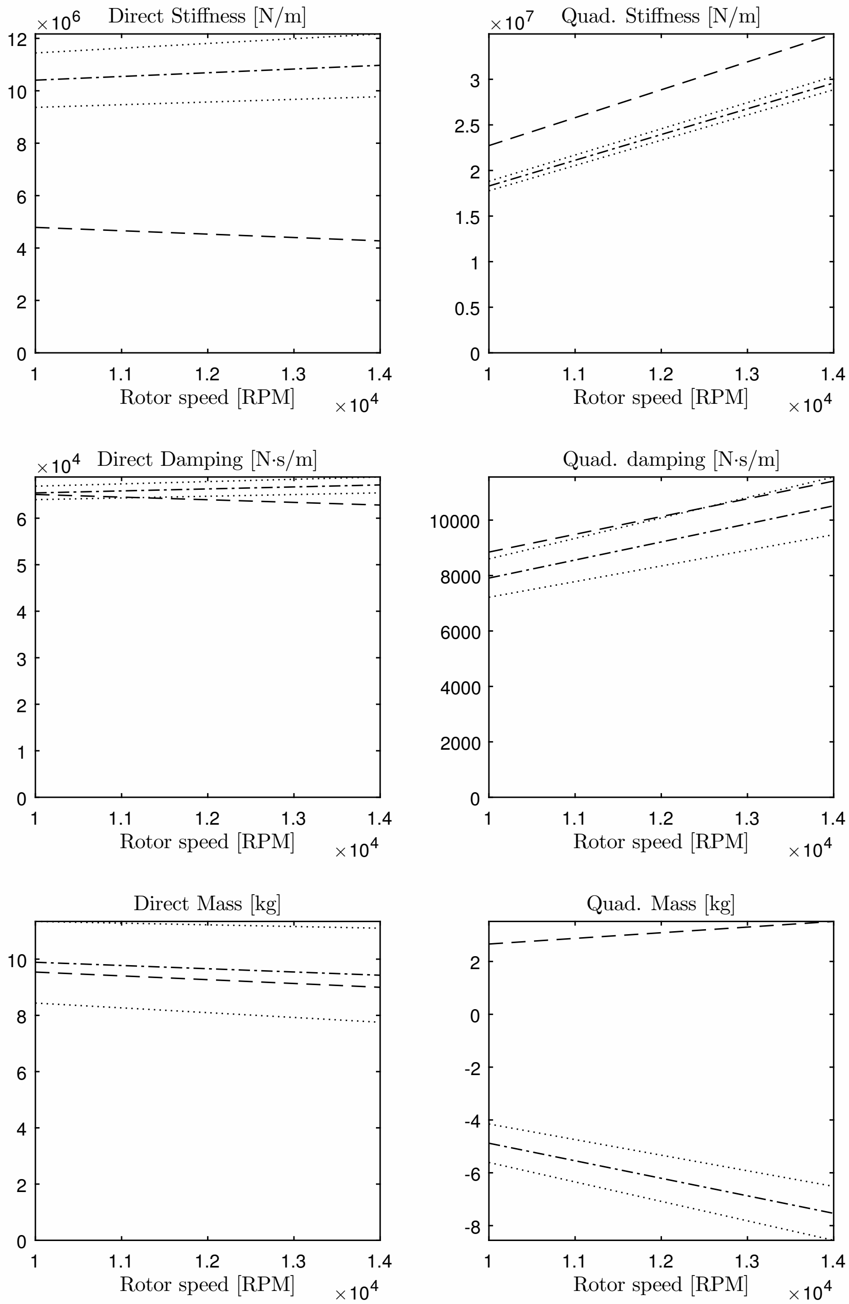

Figure B.7: Stiffness variation with the rotor speed Ω. inlet $GVF = 4.2\%$ $\Delta P_0 = 49bar$, D=89cm, L/R=1.5, $H = 0.18mm$, $\mu = 0.00364Pl$, $\rho = 900kg/m^3$, $\zeta_i = 0.2$, $\zeta_o = 1$. - - dashed line: bulk flow model, dotted lines ⋯⋯: measurements bounds (95% of confidence), dot dashed line: measurement average.

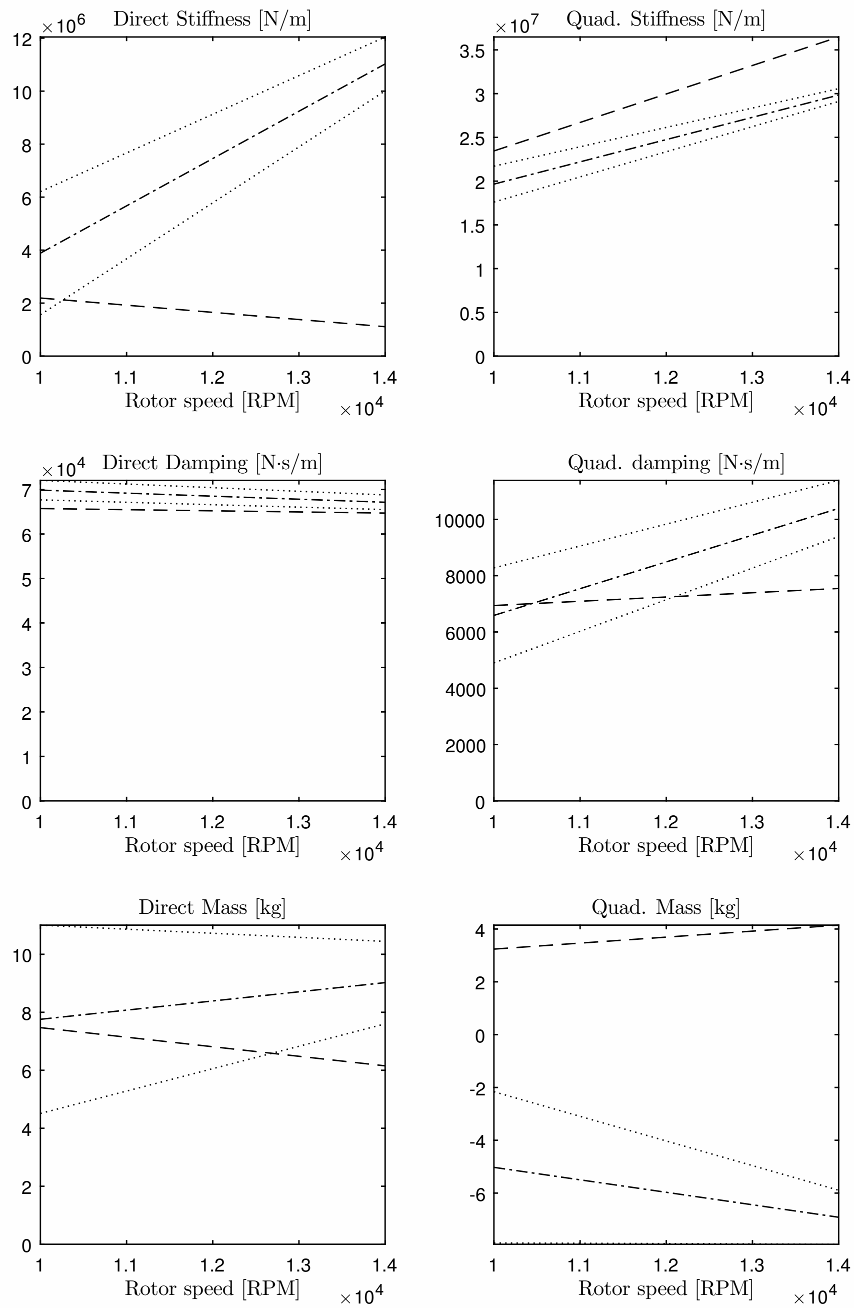

Figure B.8: Stiffness variation with the rotor speed Ω. inlet $GVF = 6.2\%$ $\Delta P_0 = 49bar$, D=89cm, L/R=1.5, $H = 0.18mm$, $\mu = 0.00364Pl$, $\rho = 900kg/m^3$, $\zeta_i = 0.2$, $\zeta_o = 1$. -- dashed line: bulk flow model, dotted lines ⋯⋯: measurements bounds (95% of confidence), dot dashed line: measurement average.

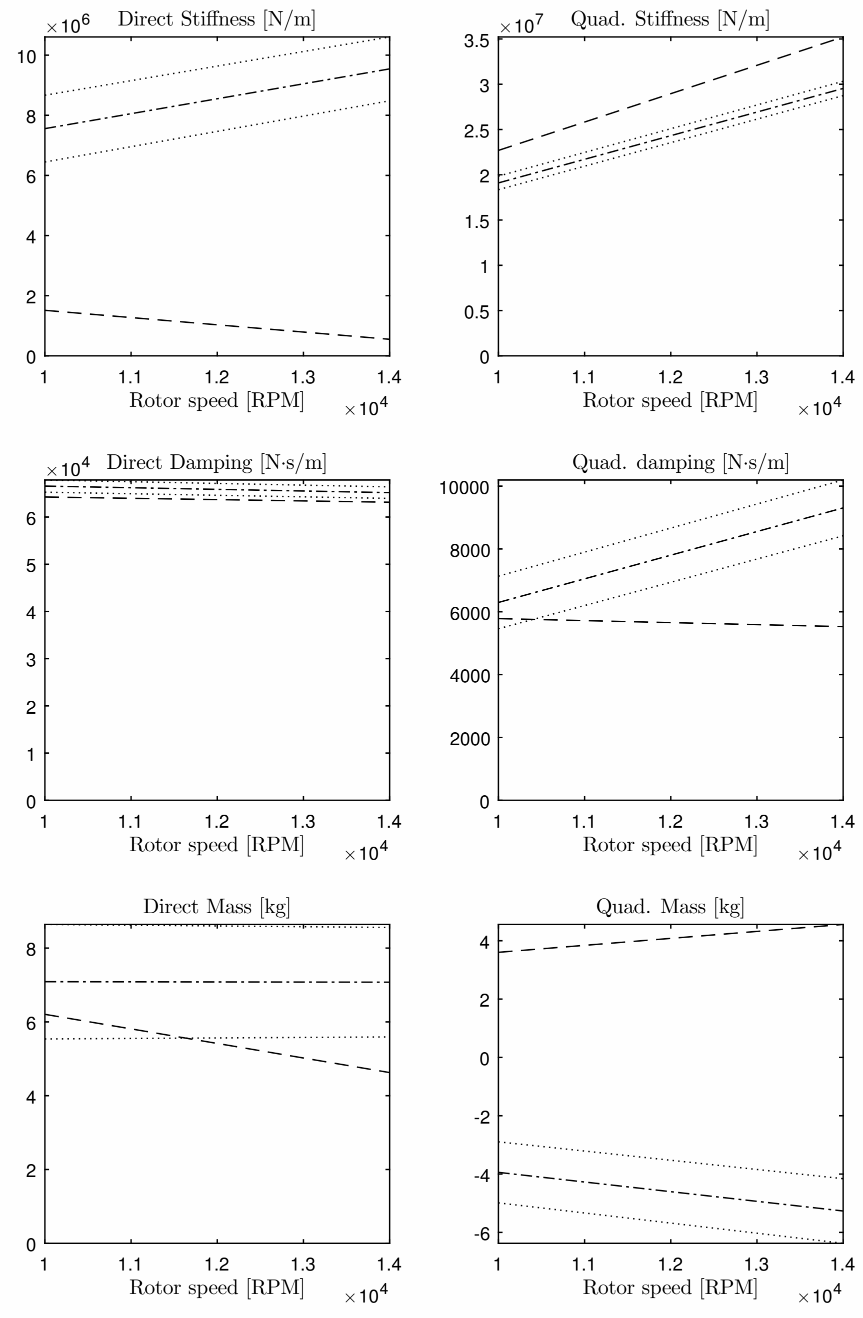

Figure B.9: Stiffness variation with the rotor speed Ω. inlet $GVF = 8.2\%$ $\Delta P_0 = 49bar$, D=89cm, L/R=1.5, $H = 0.18mm$, $\mu = 0.00364Pl$, $\rho = 900kg/m^3$, $\zeta_i = 0.2$, $\zeta_o = 1$. - - dashed line: bulk flow model, dotted lines ············: measurements bounds (95% of confidence), dot dashed line: measurement average.

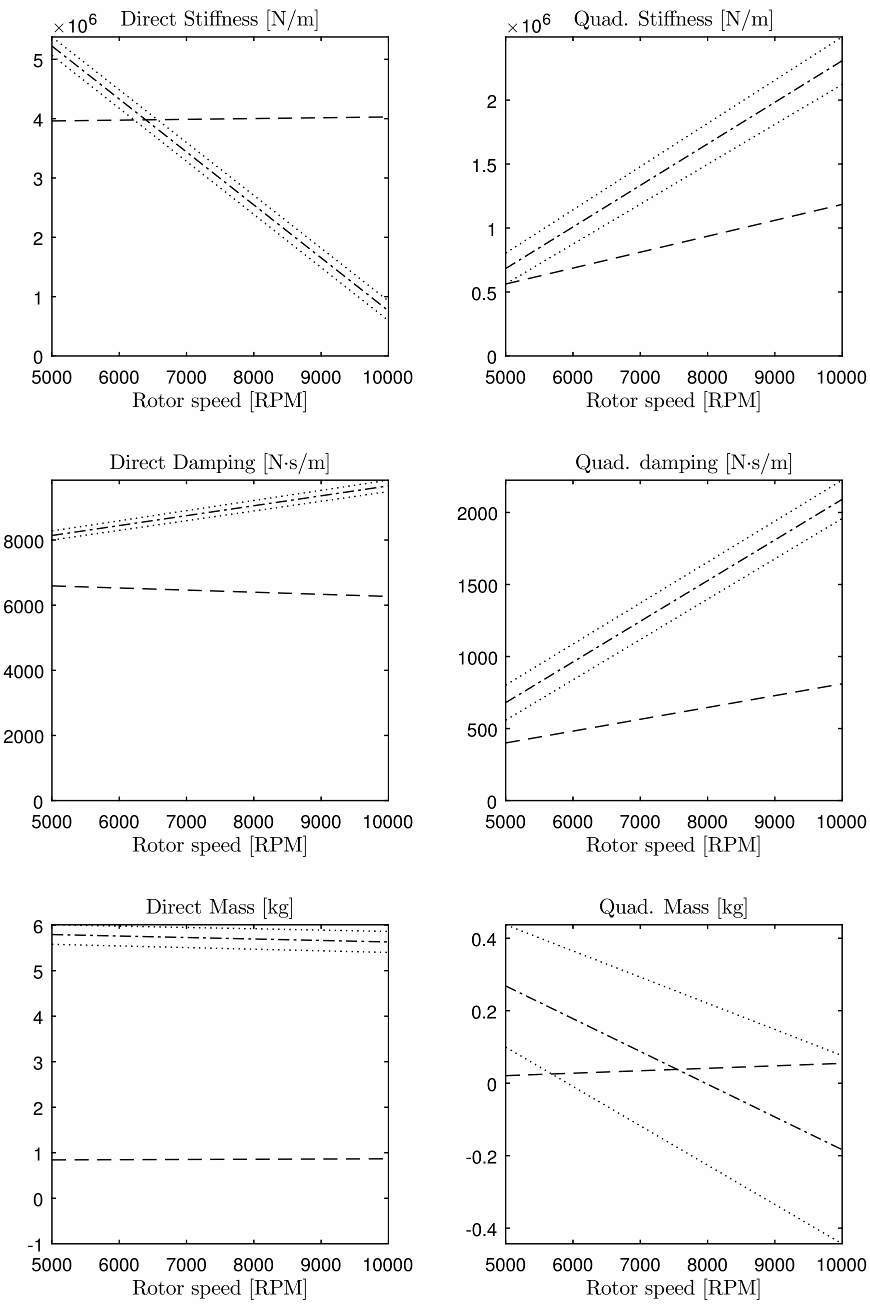

Figure B.10: Stiffness variation with the rotor speed Ω. inlet $GVF = 3\%$ $\Delta P_0 = 17.2bar$, D=89cm, L/R=0.58, $H = 0.18mm$, $\mu = 0.00364Pl$, $\rho = 900kg/m^3$, $\zeta_i = 0.2$, $\zeta_o = 1$. - - dashed line: bulk flow model, dotted lines ⋯⋯: measurements bounds (95% of confidence), dot dashed line: measurement average.

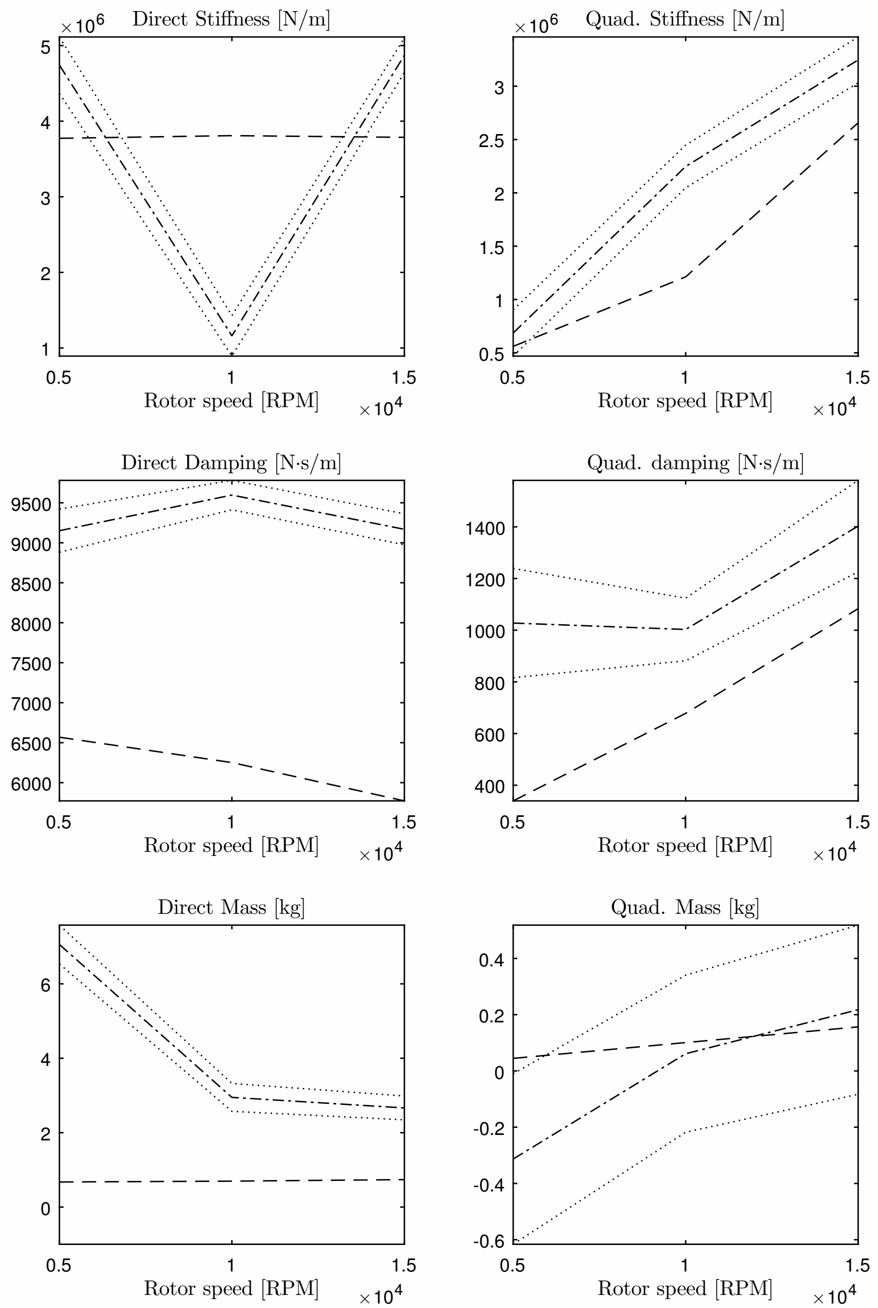

Figure B.11: Stiffness variation with the rotor speed Ω. inlet $GVF = 6\%$ $\Delta P_0 = 17.2bar$, D=89cm, L/R=0.58, $H = 0.18mm$, $\mu = 0.00364Pl$, $\rho = 900kg/m^3$, $\zeta_i = 0.2$, $\zeta_o = 1$. – – dashed line: bulk flow model, dotted lines ··········: measurements bounds (95% of confidence), dot dashed line: measurement average.

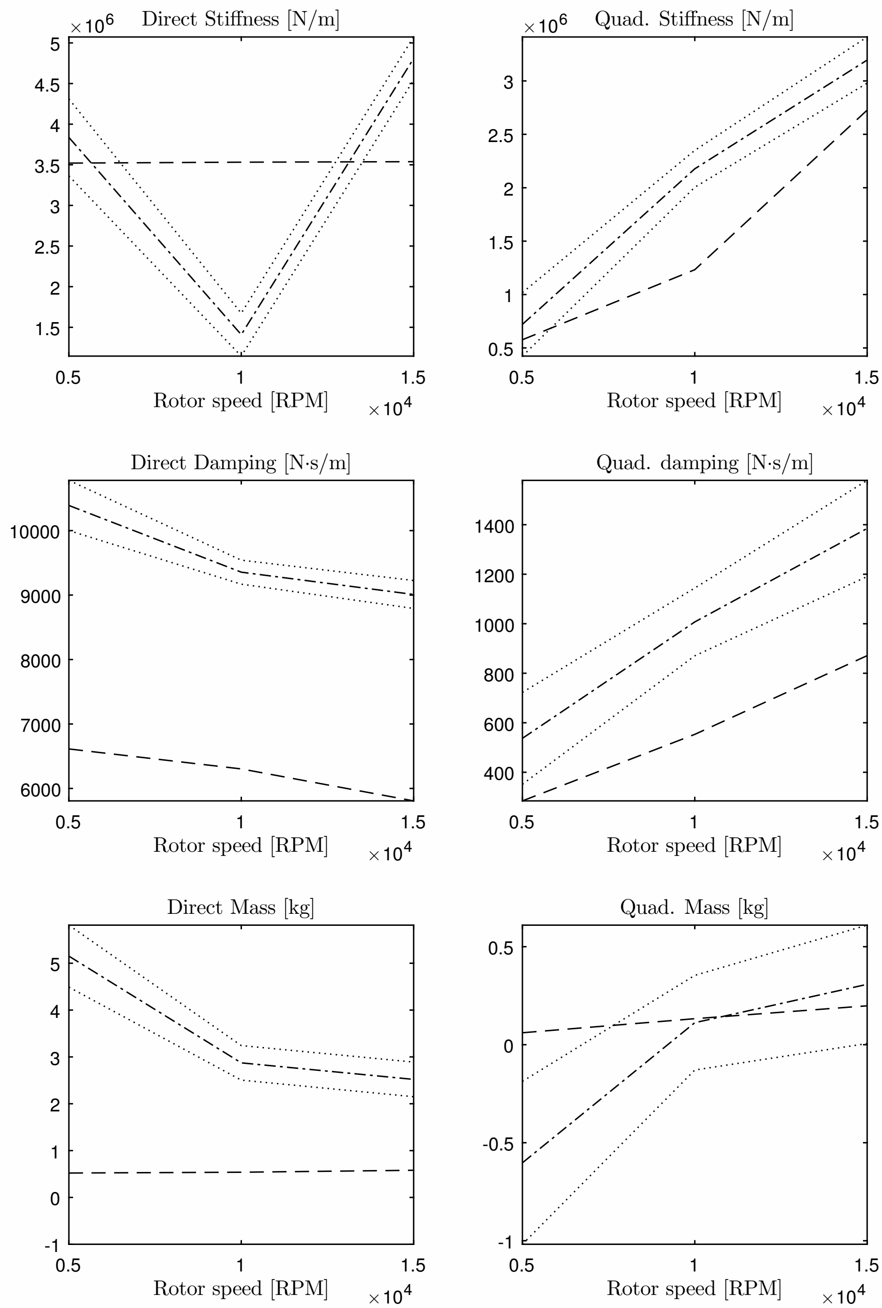

Figure B.12: Stiffness variation with the rotor speed Ω. inlet $GVF = 8.9\%$ $\Delta P_0 = 17.2bar$, D=89cm, L/R=0.58, $H = 0.18mm$, $\mu = 0.00364Pl$, $\rho = 900kg/m^3$, $\zeta_i = 0.2$, $\zeta_o = 1$. - - dashed line: bulk flow model, dotted lines ··········: measurements bounds (95% of confidence), dot dashed line: measurement average.

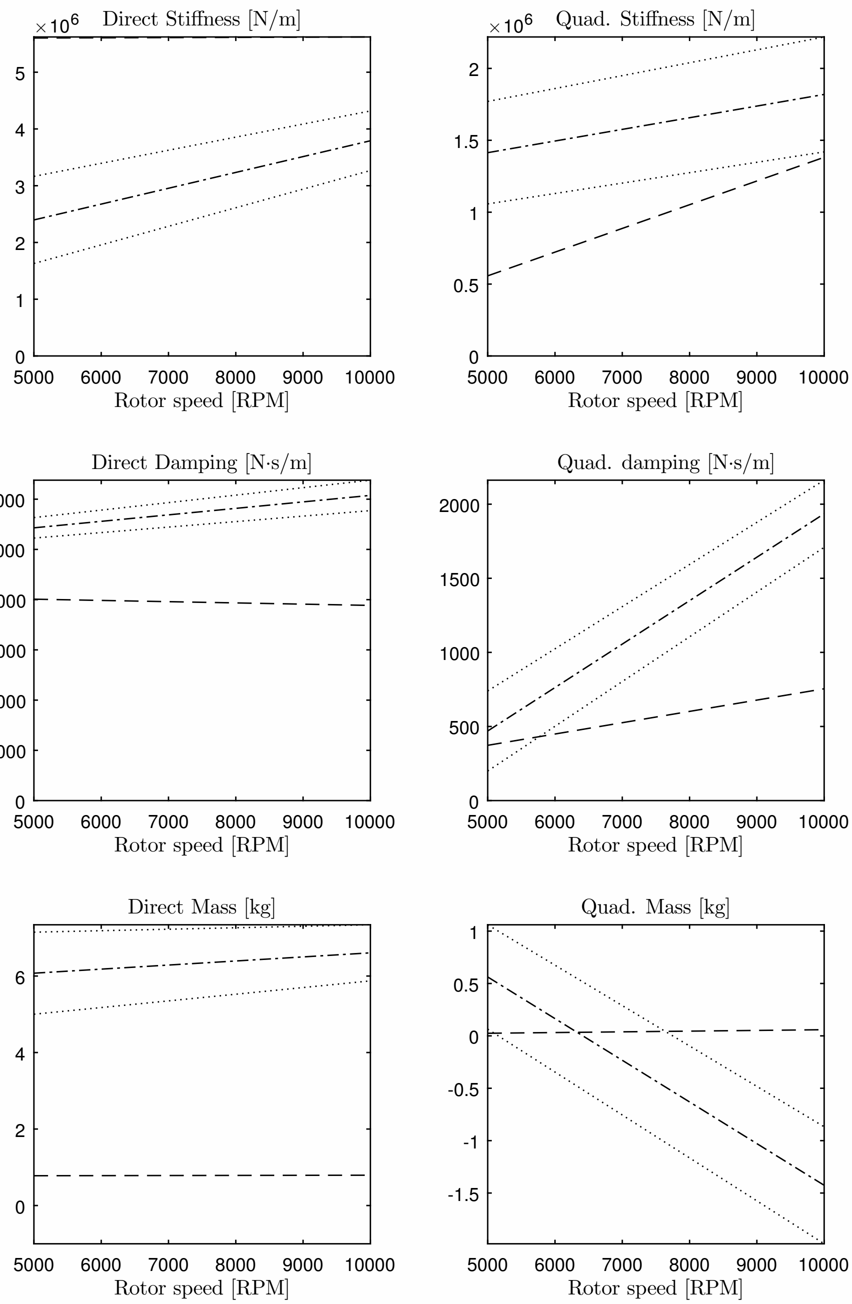

Figure B.13: Stiffness variation with the rotor speed Ω. inlet $GVF = 3\%$ $\Delta P_0 = 24.8bar$, D=89cm, L/R=0.58, $H = 0.18mm$, $\mu = 0.00364Pl$, $\rho = 900kg/m^3$, $\zeta_i = 0.2$, $\zeta_o = 1$. – – dashed line: bulk flow model, dotted lines ··········: measurements bounds (95% of confidence), dot dashed line: measurement average.

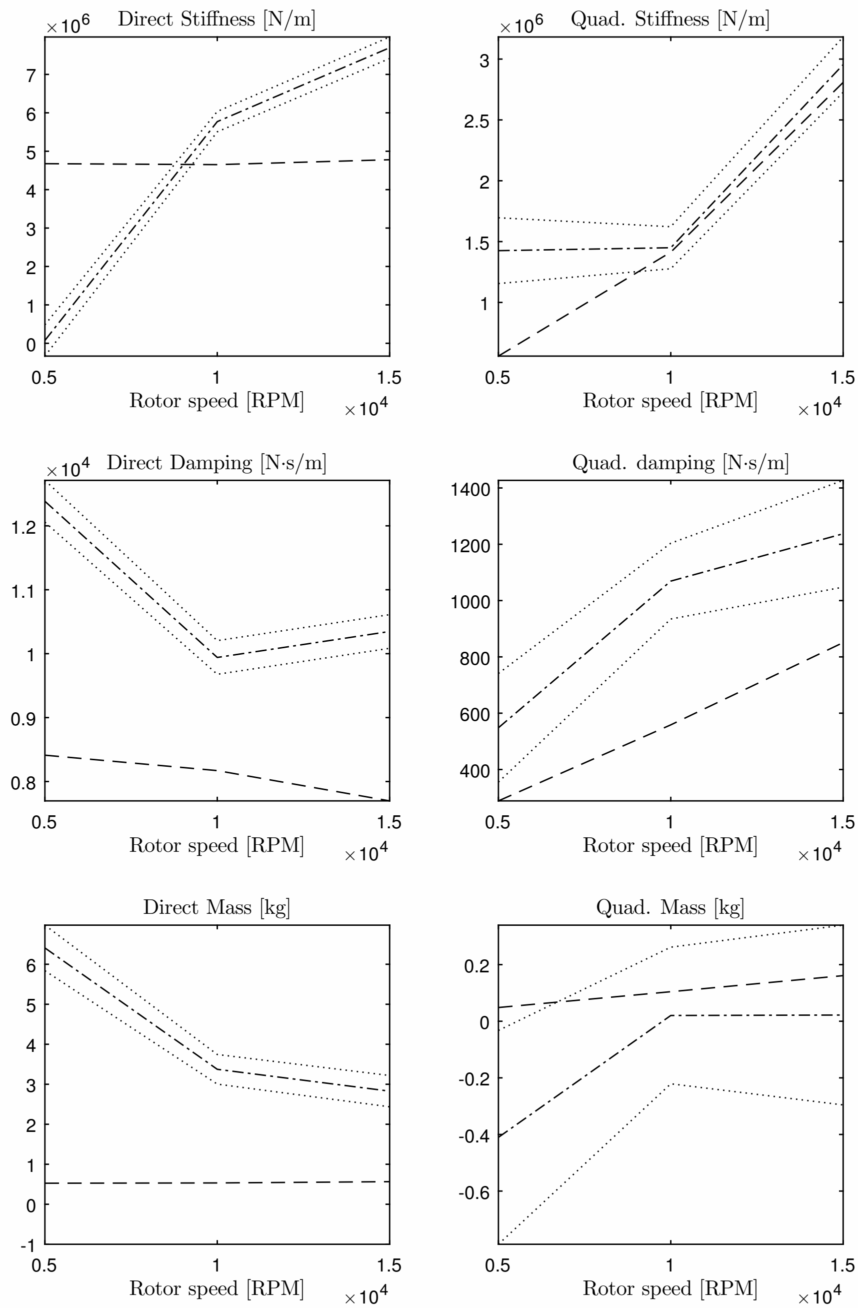

Figure B.14: Stiffness variation with the rotor speed Ω. inlet $GVF = 6\%$ $\Delta P_0 = 24.8bar$, D=89cm, L/R=0.58, $H = 0.18mm$, $\mu = 0.00364Pl$, $\rho = 900kg/m^3$, $\zeta_i = 0.2$, $\zeta_o = 1$. - - dashed line: bulk flow model, dotted lines ⋯⋯: measurements bounds (95% of confidence), dot dashed line: measurement average.

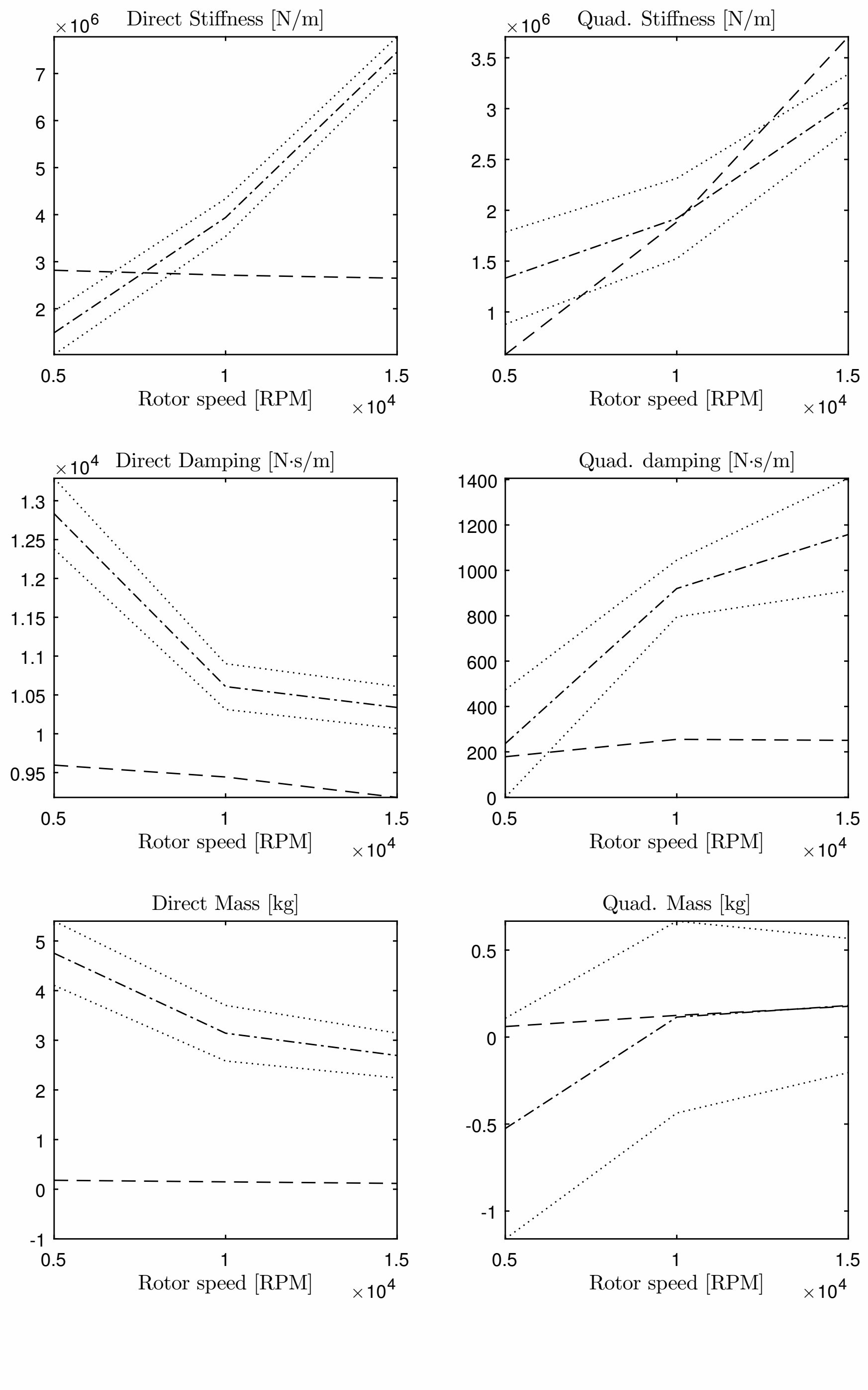

Figure B.15: Stiffness variation with the rotor speed Ω. inlet $GVF = 8.9\%$ $\Delta P_0 = 24.8bar$, D=89cm, L/R=0.58, $H = 0.18mm$, $\mu = 0.00364Pl$, $\rho = 900kg/m^3$, $\zeta_i = 0.2$, $\zeta_o = 1$. - - dashed line: bulk flow model, dotted lines ············: measurements bounds (95% of confidence), dot dashed line: measurement average.

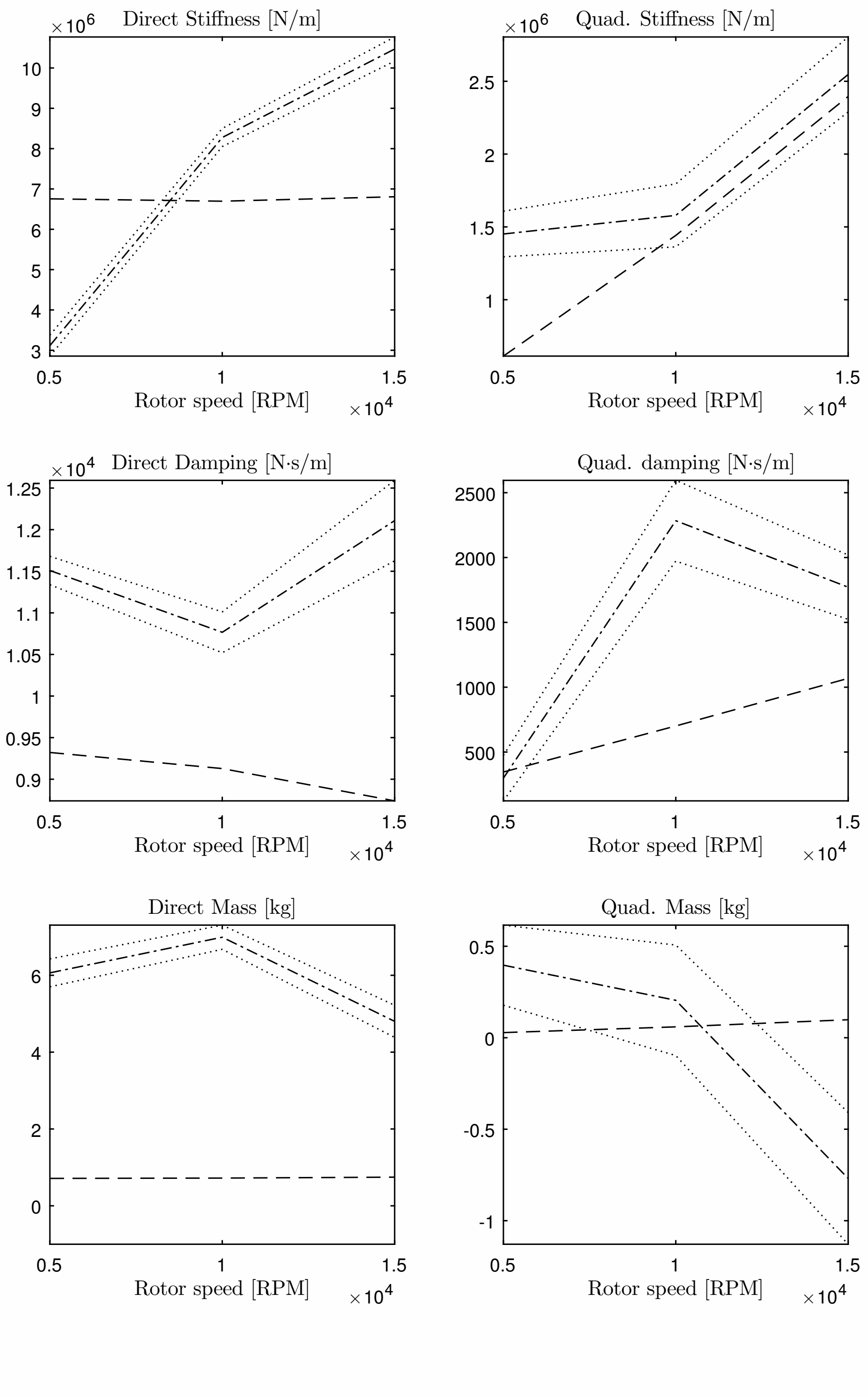

Figure B.16: Stiffness variation with the rotor speed Ω. inlet $GVF = 3\%$ $\Delta P_0 = 31.7bar$, D=89cm, L/R=0.58, $H = 0.18mm$, $\mu = 0.00364Pl$, $\rho = 900kg/m^3$, $\zeta_i = 0.2$, $\zeta_o = 1$. - - dashed line: bulk flow model, dotted lines ··········: measurements bounds (95% of confidence), dot dashed line: measurement average.

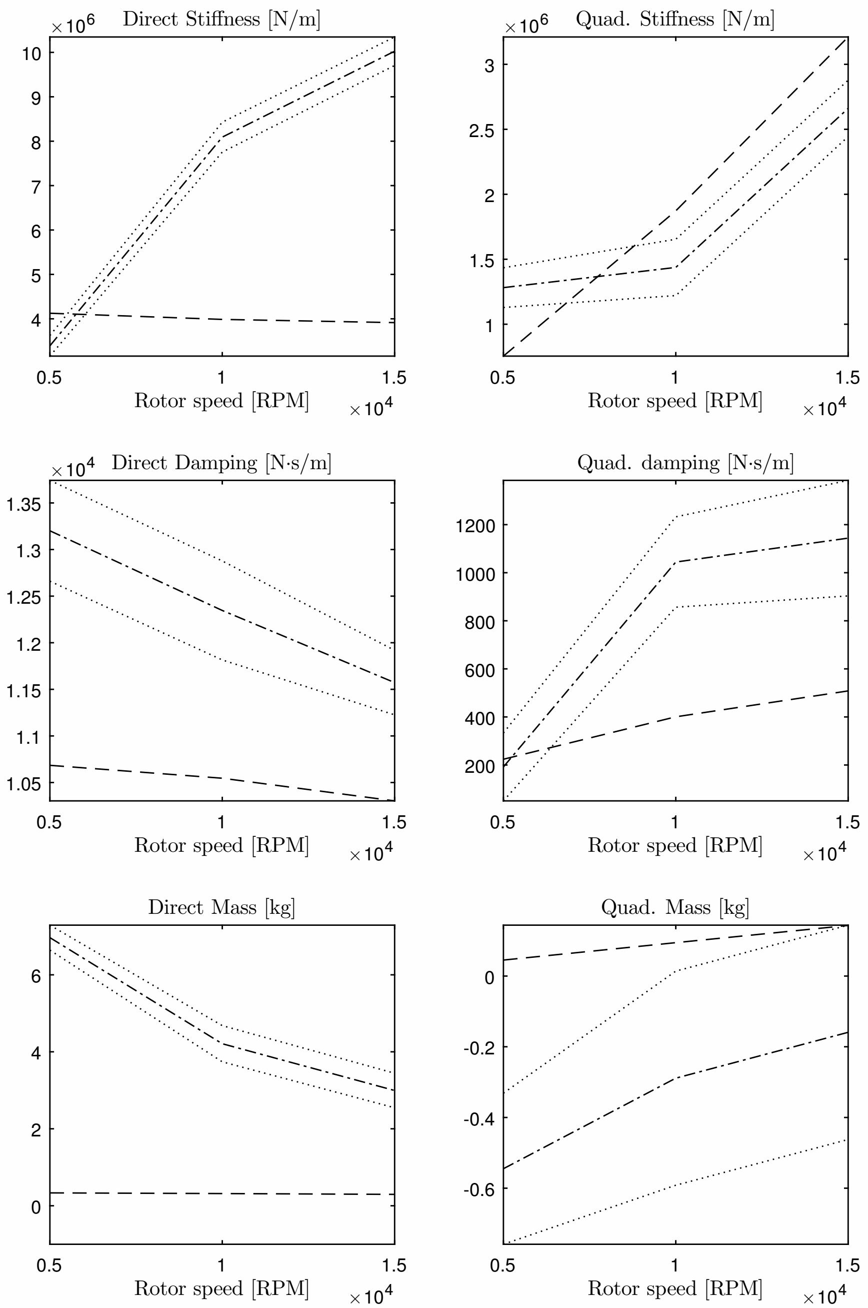

Figure B.17: Stiffness variation with the rotor speed Ω. inlet $GVF = 6\%$ $\Delta P_0 = 31.7bar$, D=89cm, L/R=0.58, $H = 0.18mm$, $\mu = 0.00364Pl$, $\rho = 900kg/m^3$, $\zeta_i = 0.2$, $\zeta_o = 1$. - - dashed line: bulk flow model, dotted lines ··········: measurements bounds (95% of confidence), dot dashed line: measurement average.

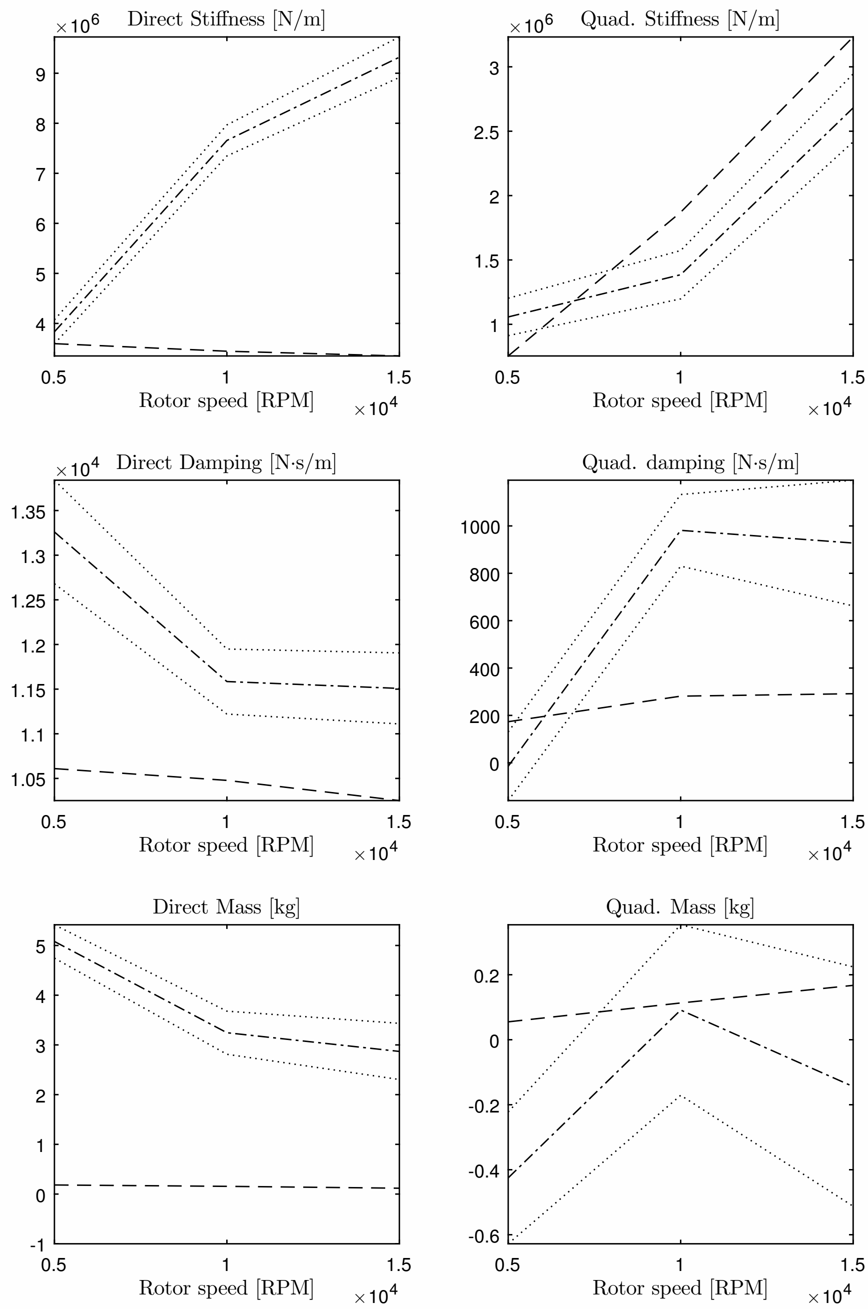

Figure B.18: Stiffness variation with the rotor speed Ω. inlet $GVF = 8.9\%$ $\Delta P_0 = 31.7bar$, D=89cm, L/R=0.58, $H = 0.18mm$, $\mu = 0.00364Pl$, $\rho = 900kg/m^3$, $\zeta_i = 0.2$, $\zeta_o = 1$. - - dashed line: bulk flow model, dotted lines ⋯⋯: measurements bounds (95% of confidence), dot dashed line: measurement average.

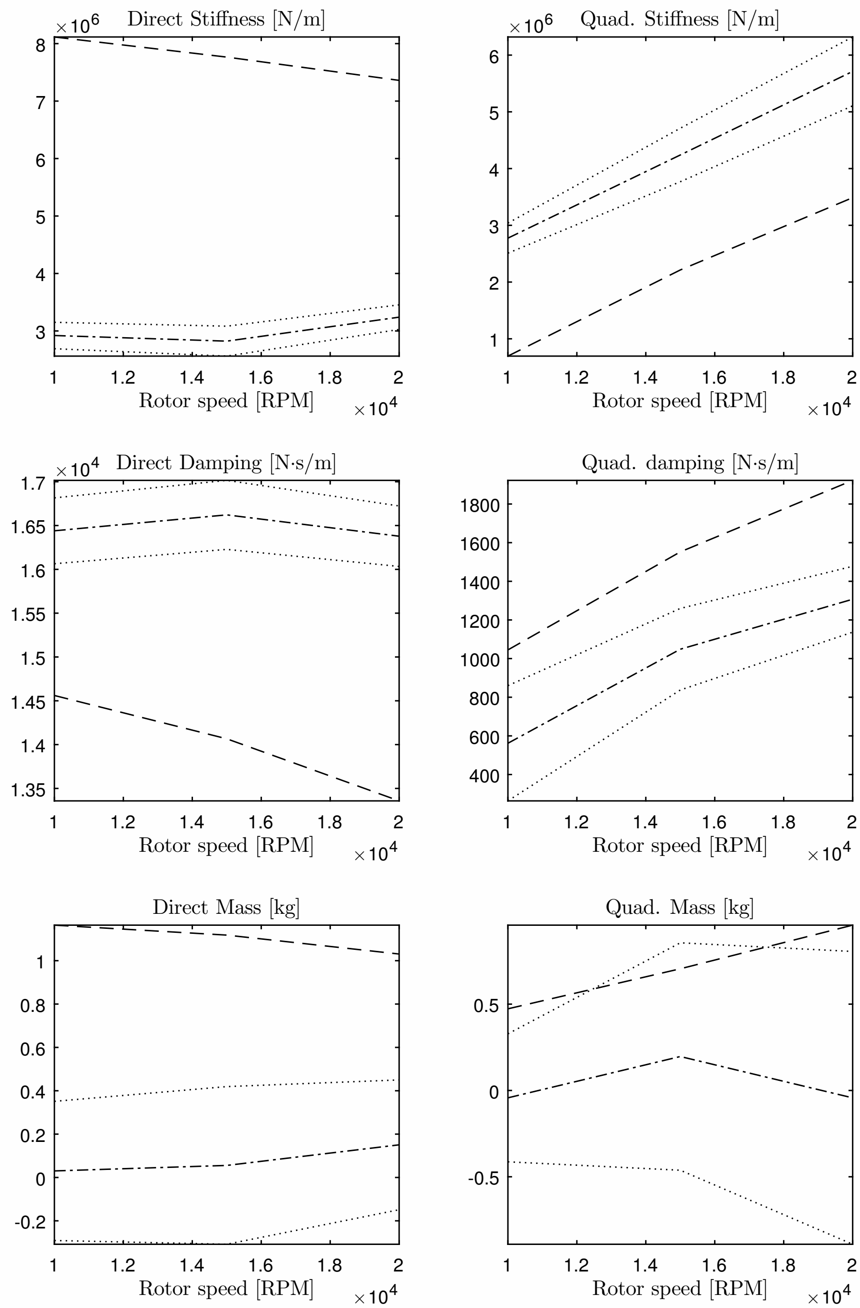

Figure B.19: Stiffness variation with the rotor speed Ω. inlet $GVF = 92.6\%$, $P_{0,inlet} = 61.2bar$,$P_{0,outlet}/P_{0,inlet} = 0.6$, D=89cm, L/R=1.5, $H = 0.18mm$, $\mu = 0.00364Pl$, $\rho = 900kg/m^3$, $\zeta_i = 0.2$, $\zeta_o = 1$. - - dashed line: bulk flow model, dotted lines ⋯⋯: measurements bounds (95% of confidence), -· dot dashed line: measurement average.

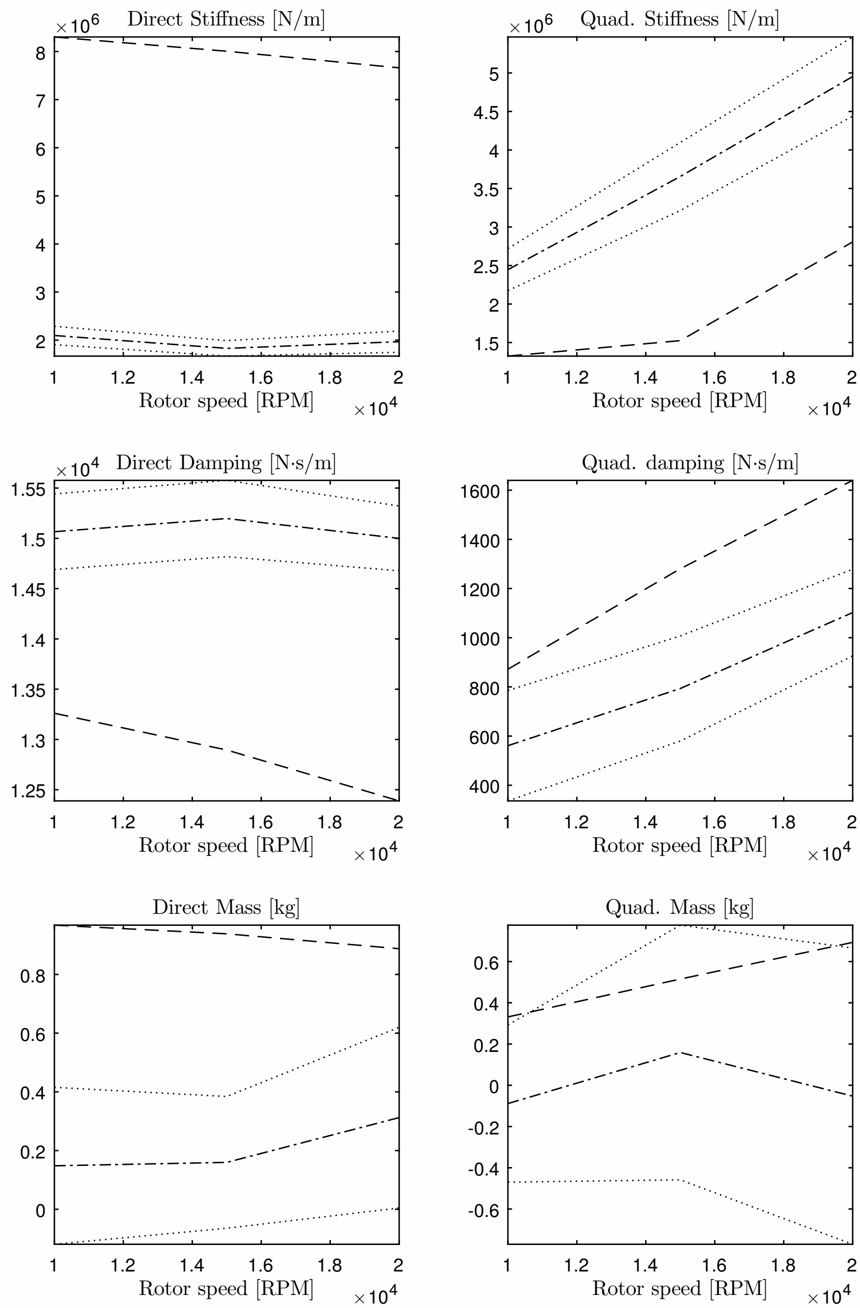

Figure B.20: Stiffness variation with the rotor speed Ω. inlet $GVF = 95.5\%$, $P_{0,inlet} = 61.2bar$,$P_{0,outlet}/P_{0,inlet} = 0.6$, D=89cm, L/R=1.5, $H = 0.18mm$, $\mu = 0.00364Pl$, $\rho = 900kg/m^3$, $\zeta_i = 0.2$, $\zeta_o = 1$. $--$ dashed line: bulk flow model, dotted lines ···········: measurements bounds (95% of confidence), $-\cdot$ dot dashed line: measurement average.

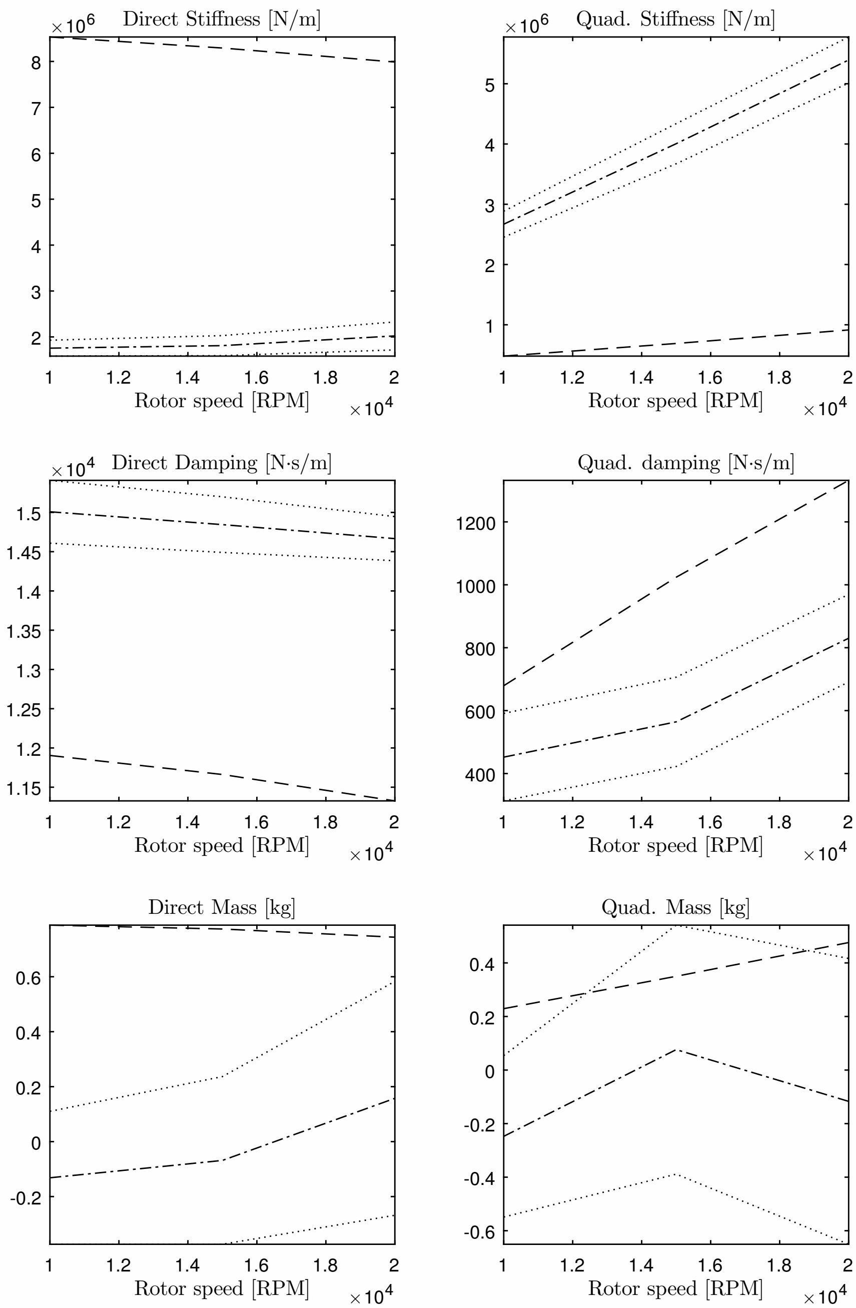

Figure B.21: Stiffness variation with the rotor speed Ω. inlet $GVF = 98.2\%$, $P_{0,inlet} = 61.2bar$, $P_{0,outlet}/P_{0,inlet} = 0.6$, D=89cm, L/R=1.5, $H = 0.18mm$, $\mu = 0.00364Pl$, $\rho = 900kg/m^3$, $\zeta_i = 0.2$, $\zeta_o = 1$. – – dashed line: bulk flow model, dotted lines ············: measurements bounds (95% of confidence), –· dot dashed line: measurement average.

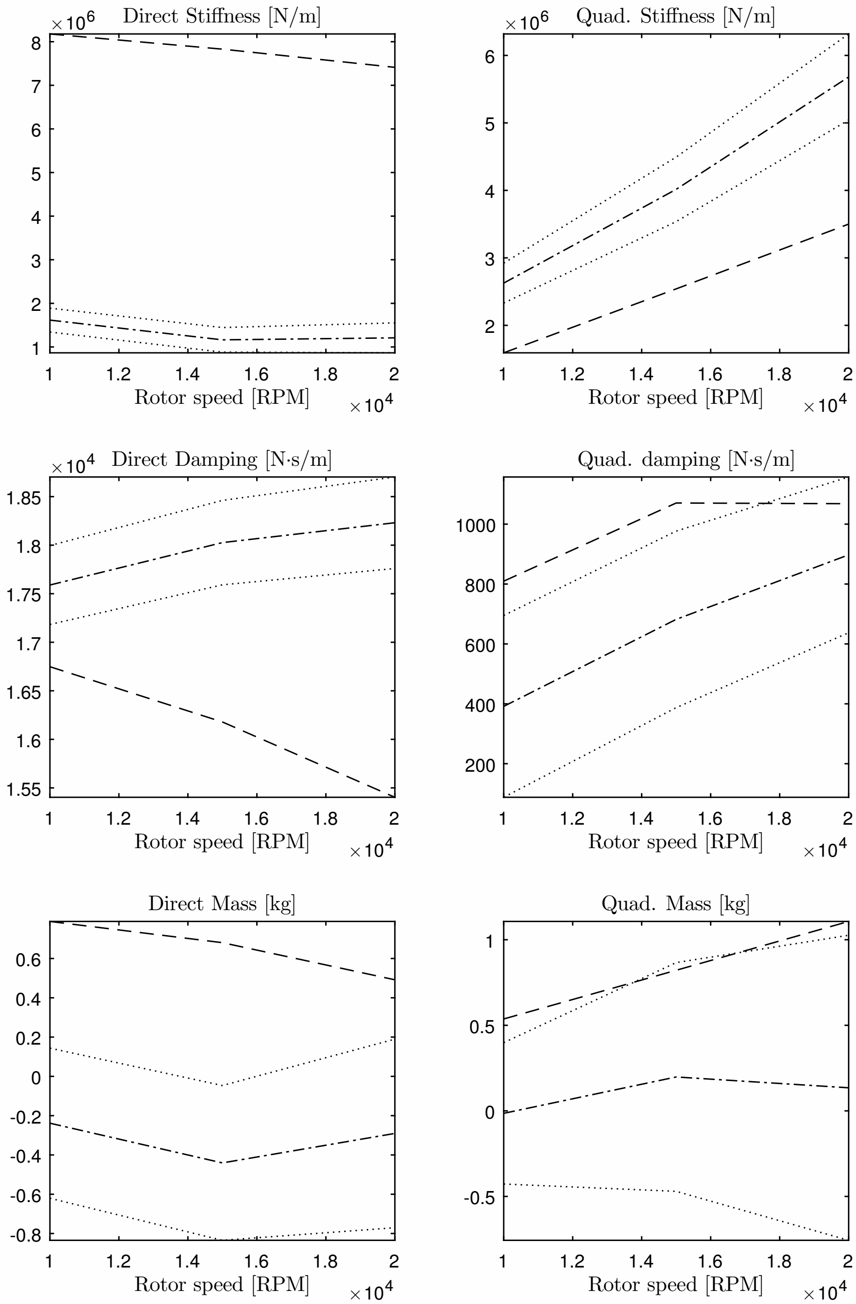

Figure B.22: Stiffness variation with the rotor speed Ω. inlet $GVF = 92.6\%$, $P_{0,inlet} = 61.2bar$,$P_{0,outlet}/P_{0,inlet} = 0.5$, D=89cm, L/R=1.5, $H = 0.18mm$, $\mu = 0.00364Pl$, $\rho = 900kg/m^3$, $\zeta_i = 0.2$, $\zeta_o = 1$. $--$ dashed line: bulk flow model, dotted lines ⋯⋯⋯: measurements bounds (95% of confidence), $-\cdot$ dot dashed line: measurement average.

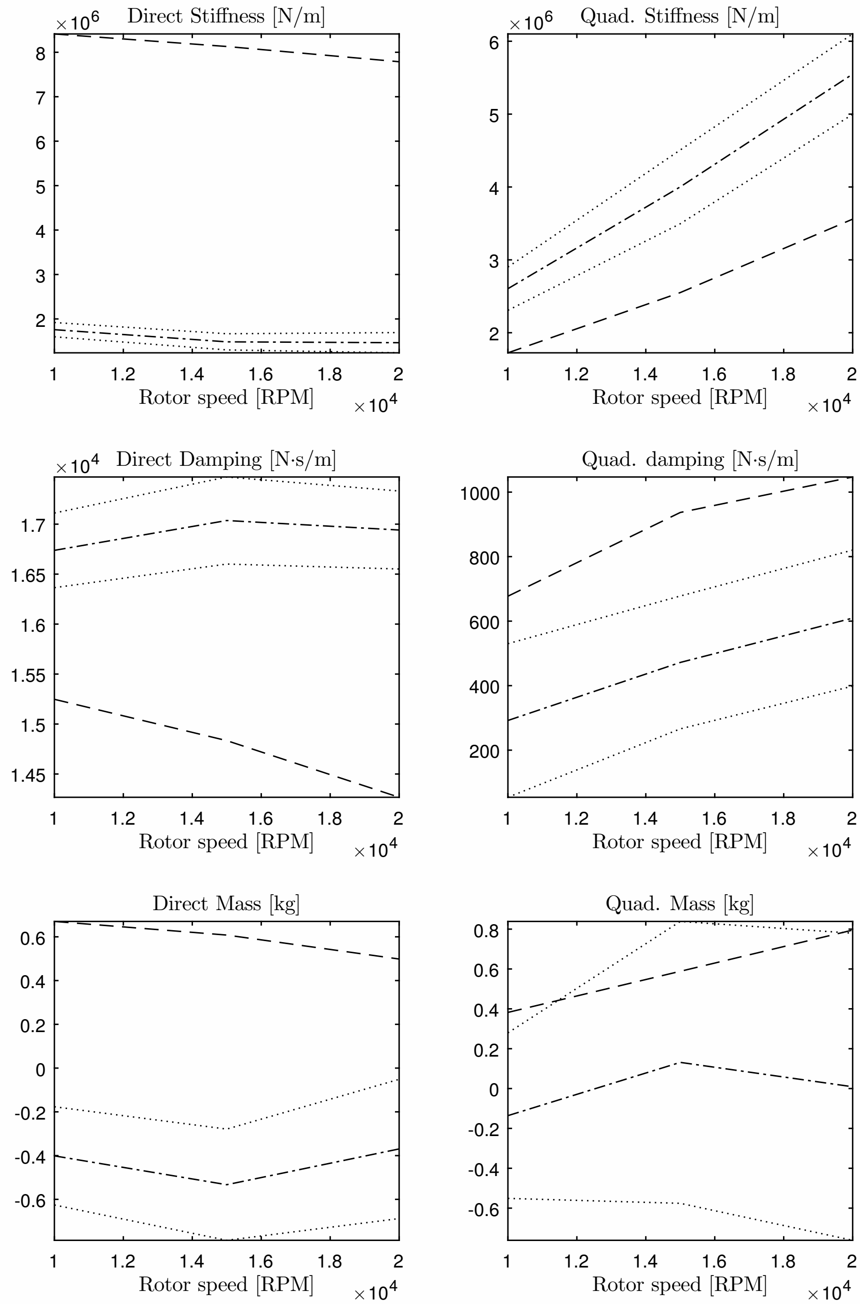

Figure B.23: Stiffness variation with the rotor speed Ω. inlet $GVF = 95.5\%$, $P_{0,inlet} = 61.2bar$,$P_{0,outlet}/P_{0,inlet} = 0.5$, D=89cm, L/R=1.5, $H = 0.18mm$, $\mu = 0.00364Pl$, $\rho = 900kg/m^3$, $\zeta_i = 0.2$, $\zeta_o = 1$. – – dashed line: bulk flow model, dotted lines ············: measurements bounds (95% of confidence), –· dot dashed line: measurement average.

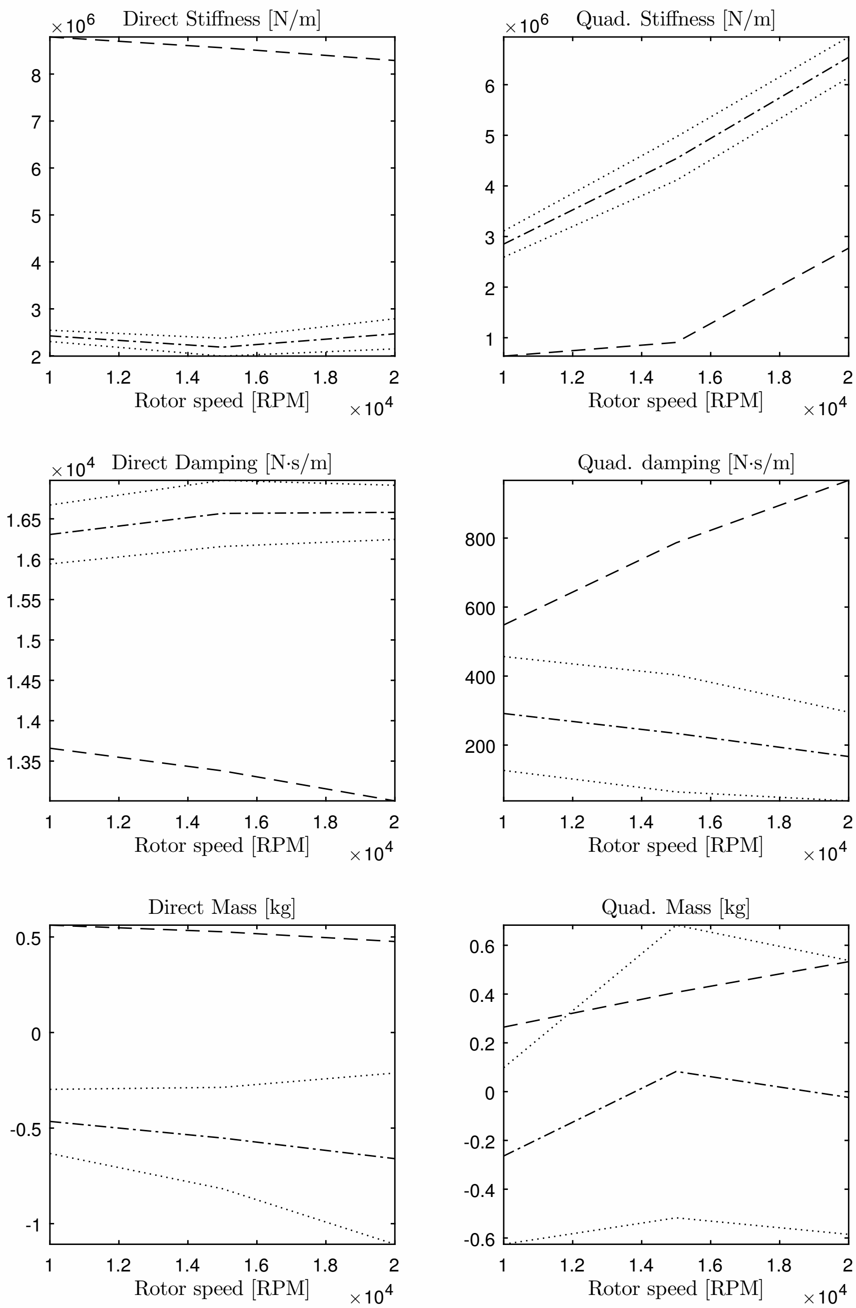

Figure B.24: Stiffness variation with the rotor speed Ω. inlet $GVF = 98.2\%$, $P_{0,inlet} = 61.2bar$,$P_{0,outlet}/P_{0,inlet} = 0.5$, D=89cm, L/R=1.5, $H = 0.18mm$, $\mu = 0.00364Pl$, $\rho = 900kg/m^3$, $\zeta_i = 0.2$, $\zeta_o = 1$. – – dashed line: bulk flow model, dotted lines ··········: measurements bounds (95% of confidence), –· dot dashed line: measurement average.

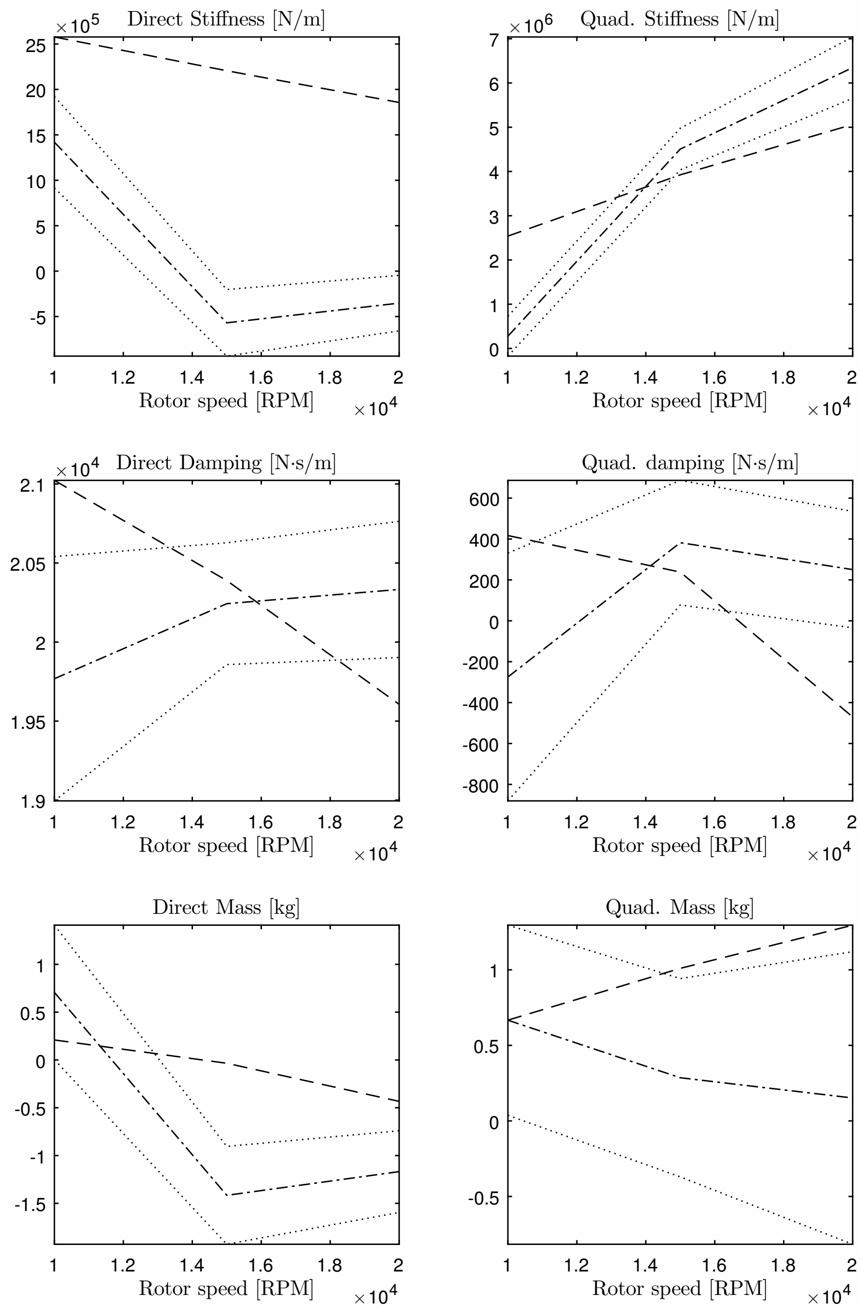

Figure B.25: Stiffness variation with the rotor speed Ω. inlet $GVF = 92.6\%$, $P_{0,inlet} = 61.2bar$,$P_{0,outlet}/P_{0,inlet} = 0.4$, D=89cm, L/R=1.5, $H = 0.18mm$, $\mu = 0.00364Pl$, $\rho = 900kg/m^3$, $\zeta_i = 0.2$, $\zeta_o = 1$. $--$ dashed line: bulk flow model, dotted lines ⋯⋯: measurements bounds (95% of confidence), $-\cdot$ dot dashed line: measurement average.

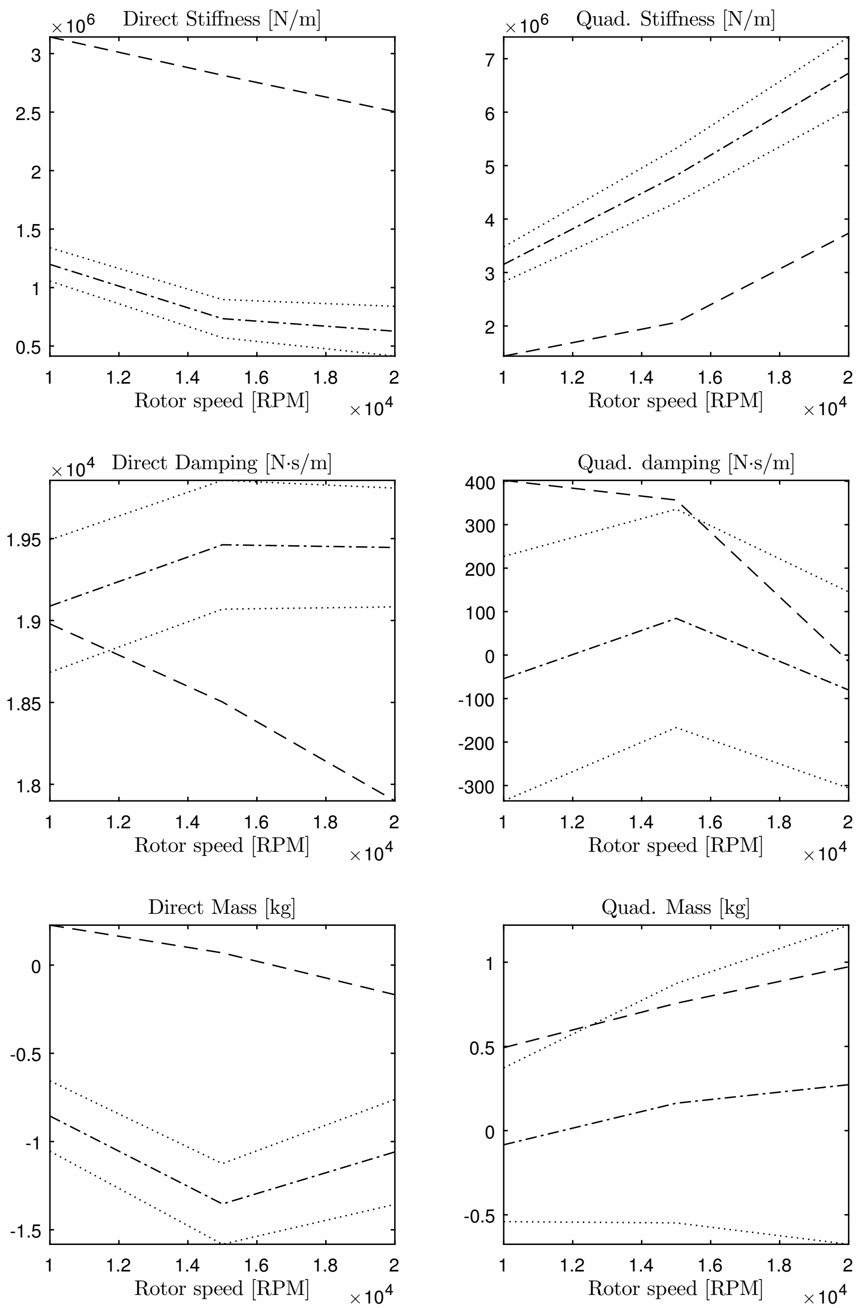

Figure B.26: Stiffness variation with the rotor speed Ω. inlet $GVF = 95.5\%$, $P_{0,inlet} = 61.2bar$,$P_{0,outlet}/P_{0,inlet} = 0.4$, D=89cm, L/R=1.5, $H = 0.18mm$, $\mu = 0.00364Pl$, $\rho = 900kg/m^3$, $\zeta_i = 0.2$, $\zeta_o = 1$. -- dashed line: bulk flow model, dotted lines ⋯⋯: measurements bounds (95% of confidence), -· dot dashed line: measurement average.

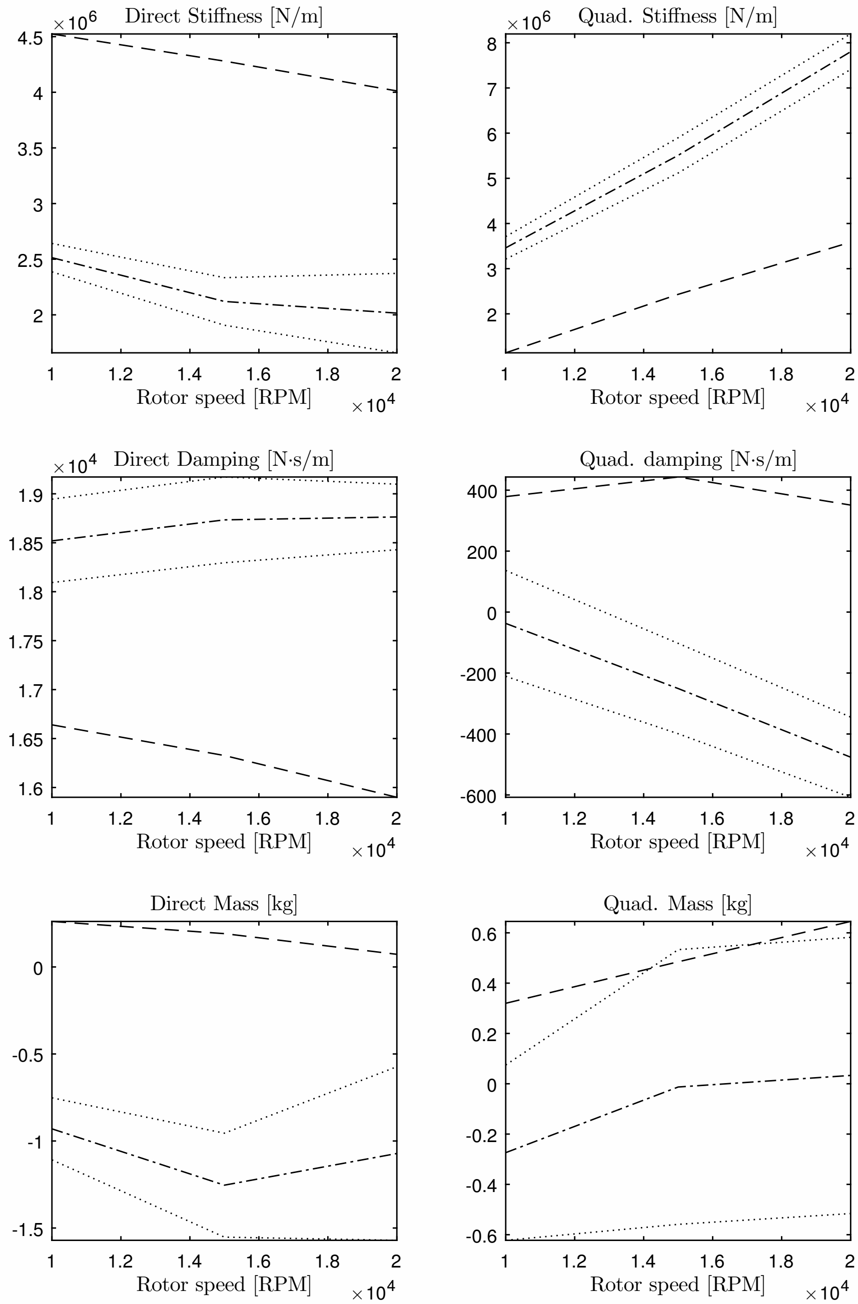

Figure B.27: Stiffness variation with the rotor speed Ω. inlet $GVF = 98.2\%$, $P_{0,inlet} = 61.2 bar$,$P_{0,outlet}/P_{0,inlet} = 0.4$, D=89cm, L/R=1.5, $H = 0.18mm$, $\mu = 0.00364Pl$, $\rho = 900kg/m^3$, $\zeta_i = 0.2$, $\zeta_o = 1$. -- dashed line: bulk flow model, dotted lines ············: measurements bounds (95% of confidence), -· dot dashed line: measurement average.

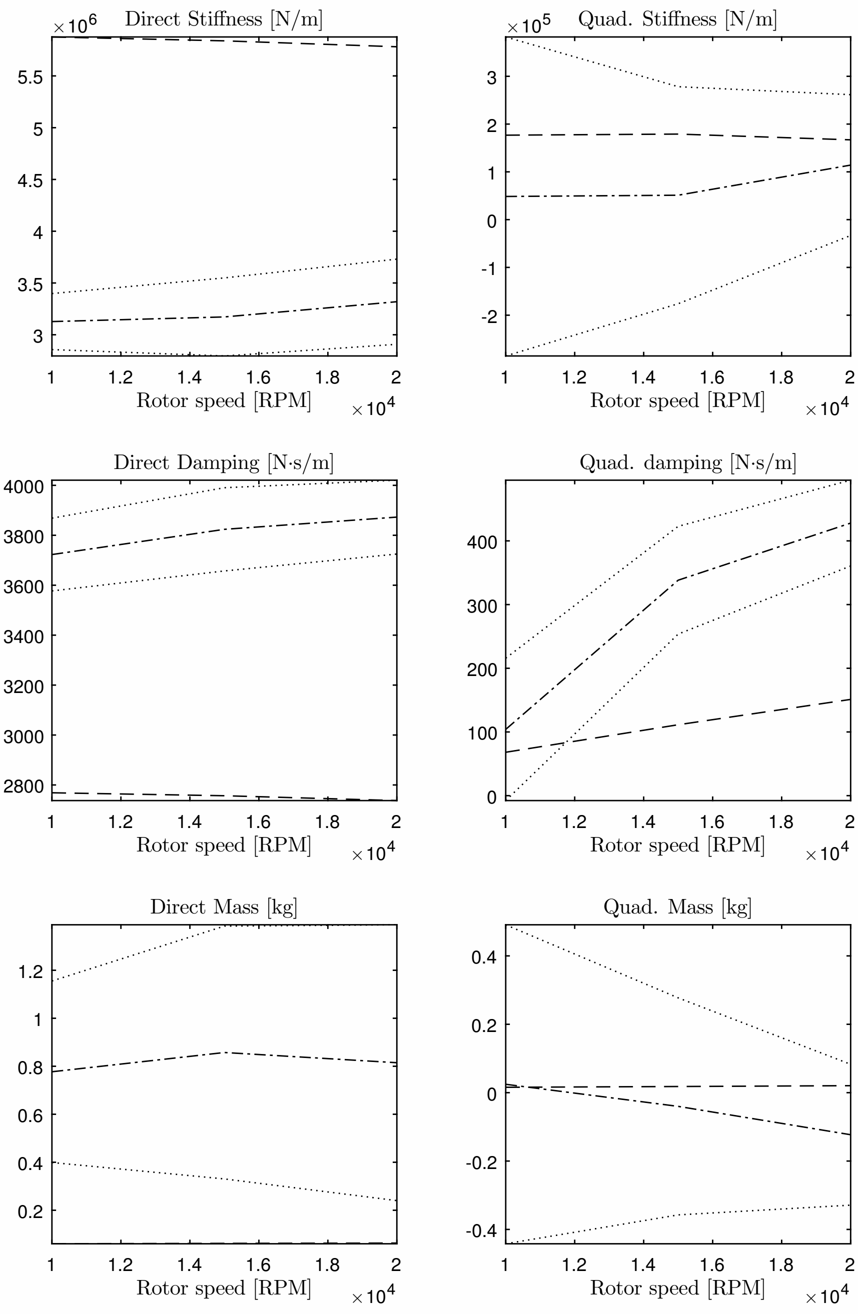

Figure B.28: Stiffness variation with the rotor speed Ω. inlet $GVF = 92.1\%$, $P_{0,inlet} = 61.2bar$,$P_{0,outlet}/P_{0,inlet} = 0.7$, D=89cm, L/R=0.58, $H = 0.18mm$, $\mu = 0.00364Pl$, $\rho = 900kg/m^3$, $\zeta_i = 0.2$, $\zeta_o = 1$. – – dashed line: bulk flow model, dotted lines ··········: measurements bounds (95% of confidence), – · dot dashed line: measurement average.

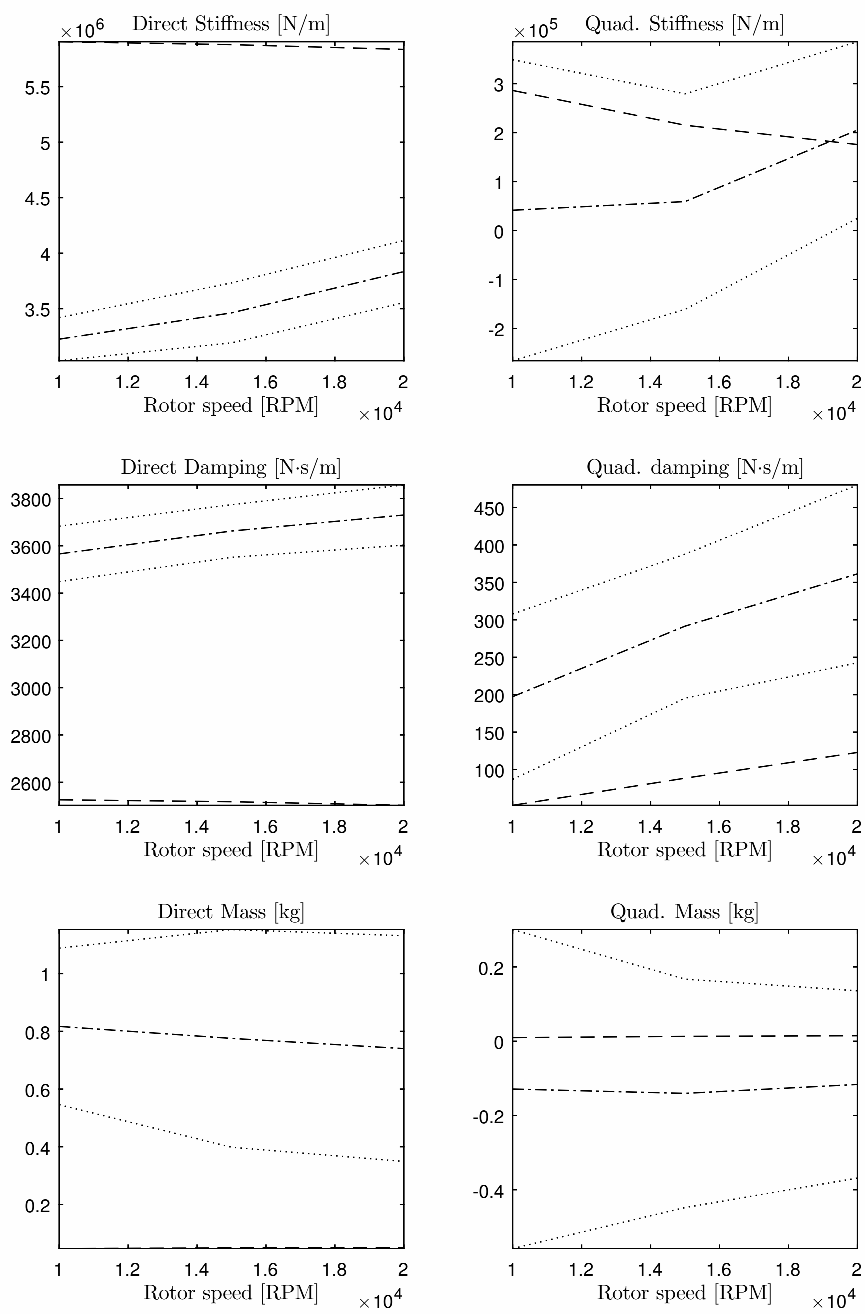

Figure B.29: Stiffness variation with the rotor speed Ω. inlet $GVF = 95.1\%$, $P_{0,inlet} = 61.2bar$,$P_{0,outlet}/P_{0,inlet} = 0.7$, D=89cm, L/R=0.58, $H = 0.18mm$, $\mu = 0.00364Pl$, $\rho = 900kg/m^3$, $\zeta_i = 0.2$, $\zeta_o = 1$. – – dashed line: bulk flow model, dotted lines ············: measurements bounds (95% of confidence), –· dot dashed line: measurement average.

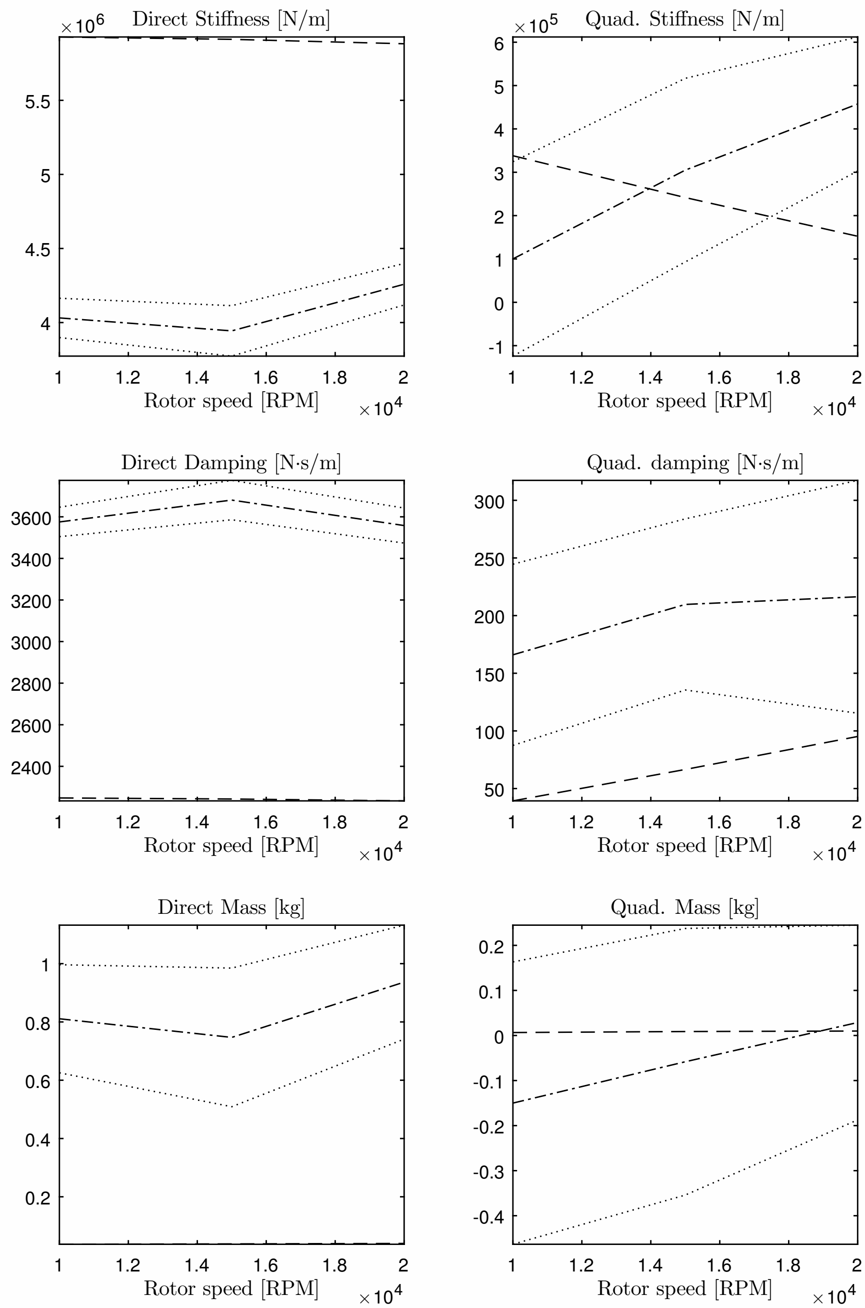

Figure B.30: Stiffness variation with the rotor speed Ω. inlet $GVF = 98.1\%$, $P_{0,inlet} = 61.2bar$,$P_{0,outlet}/P_{0,inlet} = 0.7$, D=89cm, L/R=0.58, $H = 0.18mm$, $\mu = 0.00364Pl$, $\rho = 900kg/m^3$, $\zeta_i = 0.2$, $\zeta_o = 1$. -- dashed line: bulk flow model, dotted lines ⋯⋯: measurements bounds (95% of confidence), -· dot dashed line: measurement average.

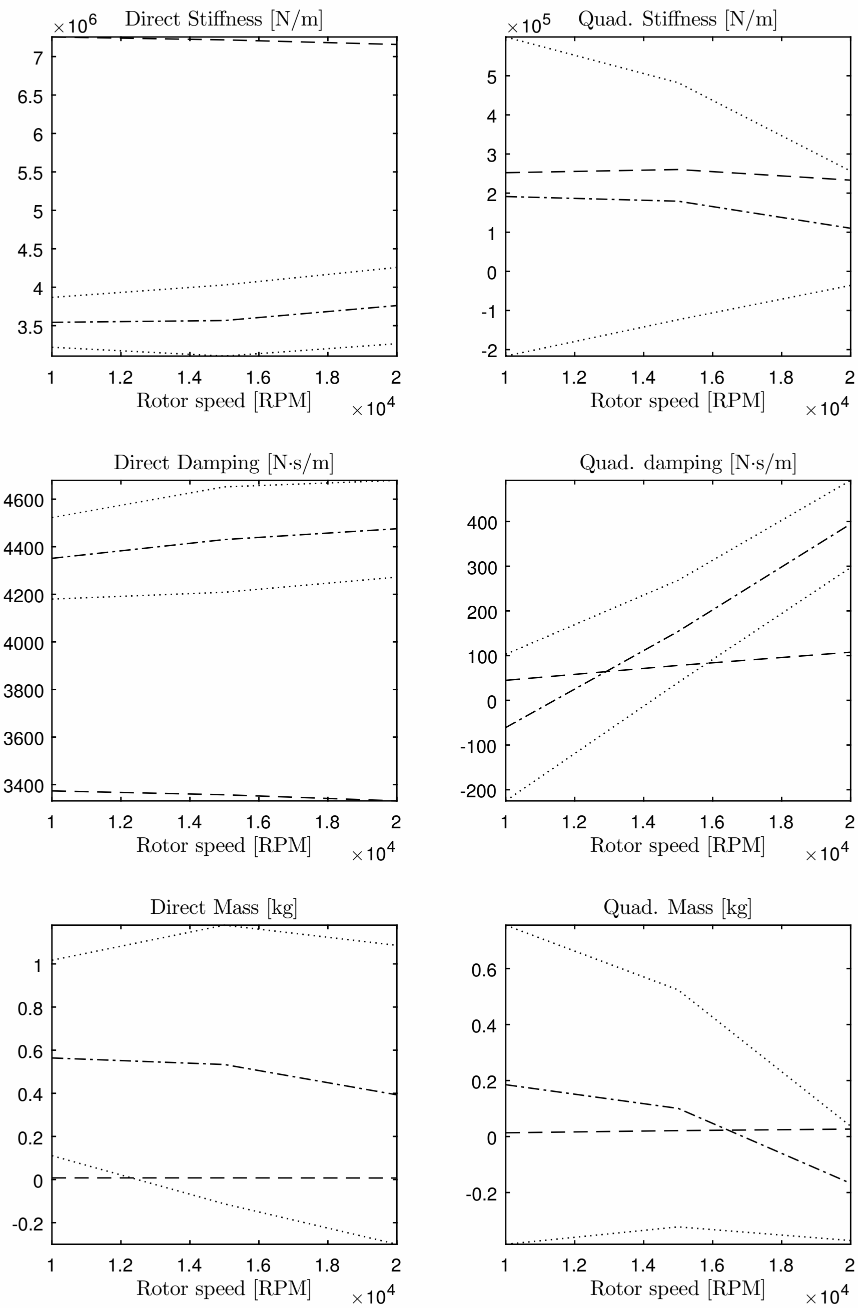

Figure B.31: Stiffness variation with the rotor speed Ω. inlet $GVF = 92.1\%$, $P_{0,inlet} = 61.2bar$,$P_{0,outlet}/P_{0,inlet} = 0.6$, D=89cm, L/R=0.58, $H = 0.18mm$, $\mu = 0.00364Pl$, $\rho = 900kg/m^3$, $\zeta_i = 0.2$, $\zeta_o = 1$. -- dashed line: bulk flow model, dotted lines ⋯⋯: measurements bounds (95% of confidence), -· dot dashed line: measurement average.

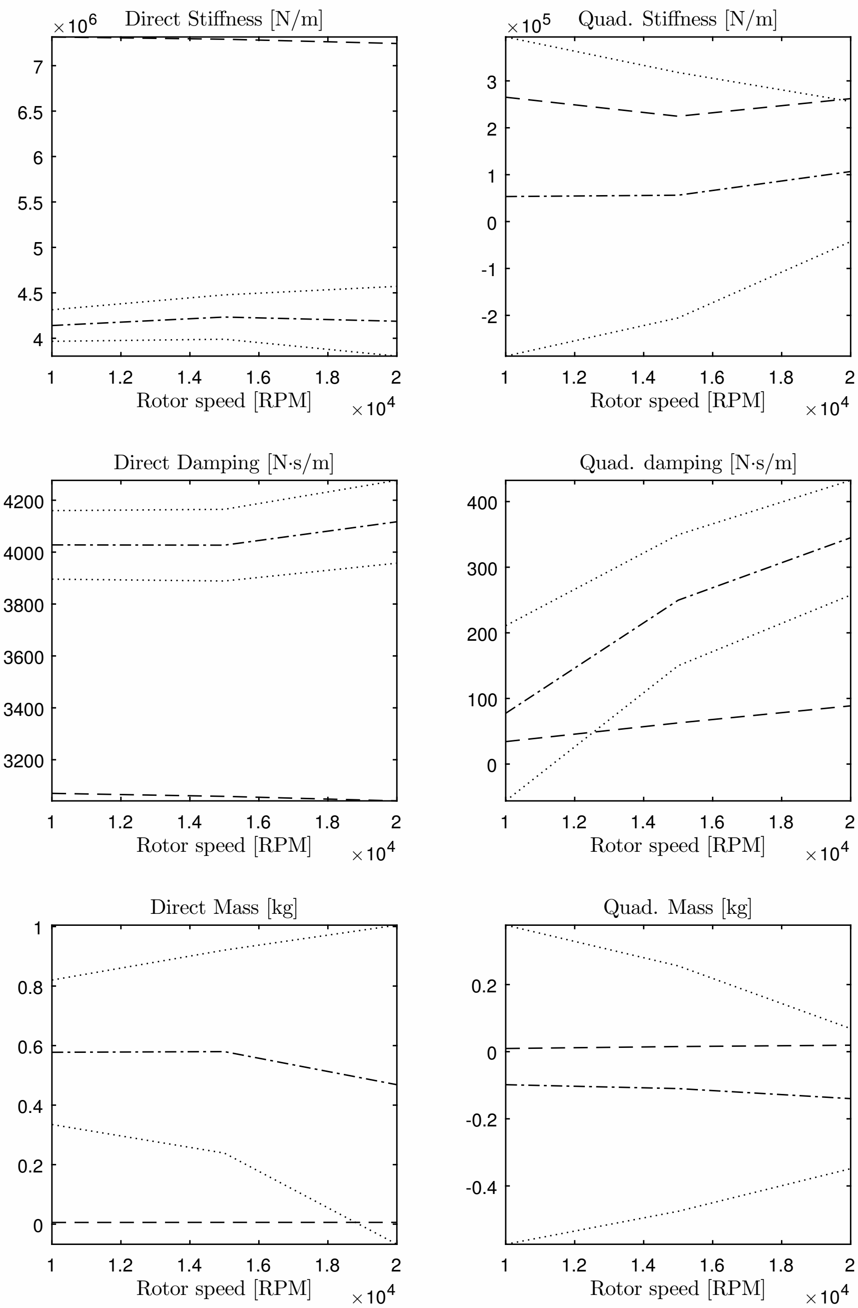

Figure B.32: Stiffness variation with the rotor speed Ω. inlet $GVF = 95.1\%$, $P_{0,inlet} = 61.2bar$,$P_{0,outlet}/P_{0,inlet} = 0.6$, D=89cm, L/R=0.58, $H = 0.18mm$, $\mu = 0.00364Pl$, $\rho = 900kg/m^3$, $\zeta_i = 0.2$, $\zeta_o = 1$. – – dashed line: bulk flow model, dotted lines ············: measurements bounds (95% of confidence), – · dot dashed line: measurement average.

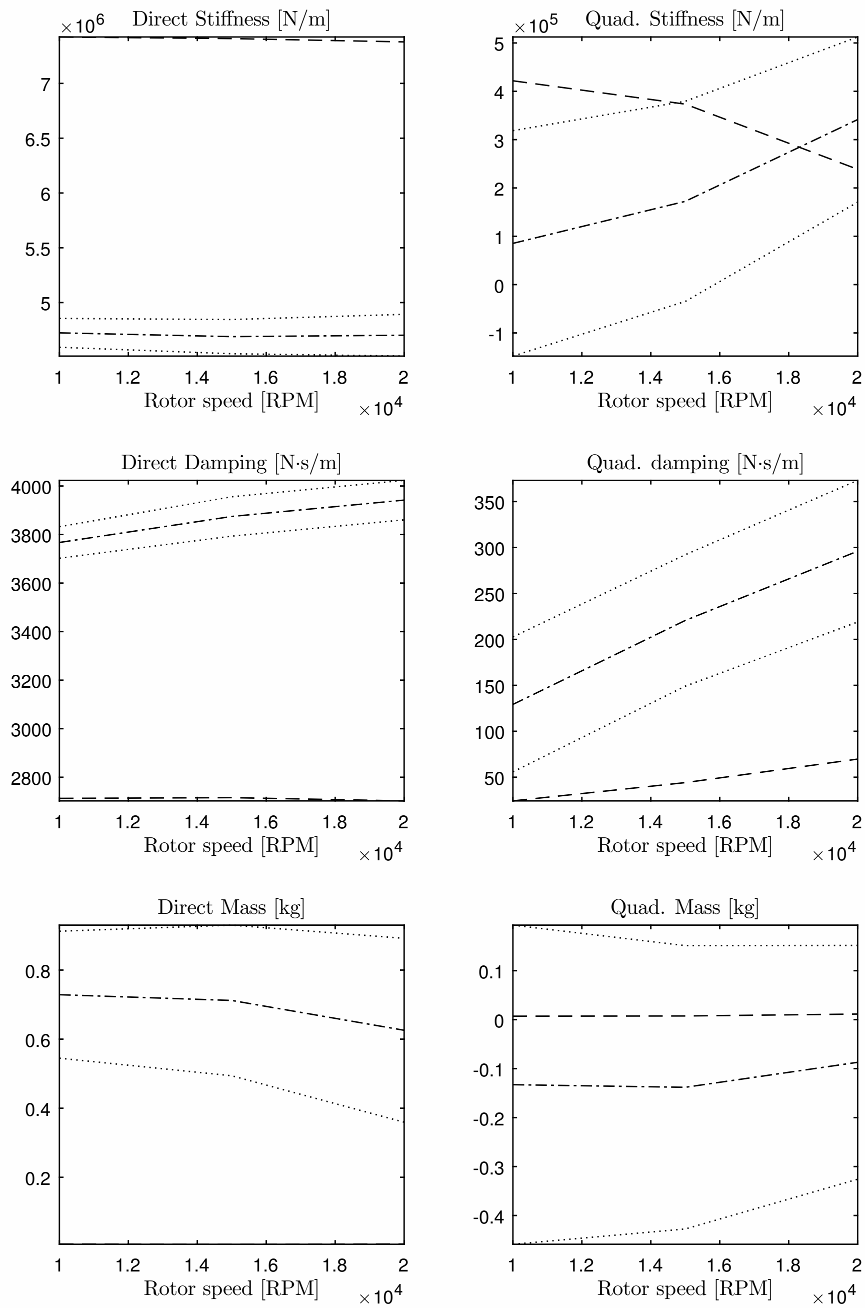

Figure B.33: Stiffness variation with the rotor speed Ω. inlet $GVF = 98.1\%$, $P_{0,inlet} = 61.2bar$,$P_{0,outlet}/P_{0,inlet} = 0.6$, D=89cm, L/R=0.58, $H = 0.18mm$, $\mu = 0.00364Pl$, $\rho = 900kg/m^3$, $\zeta_i = 0.2$, $\zeta_o = 1$. -- dashed line: bulk flow model, dotted lines ⋯⋯: measurements bounds (95% of confidence), -· dot dashed line: measurement average.

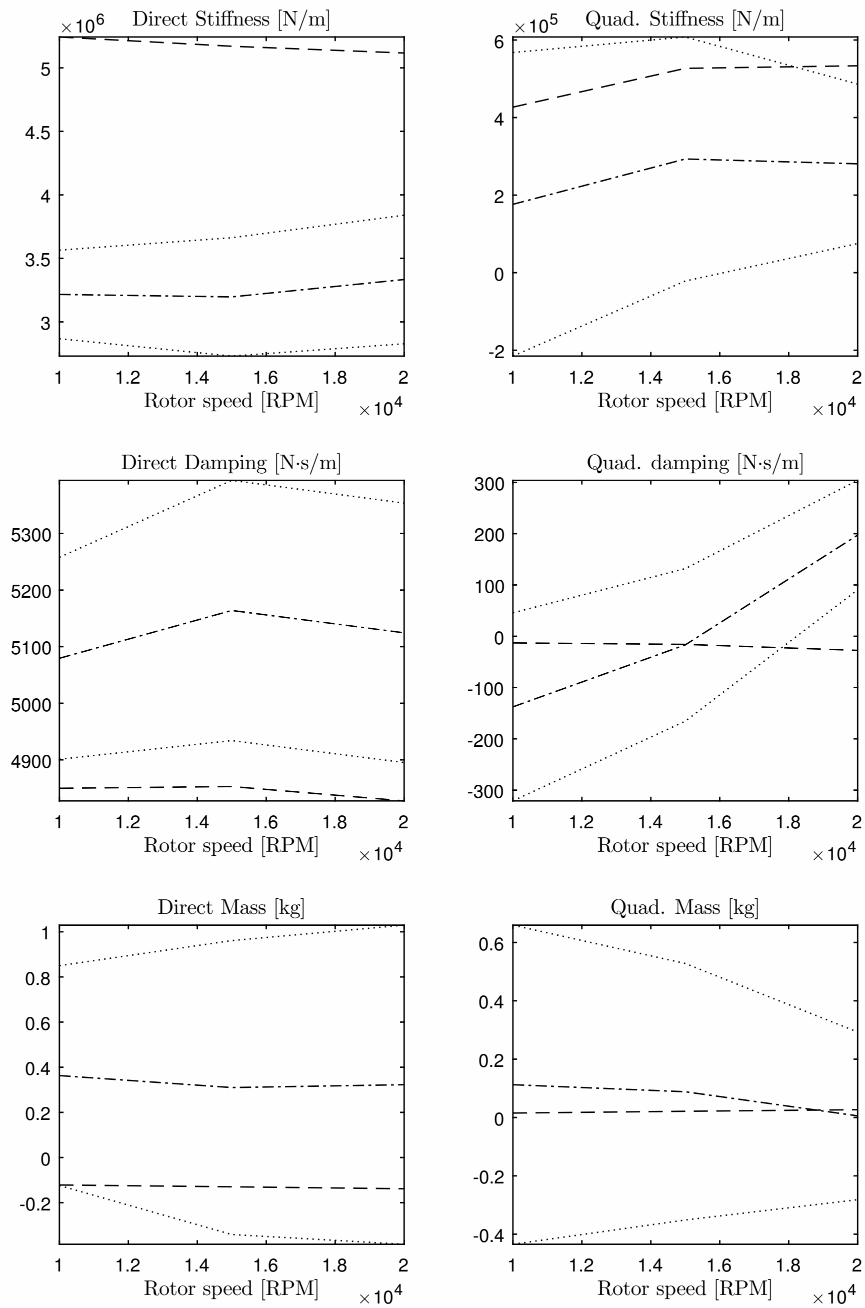

Figure B.34: Stiffness variation with the rotor speed Ω. inlet $GVF = 92.1\%$, $P_{0,inlet} = 61.2bar$,$P_{0,outlet}/P_{0,inlet} = 0.5$, D=89cm, L/R=0.58, $H = 0.18mm$, $\mu = 0.00364Pl$, $\rho = 900kg/m^3$, $\zeta_i = 0.2$, $\zeta_o = 1$. – – dashed line: bulk flow model, dotted lines ··········: measurements bounds (95% of confidence), –· dot dashed line: measurement average.

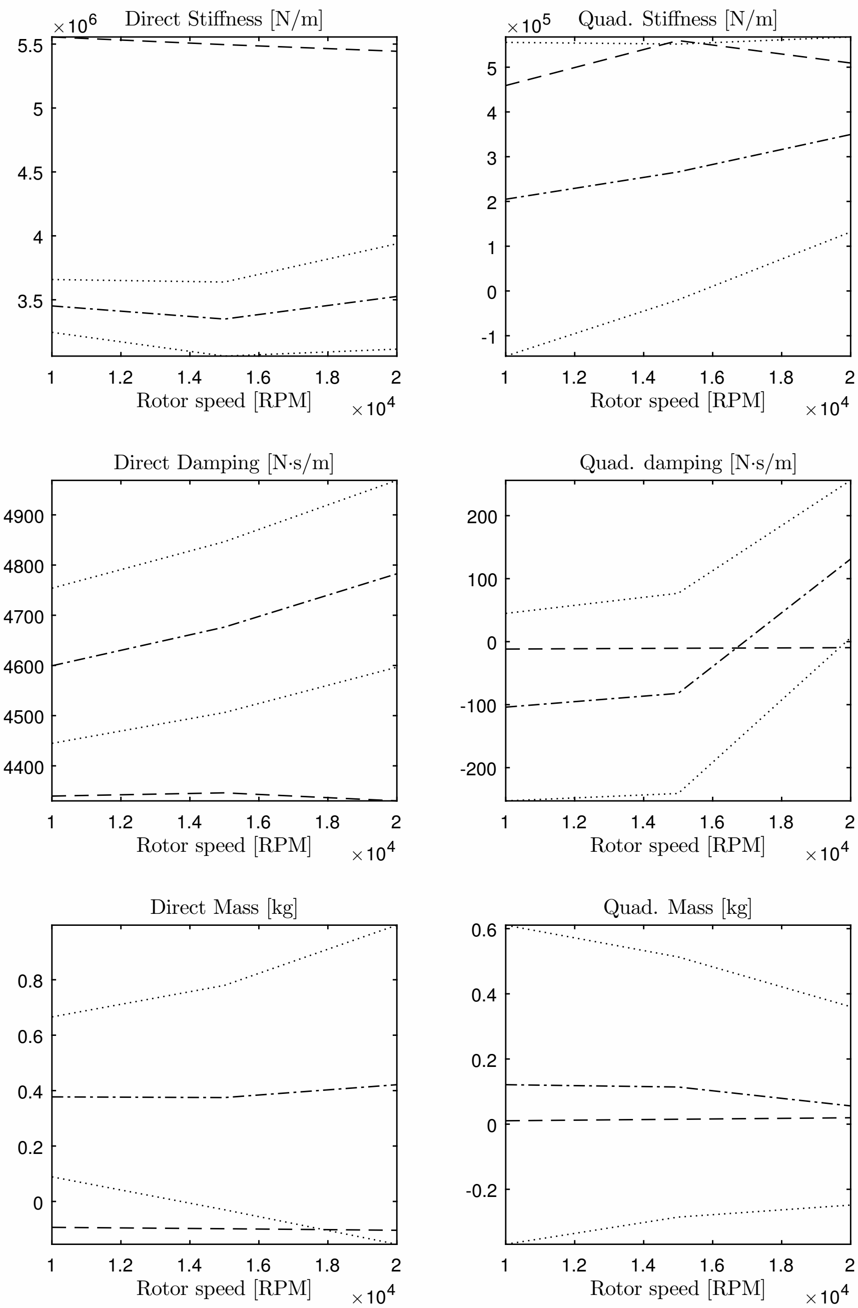

Figure B.35: Stiffness variation with the rotor speed Ω. inlet $GVF = 95.1\%$, $P_{0,inlet} = 61.2bar$,$P_{0,outlet}/P_{0,inlet} = 0.5$, D=89cm, L/R=0.58, $H = 0.18mm$, $\mu = 0.00364Pl$, $\rho = 900kg/m^3$, $\zeta_i = 0.2$, $\zeta_o = 1$. $--$ dashed line: bulk flow model, dotted lines ⋯⋯: measurements bounds (95% of confidence), $-\cdot$ dot dashed line: measurement average.

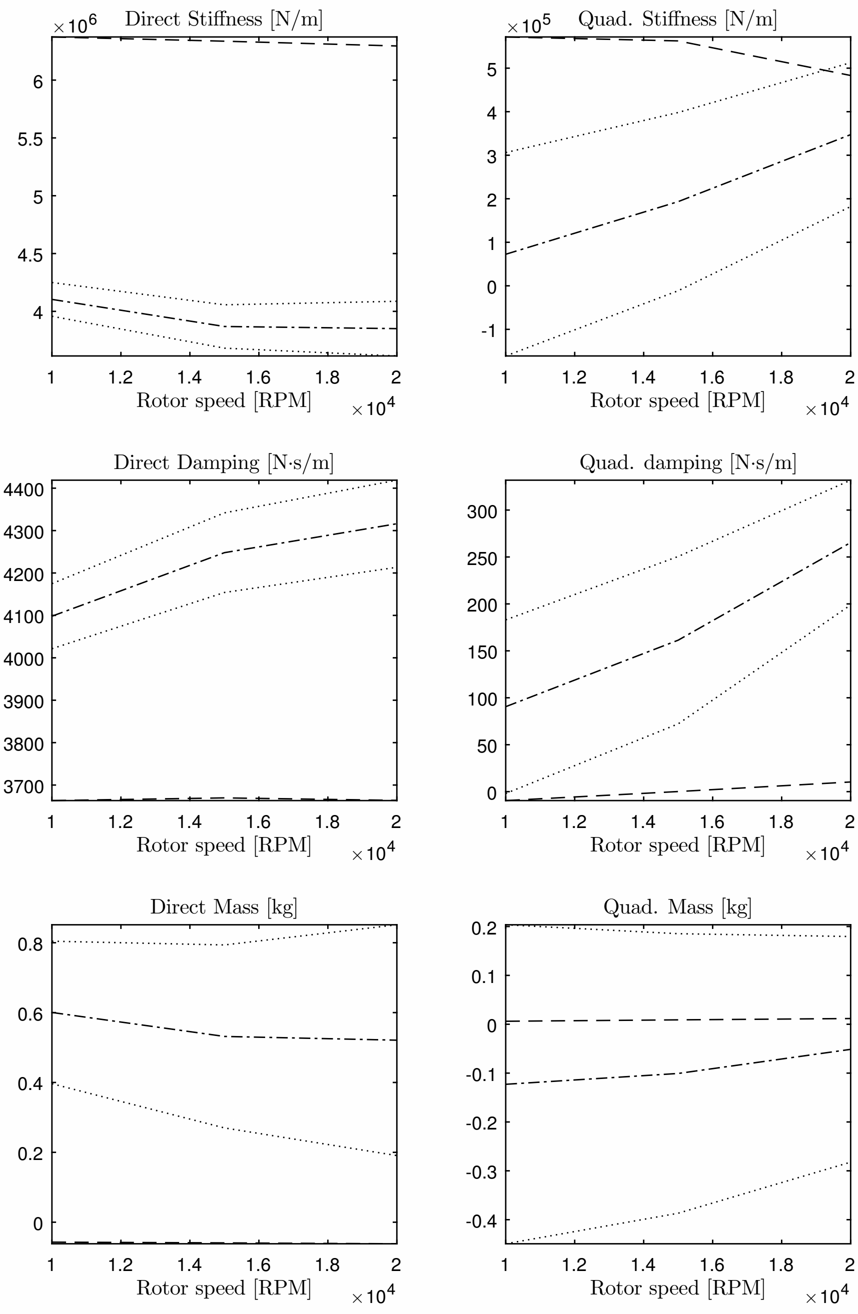

Figure B.36: Stiffness variation with the rotor speed Ω. inlet $GVF = 98.1\%$, $P_{0,inlet} = 61.2 bar$, $P_{0,outlet}/P_{0,inlet} = 0.5$, D=89cm, L/R=0.58, $H = 0.18mm$, $\mu = 0.00364Pl$, $\rho = 900kg/m^3$, $\zeta_i = 0.2$, $\zeta_o = 1$. – – dashed line: bulk flow model, dotted lines ⋯⋯: measurements bounds (95% of confidence), – · dot dashed line: measurement average.